THE UNIVERSITY *of* EDINBURGH

Thin Film Studies of Planar Transition Metal Complexes

Alexander Martin Whyte

A thesis submitted in fulfilment of the requirements

for the degree of Doctor of Philosophy to the

University of Edinburgh 2013

Abstract

At present the field of molecular electronics - also known as molecular semiconductors, organic semiconductors, plastic electronics or organic electronics - is dominated by organic materials, both polymeric and molecular, with much less attention being focused on transition metal based complexes despite the advantages they can offer. Such advantages include tuneable frontier orbitals through the ligand/metal interaction and the ability to generate stable paramagnetic species. Devices containing radical materials are particularly interesting in order to examine the interplay between conduction and spin - an effect which is not yet properly understood but can give rise to exotic behaviour.

A series of homoleptic, bis-ligand Ni(II) and Cu(II) complexes were prepared using three structurally related phenolic oxime ligands, 2-hydroxy-5-*t*-octylacetophenone oxime ($^{t\text{-}Oct}$saoH), 2-hydroxy-5-*n*-propylacetophenone oxime ($^{n\text{-}Pr}$saoH) and 2-hydroxyacetophenone oxime (^{H}saoH). The complexes were characterised by single-crystal X-ray diffraction, cyclic voltammetry, UV/Vis spectroscopy, field-effect-transistor measurements, DFT/TD-DFT calculations and in the case of the paramagnetic species, EPR and magnetic susceptibility. Variation of the substituent on the ligand from *t*-octyl to *n*-propyl to H enabled electronic isolation of the complexes in the crystal structures of M($^{t\text{-}Oct}$saoH)$_2$, which contrasted with π-stacking interactions observed in the crystal packing of M($^{n\text{-}Pr}$saoH)$_2$ and of M(^{H}saoH) (M = Ni, Cu). This was further evidenced by comparing the antiferromagnetic interactions observed in samples of Cu($^{n\text{-}Pr}$saoH)$_2$ and Cu(^{H}saoH)$_2$ with the ideal paramagnetic behaviour for Cu($^{t\text{-}Oct}$saoH)$_2$ down to 1.8 K. Despite isostructural single crystal structures for M($^{n\text{-}Pr}$saoH)$_2$, thin-film X-ray diffraction and SEM revealed different morphologies depending on the metal and the deposition method employed.

However, the complexes of M($^{n\text{-}Pr}$saoH)$_2$ and M(^{H}saoH) failed to demonstrate significant charge transport in an FET device despite displaying the ability to form π-stacking structures.

A series of planar Ni(II), Cu(II) and Co(II) dibenzotetraaza[14]annulenes (dbtaa) and dinapthotetraaza[14]annulenes (dntaa) were synthesised and studied crystallographically, optically, electrochemically and magnetically. Thin films of each of these complexes have been prepared by vacuum deposition to evaluate the field-effect transistor (FET) performance as well as the morphology and crystallinity of the film formed. Single crystal data revealed that Ni(dbtaa) and Cu(dbtaa) are isomorphous to each other, with Co(dbtaa) displaying a different crystallographic packing. The electrochemistry and UV/Vis absorption studies indicate the materials are redox active and highly coloured, with molar extinction coefficients as large as 80,000 $M^{-1}cm^{-1}$ in the visible region. The paramagnetic Cu(II) and Co(II) complexes display weak 1-dimensional antiferromagnetic interactions and were fit to the Bonner-Fisher chain model. The data revealed that the Co(II) species possesses much stronger magnetic exchange interactions compared with the Cu(II) complex. Each of the materials formed polycrystalline films when vacuum deposited and all showed p-type field-effect transistor behaviour, with modest charge carrier mobilities in the range of 10^{-5} to 10^{-9} cm^2 V^{-1} s^{-1}. SEM imaging of the substrates indicates that the central metal ion, and its sublimation temperature, has a crucial role in defining the morphology of the resulting film.

Structurally related Cu(II) and Ni(II) dithiadiazoletetraaza[14]annulene (dttaa) macrocycles were synthesised and studied in the context of their thin film electrochemical, conducting and morphological properties. Both the Ni(II) and Cu(II) complexes were found to be volatile under reduced pressure, which allowed crystals of both materials to be grown and the single crystal structures solved. Interestingly, the crystal packing of these heterocyclic macrocycles varies depending on whether the central metal ion is Cu(II) or Ni(II), which is in contrast to the analogous

dibenzotetrazaannulenes complexes. Soluble Ni(II) analogues containing benzoyl groups on the *meso*- positions of the macrocycle (dttaaBzOR) were also prepared and contrasted with the insoluble Ni(dttaa) complexes in terms of their solution optical and electrochemical properties. Thin film electrochemical studies of Cu(dttaa) and Ni(dttaa) showed chemically reversible oxidative processes but on scanning to reductive potentials the films disintegrated almost immediately as the bulky counter tetrabutylammonium cation entered the thin film. FET studies undertaken on polycrystalline films of both complexes, using various device configurations and surface treatments, failed to realise any gate effect. Thin film XRD measurements indicate that films of both complexes formed by vacuum deposition are crystalline and contain a mixture of molecular alignments, with molecules aligning "edge on" and "face down" to the substrate. SEM imaging failed to effectively resolve the morphology of the films implying the sizes of the crystallites are small, which may help to explain the lack of FET effect.

A series of *bis*-ligand diimine Ni, Cu and Pd complexes have been synthesised from the ligand 4,5-bis(dodecyloxy)benzene-1,2-diamine ($dbdaH_2$). The same ligand was also used to prepare a series of soluble Cu(II) and Ni(II) tetraaza[14]annulene macrocycles. All the *bis*-ligand diimine complexes were found to suffer from instability in air due to the ease at which the complexes are oxidised. The Ni complex, $Ni(dbda)_2$, was found to display a NIR transition in the region of 971 to 1024 nm depending on the polarity of the solvent that the molecule is dissolved in. Solution electrochemistry studies of $Ni(dbda)_2$ reaffirmed the facile nature of the first oxidative process, with the HOMO energy calculated at -4 eV by hybrid-DFT. This compound failed to yield semiconducting behaviour in an FET device despite the use of surface treatments aimed at promoting suitable molecular alignment across the conducting channel.

Declaration

I do hereby declare that this thesis was composed by myself and that the work described within is my own, except where explicitly stated otherwise.

Alexander Martin Whyte

April 2013

Publications and Thesis Format

The following list cites work published by the author during the course of this PhD:

1) Whyte, A. M.; Roach, B.; Henderson, D. K.; Tasker, P. A.; Matsushita, M. M.; Awaga, K.; White, F. J.; Richardson, P.; Robertson, N., *Inorganic Chemistry* **2011,** *50,* 12867-12876.

2) Valentine, R. A.; Whyte, A.; Awaga, K.; Robertson, N., *Tetrahedron Letters* **2011,** *53,* 657-660.

3) Maganas, D.; Krzystek, J.; Ferentinos, E.; Whyte, A. M.; Robertson, N.; Psycharis, V.; Terzis, A.; Neese, F.; Kyritsis, P., *Inorganic Chemistry* **2012,** *51,* 7218-7231.

4) Whyte, A. M.; Shuku, Y.; Nichol, G. S.; Matsushita, M. M.; Awaga, K.; Robertson, N., *Journal of Materials Chemistry* **2012,** *22,* 17967-17975.

Chapter 3 of this thesis is based on some of the work previously communicated in publication **1**, with Chapter 4 based upon studies reported in publication **4**. Chapters 2 and 3 contain large amounts of additional experimental data, most of it computational results, which are provided electronically in Appendix I and II (see attached cd). Chapters 5 and 6 comprise as yet unpublished research. Publications **2** and **3** are from unrelated, collaborative work carried out during the course of the PhD but not included in this thesis.

Acknowledgments

First and foremost, I would like to thank my supervisor, Dr Neil Robertson, for giving me the opportunity to undertake a PhD in his laboratory. I'd like to express by sincere gratitude for his guidance on my research during the project.

Crucial to almost all of the work I carried out was Prof Kunio Awaga of Nagoya University, who allowed me to visit his lab three times, took me out for dinner numerous times and, while in Japan, constantly made time to discuss science with me throughout my stays. Everybody in his group in Nagoya was extremely welcoming and I'll never forget their hospitality. His Assistant Professor, Prof Matsushita, was a constant source of advice on FET measurements and, in general, of all other things organic semiconductors. The Associate Professor in the group, Professor Yoshikawa, was also extremely kind and always made time to talk to me each day, usually entertaining me with his amusing stories or his criticisms of lazy students. Also from that group, Shuku Yoshiaki and Simon Dalgleish (formerly of the Robertson group), provided considerable help, in particular with Chapter 5 of this thesis. When I was no longer able to travel to Japan, they both kindly agreed to receive and study my samples.

I am also extremely grateful to Prof Peter Tasker for all his help with the phenolic oxime work, both in terms of practical synthetic advice and for his suggestions on my first publication. Ben Roach also deserves recognition for his contribution and useful suggestions with regard to the practical end of that project.

I would like to thank the crystallography team, Prof. Simon Parsons, Dr Gary Nicol and Dr Fraser White, for all their time and effort solving my crystal structures and for helping me with the various crystallographic problems I inevitably encounter when I try and refine a structure myself! I am also grateful for the other analytical services provided by Stephen Boyer, Alan Taylor and Lorna Murray, in the form of microanalysis, mass spectrometry and NMR, respectively.

Patricia Richardson is also due massive credit for always making time to help with my computational problems despite being extremely busy all the time.

I am indebted to all the members of the Robertson group (well, most of them) that I have worked with, past and present, for lots of useful discussions, assistance and, most importantly, office teas/cakes/biscuits. In particular, I'd like to single out Simon, Miquel, Max, Luca and Georg for special praise. Working on closely related topics, they have provided useful suggestions, theoretical discussions and, in some cases, sound synthetic advice.

I should thank my family and my girlfriend, Jennifer, for constantly supporting me, annoying me and asking me stupid questions. I know you only do it because you care.

Most importantly, I would like to thank the funding bodies EPSRC and Japanese Science and Technology Agency (JST) for supporting this UK-Japan collaborative project. I'd also like to express my extreme gratitude to the RSC who have provided funding for every major conference that I have attended and to the Chares and Barbara Tyre Trust who have provided additional funding to support my studies.

Structures

Structures synthesised during the course of this work:

Chapter 3

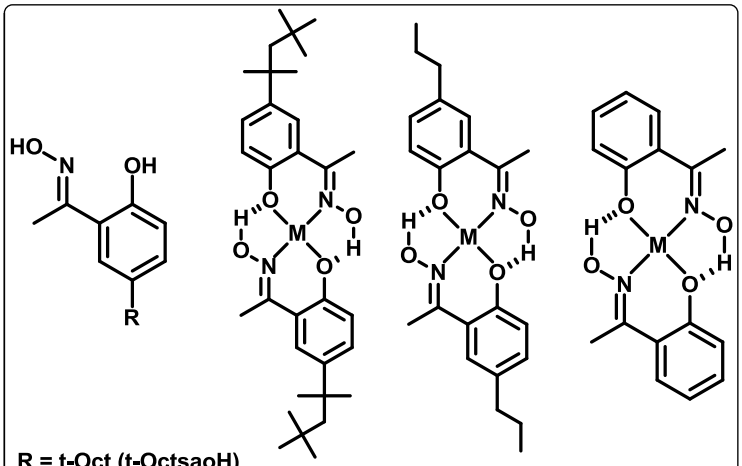

Chapter 4

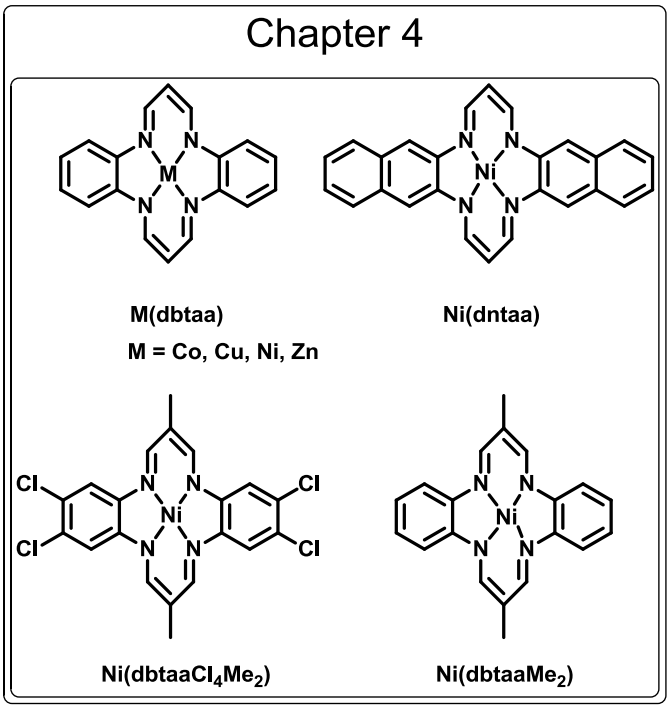

Chapter 5

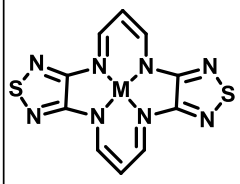

M(dttaa), M = Cu, Ni, Pd

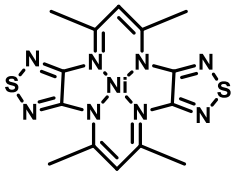

Ni(dttaaMe$_4$)

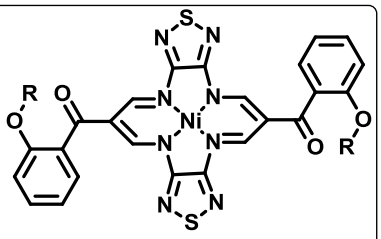

Ni(dttaaBzOR), R = ethyl, butyl

Chapter 6

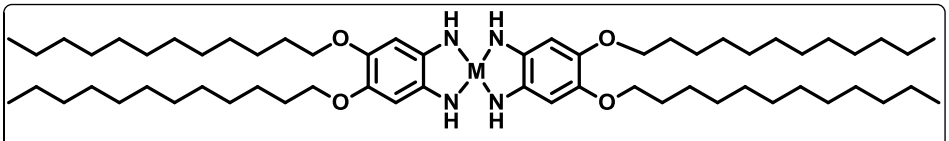

M(dbda)$_2$
M = Ni, Cu, Pd

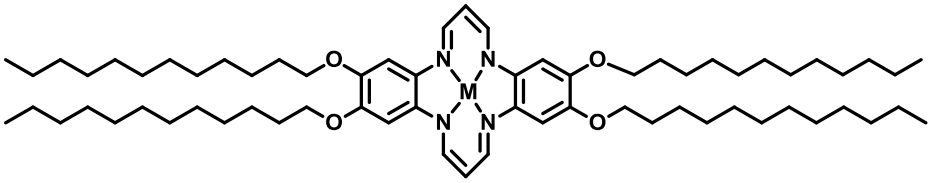

M(ddbtaa)
M = Ni, Cu

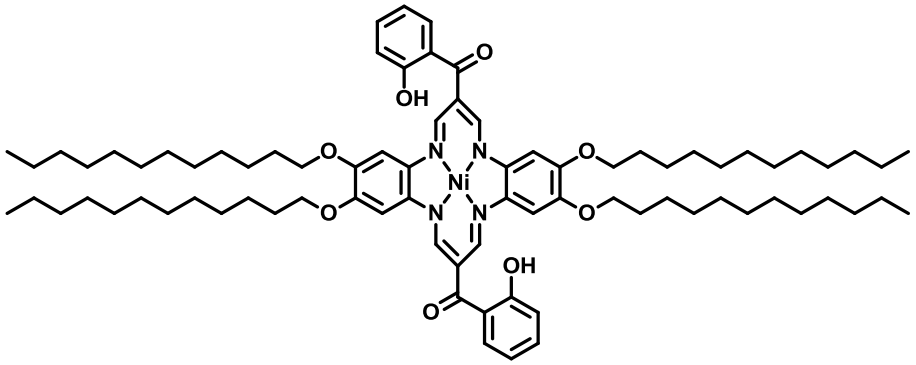

Ni(ddbtaaBz)

Abbreviations

AFM – Atomic force microscopy

$CHCl_3$ - Chloroform

CV - Cyclic voltammetry

CI – Chemical ionisation

Dbtaa – Dibenzotetraaza[14]annulene

DCM - Dichloromethane

Dntaa – Dinaphthotetraaza[14]annulene

DPV – Differential pulse voltammetry

DFT – Density functional theory

DMF – Dimethylformamide

DSC – Differential scanning calorimetry

Dttaa – Dithiadiazoletetraaza[14]annulene

EPR – Electron paramagnetic resonance

EI – Electron ionisation

ESI – Electrospray ionisation

EtOH – Ethanol

FAB – Fast atom bombardment

FET – Field effect transistor

FTO – Fluorine doped tin oxide

HF – Hartree-Fock

HH – Head to head

HMDS – Hexamethyldisiloxane

HOMO – Highest occupied molecular orbital

Hrs – Hours

HT – Head to tail

ITO – Indium tin oxide

IPA – Isopropylalcohol or propan-2-ol

IR – Infrared

LCD – Liquid crystal display

LED – Light emitting diode

LUMO – Lowest unoccupied molecular orbital

MeCN - Acetonitrile

MeOH – Methanol

MS – Mass spectrometry

NIR – Near infrared

NMR – Nuclear magnetic resonance

OFET – Organic field effect transistor

OLED – Organic light emitting diode

OTS – Octadecyltrichlorosilane

Pc - Phthalocyanine

PCM – Polarisable continuum model

PVD – Physical vapour deposition

QCM – Quartz crystal microbalance

RR – Regioregular

RT – Room temperature

Salox – Salicylaldoxime or salicylketoxime

SAM –Self assembled monolayer

SEM – Scanning electron microscopy

SMM – Single molecule magnet

SQUID – Superconducting quantum interference device

TD-DFT – Time-dependent density functional theory

TFT – Thin film transistor

TIP – Temperature independent paramagnetism

TTF - Tetrathiafulvalene

UV – Ultraviolet

Vis - Visible

XRD – X-ray diffraction

Contents

Chapter 1: Introduction

1.1. Inorganic semiconductors

1.1.1. Overview

Semiconductors form the basis of the electronic equipment used in our everyday lives, which helps to make the electronics industry the largest in the world.[1, 2] Modern electronics are based primarily on purely inorganic materials such as silicon and gallium arsenide, with single crystal silicon as the most commonly used semiconductor in modern electronic devices. Aside from crystalline materials, amorphous silicon (a-Si) has become the most economically significant semiconductor at present; it is currently the most common active layer in devices such as thin film transistors (TFTs).[3] Such TFTs find widespread use as the switching element in active matrix liquid crystal displays (AMLCDs).[4, 5]

Aside from purely inorganic materials, the field of organic semiconductors is now garnering much interest among the academic community. So called "organic semiconductors", commonly known by other aliases such as "plastic electronics", "organic electronics" and "molecular semiconductors", are now being proposed for a wide ranges of cheap and flexible applications. Such applications include display drivers and radio-frequency ID (RFIDs) tags.[6-8]

Consistent to both organic and inorganic semiconductors is that they must both conduct electrons and/or holes to find application. The conductivity of a material (σ) is given by Equation 1, where n is the number of charge carriers, e is the charge of the charge carrier and μ is the charge carrier mobility, which is an intrinsic property of a given conducting material. For TFT purposes, large charge carrier mobilities are a requirement in order to realise the kind of fast device switching speeds necessary for commercial application.[9]

Equation 1 $\sigma = n.e.\mu$

There are some notable differences between inorganic and organic semiconductors and their mode of operation. Transistors based on inorganic materials most commonly operate in charge carrier inversion mode, whereas, to date, organic materials operate only in accumulation mode.[9] In inversion mode a p-type material is placed between two n-type materials (source and drain electrodes) and applying a positive gate voltage creates an n-type channel through which current can flow.[9] Inorganic semiconductors consist of covalently bonded 3D lattices, with bond strengths as high as 300 kJ/mol in the case of Si.[10] In contrast, organic semiconductors usually comprise 1D polymeric chains or discrete molecules held together by weak supramolecular interactions, with energies less than 40 kJ/mol.[10] The obvious structural difference, between inorganic and molecular semiconductors, necessitates the use of different models to describe their conductivity, which in the case of inorganic materials is band theory and in the case of molecular systems is hopping theory. In the case of inorganic semiconductors the charge carrier type can be controlled by doping, however, in the case of organic materials the carrier type is generally a material property.

The device performance of traditional inorganic semiconductors is very good as a result of their lattice nature but the major drawback is that materials are often hard and brittle. The major advantage of molecular electronics has been the ability to produce flexible devices or displays. However, recent developments have shown that inorganic materials can also be incorporated onto large area, flexible substrates for use in displays or transistors.[3, 4]

Although advances have been made in the field of molecular electronics, materials do suffer from poor charge carrier mobility and degradation in air. In contrast, inorganic materials tend to be stable in air and generally offer much higher charge carrier mobilities. In terms of performance, single crystals of silicon can have room temperature charge carrier mobilities as high as a few 10^2 to approximately a few 10^3 $cm^2\ V^{-1}\ s^{-1}$, but in comparison the leading organic materials tend to exhibit mobilities two to three orders of magnitude lower.[11] However, the challenge for molecular electronics is not to compete with single crystal silicon but to compete with amorphous silicon, both in terms of performance and processing cost. In some cases, the charge carrier mobility of organic materials now exceeds that of amorphous silicon.[12]

Another aspect of device fabrication to consider is that inorganic TFTs have been manufactured industrially for decades and there is a wealth of experience in this area in contrast to the relatively recent manufacturing of molecular electronic devices, which can provide new challenges. Despite the superior stability and conducting properties of silicon based semiconductors, the processing of high purity single crystal silicon requires temperatures upwards of 1500 °C by the Czochralski process.[13] This purification process is expensive and for certain applications the high level of device performance obtained from crystalline silicon is simply not required,

which is why organic semiconductor materials, and amorphous silicon, are the focus of intense academic interest.

1.1.2. Band theory

Band theory is commonly used to describe bonding in metals and semiconductors and is based upon considering the energies of the molecular orbitals (MOs) in an extended solid.[13] When two atoms combine certain atomic orbitals can overlap to form molecular orbitals, both bonding and anti-bonding. As the number of atoms increases so does the number of bonding and anti-bonding MOs. Since the atomic orbitals are all of the same energy, the resulting MOs they produce are very close in energy. As the number of orbitals approaches Avogadro's number (N_A= 6.022 x10^{23}) the energy difference between the bonding and anti-bonding orbitals is so small that the MOs can be considered as a continuous band of bonding (valence band) and anti-bonding orbitals (conduction band), respectively (as shown in Figure 1). This model of continuous valence and conduction bands is used to explain conductivity in an extended solid. The width of the band formed is a result of the degree of atomic orbital overlap which gives rise to the band; weakly interacting atomic orbitals give rise to narrow bands whereas strongly interacting atomic orbitals result in wide bands.[14] Charge carriers in a wide band material are considered to be delocalised over the entire crystal and not localised on one particular molecule or unit.[15]

A band gap occurs when there is a significant difference in energy between the valence band and the conduction band. The existent of this band gap or its magnitude is used to differentiate between metals, semiconductors and insulators. In the case of metals, there is no gap between the valence and conducting bands, instead the two overlap to give rise to a partially filled band. The level to which a band is filled is

known as the Fermi level, E_F, and in metals this falls in the middle of the band, giving rise to high conductivity.[14] Insulating materials tend to have a band gap larger than 3 eV, whereas most semiconductors are typically in the range of a few tenths of an eV to 3 eV. For example the band gap of silicon is 1.1 eV.[16] In the case of semiconductors and insulators, the Fermi level lies between the conduction and valence bands in the band gap. Promotion of an electron from the valence band to the conduction band to leave behind a positively charged hole in the valence band, via thermal or photoexcitation, can give rise to conductivity in semiconducting materials. A smaller band gap can give rise to higher conductivity as it becomes easier to promote an electron to the conduction band by thermal excitation.

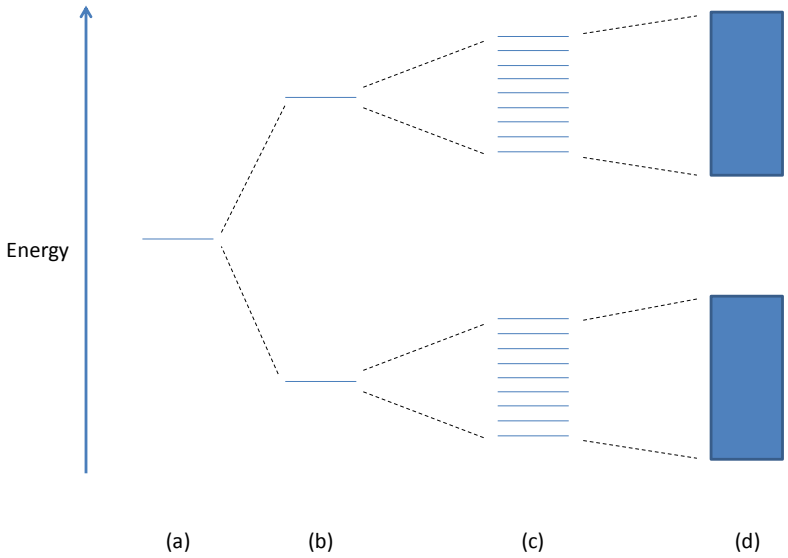

Figure 1 Orbital energies of an atom (a), a small molecule (b), a large molecule (c) and a solid (d).[17]

1.2. Molecular semiconductors

1.2.1. Introduction

Research into the field of organic semiconductors has focused on the development of new materials for potential applications in devices such as organic field effect transistors (OFETs) or organic light emitting devices (OLEDs), as well as improving the device performance of already existing materials. As the name suggests organic semiconductors are typically carbon rich molecules with structural features designed for a particular purpose, for example charge mobility or luminescent properties.[18] OFETs have been proposed for applications in radio frequency ID tags, smart cards, price tags and electronic paper.[19] Although organic semiconductors cannot rival purely inorganic materials with regards to their device performance, they do offer key advantages in terms of cost and processability. Devices made from molecular materials also have the potential to be thin, lightweight and flexible; characteristics that until recently could not be offered by inorganic materials.[20]

OFET performance is usually judged by the charge carrier mobility, on/off current ratio and the threshold voltage.[12] Any OFET with commercial applications would be required to have high charge carrier mobility, a large on/off current ratio and a low threshold voltage, as well as being air stable. Frustratingly, the charge carrier mobility of any given material can vary widely depending on the device architecture and the processing conditions. This parameter is reliant on several factors, such as the degree of structural order, atmospheric contaminants and structural imperfections such as grain boundaries.[9] The energy of the material's frontier orbitals is an important consideration in designing new materials or constructing devices, since the injection of charge carriers from the electrodes of the OFET is dependent upon the

energies of the HOMO and LUMO of the semiconductor with respect to the Fermi energy of the metal electrode. More specifically, the energy of the HOMO/LUMO will dictate the polarity of the charge carrier which is injected into the material. The size of the HOMO-LUMO gap should also be given consideration in design of molecular materials as this property is important for the realisation of ambipolar conductors. If the band gap is too small this would make the current difficult to switch off as the material may be susceptible to thermal or photoexcitation.

Organic semiconductors can be broadly classified into two main categories: discrete, conjugated molecules and conjugated, polymeric materials.[21] These materials can then be subcategorised depending upon the sign of the charge carrier they conduct, for instance, hole conducting or electron donating materials are known as p-type semiconductors whereas electron conducting or electron accepting materials are known as n-type. Materials which can transport both holes and electrons are known as ambipolar. Research into the development of p-type materials is at present significantly more advanced than that of n-type organic semiconductors, with current generation p-type materials combining both high performance with air stability,[22] whereas in contrast examples of air stable n-type materials are particularly rare.[23] However, for complimentary circuits or p-n junction diodes, air stable p- and n-type materials are both required.[22] Ambipolar materials have been achieved by blending n- and p-type materials together[24] but a step forward in the realisation of complimentary circuits is to produce transistors which display ambipolar behaviour using a single semiconducting material with a single type of electrode.[25] To achieve ambipolar charge transport in an OFET device, the semiconducting material should have a narrow band gap with the work function of the source and drain electrodes at an appropriate energy for injecting both holes into the HOMO and electrons into the LUMO of the active layer. If there is a mismatch in the energies of the electrode material relative to the semiconductor then there is likely to be a large energy barrier

to the injection of charge carriers and the hole and electron mobilities will be unbalanced, or the material will exhibit unipolar conduction only.

1.2.2. Hopping model

In contrast to classical inorganic semiconductors, where significant orbital overlap results in conductivity being described using band transport, with organic materials orbital overlap between adjacent molecules is limited and thus charge transport is usually described by another mechanism. The non-covalent interactions between molecules and the inherent disorder present in organic semiconductor devices gives rise to charge transport via a thermally activated hopping mechanism.[26] In molecular systems the lack of orbital overlap results in charge carriers becoming localised on specific sites or molecules. These weak intermolecular interactions, which are prevalent in organic materials, give rise to the formation of narrow bands, which are strongly affected by scattering and polaronic effects.[27] Hopping theory is based on the idea that charges can become localised on one specific site or moiety and then jump (or hop) to a neighbouring localised state.[15] The hopping mechanism can be regarded as a series of electron-transfer (ET) reactions between the neutral species and its radical cation (in the case of hole-transport materials) or radical anion (electron-transport).[28] Therefore, minimising reorganizational energies is an important consideration in the choice of material as this energy is related to the rate of electron transfer between molecules.

In a band regime the conductivity decreases with increasing temperature as lattice vibrations result in increased charge scattering but in the hopping regime increasing the temperature results in an increased conductivity.[29] This is due to the disordered nature of organic semiconductors, particularly in thin films, with many traps in

which charge carriers can become localised; increasing temperature can help in detrapping these charge carriers.[30] Chemical impurities, dopants or structural defects can give rise to electrically active states or traps within the band gap.[31] If the traps are energetically shallow i.e. less than a few kT deep, then the charge carriers can be thermally released but if the trap is "deep" (greater than a few kT) then thermally activated detrapping is not possible.[32]

Recently band like transport has been observed in organic systems, such as single crystal rubrene[33] and pentacene.[34, 35] In these cases, at low temperature, significant orbital overlap between the HOMO and LUMO of adjacent molecules gives rise to the formation of a valence band and a conduction band, respectively. Charge carriers are then coherently delocalised over the whole crystal with their mobility related to the bandwidth of the HOMO band in terms of holes, or the LUMO band in terms of electrons.[29] As the temperature increases the effective bandwidth is reduced as a result of lattice vibrations, and therefore the mobility also decreases with increasing temperature.[29, 36] In these systems high quality, pure (usually zone refined) single crystals with a low density of charge traps are required in order to observe band transport as chemical impurities or crystal defects can play a critical role in the mode of charge transport witnessed.

1.3. Field effect transistors

1.3.1. Device configuration

Organic field effect transistors (OFETs) usually comprise three electrodes; a gate, a source and a drain; an insulating layer, which serves as a gate dielectric, and a

semiconducting layer. The gate dielectric is commonly SiO_2 or an organic dielectric material such as an insulating polymer.[37] Two different OFET configurations are commonly employed: a top contact and a bottom contact (shown in Figure 2). In a top contact configuration, the source and drain electrodes are deposited - usually by evaporation - on top of the semiconducting layer, which lies on the dielectric layer, whereas in a bottom contact device the semiconducting layer is deposited over the source and drain electrodes, which are now sitting on top of the dielectric layer. The source electrode is earthed, and all other voltages are given in relation to this electrode. The function of the gate electrode is to modulate the size of the current flowing between the source and drain electrodes.

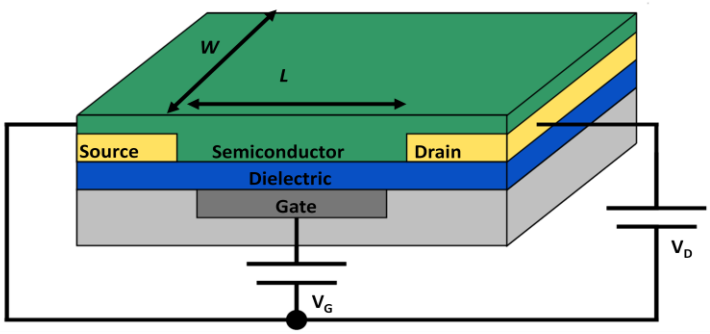

Figure 2 An OFET showing a bottom contact configuration.

1.3.2. Mechanism of operation

Charge carriers are injected into the semiconducting layer from the source/drain electrodes and under an applied gate potential charge carriers of the opposite polarity to the applied gate voltage will begin to accumulate at the interface between the semiconductor and the dielectric layer. If the gate voltage is zero, then there should be very little current flowing between the source and drain, this is referred to as the "off" state (I_{off}). If a voltage is then applied to the gate electrode charge carriers can now flow between the source to the drain and this is referred to as the "on" state (I_{on}).

The gate potential at which the device switches on is known as the threshold voltage (V_T). Charge carriers are usually injected from the source electrode; the applied source-drain voltage (V_{SD}) as well as the gate voltage (V_G) can then control the magnitude of the current flowing through the device. The applied gate potential required and the magnitude of the source-drain current (I_{SD}) is dependent upon the conducting material and its inherent charge carrier mobility.

Organic semiconductors contain localised traps of various depths that prevent the movement of charge carriers, these traps first need to be filled in order for current to flow between the source and drain electrodes. The threshold voltage is essentially a measure of the number of charge carrier traps within a film that need to be overcome before the FET is switched "on".[38] The on/off ratio is defined as the source-drain current in the "on" state versus the source-drain in the "off" state and is crucial for achieving a pronounced switching effect. Aside from the V_T and I_{on}/I_{off} ratio, the other important parameter is the charge carrier mobility (μ), which determines the size of the voltage to be applied and thus the power consumption of the transistor.

On application of V_G the HOMO and LUMO of the semiconducting material will shift, if V_G is positive then the HOMO and LUMO will shift down in energy such that the LUMO will become resonant with the Fermi level of the metal electrode and electrons can be injected into the LUMO from the source meaning that the device can now operate in electron transport mode (Figure 3). Likewise, if V_G is negative then the HOMO and LUMO shift up in energy such that the energy of the HOMO is now resonant with the Fermi level of the metal electrode and electrons can be injected from the HOMO into the source to leave behind positive holes in the semiconducting material. The device can now operate in hole transport mode.[39]

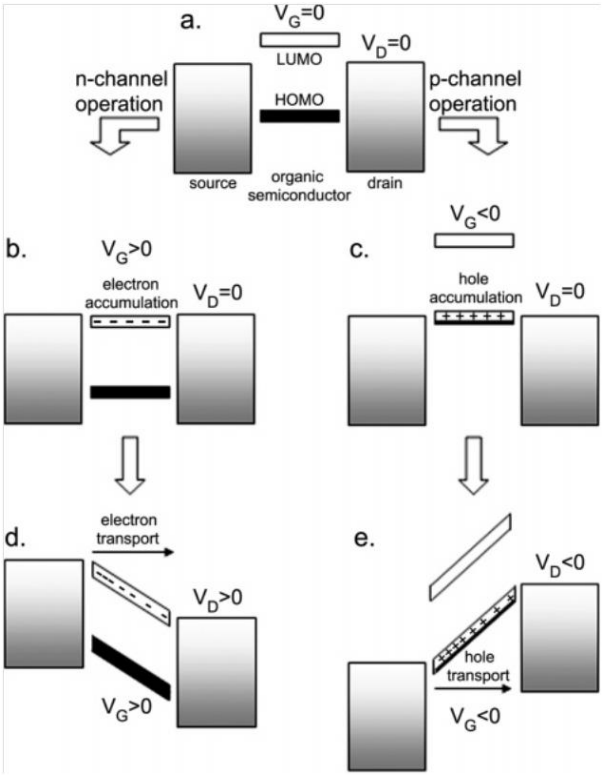

Figure 3 Schematic illustrating how an FET operates in both n-channel (electron transport) and p-type (hole transport) modes. Figure reproduced from Newman *et al.*[39]

As previously mentioned a source-drain current can only flow once trap sites have been filled. Thus, for additional charge carriers to become mobilised, the applied V_G must be greater than V_T, resulting in an effective gate voltage equal to V_G - V_T.[40] Two main regimes operate during FET measurements; a linear regime and a saturation regime (Figure 4 (d)). When V_G-V_T >> V_D the charge carrier concentration between the source and drain is uniform and the measured I_{DS} is directly proportional to the applied V_D, then the device operates under a linear regime (Figure 4 (a)).[40] With increasing V_D the carrier concentration begins to become more non-uniform, until a point is reached at which V_G-V_T = V_D and the channel becomes "pinched off" (Figure 4 (c)).[40, 41] This effectively means that there is no potential difference between the local potential at the area closest to the drain electrode and the effective gate potential (V_G-V_T), resulting in the area closest to the drain becoming depleted of

charge carriers.[41] Increasing the source-drain voltage further will only serve to increase the size of the depletion region. This so called "pinch off" point is observed as a plateau in the output characteristics (a plot of I_{DS} vs. V_G), and after this point the transistor is said to be operating in a saturation regime.

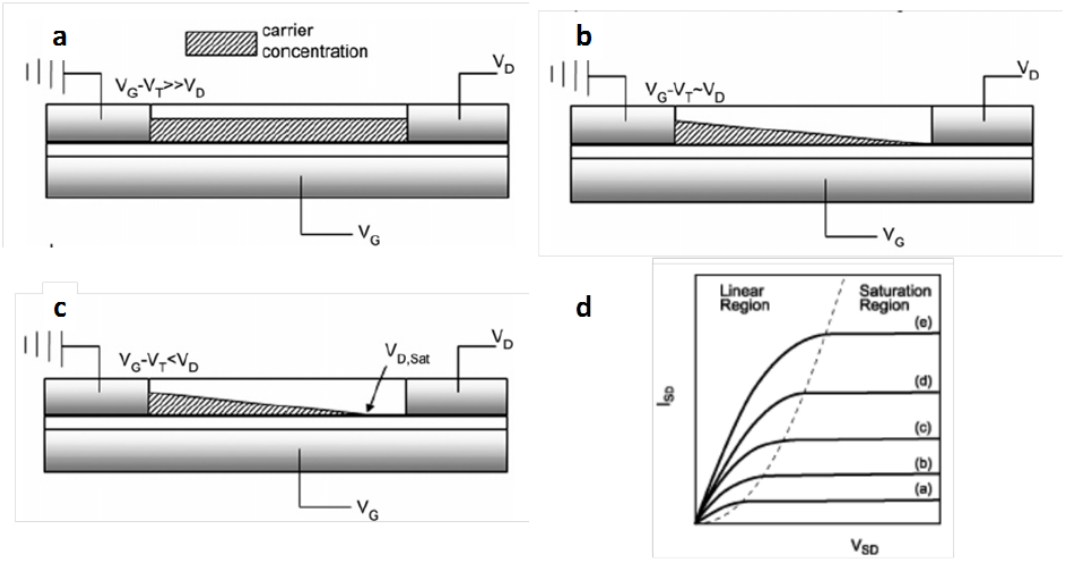

Figure 4 Operating regimes in FETs: (a) linear regime, (b) start of saturation regime when V_G-V_T = V_D and (c) saturation regime when V_G-V_T < V_D. Figures (a) to (c) are taken from Newman *et al*.[39] (d) Typical FET output characteristics where the applied gate voltage increases in the order of (a) to (e), resulting in an increase in source-drain current going from (a) to (e). Figure (d) reproduced from Shirota *et al*.[37]

1.3.3. Charge carrier mobility

The switching speed of a transistor is dependent upon the time it takes a charge carrier to move between the source and drain electrodes (= channel length, *L*).[9] The unit of measurement for the charge carrier velocity per electric field is known as the mobility (μ). The shorter the channel length (*L)* and the greater the mobility then the faster the transistor can switch. However, the channel length is limited by device processing technology and the mobility is an intrinsic material property which is

reliant upon the processing conditions and the resulting structural order afforded by this method.[9]

An appreciable aim in the field of molecular electronics is to produce thin films of semiconducting material, which have a high degree of structural order, preferably crystalline or polycrystalline. One way to attain a reasonable level of structural order is to use materials which can self arrange through intermolecular interactions such as π-π stacking, dipole-dipole or hydrogen bonding. The structural order in the film of semiconducting material is crucial to the charge transport properties and thus the conduction of the film.[37] For charge carriers to move between molecules in a solid there needs to be sufficient π-orbital overlap between adjacent molecules but this charge carrier hopping is often limited by structural disorder and/or impurities.[42] Crystalline boundaries in a thin film or polycrystalline sample can act as charge traps to the movement of charge carriers and therefore a well ordered crystalline sample is desirable for improved mobility and conductivity.

Materials purity is a crucial aspect in the quest for suitable materials for FET studies, chemical impurities can act as charge traps which disrupt π-overlap of the organic semiconductor and serve to lower the mobility and/or increase the switch on voltage. Alternatively, impurities may also be extrinsic conductors resulting in the device always being in an "on state" which displays a less pronounced gate voltage switching effect.[43]

The charge carrier mobility of a sample can be calculated by various methods[36] but one of the most common methods is from FET measurements. However, charge mobility calculated from FET results is not an intrinsic property of the semiconducting material itself. Instead it can include several factors related to the

device fabrication; these include structural defects at the semiconducting/dielectric interface, the polarity of the dielectric, the presence of charge traps in the thin film, and the contact resistance between the source/drain electrodes and the semiconducting layer.[44] All these factors serve to alter the charge carrier mobility and thus it can be expected to achieve different results from different FET architectures.

From the FET output characteristics (shown in Figure 4 (d)) it is possible to extract a value for the charge carrier mobility. During FET measurements the current that flows between the source and drain electrodes (I_{SD}) increases linearly as the source-drain voltage (V_{SD}) increases, this is known as the linear region but at a certain point the current plateaus, this is called the saturation region. Charge carrier mobility (μ) values can be calculated from analysis of either the linear or saturation region using Equations 2 and 3, respectively. From both these equations, C is the capacitance per unit area of the gate dielectric, W and L are the channel width and length respectively and V_T is the threshold voltage. These equations assume that the charge carrier mobility is constant throughout the regime being studied.

$$\boldsymbol{I_{DS}\,linear = \frac{CW\mu}{L}(V_G - V_T)\,V_{SD}} \qquad \textbf{Equation 2}$$

$$\boldsymbol{I_{DS}\,sat = \frac{CW\mu}{2L}(V_G - V_T)^2} \qquad \textbf{Equation 3}$$

The intrinsic charge carrier mobility of a semiconductor can be obtained by carrying out time of flight (TOF) measurements. The TOF method is based upon measuring the time (τ) it takes for a sheet of photogenerated unipolar charge carriers to move between two electrodes under an applied electric field. Study samples usually consist

of a single crystal or a thin film, between 5 and 20 μm thick, sandwiched between two electrodes. When charge carriers begin to drift, photocurrents flow until the charge carriers arrive at the other electrode, indicated by a kink in the observed current with time.[36] The presence of charge traps should be low enough as to allow a measurable quantity of charge carriers to flow through the material.

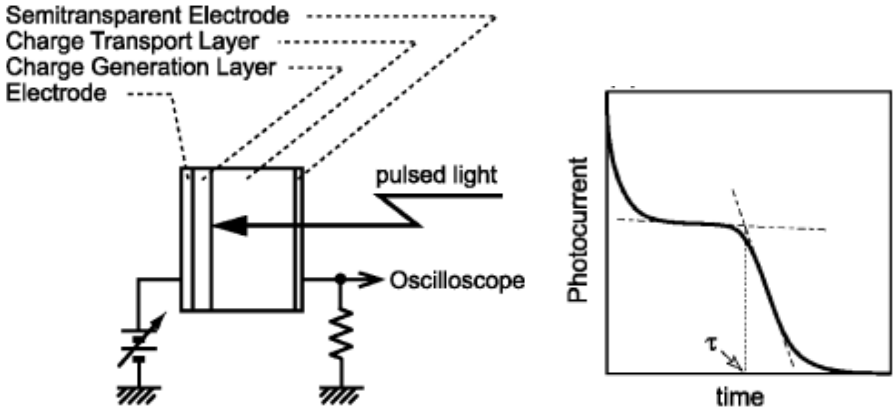

Figure 5 Left, schematic of time-of-flight apparatus (left) and typical transient photocurrent (non-dispersive) observed from the measurement (right). Image reproduced from Shirota *et al*.[37]

The velocity of the charge carrier (v) is directly related to its mobility (μ) and the applied electric field (E) as shown in Equation 4. The transient time (τ) is calculated using Equation 5, where d is the sample thickness. Combining Equations 4 and 5 the charge carrier mobility can be calculated using the expression in Equation 6, where V is the applied voltage.

$$v = \mu.E \qquad \textbf{Equation 4}$$

$$\tau = d / v \qquad \textbf{Equation 5}$$

$$\mu = d^2 / V.\tau \qquad \textbf{Equation 6}$$

1.4. Classes of materials

1.4.1. Polymers

Since the late 1970s conjugated polymers have been of interest due to the combination of material strength and non insulating electrical properties which they offer.[45] In 1986, the first solid state OFET to be fabricated utilized the organic polymer, polythiophene, as the semiconducting material.[46] One attractive feature of organic polymers is that they can be doped, chemically or electrochemically, to alter the electronic properties of the system. In addition, the optical, physical and electronic properties of polymers can be tailored by modification of the polymer backbone, the molecular weight and the polymer end groups.[47] For example, introduction of a fused ring group such as in cyclopentadithiophenes, thienothiophenes, dithienopyrroles and dithienosiloles can lead to increased conjugation and enhanced intermolecular interactions between chains, due to their aromatic, planar nature. [47]

Owing to the extremely low vapour pressure of polymers, vapour deposition is not an option and thus polymers are predominantly solution processed - via spin coating, solution casting or direct printing - to form a uniform thin film, which can then be annealed to evaporate off any remaining solvent. Although polymers can be easily solution processed in this manner, achieving ordered films is difficult and amorphous or disordered films are commonly produced. Various functional groups or side chains, usually alkyl groups, are commonly added to the polymer to improve its solubility. However, a balance exists between the size of the alkyl group and the FET performance.[48] If the side chain is too small then the material will not be soluble enough to produce a homogenous film from solution processing but if the alkyl chain

is too long then the intermolecular distance increases, π-overlap is reduced and charge carrier mobility is decreased. It has been shown that the size of the side chain has a direct impact on the crystallinity and self assembly of the polymer along with the associated FET performance, as previously mentioned.[43]

Polythiophene and its analogues have to date been some of the most widely studied polymers for organic electronic applications. Commonly polythiophenes are functionalised with alkyl chains of various lengths. These polymers have been explored for a range of applications including light emitting diodes, non-linear optical devices, rechargeable battery electrodes and FET applications.[49] The current record mobility for a solution processed polythiophene based polymer is 0.2 cm^2 V^{-1} s^{-1} and was achieved from regioregular poly-3-hexylthiophene (RR-P3HT) dip-coated onto an FET substrate.[50] In this case FETs prepared by dip-coating produced higher mobilities than those prepared by spin coating and drop casting. The UV-vis result indicated a lower onset energy for the optical absorption in the dip-coated sample compared to those prepared by other methods, implying a greater degree of structural order has been achieved by dip-coating.[50]

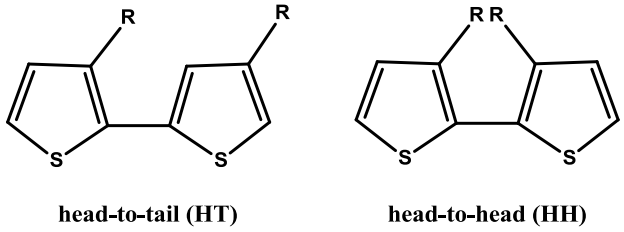

Figure 6 Poly-3-alkyl thiophenes in an HT or HH conformation. A regioregular polymer consists of either only HT or HH isomers where as a regiorandom confirmation consists of both isomers.

Polymer synthesis can often result in a variety of regioisomers being formed, which tend to be difficult to separate. Regioregular polythiophene polymers (Figure 6) have

been shown to have very different properties from their corresponding regiorandom polymers, such as smaller band gaps, better ordering and crystallinity in the solid state, and substantially improved conductivities.[21, 49] Therefore much of the chemistry involved in the synthesis of these polymers is aimed at achieving complete control over the polymer regioregularity in order to improve the device performance.

1.4.2. Discrete molecules

To date some of the most successful organic semiconductors have been based on discrete, conjugated molecules with the majority displaying p-type conductivity. The high performance of discrete molecular materials is due to their ability to self organise on substrates to form crystalline or poly-crystalline films.[21] Some notable examples include acenes such as rubrene[51-53] and pentacene[54, 55] (Figure 7) where the charge carrier mobility has now surpassed that of amorphous silicon (~1.0 $cm^2 V^{-1}s^{-1}$). The high performance of pentacene is a result of its delocalised structure and favourable crystal packing, which provides substantial overlap of its frontier orbitals in the 001 lattice plane.[21] However, pentacene suffers from being oxidatively unstable in air which adversely, and irreversibly, affects its FET performance. When exposed to oxygen or water in the presence of light pentacene becomes oxidised at the 6 and 13 positions to form 6,13-pentacenequinone (Figure 7 (b)),[56] which results in the formation of a less delocalised system by disrupting the π-conjugation of the central ring. This new chemical species, with different orbital energies to pentacene, can then act as a trap or a scattering point to the transport of charge carriers, resulting in a drastic decrease in mobility. As previously mentioned in Section 1.2.2., band like transport has now been observed in high purity single crystals of pentacene, emphasising the effect of materials purity on the mode of charge transport and the resulting mobility achieved. To illustrate this, in one particular example the charge carrier mobility was measured by ToF to be 35 $cm^2V^{-1}s^{-1}$ at room temperature but

increased on lowering the temperature to reach a mobility of 58 $cm^2V^{-1}s^{-1}$ at 225 K.[35] In addition to its air sensitivity, its low solubility makes it unrealistic for solution processing methods; however, films can be grown by thermal sublimation under vacuum.

The pentacene analogue, picene (Figure 7 (c)), is a promising candidate for FET applications with mobilities of 1.1 $cm^2V^{-1}s^{-1}$ but enhanced air stability due its HOMO being of lower energy.[57] Surprisingly, exposure to oxygen over prolonged periods of time results in an increase in, both, mobility and on/off ratio,[57, 58] which is contrary to the commonly observed effect of oxygen decreasing the on/off ratio.[59] This oxygen sensitivity has led to picene being proposed for application in thin film O_2 sensors.[60]

One of the leading molecular materials for use in conducting applications is rubrene (Figure 7 (d)), which possesses some of the highest charge carrier mobilities reported to date.[61] A wide range of high mobilities are consistently reported for high purity single crystals of rubrene, ranging from 10 to 40 $cm^2\ V^{-1}\ s^{-1}$.[33, 61-63] Incidentally, the latter value is the largest ever reported for an organic semiconductor measured at room temperature.[63] Other studies on rubrene single crystals have demonstrated their potential as an ambipolar semiconductor, however, in this investigation the resulting mobilities are a modest 1.8 $x10^{-2}$ for holes and 1.1 $x10^{-2}$ $cm^2\ V^{-1}\ s^{-1}$ for electrons.[52] It is commonly suggested that flat, conjugated molecules with substantial π-π overlap will give rise to high charge carrier mobilities, as is the case with pentacene. Conversely, the structure of rubrene is not flat and intermolecular overlap of the core tetracene π-systems is negligible.[9] This failure to relate structure to performance presents a persistent conundrum in the field of molecular electronics, which is only exacerbated by the lack of universal testing methods/devices. As a consequence, varying results are commonly reported for popular organic semiconducting materials when studied in different laboratories.

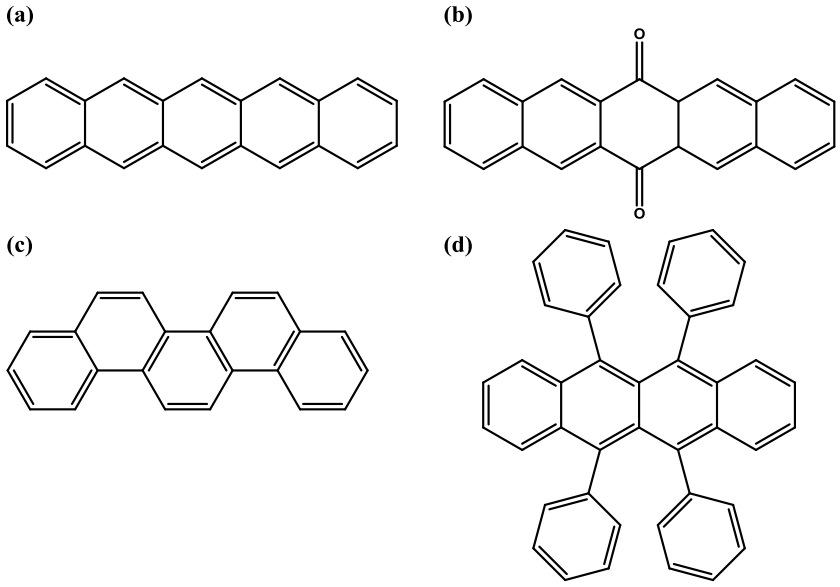

Figure 7 The structure of pentacene (a), 6,13-pentacenequinone (b), picene (c) and rubrene (d).

1.4.3. Transition metal complexes

In the study of molecular semiconductors, transition metal-organic complexes can offer some key advantages over their purely organic counterparts. Such advantages include: (i) a wider variety of redox processes[64] (ii) a tunable band gap through modification of the ligand or by exchange of the transition metal ion,[65] and the possibility of ambipolar charge transport.[66] Also, the frontier orbitals of transition metals are often non bonding in character suggesting low reorganization energies when oxidised or reduced, which is crucial to electron transfer reactions, and redox processes are often fully reversible implying that the charged species is kinetically stable.[28] Tuning the band gap through substitution of the central metal ion may allow the optical and visual properties of the complex to be readily altered, with the choice of metal ion often having a significant impact on the perceived colour of the material. Although more or less non bonding in character, the frontier orbitals tend to be delocalised to some extent over the ligand which is favourable for intermolecular

overlap.[28] The use of transition metal ions can offer the ability to generate stable paramagnetic species, often more readily than purely organic molecules. The study of paramagnetic molecular semiconductors may give rise to exotic behaviour, as discussed in Section 1.3.3. Although metal based semiconductors have been overlooked to some extent and studies of such materials are scarce, compared to their purely organic counterparts, some success has come from the study of materials such as nickel dithiolenes[28, 67-69] and copper phthalocyanines.[70-72]

Nickel dithiolenes have been nominated for a wide range of organic electronic applications and this is due to several attractive features: they are thermally and photochemically stable; their frontier orbitals are delocalised in nature; redox processes are reversible and tunable, with only small structural changes observed on reduction; and their planarity allows π-stacking interactions to control self assembly in the solid state.[28] Dithiolenes and their analogues have been explored as both n-type[23, 64, 73] and ambipolar semiconductors,[25] with an electron mobility as high as 2.8 $cm^2 V^{-1} s^{-1}$ being reported for one square planar nickel bis-dithiolene complex.[28]

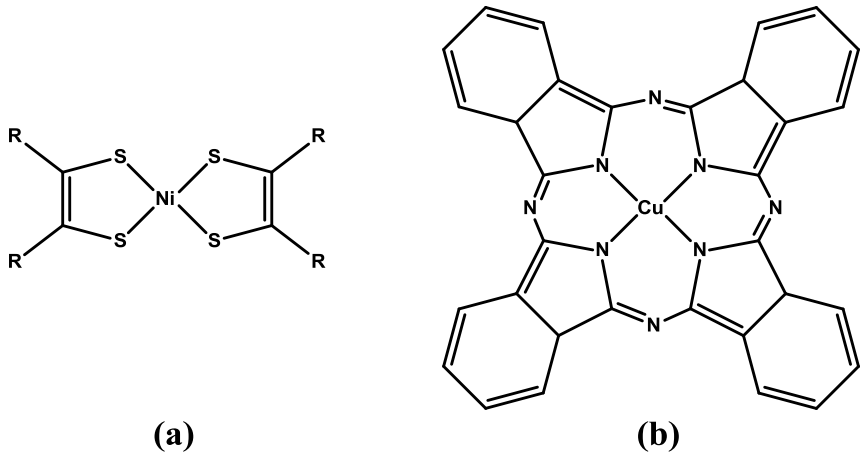

Figure 8 General structure of (a) nickel dithiolene and (b) copper phthalocyanine.

Phthalocyanine (Pc) molecules are a class of interesting organic semiconductors which have garnered much interest due to their interesting optoelectronic properties[74] that are attractive for applications in FETs, photovoltaics[75] and OLEDs.[76] They are based on a polyaromatic macrocycle which has the capacity to accommodate various metal ions into its central cavity and the electronic properties of these molecules can be modified either by adding substituents to the periphery of the molecule or through substitution of the central metal ion. The unsubstituted molecules are well known to function as p-type semiconductors both as the metal free molecule and when complexed to a transition metal centre. Interestingly, the fluorinated form, hexadecafluorophthalocyanine, displays air stable n-type behaviour when complexed to certain metal ions such as Cu(II), Co(II), Fe(II) or Zn(II).[65, 77] The unusual air stability of this n-type material is a consequence of the electron withdrawing nature of the fluorine atoms lowering the LUMO energy of F_{16}MPc by *ca.* 1.6 eV, making it less vulnerable to atmospheric oxidation.[65] The class of unsubstituted phthalocyanine molecules have been shown to be suitable for vacuum deposition techniques and have been thoroughly studied for this purpose[78] but by functionalisation of the macrocycle the solubility of the molecule can be improved such that the molecules can be spin cast from solution.[79] In fact, examples now exist of soluble phthalocyanine derivatives spin cast from solution that exhibit OFET charge carrier mobilities comparable with those attained from vacuum deposition of unsubstituted phthalocyanines.[80] In the solid state Pc based molecules self assemble to form 1D arrays through intermolecular π-π stacking of the Pc core and thus any solubilising groups added to the Pc molecule should be carefully chosen as to avoid affecting the π-π interactions, which are crucial to charge migration. Perhaps the most well studied Pc based material is that of copper(II) as the central metal ion (CuPc) with reported mobilities of 0.02 $cm^2 V^{-1} s^{-1}$ which is quite modest in comparison with some of the current organic electronic materials based on conjugated acenes.[70]

1.4.4. Paramagnetic semiconductors

Since the discovery of magnetic conducting materials much effort has been devoted to the study of materials that exhibit the coexistence of magnetism and conduction i.e. the electronic interaction of a localised spin with a conducting electron. Potentially interesting magnetic and conducting behaviour could result from the interaction of both these components but examples of suitable molecular materials are scarce.[81] It has been proposed that materials of this type could form the basis for applications in future spintronic devices.[82, 83]

Molecular magnetic conductors are commonly based on the cation radical salts of π-conjugated donor molecules with magnetic anions, particularly transition-metal anions with d-spins. These usually have crystal structures composed of alternately stacked donor and magnetic anion layers. At the interface between each pair of alternate layers there is a direct d–d interaction (usually antiferromagnetic) between the neighbouring unpaired d electrons of magnetic anions (Figure 9). Additionally, there is an indirect π-d interaction between the conduction π-electron in the donor layer and the unpaired d electron in the magnetic anion layer. The π-d interaction has a strong effect on the electron transport in the π-conduction layer. Upon increasing the π-d interaction, the scattering time (τ) of the conduction π-electron shortens, thus the electron mobility should be reduced. However, when a magnetic field (H) larger than the spin-flop field (H_{sp}) is applied to the crystal, the d electrons (spins) in the magnetic layer are forced to align in the same orientation to order ferromagnetically, which disrupts the indirect π-d interaction. As a result, the transfer integral and the scattering time of the conducting π-electron increase, enhancing the electron mobility. This is witnessed experimentally in the decrease in electrical resistivity upon applying a magnetic field; a negative magnetoresistance effect is observed.[84]

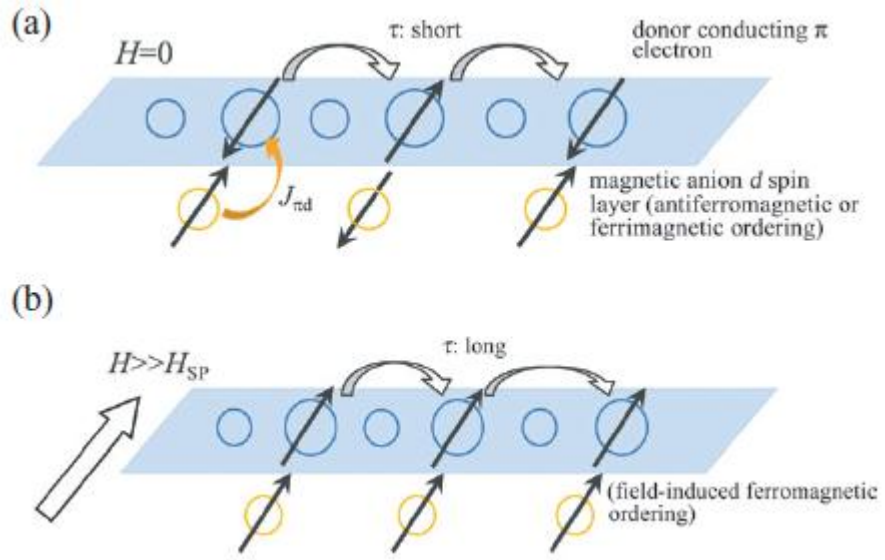

Figure 9 Interaction between π-d, π-π and d-d electrons at the interface between the conducting donor unit and the magnetic anion (a) in the absence of a magnetic field and (b) in the presence of a magnetic field. Image reproduced from Toyonari *et al.*[84]

Early work by Coronado *et al.*[85] focused on the study of bilayer materials consisting of alternating rows of magnetic and conducting materials. During their investigation the well known heterocyclic molecule BEDT-TTF (Figure 10(a)) was combined with the ferromagnetic bimetallic 2D lattice $[MnCr(C_2O_4)_3]^-$. The self assembly of the material is precisely controlled as a consequence of the negative charge of the magnetic layer and the positive charge of the conducting layer.[86] However, in this material the magnetic layer appears to have no influence on the conducting properties of the BEDT-TTF layer.

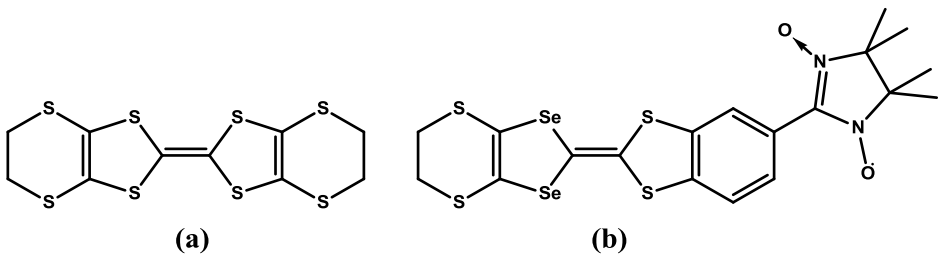

Figure 10 Structure of (a) BEDT-TTF and (b) ESBN.

Although further studies have focused on incorporating different stable radical units into the cation radical salt of TTF-based donors, significant interaction between magnetism and conductivity has yet to be realised. This is due to a lack of appropriate π-conjugation required to facilitate the exchange interaction between localised spins and conducting electrons, mainly because the conducting and magnetic electrons are on different molecules.[83, 87] Molecular alignment is crucial to the realisation of magnetoresistance effects in the study of bilayer materials. Materials where the π-conducting electron and the magnetic moment are based on the same molecule make a π-d interaction more plausible.[88]

The transition metal complex, dicyano(phthalocyaninato)iron [Fe(Pc)$(CN)_2$], has been observed to exhibit giant negative magnetoresistance effects in doped solids as a result of the interaction between the conducting electron and the magnetic spin, based on the same molecule.[88-90] In this system the conducting π-electron is based on the phthalocyanine macrocycle and the unpaired d-electron resident on the metal centre, however, the nature of the π-d interaction is unexplained. The HOMO is Pc based with no metal contribution, and the metal based SOMO is lower in energy than this Pc based HOMO. Additionally, the magnitude of the observed negative magnetoresistance is intimately linked to the molecular alignment of the material with respect to the magnetic field, reflecting the spin anisotropy present in the molecule.[88] Minimum magnetoresistance (increased conductivity) is observed when the magnetic field is approximately aligned with the cyano ligands *i.e.* perpendicular to the molecular plane.

Since then studies have focused on not only transition metal based materials but also organic radical based salts with the aim of strengthening the interaction between localised spins and conducting electrons. In 2007 Matsushita *et al.*[83, 91] reported the first example of an organic material containing a coexisting system combining a localised spin with a conducting electron; a spin carrying donor molecule known as

ESBN (Figure 10 (b)). The ion radical salt, $ESBN_2(ClO)_4$, was found to exhibit both a non linear conductivity and a giant magnetoresistance at low temperature (-70% at 2 K in a 9 T magnetic field). The authors propose the non-linear conductivity is a result of the partial melting of the charge ordered phase shown in Figure 11 (a), where oxidised molecules (purple) are separated by neutral molecules (green) to minimise repulsive interactions. Under a high electric field (Figure 11 (b)) the conducting β electron (blue "spin down" electron without circle) hops to an adjacent molecule containing an α electron in the SOMO (red "spin up" electron in circle). The sites marked in orange represents molecules where an intramolecular ferromagnetic interaction exists between the unpaired α electron in the SOMO and the unpaired electron in the HOMO (represented as +1/2). In this situation there also exists an intermolecular ferromagnetic exchange interaction, which helps to increase the coherence length of the conducting electron by reducing charge carrier scattering. Under application of a magnetic field, the majority of localised spins align ferromagnetically and further suppress the scattering of the conducting electron, resulting in the observed giant magnetoresistance (Figure 11 (c)). Various TTF-based analogues have now been prepared and characterised in the context of their coexisting magnetic and conducting properties.[82, 92]

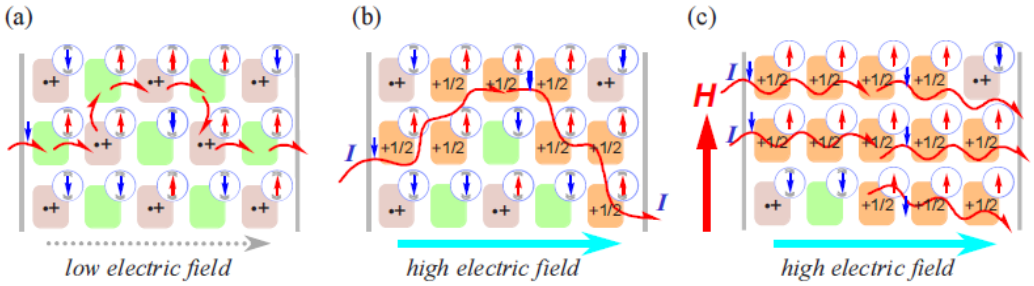

Figure 11 Speculated mechanism for giant magnetoresistance and non linear conductivity under electric and magnetic field. The diagram displays the movement of a β electron (blue) between molecules containing α electrons (red) in a low electric field and a high electric field with and without an applied magnetic field. Image reproduced from Matsushita *et al*.[83]

Despite progress in the development of materials exhibiting coexisting magnetism and conductivity, examples still remain limited. For a molecular system to display cooperative conductivity and magnetism it must have a suitable electronic structure and form columnar stacks through which charge carriers can propagate. More specifically, one-electron oxidation should result in a diradical cation with a triplet ground state, as opposed to a singlet diamagnetic cation.[90] For this criteria to be realised the SOMO must be lower in energy than the HOMO, with the HOMO of the donor moiety spin polarised by the unpaired electron on the radical unit (Figure 12). Materials of this type are designated as *spin-polarised donors* and will give rise to diradical cations upon one-electron oxidation.[90, 93] Upon one-electron oxidation the unpaired α-electron in the HOMO will align with the unpaired SOMO due to a ferromagnetic exchange interaction, which can then lead to spin dependent charge transport as shown in Figure 12 (right).[90] In this situation, 1D conductivity arises from the migration of β-electrons from molecule to molecule through the overlapping π-based HOMO orbitals. Under this ferromagnetic alignment of localised spins, scattering of the conduction electron (β) is minimised and negative magnetoresistance effects can be witnessed.

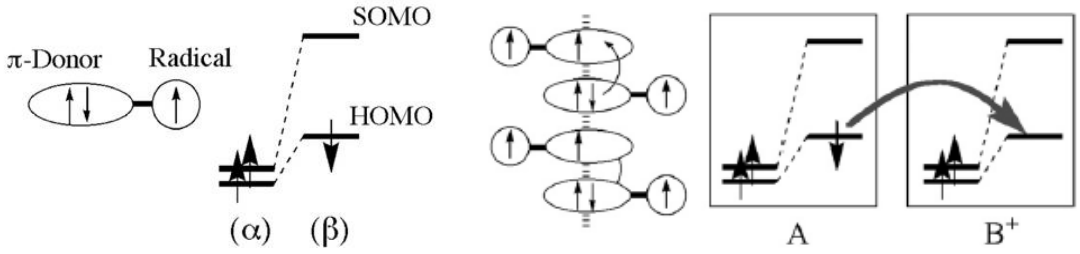

Figure 12 Electronic structure of a spin-polarised donor, left, and one dimensional charge transport between neutral (A) and singly oxidised donor-radicals (B), right. Image reproduced from Sugawara *et al.*[93]

1.5. Processing methods

1.5.1. Introduction

Crucial to the performance of an OFET is the deposition technique employed.[94] The method of depositing a thin film can hugely affect the morphology, crystallinity and molecular orientation of the conducting material. There are various methods available to form thin films on devices depending on the solubility and volatility of the organic material. Such deposition methods include spin coating, drop casting, dip coating and various forms of vacuum deposition. Other factors such as pre-treatment of electrodes and dielectric layers should also be given some consideration as they can affect both the workfunction of the electrodes and the resulting molecular orientation of the conducting material. Post treatment annealing is also another parameter to take into account; this is commonly employed in solution deposition methods to remove from the film any remaining solvent or to induce a favourable phase transition.

1.5.2. Solution processing

A primary advantage of molecular semiconductors over traditional silicon semiconductors is the lower processing temperatures and the ability to solution process, in the case of soluble materials. With processing temperatures greater than 350°C required to produce thin film transistors based on amorphous silicon, soluble organic semiconductors can offer a significantly lower processing temperature.[38]

The processing methods available to soluble molecular materials include solution methods such as spin coating, drop casting or direct printing onto a substrate. Solution processing is a cheaper and simpler alternative to vacuum deposition but the film formation can be more difficult to control and often results in lower charge carrier mobility.

Spin coating is a method of deposition commonly utilised when studying polymers; this method involves depositing a solution of material onto a substrate, which is then rotated rapidly (Figure 13). As the substrate spins, the effect of centrifugal force causes the solution to spread out over the entire substrate with excess solvent ejected off the sides of the substrate.[95] As the rapid rotation continues the film thins until solvent evaporation results in a large increase in viscosity leaving a solid-like film. Further evaporation of the remaining solvent or annealing leaves behind a solid thin film. The final film thickness, as well as the homogeneity of the resulting film depends on various factors such as solution concentration, solvent viscosity, evaporation rate, angular velocity and spinning time. The choice of solvent plays an important role in the film formation with the charge carrier mobility showing a strong solvent dependence in the case of poly-3-alkylthiophene.[49]

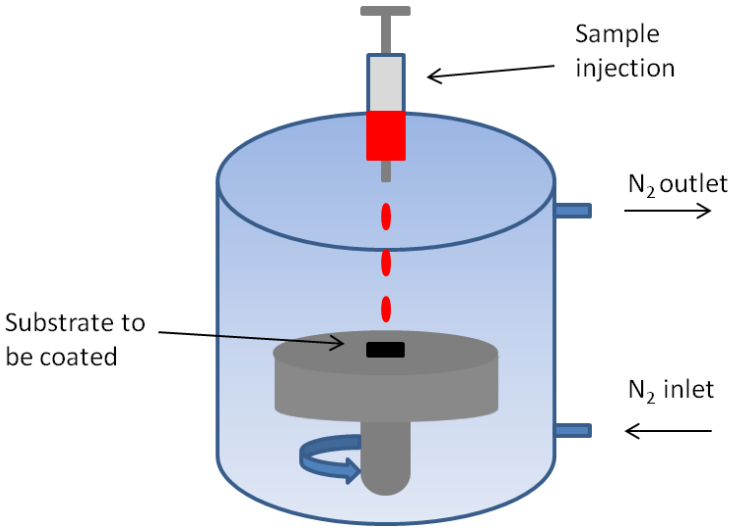

Figure 13 Schematic of a basic spin-coater.

Polymer thin films can also be attained through electrochemical polymerisation directly onto an electrode. An advantage of this method is that the film deposited onto the electrodes is the electrically conducting polymer free of any impurities.[96] Not only are polymer films easier to process than insoluble small molecules but the films generally offer more flexibility compared to polycrystalline films produced by vapour deposition.

An alternative method of thin film preparation involves the use of soluble precursors which can be cast onto a solution and then converted into the insoluble product, usually via elimination of soluble side chains or functional groups. This method has been employed to produce thin films of pentacene;[45] a soluble pentacene analogue (Figure 14) has been spin coated from DCM to produce an amorphous film, which then undergoes a heat treatment under vacuum to produce a microcrystalline film consisting of unsubstituted pentacene. The final morphology and the semiconducting properties are particularly sensitive to the annealing temperature and vacuum conditions used in the conversion to pentacene. Charge-carrier mobilities of up to 0.2 $cm^2 V^{-1} s^{-1}$ have been measured in field effect transistors with pentacene prepared in this way.[38]

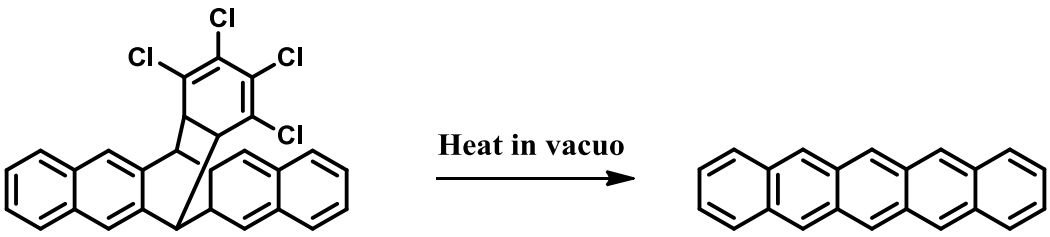

Figure 14 Conversion of pentacene analogue into pentacene.[45]

1.5.3. Vacuum processing

Techniques such as spin coating require solutions of high viscosity making this method less applicable to molecular materials in comparison to polymers.[97] However, in the study of discrete molecules it is possible to prepare thin films by vapour deposition; this is commonly used for materials with limited solubility in organic solvents. These experiments are almost always done under a high or ultra high vacuum whilst heating the sample, through a resistive medium, until it sublimes onto a substrate (Figure 15). Once sublimation begins the rate of sublimation can be monitored and controlled to produce an ordered film of a known thickness. In some cases the temperature of the substrate can also be controlled to affect the thin film formation. Small molecules have the advantage that they can order themselves very well in the solid state to form crystalline or polycrystalline films, although, this is best achieved when employing a slow rate of sublimation. Generally, vacuum deposition produces a good quality, well ordered thin film with good run-to-run reproducibility.[94] Vacuum deposition also has the advantage of allowing multiple materials to be co-sublimed simultaneously, or to carry out multiple layer depositions without worrying about the dissolution of previous layers.[94] On the down side, the initial cost of buying the required equipment is high and this method is less applicable for large area fabrication.

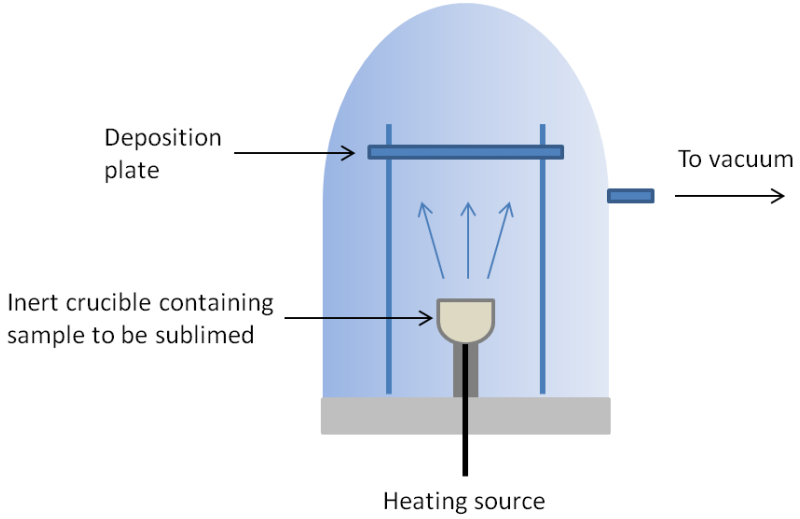

Figure 15 Schematic of a simple vacuum deposition chamber.

1.6. References

1. Pei, Z. J.; Fisher, G. R.; Liu, J., *International Journal of Machine Tools and Manufacture* **2008,** *48*, 1297-1307.
2. May, G. S.; Spanos, C. J., Fundamentals of Semiconductor Manufacturing and Process Control. In Wiley - IEEE Press: 2006.
3. Sun, Y.; Rogers, J. A., *Inorganic semiconductors for flexible electronics*. Wiley: Weinheim, ALLEMAGNE, 2007; Vol. 19, p 20.
4. Chen, Y.; Au, J.; Kazlas, P.; Ritenour, A.; Gates, H.; McCreary, M., *Nature* **2003,** *423*, 136-136.
5. Gelinck, G. H.; Huitema, H. E. A.; van Veenendaal, E.; Cantatore, E.; Schrijnemakers, L.; van der Putten, J. B. P. H.; Geuns, T. C. T.; Beenhakkers, M.; Giesbers, J. B.; Huisman, B.-H.; Meijer, E. J.; Benito, E. M.; Touwslager, F. J.; Marsman, A. W.; van Rens, B. J. E.; de Leeuw, D. M., *Nat Mater* **2004,** *3*, 106-110.
6. Katz, H. E.; Huang, J., *Annual Review of Materials Research* **2009,** *39*, 71-92.
7. Kelley, T. W.; Baude, P. F.; Gerlach, C.; Ender, D. E.; Muyres, D.; Haase, M. A.; Vogel, D. E.; Theiss, S. D., *Chemistry of Materials* **2004,** *16*, 4413-4422.
8. Chason, M.; Brazis, P. W.; Zhang, J.; Kalyanasundaram, K.; Gamota, D. R., *Proceedings of the IEEE* **2005,** *93*, 1348-1356.
9. *Physical and Chemical Aspects of Organic Electronics*. Wiley-VCH: 2009.
10. Małachowski, M.; Żmija, J., *Opto-Electronics Review* **2010,** *18*, 121-136.
11. Yang, X.; Wang, L.; Wang, C.; Long, W.; Shuai, Z., *Chemistry of Materials* **2008,** *20*, 3205-3211.
12. Yamashita, Y., *Science and Technology of Advanced Materials* **2009,** *10*, 024313.
13. Housecraft, C. E.; Sharpe, A. G., *Inorganic Chemistry* Second Edition ed.; Prentice Hall: 2005.
14. Weller, M. T., *Inorganic Materials Chemistry*. Oxford University Press: Oxford, 1994.
15. Stallinga, P., *Advanced Materials 23*, 3356-3362.
16. Mitzi, D. B., *Journal of Materials Chemistry* **2004,** *14*, 2355-2365.
17. Cox, P. A., *The Electronic Structure and Chemistry of Solids*. Oxford University Press: 1987.
18. Forrest, S. R., *Nature* **2004,** *428*, 911-918.
19. Mas-Torrent, M.; Rovira, C., *Chemical Society Reviews* **2008,** *37*, 827-838.
20. Service, R. F., *Science* **2006,** *312*, 1593-1594.
21. Klauk, H., *Chemical Society Reviews* **2010,** *39*, 2643-2666.
22. Jones, B. A.; Facchetti, A.; Wasielewski, M. R.; Marks, T. J., *Journal of the American Chemical Society* **2007,** *129*, 15259-15278.
23. Taguchi, T.; Wada, H.; Kambayashi, T.; Noda, B.; Goto, M.; Mori, T.; Ishikawa, K.; Takezoe, H., *Chemical Physics Letters* **2006,** *421*, 395-398.

24. Brütting, W.; Bronner, M.; Götzenbrugger, M.; Opitz, A., *Macromolecular Symposia* **2008,** *268*, 38-42.
25. Smits, E. C. P.; Anthopoulos, T. D.; Setayesh, S.; van Veenendaal, E.; Coehoorn, R.; Blom, P. W. M.; de Boer, B.; de Leeuw, D. M., *Physical Review B* **2006,** *73*, 205316.
26. Xu, Y.; Benwadih, M.; Gwoziecki, R.; Coppard, R.; Minari, T.; Liu, C.; Tsukagoshi, K.; Chroboczek, J.; Balestra, F.; Ghibaudo, G., *Journal of Applied Physics 110*, 104513.
27. Frank, O.; Friedhelm, B.; Karsten, H., *New Journal of Physics* **2010,** *12*, 023011.
28. Cho, J.-Y.; Domercq, B.; Jones, S. C.; Yu, J.; Zhang, X.; An, Z.; Bishop, M.; Barlow, S.; Marder, S. R.; Kippelen, B., *Journal of Materials Chemistry* **2007,** *17*, 2642-2647.
29. Olivier, Y.; Lemaur, V.; Bredas, J. L.; Cornil, J., *The Journal of Physical Chemistry A* **2006,** *110*, 6356-6364.
30. Podzorov, V.; Menard, E.; Borissov, A.; Kiryukhin, V.; Rogers, J. A.; Gershenson, M. E., *Physical Review Letters* **2004,** *93*, 086602.
31. Krellner, C.; Haas, S.; Goldmann, C.; Pernstich, K. P.; Gundlach, D. J.; Batlogg, B., *Physical Review B* **2007,** *75*, 245115.
32. Karl, N.; Kraft, K. H.; Marktanner, J.; Munch, M.; Schatz, F.; Stehle, R.; Uhde, H. M. In *Fast electronic transport in organic molecular solids?*, Papers from the 45th National Symposium of the American Vacuum Society, Baltimore, Maryland (USA), 1999; AVS: Baltimore, Maryland (USA), 1999; pp 2318-2328.
33. Takeya, J.; Kato, J.; Hara, K.; Yamagishi, M.; Hirahara, R.; Yamada, K.; Nakazawa, Y.; Ikehata, S.; Tsukagoshi, K.; Aoyagi, Y.; Takenobu, T.; Iwasa, Y., *Physical Review Letters* **2007,** *98*, 196804.
34. Ostroverkhova, O.; Cooke, D. G.; Shcherbyna, S.; Egerton, R. F.; Hegmann, F. A.; Tykwinski, R. R.; Anthony, J. E., *Physical Review B* **2005,** *71*, 035204.
35. Jurchescu, O. D.; Baas, J.; Palstra, T. T. M., *Applied Physics Letters* **2004,** *84*, 3061-3063.
36. Karl, N., *Synthetic Metals* **2003,** *133-134*, 649-657.
37. Shirota, Y.; Kageyama, H., *Chemical Reviews* **2007,** *107*, 953-1010.
38. Allard, S.; Forster, M.; Souharce, B.; Thiem, H.; Scherf, U., *Angewandte Chemie International Edition* **2008,** *47*, 4070-4098.
39. Newman, C. R.; Frisbie, C. D.; da Silva Filho, D. A.; Bredas, J.-L.; Ewbank, P. C.; Mann, K. R., *Chemistry of Materials* **2004,** *16*, 4436-4451.
40. Zaumseil, J.; Sirringhaus, H., *Chemical Reviews* **2007,** *107*, 1296-1323.
41. Newman, C. R.; Frisbie, C. D.; da Silva Filho, D. A.; BrÃ©das, J.-L.; Ewbank, P. C.; Mann, K. R., *Chemistry of Materials* **2004,** *16*, 4436-4451.
42. Lim, J. A.; Lee, H. S.; Lee, W. H.; Cho, K., *Advanced Functional Materials* **2009,** *19*, 1515-1525.
43. Katz, H. E.; Bao, Z.; Gilat, S. L., *Accounts of Chemical Research* **2001,** *34*, 359-369.

44. Coropceanu, V.; Cornil, J.; da Silva Filho, D. A.; Olivier, Y.; Silbey, R.; Bredas, J.-L., *Chemical Reviews* **2007,** *107*, 926-952.
45. Brown, A. R.; Jarrett, C. P.; de Leeuw, D. M.; Matters, M., *Synthetic Metals* **1997,** *88*, 37-55.
46. Tsumura, A.; Koezuka, H.; Ando, T., *Applied Physics Letters* **1986,** *49*, 1210-1212.
47. Horie, M.; Majewski, L. A.; Fearn, M. J.; Yu, C.-Y.; Luo, Y.; Song, A.; Saunders, B. R.; Turner, M. L., *Journal of Materials Chemistry* **2010,** *20*, 4347-4355.
48. Bao, Z.; Lovinger, A. J., *Chemistry of Materials* **1999,** *11*, 2607-2612.
49. Bao, Z.; Dodabalapur, A.; Lovinger, A. J., *Applied Physics Letters* **1996,** *69*, 4108-4110.
50. Wang, G.; Swensen, J.; Moses, D.; Heeger, A. J., *Journal of Applied Physics* **2003,** *93*, 6137-6141.
51. Di, C.-a.; Yu, G.; Liu, Y.; Guo, Y.; Sun, X.; Zheng, J.; Wen, Y.; Wu, W.; Zhu, D., *Chemistry of Materials* **2009,** *21*, 4873-4879.
52. Takahashi, T.; Takenobu, T.; Takeya, J.; Iwasa, Y., *Applied Physics Letters* **2006,** *88*, 033505-3.
53. Podzorov, V.; Sysoev, S. E.; Loginova, E.; Pudalov, V. M.; Gershenson, M. E., *Applied Physics Letters* **2003,** *83*, 3504-3506.
54. Lin, Y. Y.; Gundlach, D. J.; Nelson, S. F.; Jackson, T. N., *Electron Device Letters, IEEE* **1997,** *18*, 606-608.
55. Chia-Yu, W.; Shu-Hao, K.; Yu-Ming, H.; Wen-Chieh, H.; Adriyanto, F.; Yeong-Her, W., *Electron Device Letters, IEEE* **2011,** *32*, 90-92.
56. Vollmer, A.; Jurchescu, O. D.; Arfaoui, I.; Salzmann, I.; Palstra, T. T. M.; Rudolf, P.; Niemax, J.; Pflaum, J.; Rabe, J. P.; Koch, N., *The European Physical Journal E: Soft Matter and Biological Physics* **2005,** *17*, 339-343.
57. Okamoto, H.; Kawasaki, N.; Kaji, Y.; Kubozono, Y.; Fujiwara, A.; Yamaji, M., *Journal of the American Chemical Society* **2008,** *130*, 10470-10471.
58. Kawasaki, N.; Kubozono, Y.; Okamoto, H.; Fujiwara, A.; Yamaji, M., *Applied Physics Letters* **2009,** *94*, 043310-3.
59. Meijer, E. J.; Detcheverry, C.; Baesjou, P. J.; van Veenendaal, E.; de Leeuw, D. M.; Klapwijk, T. M., *Journal of Applied Physics* **2003,** *93*, 4831-4835.
60. Kawasaki, N.; Kalb, W. L.; Mathis, T.; Kaji, Y.; Mitsuhashi, R.; Okamoto, H.; Sugawara, Y.; Fujiwara, A.; Kubozono, Y.; Batlogg, B., *Applied Physics Letters* **2010,** *96*, 113305-3.
61. Tatsuo, H.; Jun, T., *Science and Technology of Advanced Materials* **2009,** *10*, 024314.
62. Sundar, V. C.; Zaumseil, J.; Podzorov, V.; Menard, E.; Willett, R. L.; Someya, T.; Gershenson, M. E.; Rogers, J. A., *Science* **2004,** *303*, 1644-1646.
63. Takeya, J.; Yamagishi, M.; Tominari, Y.; Hirahara, R.; Nakazawa, Y.; Nishikawa, T.; Kawase, T.; Shimoda, T.; Ogawa, S., *Applied Physics Letters* **2007,** *90*, 102120-3.
64. Wada, H.; Taguchi, T.; Noda, B.; Kambayashi, T.; Mori, T.; Ishikawa, K.; Takezoe, H., *Organic Electronics* **2007,** *8*, 759-766.

65. Bao, Z.; Lovinger, A. J.; Brown, J., *Journal of the American Chemical Society* **1998,** *120*, 207-208.
66. Shin-ichiro, N.; Taishi, T.; Yoshihiro, I.; Ho-Chol, C.; Susumu, K.; Tomoyuki, A.; Takayoshi, N., *Advanced Materials* **2008,** *20*, 3399-3403.
67. Dalgleish, S.; Yoshikawa, H.; Matsushita, M. M.; Awaga, K.; Robertson, N., *Chemical Science* **2011,** *2*, 316-320.
68. Dalgleish, S.; Morrison, C. A.; Middlemiss, D. S.; Mount, A. R.; Collins, A.; Pilia, L.; Serpe, A.; Mercuri, M. L.; Roberts-Bleming, S. J.; Charlton, A.; Deplano, P.; Murphy, P. J.; Robertson, N., *Journal of Materials Chemistry* **2009,** *19*, 6194-6200.
69. Dalgleish, S.; Labram, J. G.; Li, Z.; Wang, J.; McNeill, C. R.; Anthopoulos, T. D.; Greenham, N. C.; Robertson, N., *Journal of Materials Chemistry* **2011,** *21*, 15422-15430.
70. Bao, Z.; Lovinger, A. J.; Dodabalapur, A., *Applied Physics Letters* **1996,** *69*, 3066-3068.
71. Puigdollers, J.; Voz, C.; Fonrodona, M.; Cheylan, S.; Stella, M.; Andreu, J.; Vetter, M.; Alcubilla, R., *Journal of Non-Crystalline Solids* **2006,** *352*, 1778-1782.
72. Liqiang Li; Qingxin Tang; Hongxiang Li; Wenping Hu; Xiaodi Yang; Zhigang Shuai; Yunqi Liu; Zhu, D., *Pure Appl. Chem.* **2008,** *80*, 2231–2240.
73. Qu, L.; Guo, Y.; Luo, H.; Zhong, C.; Yu, G.; Liu, Y.; Qin, J., *Chemical Communications* **2012**.
74. Heutz, S.; Mitra, C.; Wu, W.; Fisher, A. J.; Kerridge, A.; Stoneham, M.; Harker, A. H.; Gardener, J.; Tseng, H. H.; Jones, T. S.; Renner, C.; Aeppli, G., *Advanced Materials* **2007,** *19*, 3618-3622.
75. Xue, J.; Rand, B. P.; Uchida, S.; Forrest, S. R., *Advanced Materials* **2005,** *17*, 66-71.
76. Hohnholz, D.; Steinbrecher, S.; Hanack, M., *Journal of Molecular Structure* **2000,** *521*, 231-237.
77. Kol'tsov, E.; Basova, T.; Semyannikov, P.; Igumenov, I., *Materials Chemistry and Physics* **2004,** *86*, 222-227.
78. Plyashkevich, V.; Basova, T.; Yushina, I.; Igumenov, I., *Journal of Surface Investigation: X-ray, Synchrotron and Neutron Techniques* **2008,** *2*, 423-428.
79. Chaure, N. B.; Sosa-Sanchez, J. L.; Cammidge, A. N.; Cook, M. J.; Ray, A. K., *Organic Electronics* **2009,** *11*, 434-438.
80. Miyazaki, E.; Kaku, A.; Mori, H.; Iwatani, M.; Takimiya, K., *Journal of Materials Chemistry* **2009,** *19*, 5913-5915.
81. Robertson, C. M.; Myles, D. J. T.; Leitch, A. A.; Reed, R. W.; Dooley, B. M.; Frank, N. L.; Dube, P. A.; Thompson, L. K.; Oakley, R. T., *Journal of the American Chemical Society* **2007,** *129*, 12688-12689.
82. Komatsu, H.; Matsushita, M. M.; Yamamura, S.; Sugawara, Y.; Suzuki, K.; Sugawara, T., *Journal of the American Chemical Society* **2010,** *132*, 4528-4529.
83. Matsushita, M. M.; Kawakami, H.; Sugawara, T.; Ogata, M., *Physical Review B* **2008,** *77*, 195208.

84. Toyonari, S.; Fujiwara, H.; Noguchi, S.; Murata, K., *Science and Technology of Advanced Materials* **2009,** *10*, 024302.
85. Coronado, E.; Galan-Mascaros, J. R.; Gomez-Garcia, C. J.; Laukhin, V., *Nature* **2000,** *408*, 447-449.
86. Palacio, F.; Miller, J. S., *Nature* **2000,** *408*, 421-422.
87. Nishijo, J.; Miyazaki, A.; Enoki, T.; Watanabe, R.; Kuwatani, Y.; Iyoda, M., *Inorganic Chemistry* **2005,** *44*, 2493-2506.
88. Hanasaki, N.; Matsuda, M.; Tajima, H.; Ohmichi, E.; Osada, T.; Naito, T.; Inabe, T., *Journal of the Physical Society of Japan* **2006,** *75*.
89. Matsuda, M.; Hanasaki, N.; Ikeda, S.; Tajima, H.; Naito, T.; Inabe, T., *JOURNAL DE PHYSIQUE IV* **2004,** *114*, 541-543.
90. Sugawara, T.; Komatsu, H.; Suzuki, K., *Chemical Society Reviews* **2011,** *40*, 3105-3118.
91. Matsushita, M. M.; Kawakami, H.; Kawada, Y.; Sugawara, T., *Chemistry Letters* **2007,** *36*.
92. Komatsu, H.; Mogi, R.; Matsushita, M. M.; Miyagi, T.; Kawada, Y.; Sugawara, T., *Polyhedron* **2009,** *28*, 1996-2000.
93. Sugawara, T.; Matsushita, M. M., *Journal of Materials Chemistry* **2009,** *19*, 1738-1753.
94. Ling, M. M.; Bao, Z., *Chemistry of Materials* **2004,** *16*, 4824-4840.
95. Hall, D. B.; Underhill, P.; Torkelson, J. M., *Polymer Engineering & Science* **1998,** *38*, 2039-2045.
96. Pud, A. A.; Fateeva, E. Y.; Shapoval, G. S., *Theoretical and Experimental Chemistry* **2002,** *38*, 33-36.
97. Horowitz, G., *Advanced Materials* **1998,** *10*, 365-377.

Chapter 2: Experimental Techniques

2.1. Overview

Owing to the multidisciplinary nature of this field of work, a wide range of techniques has been utilised over the course of this PhD. This chapter is intended to give the reader a brief introduction into the theory behind the commonly used techniques. Methods of analysis such as ^{1}H and ^{13}C Nuclear Magnetic Resonance (NMR), Mass Spectrometry (MS) and Microanalysis (or CHN analysis) are not discussed further in this chapter as their use is considered routine, and in the case of Mass Spectrometry and Microanalysis the analysis was performed by a service analyst/technician.

Absorption Spectroscopy, Electrochemistry, Crystallography, Electron Paramagnetic Resonance and Magnetic Susceptibility are all commonly used methods of analysis that are available "in-house" and, as such, are designated a section discussing the relevant theoretical principles behind the technique. Instrumentation not available in this department but used as part of a collaborative project, namely Thin Film XRD and SEM, are also briefly outlined below as they are considered crucial to the conclusions drawn in all of the thin film studies in Chapters 3, 4 and 5. The reader is also directed to more specialised texts on certain techniques where an extensive elaboration of theoretical aspects is offered. Specific experimental details of instrumentation and software used are not mentioned here but are instead given in the "Experimental Methods" section of the relevant chapter.

2.2. Absorption spectroscopy

Absorption (or electronic) spectroscopy monitors the absorbance of radiation by a sample as a function of wavelength or frequency. When a sample is irradiated, with radiation from the UV/visible/NIR region (~200 - 2500 nm) of the electromagnetic spectrum, transitions from electronic energy levels can occur. These excitations are usually from a bonding or lone pair orbital to an anti-bonding or non-bonding orbital.[1] The wavelength of the absorption is then related to the energy difference between the orbitals involved in the transition. Transition metal complexes are often brightly coloured as a result of the absorption of light in the visible region. The colours can arise from electronic transitions from the metal based orbitals, usually d-d transitions, or from charge transfer transitions between the metal and ligand based molecular orbitals. Charge transfer transitions between the metal and ligand can take the form of metal-to-ligand charge transfer (MLCT) or ligand-to-metal charge transfer (LMCT).

The probability of observing a transition is governed by selection rules; the spin selection rule and laporte selection rule. The spin selection rule states that for transitions to occur there must be no change in multiplicity ($\Delta S = 0$) on going from the ground state to the excited state *i.e.* singlet to singlet, or triplet to triplet states are allowed. The laporte transition rules state that electronic transitions are allowed if the there is a change in parity on going from the ground state orbital to the excited state orbital *i.e.* s → p, p→ d, d→ f are allowed, but s → s, p → p, d → d are forbidden.[2] Although d-d transitions are formally forbidden they are commonly observed as a result of vibronic coupling which disrupts the centrosymmetry in the molecule, making the transition partially allowed. The absorption intensity is related to two empirical laws; Lambert's law and Beer's law.[1] Lambert's law states that the portion of incident light absorbed is independent of the source intensity, and Beer's law states that the absorption is proportional to the number of absorbing molecules. Combined these laws give the Beer-Lambert law (Equation 1), where I_0 and I are the

intensities of the incident and transmitted light, respectively, with $\log_{10}(I_0/I)$ known as the optical density or absorbance, l is the path length, c is the concentration and ε is the molar extinction coefficient.[1] Care should be exercised when studying solutions of high concentrations as molecules can begin to aggregate, causing the relationship between absorbance and concentration to deviate from linearity. The magnitude of the molar extinction coefficient can reveal information on the type of transition that is occurring; for instance, if the transition is spin or Laporte "forbidden" then ε_{max} will be small, typically <10 $dm^3mol^{-1}cm^{-1}$ for a spin forbidden transition and <100 $dm^3mol^{-1}cm^{-1}$ for a Laporte forbidden transition. If ε_{max} is large, typically 1000-50,000 $dm^3mol^{-1}cm^{-1}$, then a fully allowed charge transfer transition has occurred.[2]

Equation 1

$$\log_{10}\frac{I_0}{I} = \varepsilon . l . c$$

Typically a measurement would involve making up a dilute solution of the chromophoric molecule in a non absorbing solvent. Commonly an initial background scan is carried out to compensate for any absorption attributable to the solvent. The sample is then irradiated beginning at a longer wavelength (low energy) going to the shorter wavelength (high energy) region of the electromagnetic spectrum, with the absorbance measured at each wavelength. From the resulting plot of absorbance vs. wavelength (or wavenumbers) the molar extinction coefficient can be calculated and used to help assign the transitions observed.

The use of absorption spectroscopy in materials chemistry can be a useful tool in evaluating the electronic structure of the sample in question. It can provide information on the HOMO-LUMO gap of solution samples, if this transition is observed, and it can also allow one to measure the band gap of a solid state sample. This can be achieved by measurements on either a thin film or through incorporating the material into a reflective, non-absorbing medium, such as barium sulphate or

potassium bromide, and carrying out Diffuse Reflectance Spectroscopy.[3] This latter method concerns the irradiation of a powder sample with a beam of incident light (I_0) and analysing the reflected light, rather than the transmitted light (I), which is measured in solution or thin film samples. Commonly, a 1-5 % by weight sample of material is homogeneously mixed with an opaque medium such as KBr or $BaSO_4$. Much of the incoming beam is reflected from the opaque surface of the sample and is known as *specular reflection* (Figure 1).[4, 5] Radiation that does penetrate the surface can be scattered or transmitted through the solid sample in various directions, before a fraction of this scattered light will leave the solid.[3] The back reflected, diffusely scattered light, which is not absorbed by the sample, is collected using an integrating sphere attachment on the spectrophotometer and can be processed to yield a plot of absorbance vs. wavelength. The solution spectrum can be compared with that obtained from diffuse reflectance or thin film spectrum; differences from the solution spectrum are often attributed to changes in the dielectric environment around the chromophore. Intermolecular interactions prevalent in the solid state sample can also lead to a "red-shifting" of the absorbance, compared with the solution spectra, if frontier orbital overlap between adjacent molecules is significant in the solid state. Orbital overlap is crucial to charge transport thus absorption spectroscopy can provide useful information on the applicability of conjugated molecules to solid state devices.

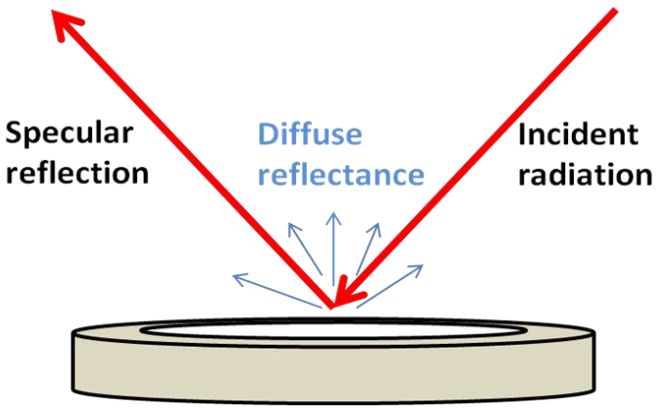

Figure 1 Schematic of incoming radiation interacting with a powder sample in a typical Diffuse Reflectance Spectroscopy measurement.[5]

2.3. Electrochemistry

Cyclic voltammetry (CV) and differential pulse voltammetry (DPV) are versatile electrochemical techniques that can be used to study the redox potentials of soluble, electroactive species. These techniques usually comprise a three electrode setup (shown in Figure 2), a high dielectric solvent containing a supporting electrolyte and an analyte in low concentrations. The electrolyte is added to ensure the electrochemical reaction is diffusion controlled by preventing the migration of analyte to and from the electrode as a result of electric field effects.[6] Electrolyte is usually present in concentrations 50-100 times greater than the analyte.[7]

During a CV experiment a voltage applied to an electrode, known as the working electrode, is cycled across a defined range as the resulting current is measured. The potential of this working electrode is controlled versus a reference electrode, which is also present in the electrochemical cell.[8] The working electrode is where the electron transfer reactions take place and where the current is measured. The third electrode in the cell is known as the counter or auxiliary electrode. In a three electrode cell, electricity can flow between the counter and working electrode, without passing a large current through the reference electrode.[6] The voltage is scanned linearly, at a fixed scan rate, from an initial potential, E_i, to another predetermined potential, E_1, before the direction of the potential is switched and the scan continued to another set potential, E_2.[9] This measurement produces a plot of current vs. voltage, also known as a voltammogram, which can be considered as the response signal to the potential excitation signal.[8]

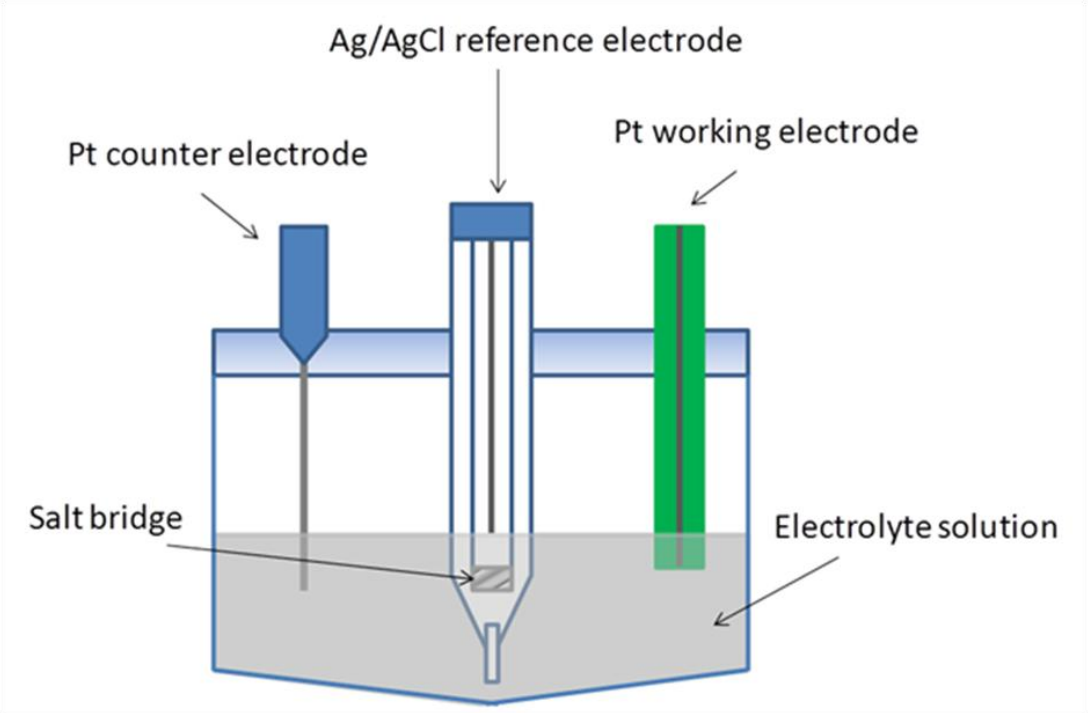

Figure 2 Three electrode setup used for electrochemical measurements.

A voltammogram of $Fe(CN)_6^{3-}$ is shown in Figure 3, where the voltage applied to the working electrode is scanned linearly from the starting point, E_i, to a predetermined point, $E_{\lambda 1}$, at which point the scan direction is reversed and the voltage is scanned to a second predetermined point, $E_{\lambda 2}$. As the potential is scanned to electronegative potentials, from E_i to $E_{\lambda 1}$, the current increases steeply, as $Fe(CN)_6^{3-}$ at the electrode surface is steadily oxidised to $Fe(CN)_6^{4-}$, and then falls as the potential approaches $E_{\lambda 1}$, due to the depletion of $Fe(CN)_6^{3-}$ around the electrode surface. After switching the scan direction, and moving from $E_{\lambda 1}$ to $E_{\lambda 2}$, the current again rises sharply (in the opposite direction to the reduction) before decreasing and beginning to plateau, which indicates oxidation of $Fe(CN)_6^{4-}$ back to $Fe(CN)_6^{3-}$. The forward and reverse scan current depends on, both, the movement of the redox active species to the surface of the working electrode i.e. mass transfer, and the electron transfer reaction between the analyte and the electrode.[9]

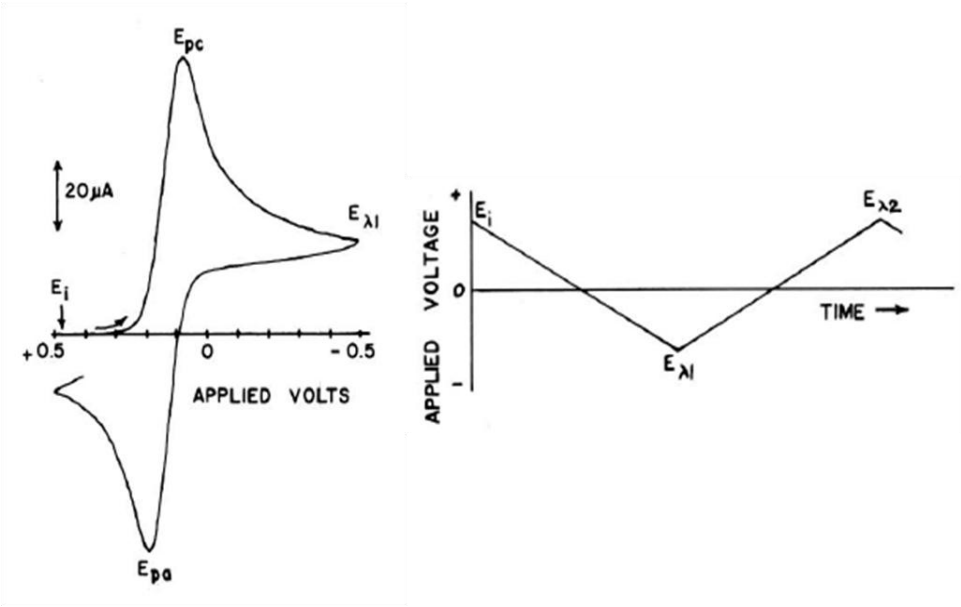

Figure 3 Cyclic voltammogram of $K_3Fe(CN)_6$ at a platinum electrode in aqueous 0.1 M KCl solution vs. Ag/AgCl (left) and the applied potential program (right). Image reproduced from Mabbott.[9]

The $Fe(CN)_6^{3-}/Fe(CN)_6^{4-}$ redox reaction can be understood by consideration of the Nernst equation (Equation 2), which describes the relationship between cell potential and concentrations.[6] The formal reduction potential of the $Fe(CN)_6^{3-}/Fe(CN)_6^{4-}$ couple is given by $E°$, the number of electrons involved in the process is given by n, and the extent of the applied potential, E, can control the ratio of $Fe(CN)_6^{3-}$ to $Fe(CN)_6^{4-}$ at the surface of the working electrode. Application of an initial voltage at a sufficiently positive potential (e.g. 0.5 V vs. Ag/AgCl) ensures that $Fe(CN)_6^{3-}$ is the predominant species in solution and negligible current is recorded, but on scanning to more negative potentials $Fe(CN)_6^{3-}$ is reduced to $Fe(CN)_6^{4-}$ in order to maintain the appropriate concentration ratio dictated by the Nernst equation.[6, 8, 9] The logarithmic relationship between E and $[Fe(CN)_6^{3-}]/[Fe(CN)_6^{4-}]$ is reflected in the dramatic increase in current as E approaches $E°$ i.e. $[Fe(CN)_6^{3-}]/[Fe(CN)_6^{4-}] = 1$.[8]

Equation 2

$$E = E° - \frac{RT}{nF} \log\left(\frac{[Reduced\ form]}{[Oxidised\ form]}\right)$$

Electrochemical techniques such as Cyclic Voltammetry, Differential Pulse Voltammetry and Square Wave Voltammetry usually require that the movement of species to and from the working electrode is diffusion controlled solely as a consequence of local concentration differences, and not as a result of convection from heating or stirring, or migration as a result of electric fields. Once the redox species has reached the working electrode, the rate of electron transfer must be fast, such that mass transport is the rate limiting factor. Additionally, for an electrochemically reversible, one-electron process the separation between the anodic and cathodic peak potentials should be no greater than 59 mV i.e. $\Delta E_p = E_{pa} - E_{pc} \leq 59/n$ mV, and the peak potential should not vary with scan rate. Under such Nernstian conditions the value of E° obtained is valid (Equation 3).

Equation 3

$$E^\circ = \frac{Epa + Epc}{2}$$

In reality many materials deviate from ideal Nernstian behaviour - the voltammogram may indicate chemical reversibility of the redox process with peak separation greater than 59 mV, or chemically irreversible if no return wave is observed after the initial oxidation or reduction. Chemically reversible, but electrochemically irreversible, processes can often be observed where the initial oxidation/reduction has accompanied a structural change in the redox species or in solvents where solution resistance is high. Chemical irreversibility is often the result of sample decomposition, which is not uncommon given the typical timescale of several seconds for cyclic voltammetry measurements and the inherent reactivity of organic radicals.

Cyclic Voltammetry involves increasing the potential linearly; however, increased electrochemical sensitivity can be achieved by modulating the applied potential. Such techniques include Square-Wave Voltammetry (SWV), Normal Pulse Voltammetry (NPV) and Differential Pulse Voltammetry (DPV).[7] These techniques

can be employed using the same three electrode setup as is used for CV studies. In the case of DPV, the applied potential is increased, or pulsed, in a series of small, fixed increments with the current being measured before and after each pulse (Figure 4). The difference in current between these two points is then plotted vs. the applied potential. The elimination of background current means that this technique is capable of detecting current with greater sensitivity than linear sweep voltammetric techniques such as CV, which makes it particularly useful for materials with limited solubility in organic solvents.

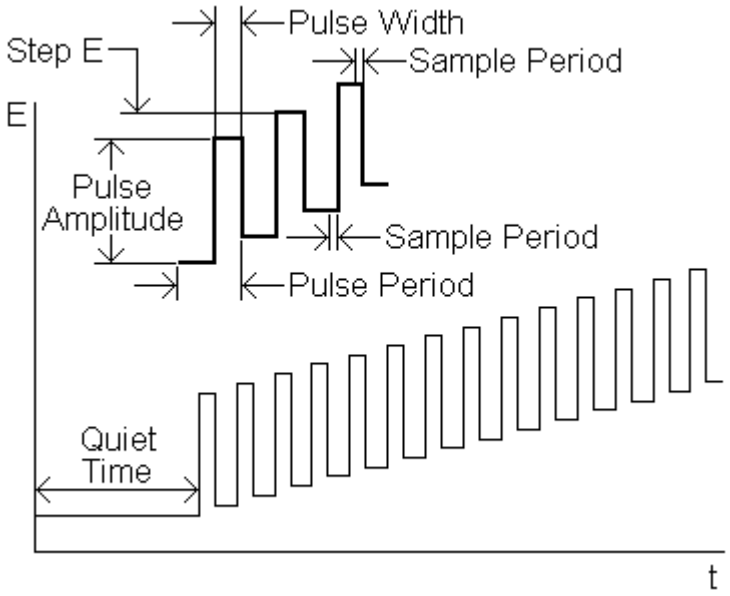

Figure 4 The applied potential program used in a typical Differential Pulse Voltammogram measurement. Image reproduced from Basi Epsilon instruction manual.[10]

2.4. Crystallography

All crystalline materials, in the solid state, display a regular array of atoms, molecules or ions. This regular (or periodic) array is repeated many times in all directions to give a highly ordered, crystalline solid.[11] The interaction of radiation, in

the form of X-rays, with this crystalline solid forms the basis of crystallography. It relies upon the interatomic distances in solids (usually a few Angstroms apart) being of comparable magnitude to the wavelength of incoming X-rays.[12] During a typical experiment, the wavelength of incoming radiation is usually fixed and the variation of intensity with direction is measured, as the X-rays are scattered. This intensity variation of the scattered radiation is an example of X-ray wave interference, also known as X-ray diffraction (XRD).[11]

2.4.1 Single crystal X-ray diffraction

X-ray diffraction carried out on a single crystal can provide a wealth of information such as unequivocal structural analysis, unit cell dimensions, bond lengths, bond angles and intermolecular interactions. More specifically, for device studies of molecular materials, the information that is afforded by XRD is vitally important and should not be understated. It can provide information on the degree of conjugation across bonds as well as the strength of intermolecular interactions within the lattice, both crucially important to the conductivity.

A single crystal is made up of small repeating units that are linked together by translation to form an extended three dimensional structure. This repeating unit is known as the unit cell. Depending on the material the unit cell can range from containing just a single atom to several molecules, in a fixed arrangement. Structures are then further defined by their lattice system and associated symmetry as a result of the lengths of the unit cell axis (*a*, *b* and *c*) and the angles between them (α, β and γ); these lengths and angles are known as lattice parameters. There are seven commonly observed crystal systems classified by the rotational symmetry elements of the unit cell; Cubic, Tetragonal, Hexagonal, Rhombohedral, Orthorhombic, Monoclinic and Triclinic.[13] Within those crystal systems there are a total of 14 distinct Bravais lattices, with each one classified based on translational symmetry. Structures can be

further classified by using Space Groups, of which 230 exist. This distinction is based upon translational symmetry of the unit cell and all point group symmetry operations.

Diffraction from a single crystal will only occur if Bragg's equation (Equation 4) is satisfied, namely, the interaction of X-rays gives rise to constructive interference. Consider two beams of incoming X-rays approaching a crystalline solid as shown in Figure 5 (right); one beam strikes point A whilst the other travels additional distance, BC, and strikes point D on the lattice plane beneath. The overall path length difference of the two rays is then: BD + CD = 2d sinθ, where θ is the glancing angle, d is the interplanar distance and λ is the wavelength of the incoming radiation.[13] If the path length difference (BD + CD) is an integer number of wavelengths then in-phase diffracted X-rays (constructive interference) will be observed. However, if the path length difference is not an integer number of wavelengths then the reflected X-rays will be out-of-phase resulting in destructive interference.

Equation 4 $$n\lambda = 2d\ sin\ \theta$$

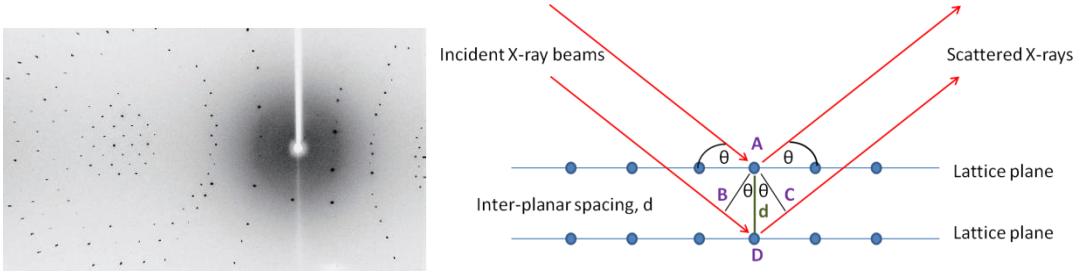

Figure 5 A typical diffraction pattern obtained from a single crystal (left) reproduced from Hasegawa *et al*,[14] and how the incoming X-ray interacts with the crystalline lattice (right).

A typical single crystal XRD experiment involves taking a single crystal, mounting it onto a fibre on a goniometer and focusing a beam of monochromatic X-rays onto the

sample. The single crystal is rotated in the beam to bring all atomic planes into a diffracting position. The interaction of X-rays with electron density causes scattering, with the scattering power of an atom dependant on the number of electrons around its nuclei.[2] These scattered X-rays are then recorded using a detector, usually an image plate or charge-couple detector (CCD). The collected X-rays take the form of diffraction spots on the detector, with the intensity and location of these spots providing structural information (Figure 5, left).[14] Using a mathematical transformation, known as a Fourier Transform, allows an electron density map to be calculated from the diffraction pattern (Figure 6).[14] After data collection, the final step is to solve the structure which can be achieved by use of computational software (and a skilled operator) to produce an atomic level structure.

A lengthy discussion of single-crystal structure determination is outwith the scope of this brief introduction, as in all cases the structures reported in this thesis were either determined by a trained crystallographer or with the help of a trained crystallographer. However, more thorough discussions of the practises and principles behind this process can be found by Clegg[11] and/or Massa.[15]

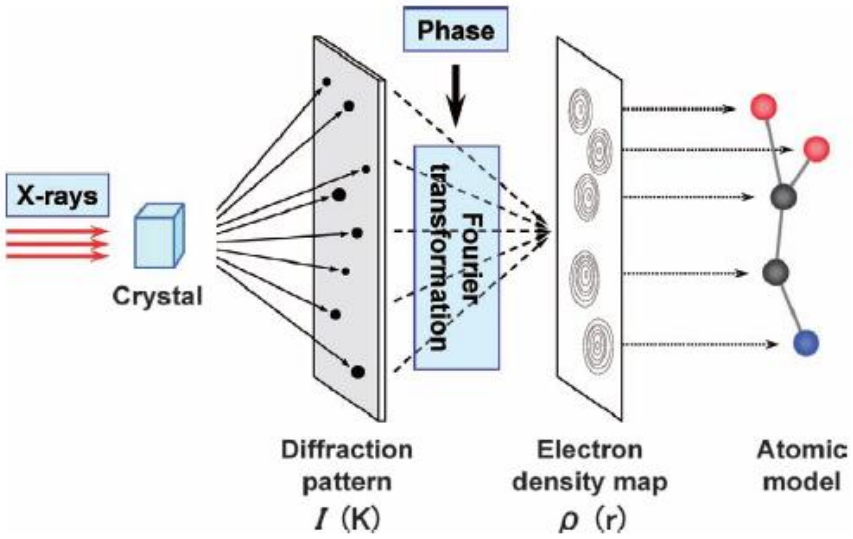

Figure 6 A schematic of the simplified process of obtaining a structure solution from a single crystal sample. Image reproduced from Hasegawa *et al*.[14]

2.4.2 Powder X-ray diffraction

As the name suggests, Powder X-ray Diffraction involves the study of a homogeneous powder or polycrystalline sample using X-ray diffraction. The technique finds widespread application in materials chemistry and can reveal vital information on, but not limited to, the following: phase purity, preferred orientation, crystallinity, lattice parameters, structure refinement and determination, crystallite size and phase transitions.[12] Clearly, the powder XRD data obtained will depend on the crystallinity of the sample and the structure it adopts. A powder or polycrystalline sample contains a huge number of small crystallites orientated in different directions. These random orientations of crystallites will thus give rise to a series of diffraction peaks, as governed by the Bragg equation (Equation 4). Using this information, the interplanar distance can be calculated from the angle of diffraction as determined from the powder pattern (commonly recorded as 2θ), with the shape of the reflection related to the crystallinity of the sample i.e. crystalline solids give rise to sharp diffraction peaks, amorphous materials result in broad, less defined peaks. The intensity of the peaks is dependent upon the scattering factor of the atoms that comprise the unit cell.[16]

The technique is commonly used to check the phase purity of a polycrystalline sample, by comparison with the known diffraction pattern obtained by single crystal studies. In this context, the obtained powder pattern can additionally be screened against a database of previously reported results allowing an unknown material, or impurity, to be identified from its diffraction pattern. Structure determination from first principles is more complicated using powder XRD methods. In a powder measurement all the reflections occur along a single axis, 2θ, and at higher values of 2θ reflections have a tendency to overlap. This makes the extraction of information on individual peak intensities, necessary for structure determination, troublesome.[12] However, from powder XRD data structure refinement can be attempted using a method known as the Rietveld refinement.[12] This involves creating a trial structure

and generating a predicted powder pattern based upon this trial structure. The lattice parameters of this trial structure are then optimised until the predicted pattern gives a good match to the experimentally observed powder pattern.

Determination of the particle size can be achieved by inspection of the breadth of powder XRD peaks using the Scherrer Equation (Figure 5); where t is the crystallite thickness, λ is the X-ray wavelength, θ is the Bragg angle, and B_M and B_S are the width in radians of the diffraction peaks from the sample and a standard at half height.

Equation 5

$$t = \frac{0.9\lambda}{\sqrt{B_M^2 - B_S^2}\cos\theta}$$

Additionally, identification of phase changes as a function of temperature is another piece of useful information which can be achieved using a powder diffractometer with a furnace or cryostat. Phase transitions will give rise to marked differences in the diffraction pattern. This is particularly important when studying the magnetic or conducting properties of a compound and basing the interpretation of the results on a single crystal structure determined at a different temperature. For example, molecular semiconductors are most commonly studied in FET devices at room temperature but their structure is most likely to have been determined at a much lower temperature, perhaps ~100 K lower. In this scenario, the powder pattern at room temperature should be determined and compared to the powder pattern predicted from the single crystal structure to ensure that any conclusions drawn on structure-activity relationships are valid.

2.4.3 Thin film X-ray diffraction

The crystal packing of a molecular semiconductor in a thin film is crucial to the performance of a device such as an FET or p/n junction solar cell. Charge transport is reliant on good intermolecular overlap and different polymorphs will give rise to different conductive properties, therefore elucidation of the thin film morphology is crucial to understanding the thin film performance.[17] However, the diffraction intensities from thin film samples deposited on substrates can be relatively weak when compared to the background reflections from the substrate. Thin film XRD with a grazing incident X-ray beam is commonly used to enhance the diffraction intensity from the sample, relative to the substrate and can be used in conjunction with single crystal data to interpret the surface structure.[18, 19] When deposited onto a substrate, molecules often tend to adopt a preferred orientation or alignment as a consequence of the interaction with the substrate. The film is two-dimensionally formed with the materials commonly exhibiting a large anisotropy either parallel to the substrate (out-of-plane) or perpendicular to the substrate (in-plane).

In a conventional $2\theta/\theta$ powder XRD measurement (Figure 7, top left) information is obtained on the molecular alignment of the crystallites parallel to the substrate.[20] In this "symmetrical" mode the angle of θ is the same for the incident and diffracted beam. As a result the beam penetrates deep into the sample, tens of μm, and the sample reflections are masked by the more intense reflections from the substrate.[21] Alternatively, positioning the incident X-rays at a shallow angle relative to the substrate and scanning the detector to measure inclined lattice planes allows information to be attained on the thin film structure (Figure 7, top right).[20] In this "asymmetrical" method the penetration of the incident beam into the film can be controlled to several μm or less, meaning that reflections from the substrate can be suppressed, therefore enhancing the relative sample signals.[21] A highly orientated material may only give rise to a reflection from one crystallographic plane. Both the

symmetric and asymmetric methods are known as Out-of-Plane measurements since the scattering vector is pointed out from the sample surface.

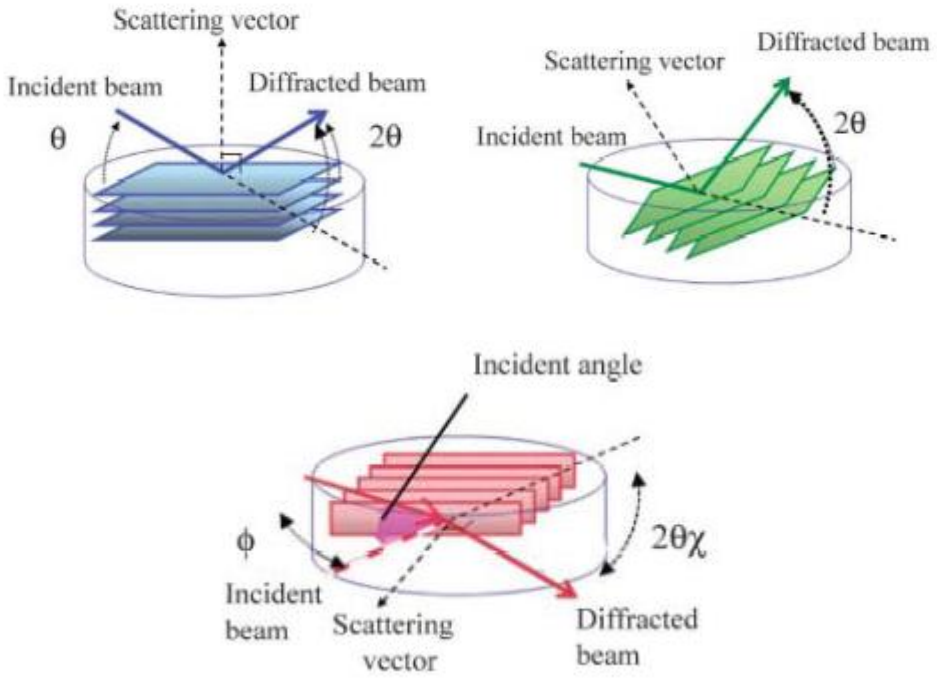

Figure 7 Schematic illustrating the crystallographic planes measured in Out-of-Plane (top left), Out-of-Plane in Thin Film mode (top right) and In-Plane XRD (bottom). Image reproduced from Kobayashi.[19]

A method for providing information on the lattice planes perpendicular to the substrate is known as In-Plane XRD (Figure 7, bottom), where the scattering vector lies parallel to the sample surface. In this measurement mode the incident X-ray beam is positioned at low angles such that it can penetrate deep into the sample to obtain high intensity sample reflections, whilst minimising substrate signals.[19] The angle of the incident beam can be controlled by varying the sample rotation angle (φ) and the position of the detector ($2\theta\chi$) as shown in Figure 7, bottom. Additionally, unlike Out-of-Plane modes, this technique can also provide depth-profile information by varying the incidence angle. For further information on In-Plane and Out-of-Plane grazing incidence XRD then the reader is referred to some excellent review articles from Rigaku[19-21] which describe the techniques in far more detail.

2.5. Electron paramagnetic resonance spectroscopy

Electron paramagnetic resonance (EPR), also known as electron spin resonance (ESR), is a technique for studying materials with unpaired electrons, either organic radicals or paramagnetic transition metal complexes. It is analogous to NMR spectroscopy but instead of exciting a nuclear spin, an unpaired electron is excited. As each electron has an intrinsic angular momentum (spin) associated with it, this gives rise to a magnetic dipole moment.[22] For spin angular momentum (S), $2S+1$ non degenerate energy levels can be obtained in the presence of a magnetic field.[23] For example, considering an $S=1/2$ system, two non-degenerate energy levels are possible, $M_s= -1/2$ or $M_s= +1/2$, which correspond to the unpaired electron being aligned with or opposed to the magnetic field. The splitting of degenerate energy levels in the presence of a magnetic field is known as the Zeeman effect (Figure 8) and the likelihood of a transition occurring is governed by the selection rule, $\Delta M_s= \pm 1$. In a typical EPR experiment the frequency of the radiation (v) is fixed and the magnetic field (H) is swept; at a certain field strength there is an absorption of energy which results in the electron spin being promoted from the $M_s= -1/2$ to the $M_s= +1/2$ energy level. The separation between the energy levels is given by Equation 6, where h is Planck's constant, μ_B is the Bohr magneton and g is the g-factor.[24] The g-factor is a fundamental constant related to the magnetic moment of the electron; for a free electron $g_e= 2.002319$. However, in reality g often varies from the free electron value (g_e) because of orbital angular momentum contributions; this is particularly prominent in transition metal complexes. This mixing of orbital angular momentum and spin angular momentum is known as spin orbit coupling and is more significant for heavier elements. In 2nd and 3rd row transition metal complexes spin-orbit coupling constants can become quite significant and therefore the measured g-value varies greatly from the free electron value. Thus the measured g-value can often provide information on the location of the unpaired electron as well as the extent of delocalisation in a paramagnetic material *i.e.* is the SOMO metal based, ligand based or a combination of the two.

Equation 6 $$\Delta E = h\nu = g\,\mu_B\,H$$

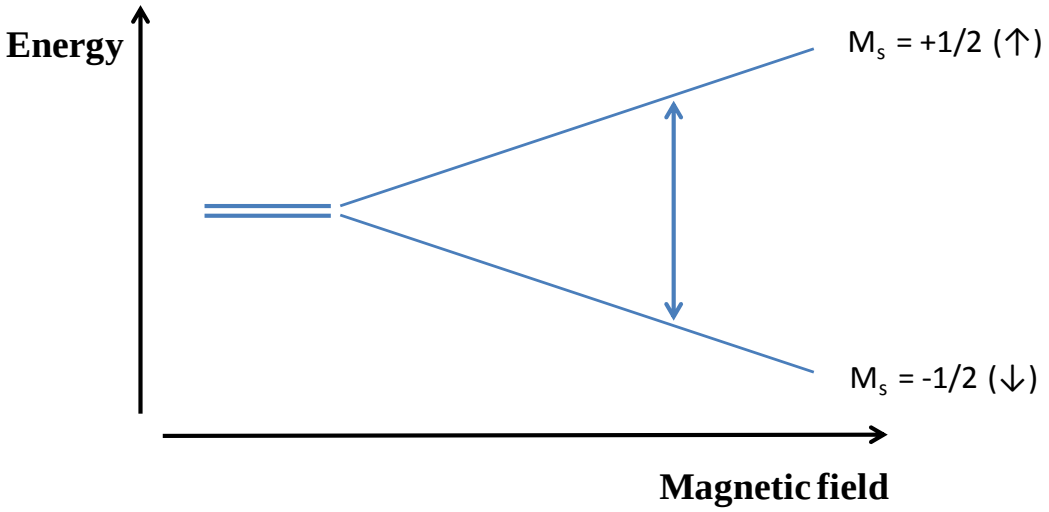

Figure 8 Zeeman splitting under an applied magnetic field.

Also witnessed by EPR is hyperfine coupling, which is the result of coupling between the unpaired electron and the nuclear spin (I); this is analogous to nuclear spin-nuclear spin (J) coupling in NMR. Interaction between the unpaired electron and nuclear spin causes additional splitting of the electronic states into $2I+1$ sublevels, where the selection rule is $\Delta M_I = 0$. Since the nuclear magnetic moment is about 1000 times smaller than an electron's magnetic moment, the splitting between M_I states is very small and transitions between these states gives rise to hyperfine splitting of the spectra.[23] The presence of hyperfine coupling as a consequence of an unpaired d-electron interacting with a nuclear spin on a ligand provides direct evidence of delocalisation in the complex.[25] The hyperfine splitting can be quantified by coupling constant A (or a in the case of organic radicals). As a result of the interaction between the unpaired electron and nuclear spin, information on the magnitude of delocalisation across the molecule can be estimated. The extent of delocalisation is an important consideration in the study of molecular

semiconductors, where delocalised frontier orbitals are required in order to help facilitate improved charge transport. Additional important information that can be derived from EPR includes the composition of the SOMO and the degree of metal-ligand covalency.[25] A more in-depth discussion of EPR, beyond the scope of this introduction, can be found in Ayscough, 1967.[22]

2.6. Magnetic susceptibility

The magnetic susceptibility is the quantified measure of the response of a material to an applied magnetic field.[24] Unpaired electrons in a molecule can give rise to paramagnetic behaviour, however, all electrons, both unpaired and paired, result in a diamagnetic response.[26] Diamagnetic materials are repelled by a magnetic field and this response is independent of temperature, where as paramagnetic materials are attracted to the field and their magnetic susceptibility is temperature dependent. Paramagnetic materials can often give rise to antiferromagnetic, ferromagnetic or ferrimagnetic interactions below a certain ordering temperature. The measured magnetic susceptibility of a sample is the result of its diamagnetic and paramagnetic contributions (Equation 7). All paramagnetic compounds have a diamagnetic component, which must be calculated in order to determine the paramagnetic susceptibility accurately. Diamagnetic contributions to a compound can be measured and subtracted from the total magnetic susceptibility e.g. by measuring the diamagnetic response from the ligand(s) in the absence of the paramagnetic ion and using this value. Alternatively, the diamagnetic component can be estimated using Pascal's Constants, which take into account contributions from the metal ions and additional contributions from bonding interactions.[26]

Equation 7 $$\chi_M = \chi_P + \chi_D$$

Normal paramagnetic materials obey the Curie Law shown in Equation 8, and Equation 9 where the Curie constant (C) is equal to $(Ng^2\beta^2/3k)/S(S+1)$. This results in the magnetic susceptibility being inversely proportional to temperature and the magnetic moment (μ) constant with temperature. However, not all paramagnetic materials obey Curie type behaviour. Compounds can deviate from Curie's Law as a consequence of interactions between metal centres and/or spin-orbit coupling effects. This can be observed by plotting $1/\chi$ vs. T; Curie type paramagnets will result in a straight line intercepting the x-axis at zero but paramagnets that do not obey the Curie Law will not intercept the temperature axis at zero. As a result, an additional factor known as the Weiss constant (θ) is added to the Curie equation to produce the Curie-Weiss law (Equation 10). In the absence of significant spin-orbit coupling, the sign of θ provides information on the type magnetic ordering interactions occurring in the compound, with $\theta > 0$ indicating ferromagnetic interactions and $\theta < 0$ indicating antiferromagnetic interactions.

Equation 8

$$\chi_P = \frac{C}{T}$$

Equation 9

$$\chi_P T = \frac{N_A g^2 \beta^2}{3K_B}[S(S+1)]$$

Equation 10

$$\chi_P = \frac{C}{T-\theta}$$

Macroscopic properties of a compound such as χ and M can be linked to individual molecular properties by calculating the effective magnetic moment per moment (μ_{eff}) given in Equation 11, where S is the total spin quantum number and L is the total orbital angular momentum quantum number. Often the orbital contribution to the magnetic momentum is considerably less than the spin contribution, particularly for first row transition metals, and in these cases the orbital contribution can often be neglected. In such a scenario, the spin-only magnetic moment (μ_{SO}) can be used

(Equation 12), which does not consider an orbital contribution to the magnetic moment. If both spin and orbital angular momentum contributions affect the magnetic moment of a metal ion, this interaction between spin and its motion around the nucleus is known as *spin-orbit coupling*. In situations where spin-orbit coupling is negligible the g-factor is close to the free electron value of 2.0023. Large deviations from the free electron value are often witnessed in the study of second and third row transition metals ions, where the spin-orbit coupling contributions are significant.

Equation 11 $$\mu_{eff} = \sqrt{4S(S+1) + L(L+1)}$$

Equation 12 $$\mu_{SO} = g\sqrt{S(S+1)}$$

Materials which deviate from the Curie Law at low temperatures are often the most interesting candidates to study. At high temperatures thermal energy causes spins to fluctuate randomly and, as such, paramagnetic behaviour is observed. At low temperatures the driving force for magnetic moments to order becomes sufficient such that it can overcome this thermal energy barrier.[27] As a result, long range magnetic ordering interactions such as ferromagnetism, antiferromagnetism or ferrimagnetism (Figure 9) are observed.

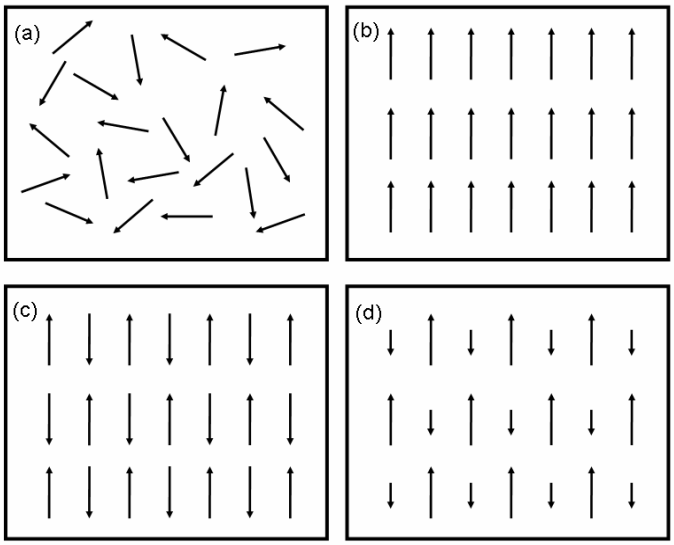

Figure 9 In the absence of magnetic ordering, or at high temperatures, paramagnetism (a) is observed. At a certain temperature the magnetic ions can order spontaneously and the magnetic moments can align parallel, resulting in ferromagnetism (b), or align anti-parallel resulting in antiferromagnetism (c). If the magnetic moments aligned anti-parallel to each other are of different size this is known as ferrimagnetism (d). Image taken from Robertson *et al*.[27]

The ordering interaction between adjacent magnetic moments is known as *magnetic exchange* and it can occur by two mechanisms, namely, superexchange or direct exchange.[24] If there is direct orbital overlap between adjacent paramagnetic metal ions then a direct exchange interaction can occur. The most commonly observed metal to metal interaction is mediated through a non-magnetic ligand i.e. M-L-M and this is known as superexchange.[24, 27] The magnetic exchange interaction is denoted by *J*. The sign of *J* is dependent upon the type of magnetic ordering interaction i.e. antiferromagnetic (negative) or ferromagnetic (positive), with the magnitude of *J* providing information on the strength of the interaction. Described in Equation 13 is the isotropic Heisenberg spin Hamiltonian, $\hat{H}$, which only involves spin operators, $\hat{S}$; using this we can calculate the magnitude and sign of the magnetic exchange interaction. This simple Hamiltonian is applied to the study of equally spaced, identical spin centres in a one dimensional chain. Additionally, only nearest neighbour interactions are considered. This Hamiltonian generally works quite well

for Cu(II) ions but becomes less suitable for ions with a large spin or a significant orbital angular momentum contribution to its magnetic moment.[27]

Equation 13 $$\widehat{\boldsymbol{H}} = -\boldsymbol{J}\sum_{\boldsymbol{i=1}}^{\boldsymbol{n-1}} \widehat{\boldsymbol{S}}_{\boldsymbol{A_i}} . \widehat{\boldsymbol{S}}_{\boldsymbol{A_{i+1}}}$$

A wide range of other Hamiltonians exist that take into account more complicated spin systems such as those with more than one unpaired electron as well as systems with anisotopic exchange interactions. However, a discussion of these more complex topics is beyond this introduction and instead the reader is directed to a more advanced text such as those written by Kahn[28] and/or Carlin.[24] Indeed, a more detailed discussion of magnetism in general can also be obtained from these books.

The measurement of magnetic susceptibility has been achieved using a Magnetic Property Measurement System (MPMS). The MPMS consists of several superconducting components: a superconducting magnetic to generate large magnetic fields; a superconducting detection coil, which is inductively coupled to the sample; a superconducting quantum interference device (SQUID) connected to the detection coil; and a superconducting magnetic shield surrounding the SQUID.[29] The instrument is configured to measure the magnetic moment but from this magnetisation (M) and magnetic susceptibility (χ) information can be obtained.

2.7. Computational methods

Computational chemistry, often referred to as molecular modelling, is becoming increasingly popular in chemical research and can help shed light on a wide range of topics. Examples of the types of information that theoretical modelling can provide

include: geometry optimised structures and their energies, molecular properties, reaction rates, time dependence of molecular structures and properties, and how different molecules interact with one another.[30] Computational calculations are particularly useful when coupled with experimental data to help predict the results prior to carrying out lengthy experimental work, or to help interpret the results post experiment. It has become an indispensable tool to the modern day medicinal chemist in the quest for new drug targets; a pharmacophore can be created virtually and screened against a molecular database to find compounds capable of affecting the desired target. This method can help to efficiently pinpoint a suitable drug candidate, as well as eliminate an unsuitable candidate, prior to investing large amounts of time, money and effort into synthesis. However, one must be wary of becoming over reliant on calculation by assuming that the answers it can provide are always correct. The quality of the data produced relies heavily upon the input data and the question being asked. Thus, the starting structure(s) and level of theory employed is crucial to any result produced and, most likely, the result obtained will change upon altering the input data.

There are essentially two main methods of calculating molecular structures, *molecular mechanics* and *quantum mechanics*. The classical approach is molecular mechanics, commonly referred to as force field methods, and is based upon Newton's equation. Force field methods treat atoms as single particles connected to other atoms by bonds which act as springs. The bond lengths and angles are assigned an initial equilibrium value from experimentally obtained spectroscopic and crystallographic data and the energy of the structure is calculated as the conformation of the molecule changes.[31] This method is computationally inexpensive and finds wide spread application when calculating energy minimised structures especially in the case of large biological molecules such as proteins.[32] However, one of the major limitations in this method is that it neglects electrons. This means that no information on electronic structure - such as bonding, chemical reactivity, excited state properties etc - can be obtained using this method of modelling.[33]

In contrast, quantum mechanical methods are based upon solving the Schrödinger equation (Equation 14),[30, 31] where H is the Hamiltonian operator which comprises the potential and kinetic energy terms for a system containing electrons and nuclei, where E is the energy and Ψ is the wavefunction. The Hamiltonian is composed of five terms (Equation 15); electron (T_E) and nuclei (T_N) kinetic energy terms as well as potential energy terms considering interactions such as electron-electron (V_{EE}), nuclei-nuclei (V_{NN}) and electron-nuclei (V_{NE}). Calculations that rely solely on solutions to the Schrödinger equation, without the use of any experimental data, are referred to as *ab-initio*, meaning "from scratch" in Latin.

Equation 14 $$\boldsymbol{H\Psi = E\Psi}$$

Equation 15 $$\boldsymbol{H = T_E + T_N + V_{NE} + V_{NN} + V_{EE}}$$

However, due to the overwhelming mathematical complexity involved, the Schrödinger equation can only be solved exactly for systems comprising one electron. In order to perform calculations on systems containing more than one electron approximations must be made. Since the motion of electrons is much greater than that of nuclei, the Born-Oppenheimer approximation allows the electronic and nuclear motion terms to be treated independently of one another.[33] In essence, we can treat the nuclei as stationary relative to the electrons and the Hamiltonian can be reduced to the "electronic" Schrödinger equation (Equation 16). In this situation the kinetic energy term of the nuclei is neglected and the repulsive nuclei-nuclei interaction is described using a constant, calculated from Coulomb's Law.[33]

Equation 16 $$\boldsymbol{H\Psi_E = E\Psi_E}$$

Ideally, the Schrödinger equation could be solved one electron at a time to give N solutions (where N = the number of electrons) and the total energy of the system could then be calculated by summation of the individual solutions for each electron. However, this approach fails to account for correlation (i.e. how the motion of one electron affects another), and electrostatic electron-electron repulsions are far too significant to ignore especially in many electron systems. So, despite being simplified, the electronic Schrödinger equation is still too complex and further approximations are required. Hartree theory simplifies the situation further by ignoring correlation and as a consequence the electron-electron (V_{EE}) repulsion is not explicitly taken into account. Instead, we assume that each electron is moving in a uniform field of other electrons and an average Coulombic repulsive effect is accounted for. In order to model a many electron system, electronic exchange interactions (i.e. pairing up of opposite spins) must also be taken in account and this is achieved using Fock theory. Bearing in mind the Pauli Exclusion Principle, Fock theory uses an anti-symmetric wavefunction allowing electrons of opposite spins to be paired up. The combination of Hartree and Fock theory - aptly named Hartree-Fock (HF) theory - typically accounts for approximately 99 % of the total energy in the system, with the missing energy due to neglection of the correlation term.[30] Fortunately, electronic exchange interactions are modelled very accurately. The accuracy of HF calculations can be improved upon by looking at various levels of theory, which take HF as a starting point and incorporate additional terms to try and better model exchange interactions. Modelling of many electron systems is very complex and computationally demanding but HF offers a significant saving on computational resources whilst providing an acceptable level of accuracy.[30]

An alternative approach to better predicting electronic correlation is to use Density Functional Theory (DFT). This approach relies on calculating the ground state energy (E) of a system from its three-dimensional electron density (ρ).[34] An attractive feature is that the many-body effect of electron correlation is modelled by electron density, an experimental observable, as opposed to calculation of the many-electron wavefunction used in HF methods.[33] Early work by Hohenberg[35] and Kohn

proved that, in principle, it was possible to exactly calculate the ground state energy of a uniform electron gas from its electron density; however, it does not say what this functional is that relates electron density to energy. Nowadays, DFT is almost always based on the formalism described by Kohn and Sham,[34, 36] where the kinetic energy of the electron can be derived from an auxiliary set of orbitals used to represent exactly the electron density of the real system.[30, 31, 37] In these equations an additional term is added to account for the exchange-correlation (XC) energy in terms of electron density. The XC term represent only a small portion of the overall energy of the system but it is still an unknown functional and as a result various different approximations are used to try and better model this. These approximations include Local Density Approximation (LDA), which treats the system as a uniform electron gas that has a constant electron density throughout, and Generalised Gradient Approximation (GGA) which does take into account varying electron density throughout the system. Clearly, LDA may work well for systems such as metals and GGA may be more appropriate for molecular systems but the real value of XC still remains an unknown parameter. DFT is similar to HF in terms of computational demand and tends to produce more accurate results, but the major limitation is that there is no systematic way of improving the results obtained by DFT towards an accurate solution.[30]

Combining DFT and HF gives rise to hybrid-Density Functional Theory, which can bring together the best aspects of both methods. Where HF ignores correlation, DFT approximates it and where HF accurately models exchange, DFT approximates. Thus improved computational accuracy, without being computationally demanding, can be achieved by combining the accurate exchange determined by HF with the approximate correlation determined by DFT. As an illustration of the combined power of DFT and HF, the hybrid functional B3LYP has to date become the most commonly used approximation in chemistry.[37]

During the course of this work gas phase calculations on isolated molecules have been carried out to calculate the energy minimised structures as well as to help better understand their electronic and optical properties. All calculations have been carried out using hybrid-Density Functional Theory at the B3LYP/6-31G(d,p) level of theory. Input structures have been created using ArgusLab software[38] using single crystal structures as the starting coordinates, where possible. The calculations have been carried out using Gaussian 03,[39] and later Gaussian 09,[40] software packages.

2.8. Scanning electron microscopy

When preparing thin film devices it is necessary to study the morphology of the deposited material to understand more about the device performance. The thin film morphology and crystallite size is particularly important for conducting devices such as FETs and p/n junction solar cells. Scanning electron microscopy (SEM) is a technique for producing high resolution images of the surface morphology and topography, far superior to those obtained by optical microscopy. Surface features as small as 1 nm can be resolved using SEM.[41]

A scanning electron microscope operates by focusing a beam of incident electrons, typically up to 40 keV, onto a solid sample and measuring the signal generated from the solid sample.[42] The beam of electrons is typically produced by heating a tungsten filament under high vacuum, and then accelerated down a column through a voltage potential.[43, 44] The interaction of the incoming incident electrons with the solid sample produces backscattered, secondary and Auger electrons, as well as X-rays (Figure 10). The electrons can be scattered elastically, without loss of energy, in the case of backscattered electrons, or inelastically, with loss of energy, in the case of secondary and Auger electrons.[41, 44]

After illumination of the solid surface, secondary and backscattered electrons from the sample surface are recorded and an image is rendered. Secondary electrons, ejected from valence orbitals, typically have energies less than 50 eV and provide high resolution topographic images as they have been displaced from atoms near the surface of the solid sample. Higher energy backscattered electrons provide less resolved images because they come from deeper within the sample, but they can provide information on the composition of the sample, with heavier elements producing brighter contrast.[41] Auger electrons emitted close to the solid surface provide valuable information on the surface chemistry but the difficulty in precisely measuring their energies limits Auger electron imaging to specialised instruments.[41]

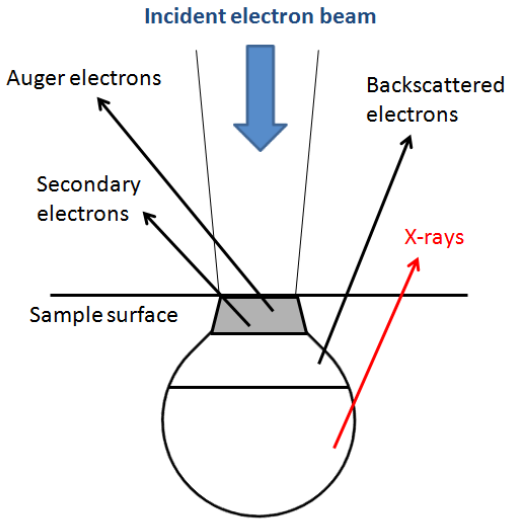

Figure 10 Penetration of the electron beam into the solid and the regions from which secondary, backscattered and Auger electrons, and X-rays, are produced. Image modified from Reimschuessel.[44]

If the accelerated beam of electrons has sufficient energy then it may displace core electrons from the target material, which gives rise to characteristic X-ray emissions for each element, as an electron from a higher energy orbital falls into the orbital vacated by the ejected electron. Generation of characteristic X-rays makes it possible to chemically analyse the contents of each sample quantitatively. The energy of each individual X-ray is counted and an energy distribution histogram is generated.[43] This

method of chemical analysis is known as Energy Dispersive X-ray Spectroscopy (EDX) and most scanning electron microscopes come equipped with EDX capabilities.[43, 45]

2.9. References

1. Williams, D. H.; Fleming, I., *Spectoscopic Methods in Organic Chemistry*. Fifth ed.; McGraw-Hill Higher Education: 1995.
2. Housecraft, C. E.; Sharpe, A. G., *Inorganic Chemistry* Second Edition ed.; Prentice Hall: 2005.
3. Torrent, J.; Barron, V., Diffuse Reflectance Spectroscopy of Iron Oxides. In *Encyclopedia of Surface and Colloid Science*, Cordoba, 2002; pp 1438-1446.
4. Torrent, J.; Barron, V., Diffuse Reflectance Spectroscopy. In *Methods of Soil Analysis. Part 5. Mineralogical Methods.*, Soil Science Society of America: 2008; pp 367-385.
5. Technologies, P., Diffuse Reflectance – *Theory and Applications*. In Application Note, 2011.
6. Marusak, R. A.; Doan, K.; Cummings, S. D., Appendix 2: Introduction to Cyclic Voltammetry1–6. In *Integrated Approach to Coordination Chemistry*, John Wiley & Sons, Inc.: 2006; pp 235-241.
7. Kounaves, S. P., "Voltammetric Techniques" In *Handbook of Instrumental Techniques for Analytical Chemistry*, Prentice Hall PTR: Upper Saddle River, 1997.
8. Kissinger, P. T.; Heineman, W. R., *Journal of Chemical Education* **1983,** *60*, 702.
9. Mabbott, G. A., *Journal of Chemical Education* **1983,** *60*, 697.
10. BASi *INSTRUCTION MANUAL FOR BASi EPSILON FOR ELECTROCHEMISTRY*, 2.10.73; Bioanalytical Systems: 2000-2009.
11. Clegg, W., *Crystal Structure Determination*. Oxford University Press: Oxford, 1998.
12. Weller, M. T., *Inorganic Materials Chemistry*. Oxford University Press: Oxford, 1994.
13. Atkins, P.; de Paulo, J., *Atkins' Physical Chemistry*. Seventh ed.; Oxford University Press: New York, 2002.
14. Hasegawa, K., *The Rigaku Journal* **2012,** *28*, 14-18.
15. Massa, W., *Crystal Structure Determination*. Springer: 2004.
16. Butera, R. A.; Waldeck, D. H., *Journal of Chemical Education* **1997,** *74*, 115.
17. Yoshimoto, N.; Aosawa, K.; Taniswa, T.; Omote, K.; Ackermann, J.; Videlot-Ackermann, C.; Brisset, H.; Fages, F., *Crystal Research and Technology* **2007,** *42*, 1228-1231.
18. Tanner, B. K.; Hase, T. P. A.; Lafford, T. A.; Goorsky, M. S., *Powder Diffraction* **2004,** *19*, 45-48.
19. Kobayashi, S., *The Rigaku Journal* **2010,** *26*, 3-11.
20. Inaba, K., *The Rigaku Journal* **2008,** *24*, 10-15.
21. Mitsunaga, T., *The Rigaku Journal* **2009,** *25*, 7-12.
22. Ayscough, P. B., *Electron Spin Resonance in Chemistry*. Methuen & Co LTD: London, 1967.
23. Basu, P., *Journal of Chemical Education* **2001,** *78*, 666-null.

24. Carlin, R. L., *Magnetochemistry*. Springer-Verlag Berlin and Heidelberg GmbH & Co. K: 1986.
25. Orchard, A. F., *Magnetochemistry*. Oxford University Press: Oxford, 2003.
26. Bain, G. A.; Berry, J. F., *Journal of Chemical Education* **2008,** *85*, 532.
27. Robertson, N.; Yee, G. T., Molecular Magnetic Materials. In *Molecular Materials*, John Wiley & Sons, Ltd: 2010; pp 143-209.
28. Kahn, O., *Molecular Magnetism*. Wiley-Blackwell: 1993.
29. McElfresh, M., Fundamentals of Magnetism and Magnetic Measurements Featuring Quantum Design's Magnetic Property Measurement System. In Quantum Design: Purdue University, 1994.
30. Jensen, F., *Introduction to Computational Chemistry*. Second ed.; Wiley: 2007.
31. Cramer, C. J., *Essentials of Computational Chemistry*. Second ed.; Wiley: 2004.
32. Rappe, A. K.; Casewit, C. J. R., *Molecular Mechanics Across Chemistry*. Univ Science Books: 1997.
33. Hehre, W. J., A Guide to Molecular Mechanics and Quantum Chemical Calculations. In Wavefunction: 2003.
34. Cramer, C. J.; Truhlar, D. G., *Physical Chemistry Chemical Physics* **2009,** *11*, 10757-10816.
35. Hohenberg, P.; Kohn, W., *Physical Review* **1964,** *136*, B864-B871.
36. Kohn, W.; Sham, L. J., *Physical Review* **1965,** *140*, A1133-A1138.
37. Burke, K., *The Journal of Chemical Physics* **2012,** *136*, 150901-9.
38. Thompson, M. A. *ArgusLab 4.0.1*, Planaria Software LLC: Seattle, WA.
39. Frisch, M. J.; Trucks, G. W.; Schlegel, H. B.; Scuseria, G. E.; Robb, M. A.; Cheeseman, J. R.; Montgomery, J. A.; Vreven, T.; Kudin, K. N.; Burant, J. C.; Millam, J. M.; Iyengar, S. S.; Tomasi, J.; Barone, V.; Mennucci, B.; Cossi, M.; Scalmani, G.; Rega, N.; Petersson, G. A.; Nakatsuji, H.; Hada, M.; Ehara, M.; Toyota, K.; Fukuda, R.; Hasegawa, J.; Ishida, M.; Nakajima, T.; Honda, Y.; Kitao, O.; Nakai, H.; Klene, M.; Li, X.; Knox, J. E.; Hratchian, H. P.; Cross, J. B.; Bakken, V.; Adamo, C.; Jaramillo, J.; Gomperts, R.; Stratmann, R. E.; Yazyev, O.; Austin, A. J.; Cammi, R.; Pomelli, C.; Ochterski, J. W.; Ayala, P. Y.; Morokuma, K.; Voth, G. A.; Salvador, P.; Dannenberg, J. J.; Zakrzewski, V. G.; Dapprich, S.; Daniels, A. D.; Strain, M. C.; Farkas, O.; Malick, D. K.; Rabuck, A. D.; Raghavachari, K.; Foresman, J. B.; Ortiz, J. V.; Cui, Q.; Baboul, A. G.; Clifford, S.; Cioslowski, J.; Stefanov, B. B.; Liu, G.; Liashenko, A.; Piskorz, P.; Komaromi, I.; Martin, R. L.; Fox, D. J.; Keith, T.; Laham, A.; Peng, C. Y.; Nanayakkara, A.; Challacombe, M.; Gill, P. M. W.; Johnson, B.; Chen, W.; Wong, M. W.; Gonzalez, C.; Pople, J. A., Gaussian 03, Revision E.01. In *Gaussian, Inc., Wallingford CT*, Wallingford CT, 2004.
40. Frisch, M. J.; Trucks, G. W.; Schlegel, H. B.; Scuseria, G. E.; Robb, M. A.; Cheeseman, J. R.; Scalmani, G.; Barone, V.; Mennucci, B.; Petersson, G. A.; Nakatsuji, H.; Caricato, M.; Li, X.; Hratchian, H. P.; Izmaylov, A. F.; Bloino, J.; Zheng, G.; Sonnenberg, J. L.; Hada, M.; Ehara, M.; Toyota, K.; Fukuda, R.; Hasegawa, J.; Ishida, M.; Nakajima, T.; Honda, Y.; Kitao, O.; Nakai, H.; Vreven, T.; Montgomery, J. A.; Peralta, J. E.; Ogliaro, F.; Bearpark, M.; Heyd, J. J.; Brothers, E.; Kudin, K. N.; Staroverov, V. N.; Kobayashi, R.;

Normand, J.; Raghavachari, K.; Rendell, A.; Burant, J. C.; Iyengar, S. S.; Tomasi, J.; Cossi, M.; Rega, N.; Millam, J. M.; Klene, M.; Knox, J. E.; Cross, J. B.; Bakken, V.; Adamo, C.; Jaramillo, J.; Gomperts, R.; Stratmann, R. E.; Yazyev, O.; Austin, A. J.; Cammi, R.; Pomelli, C.; Ochterski, J. W.; Martin, R. L.; Morokuma, K.; Zakrzewski, V. G.; Voth, G. A.; Salvador, P.; Dannenberg, J. J.; Dapprich, S.; Daniels, A. D.; Farkas; Foresman, J. B.; Ortiz, J. V.; Cioslowski, J.; Fox, D. J., Gaussian 09, Revision B.01. In *Gaussian 09, Revision B.01, Gaussian, Inc., Wallingford CT*, Wallingford CT, 2009.

41. Vernon-Parry, K. D., *III-Vs Review* **2000,** *13*, 40-44.
42. Bogner, A.; Jouneau, P. H.; Thollet, G.; Basset, D.; Gauthier, C., *Micron* **2007,** *38*, 390-401.
43. Argast, A.; Tennis, C. F., *Journal of Geoscience Education* **2004,** *52*, 213.
44. Reimschuessel, A. C., *Journal of Chemical Education* **1972,** *49*, A413.
45. Beane, R. J., *Journal of Geoscience Education* **2004,** *52*, 250-253.

Chapter 3: Phenolic Oxime Complexes

3.1. Introduction

Metal complexes with planar, electronically-delocalised structures have proven particularly attractive for development of cooperative electronic properties due to the strong molecule-molecule interactions that can arise from π-stacking of the planar units.[1-3] The majority of research in this field however, has focused on well-established families of planar metal complexes such as metal-bis-1,2-dithiolenes,[4-6] metal phthalocyanines[7] and structurally related analogues such as bis(*o*-diiminobenzosemiquinonate) nickel(II),[8, 9] with much less attention given to the exploration of alternative transition metal complexes.

In this context it is important to investigate new classes of planar, electronically-delocalised metal complexes or to re-evaluate appropriate existing materials previously used for a different purpose. This requires an extensive study of different classes of planar metal complexes to assess their electronic structure; their processibility into thin films by evaporation or solution methods; their molecular packing in the solid state; the resulting intermolecular interactions, their magnetic properties and the possibility of charge-transport properties. Phenolic oxime ligands are used extensively in extractive hydrometallurgy[10-12] but the cooperative electronic properties in materials formed by transition metal complexes of these ligands has to date been overlooked. We have prepared homoleptic nickel(II) and copper(II) complexes using three structurally related phenolic oxime ligands, 2-hydroxy-5-*t*-

octylacetophenone oxime ($^{t\text{-}Oct}$saoH), 2-hydroxy-5-*n*-propylacetophenone oxime ($^{n\text{-}Pr}$saoH) and 2-hydroxyacetophenone oxime (^{H}saoH). The size of the substituent at the 5-position on the aromatic ring has been varied, which affects both the solubility of the resulting complexes formed and thus the processing methods available, and also intermolecular interactions in the solid state, which determine the packing adopted by the molecules and the corresponding cooperative electronic and magnetic properties that arise.

The salicylketoxime (sao) ligands discussed in this work are planar, bidentate and bind through two heteroatoms making them interesting candidates for investigation to assess their potential in magnetic or conducting materials.

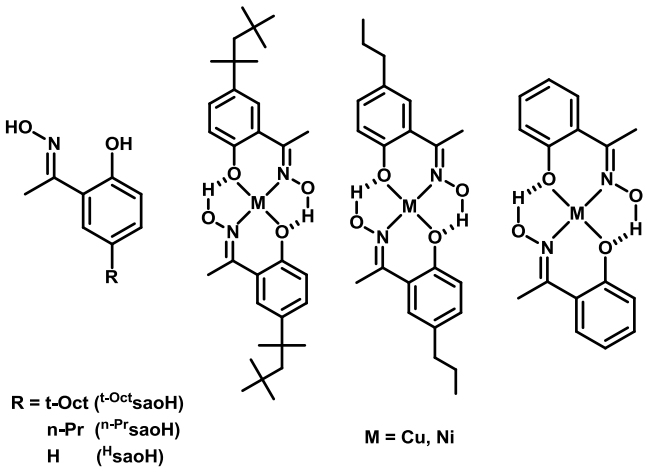

Figure 1 Molecular structure of the three ligands and the six complexes discussed in this chapter.

3.2. Experimental

3.2.1 Synthesis of ligands

All chemicals were purchased from Sigma Aldrich and used as bought without further purification. The ligand, 2-hydroxy-5-t-octylacetophenone oxime, was synthesised by Benjamin Roach of the Tasker group.

2-Hydroxy-5-t-octylacetophenone oxime ($^{t\text{-}Oct}$saoH)

Acetyl chloride (86.3g, 1.1 mol) was added drop wise to a solution of 4-*tert*-octylphenol (206.3g, 1 mol) in toluene (600 ml) and the resulting solution refluxed for 4 hours and then stirred overnight. Aluminium trichloride (133.3g, 1.0 mol) was added in portions to the stirred solution over 4 hours and the reaction mixture was then heated to reflux for 3 hours and stirred overnight at RT. The reaction was quenched with excess HCl (20%, 500 ml) which was added drop wise over 1h. The organic phase was separated from the aqueous, washed with distilled water (2 x 250 ml) and filtered using phase separation paper. The solvent was removed *in vacuo* yielding a viscous yellow oil (230.2g) 67% pure by GC. Hydroxylamine sulphate (221.5 g, 1.35 mol) and sodium acetate (221.4 g, 2.7 mol) were added to a solution of crude phenolic ketone (230.2g, 0.9 mol) in ethanol (600 ml). The resulting suspension was refluxed for 2h, allowed to cool and poured onto toluene (500 ml) and distilled water (300 ml). The organic layer was separated, washed with distilled water (2 x 100 ml) and brine (100 ml) and filtered through phase separation paper. The solvent was removed in vacuo and the resulting yellow solid was purified via complexation with copper, using the same general procedure as detailed below. The complex solution was stripped using sulphuric acid solution (0.1 M, 3 x 200 ml), washed with distilled water (200 ml) and filtered through phase separation paper. The solvent was removed in vacuo and the resulting off-yellow solid was

recrystallised from hexane yielding an off-white solid (135.2g, 0.51 mol, 51% yield). ^{1}H NMR ($CDCl_3$): δ (ppm) = 0.78 (s, 9H), 1.43 (s, 6H), 1.78 (s, 2H), 2.44 (s, 3H), 7.32 (d, 1H, 8.4 Hz), 7.43 (s, 1H), 7.46 (d, 1H, 6.4 Hz). MS (ESI): m/z (%) = 264.20 (100%) $[M+H]^+$. Melting point: 100-101 °C.

2-Hydroxy-5-n-propylacetophenone oxime ($^{n\text{-}Pr}$saoH)

Acetyl chloride (11.77g, 0.15 mol) was added dropwise to a stirred solution of 4-*n*-propylphenol (13.62g, 0.1 mol) in toluene (250 ml) and the resulting mixture was refluxed for 4 hours and stirred overnight at RT. Aluminium trichloride (16.00g, 0.12 mol) was added in 1g portions to the stirred solution over 4 hours at 10 minute intervals, and the reaction was then refluxed for 3 hours before being quenched with aqueous hydrochloric acid (18%, 100 ml) added dropwise over an hour. The organic layer was separated from the aqueous, washed with distilled water (2 x 50 ml) and then dried using excess magnesium sulfate. Evaporation of the solvent under reduced pressure gave an orange oil which was dissolved in ethanol (200 ml). A filtered solution of hydroxylamine hydrochloride (10.42 g, 0.15 mol) and potassium hydroxide (8.42 g, 0.15 mol) was added and the resulting reaction mixture heated at reflux for 3 hours, allowed to cool, and then poured into a toluene/water (100 ml: 100 ml) solution. The organic layer was washed (50 ml water, 50 ml brine) and dried *in vacuo* to yield an orange oil. The salicylketoxime ligand was then recrystallised as an off-white solid (12.52 g, 65 %) by cooling a concentrated *n*-heptane (50 ml) solution. ^{1}H NMR ($CDCl_3$): δ = 0.96 (t, 3H, 7.5 Hz), 1.64 (m, 2H, 7.5 Hz), 2.58 (t, 2H, 7.5 Hz), 2.61 (s, 3H), 7.26 (d, 1H, 6 Hz), 7.32 (s, 1H), 7.42 (d, 1H, 8.5 Hz). MS (ESI): m/z (%) = 194.31 (100%) $[M+H]^+$. Melting point: 115-117 °C.

2-Hydroxyacetophenone oxime (^{H}saoH)

2'-hydroxyacetophenone (4.08g, 0.03 mol) was refluxed in ethanol (50 ml) with hydroxylamine hydrochloride (3.13g, 0.045 mol) and potassium hydroxide (2.52g, 0.045 mol) for 2 hours. The reaction mixture was poured into a toluene/water (20 ml: 20 ml) solution. The organic layer was extracted then washed with water (2x20 ml)

and then dried in vacuo to produce a white powder (4.36 g, 97 %). ^{1}H NMR ($CDCl_3$): δ = 2.21 (s, 3H), 6.93 (m, 1H, 8 Hz), 6.99 (dd, 1H, 7 and 1.5 Hz), 7.30 (d, 1H, 6.5 Hz), 7.46 (dd, 1H, 6.5 and 1.5 Hz). MS (ESI): m/z (%) = 151.1 (100) $[M+H]^+$. Melting point: 120-121 °C.

3.2.2 Metal complexation

The same general procedure was adopted for the synthesis of all of the metal complexes. The ligand (0.02 mol) was added to a stirred solution of $Cu(OAc)_2.H_2O$ or $Ni(OAc)_2.4H_2O$ (0.01 mol) in ethanol (50 ml). The resulting solution was stirred for 24 hours at room temperature and the precipitate was collected by filtration, washed with ethanol (10 ml), then cold *n*-hexane (10 ml). The complexes were recrystallised from a concentrated DCM solution by slow evaporation over 24 hours before being dried in a vacuum desiccator overnight.

Cu($^{t\text{-Oct}}$sao)$_2$

Yield: 6.26 g, 94 %. MS (ESI): m/z (%) = 588.15 (76.41%) $[M^+]$. Calculated for $C_{32}H_{48}CuN_2O_4$, C 65.33, H 8.22, N 4.76; found C 65.34, H 8.24, N 4.76. Melting point: 183-185 °C.

Ni($^{t\text{-Oct}}$sao)$_2$

Yield: 4.90 g, 84 %. ^{1}H NMR ($CDCl_3$): 0.64 (s, 9H), 1.25 (s, 6H), 1.49 (s, 2H), 2.42 (s, 3H), 6.62 (d, 1H, 8.5 Hz), 7.12 (dd, 1H, 2.25 and 8.75 Hz), 7.24 (s, 1H), 10.90 (s, 1H). MS (ESI): m/z (%) = 583.11 (89.08%) $[M^+]$. Calculated for $C_{32}H_{48}NiN_2O_4$, C 65.88, H 8.29, N 4.80; found C 65.78, H 8.95, N 4.95. Melting point: 173-174 °C.

Cu($^{n\text{-Pr}}$sao)$_2$

Yield: 4.03 g, 97 %. MS (ESI): m/z (%) = 447.4 (100%) $[M^+]$. Calculated for $C_{32}H_{28}CuN_2O_4$, C 58.98, H 6.30, N 6.25; found C 59.04, H 6.16, N 6.13. Melting point: 205-207 °C.

Ni($^{n\text{-}Pr}$sao)$_2$

Yield: 3.97 g, 90 %. ^{1}H NMR ($CDCl_3$): 0.96 (t, 3H), 1.64 (m, 2H), 2.40 (s, 3H), 2.57 (t, 2H), 6.94 (d, 1H, 8.7 Hz), 7.12 (d, 1H, 7.5 Hz), 7.24 (s, 1H). MS (EI): m/z (%) = 442.1 (100%) [M^+]. Calculated for $C_{32}H_{28}NiN_2O_4$, C 59.62, H 6.37, N 6.32; found C 59.72, H 6.30, N 6.21. Melting point: 198-200 °C.

Cu(^{H}sao)$_2$

Yield: 2.53 g, 70 %. MS (EI): m/z (%) = 362.1 (51.93) [M^+]. Calculated for $C_{16}H_{16}CuN_2O_4$, C 52.82, H 4.43, N 7.70; found C 53.01, H 4.50, N 7.74. Melting point: 241-242 °C.

Ni(^{H}sao)$_2$

Yield: 1.83 g, 51 %. ^{1}H NMR ($CDCl_3$): 2.50 (s, 3H), 6.74 (t, 1H, 8 Hz), 6.78 (d, 1H, 8.3 Hz), 7.14 (t, 1H, 7.5 Hz), 7.42 (d, 1H, 8 Hz), 10.96 (s, 1H). MS (EI): m/z (%) = 358.92 (65.62) [M^+]. Calculated for $C_{16}H_{16}NiN_2O_4$, C 53.53, H 4.49, N 7.80; found C 53.64, H 4.58, N 7.90. Melting point: 236-237 °C.

3.2.3 Experimental methods

Crystallographic data were routinely collected at 100 K. Single crystals suitable for X-ray diffraction were prepared by various methods: Cu($^{t\text{-}Oct}$sao)$_2$ by slow evaporation of a MeOH/DCM/THF solution; Cu($^{t\text{-}Oct}$sao)$_2$.DMSO by recrystallisation from a concentrated DMSO solution; Cu($^{n\text{-}Pr}$sao)$_2$ by vapour diffusion of EtOH into a $CHCl_3$ solution; Ni($^{t\text{-}Oct}$sao)$_2$ by slow evaporation of a $(CH_3O)_2CO$ solution and Ni($^{n\text{-}Pr}$sao)$_2$ by vapour diffusion of MeCN into a $CHCl_3$ solution. A table of crystallographic data is included in Section 3.3. Thin film XRD was carried out on a Rigaku ultraX-18HB at room temperature. Data were collected from 2θ angle of 5-40° at a rate of 2° per minute. Powder XRD was carried out using a Bruker AXS D8 diffractometer. Thin films were grown in a vacuum chamber on various substrates: Si (1,0,0), quartz, indium tin oxide (ITO), glass, FET (bottom contact configuration) substrates and polyethylene terephthalate (PET). Different substrates were required

for the different types of characterisation: Si was used for thin film XRD and infrared spectroscopy (IR); quartz for UV/Vis and SEM; glass for UV/vis and PET for electron paramagnetic resonance (EPR). All the substrates, except PET and the FETs, were cleaned in individual solutions of IPA, acetone and then chloroform prior to use. Deposition was carried out via vacuum sublimation in a temperature range between 135°C and 210°C at a pressure of 2.8×10^{-4} Pa. This resulted in a growth rate of 0.1-0.3 Å/s which was monitored using a quartz crystal microbalance (QCM). The material to be sublimed was heated inside an inert crucible by applying a current. Films of approximately 100 nm thickness were grown as estimated from the QCM. All cyclic voltammetry measurements were carried out in dry DCM using 0.3 M $TBABF_4$ electrolyte in a three electrode system, with each solution being purged with N_2 prior to measurement. The working electrode was a 0.2 mm^2 Pt wire sealed in glass. The reference electrode was Ag/AgCl calibrated against ferrocene/ferrocenium in the background electrolyte, and the counter electrode was a Pt rod. All measurements were made at room temperature using a μAUTOLAB Type III potentiostat, driven by the electrochemical software GPES. CV measurements used scan rates of 0.1 V/s and DPV was carried out at a step potential of 0.01 V, modulation amplitude of 0.10005 V, modulation time of 0.05 s and an interval time of 0.5 s. Solution UV/Vis spectra were recorded in solution in DCM using a quartz cell of path length 1 cm on a Perkin-Elmer Lambda 9 spectrophotometer, controlled by a datalink PC, running UV/Winlab software and in thin films on a Jasco V-570 UV/Vis/NIR spectrophotometer. Magnetic susceptibility measurements were performed on powder samples from 1.8 to 300 K using a Quantum Design MPMS-XL SQUID magnetometer with MPMS MultiVu Application software to process the data. The magnetic field used was 0.1 T. Diamagnetic corrections were applied to the observed paramagnetic susceptibilities by using Pascal's constants. EPR spectra were measured on a Bruker ER200D X-band spectrometer with simulations using the Bruker EPR simulation package SimFonia.[13] EPR spectra of dry DCM solutions were recorded at room temperature. Thin film EPR spectra were obtained on a JEOL JES-FA200 ESR Spectrometer using 100nm films on a PET substrate with a centre field of 312 mT and a sweep width +/- 100 mT. Geometry optimisations of the isolated complexes, $Cu(^{n\text{-}Pr}sao)_2$

and Ni($^{n\text{-}Pr}$sao)$_2$, were carried out at the B3LYP/6-31G(d,p) level of theory,[14-16] using Gaussian 03.[17] The X-ray crystallographic coordinates were used as the starting structures, and minima on the potential energy surface were confirmed by the absence of any imaginary frequencies. The molecular orbital isosurfaces were visualised using ArgusLab 4.0.[18] FET measurements were carried out using bottom contact devices consisting of interdigitated platinum source and drain electrodes with a silicon dioxide dielectric layer. The source and drain electrodes were 8 μm thick with a gap between the interdigitated electrodes of 2 μm. The dielectric layer was 300 nm thick and the gate electrode was made from an n-doped silicon wafer. FET testing was done in darkness and under vacuum. Imaging of thin films was carried out using a Hitachi S-4300 Scanning Electron Microscope.

Due to the computational complexity involved, considerable work regarding the electronic structure calculation of Cu(^{nPr}sao)$_2$ in Section 3.6.2 of this chapter was carried out by Dr Patricia Richardson.

3.3. Results and discussion

Synthesis of both Ni and Cu complexes of two different phenolic oxime ligands was readily achieved by direct reaction of the metal acetate salt with the protonated ligand in ethanol, enabling comparison of the role of the central metal in the electronic properties, and the role of the alkyl chain in the packing properties of the molecules. The complexes achieve good stability through the pseudomacrocylic arrangement arising from hydrogen bonding between the oxymic hydrogen and the phenolic oxygen of the opposing ligands. A systematic study of the electronic, magnetic, structural and thin-film properties of these materials has been carried out to provide a thorough assessment of their potential for use in conducting devices.

3.3.1. Crystallography

In the course of this work, five previously unreported structures of Cu($^{t\text{-Oct}}$sao)$_2$, Cu($^{t\text{-Oct}}$sao)$_2$.DMSO, Ni($^{t\text{-Oct}}$sao)$_2$, Cu($^{n\text{-Pr}}$sao)$_2$ and Ni($^{n\text{-Pr}}$sao)$_2$ were elucidated using single crystal X-ray diffraction (crystallographic data shown in Table 1). Crystals of Cu(^{H}sao)$_2$ and Ni(^{H}sao)$_2$ that were grown both by sublimation and solution methods, match previously reported structures.[19, 20] Additionally, crystals of Cu($^{n\text{-Pr}}$sao)$_2$ and Ni($^{n\text{-Pr}}$sao)$_2$ were also grown by sublimation but their unit cell dimensions were found to be the same as that of the solution grown structures. In the crystal structures of the four unsolvated complexes - Cu($^{t\text{-Oct}}$sao)$_2$, Ni($^{t\text{-Oct}}$sao)$_2$, Cu($^{n\text{-Pr}}$sao)$_2$ and Ni($^{n\text{-Pr}}$sao)$_2$ - the metal atom lies on an a crystallographic inversion centre which results in perfectly planar $N_2O_2^{2-}$ donor sets. Bond lengths, bond angles, the chelate bite distances in the coordination sphere, and the O$\cdots$O contact distances in the outer sphere, which are associated with oxime OH to phenolate oxygen hydrogen bond, are shown below (Table 2). As noted previously for complexes of this type,[10] the bond lengths to the Ni(II) atom are significantly shorter than those to the Cu(II) atom. As

might be expected,[21] the $N_2O_2^{2-}$ donor set forms longer bonds to the Cu(II) atom in the DMSO adduct, $[Cu(L^1)_2DMSO]$, which has a five coordinate square pyramidal structure. The bite angle is larger in the Ni(II) complexes, which is a consequence of the shorter Ni-O and Ni-N bonds requiring the metal atom to move towards the centre of the N···O bite.

Table 1 Crystallographic data for $Cu(^{t\text{-}Oct}sao)_2$, $Cu(^{t\text{-}Oct}sao)_2$.DMSO, $Ni(^{t\text{-}Oct}sao)_2$, $Cu(^{n\text{-}Pr}sao)_2$ and $Ni(^{n\text{-}Pr}sao)_2$.

Complex	**$Cu(^{t\text{-}Oct}sao)_2$**	**$Cu(^{t\text{-}Oct}sao)_2$. DMSO**	**$Cu(^{n\text{-}Pr}sao)_2$**	**$Ni(^{t\text{-}Oct}sao)_2$**	**$Ni(^{n\text{-}Pr}sao)_2$**
Morphology	Brown block (0.37 x 0.31 x 0.12)	Green block (0.39 x 0.24 x 0.24)	Brown rod (0.62 x 0.09 x 0.03)	Green rectangle (0.26 x 0.21x 0.18)	Green needle (0.74 x 0.12 x 0.12)
Empirical formula	$C_{32}H_{48}CuN_2O_4$	$C_{34}H_{54}CuN_2O_5S$	$C_{22}H_{28}CuN_2O_4$	$C_{32}H_{48}NiN_2O_4$	$C_{22}H_{28}N_2NiO_4$
T (K)	100	150	100	100	100
Space group	P 21/c	P-1	P 21/c	C 2/c	P 21/c
M_r	588.26	666.43	448.00	583.45	443.19
a	6.1722(2)	8.0420(4)	10.8857(3)	21.7524(5)	10.8277(5)
b	13.2067(4)	12.8510(8)	4.73780(10)	9.95251(18)	4.6891(2)
c	18.4654(4)	17.6720(10)	19.6051(5)	14.7187(3)	19.8063(10)
α	90.00	99.417(4)	90.00	90.00	90.00
β	99.1820(10)	97.842(3)	92.726(2)	107.396(2)	92.130(2)
γ	90.00	104.953(3)	90.00	90.00	90.00
V	1485.91(7)	1709.88(17)	1009.97(4)	3040.72(12)	1004.91(8)
D_c	1.315	1.29	1.473	1.274	1.465
M	0.774	0.741	1.113	0.676	0.997
No. of reflections measured	14285	28516	10838	20261	7435
θ_{max}	27.11	26.473	26.27	28.668	27.090
Z	2	2	2	4	2
R_{int}	0.0217	0.076	0.1526	0.028	0.028
T_{min}/T_{max}	0.8078/0.9095	0.8370/0.8370	0.8022/0.9690	0.64/0.89	0.71/0.89
R_1 (I > 2σ(I))	0.0299	0.0539	0.0385	0.0374	0.0254
wR (F^2) (I > 2σ(I))	0.0819	0.1325	0.1017	0.1034	0.0707

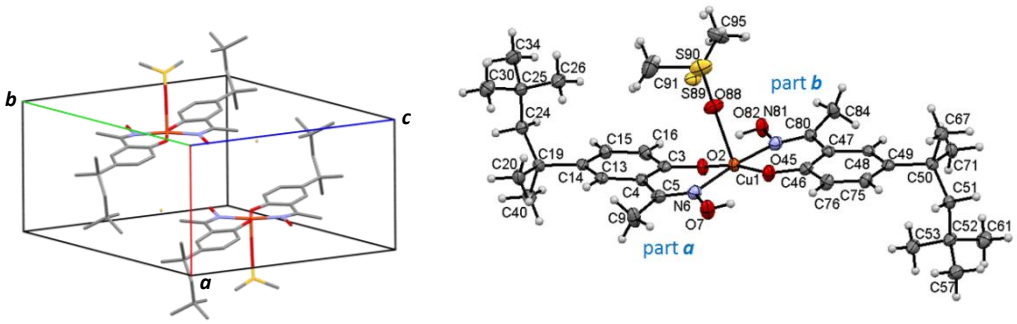

Figure 2 Left, the unit cell of Cu($^{t\text{-Oct}}$sao)$_2$.DMSO. Hydrogen atoms have been omitted for clarity and only the higher occupancy site of the disordered $(CH_3)_2S$ unit of the DMSO is shown. Right, the crystal structure of Cu($^{t\text{-Oct}}$sao)$_2$.DMSO with numbering scheme.

Table 2 Selected bond length and angles.

	[Cu($^{t\text{-Oct}}$sao)$_2$.DMSO][i] part *a*	part *b*	Cu($^{t\text{-Oct}}$sao)$_2$	Ni($^{t\text{-Oct}}$sao)$_2$	Cu($^{n\text{-Pr}}$sao)$_2$	Ni($^{n\text{-Pr}}$sao)$_2$
M-O (Å)	1.919(2)	1.901(3)	1.870(1)	1.819(1)	1.883(1)	1.827(1)
M-N (Å)	1.957(4)	1.964(4)	1.962(1)	1.883(2)	1.948(2)	1.883(1)
O-M-N (^{o})	89.7(1)	90.5(1)	91.05(5)	92.12(6)	91.84(7)	92.40(5)
O-M-N' (^{o})	89.5(1)	88.9(1)	89.95(5)	87.88(6)	88.16(7)	87.60(5)
N···O bite distance (Å)	2.745(5)	2.733(5)	2.735(2)	2.666(2)	2.753(2)	2.678(2)
MO···OH (Å)	2.598(4)	2.591(4)	2.583(2)	2.482(2)	2.551(2)	2.471(1)

[i] This complex has no crystallographically imposed symmetry and the two lengths and angles associated with the chelate units ***a*** and ***b*** are shown in Figure 2. The DMSO oxygen atom forms a bond to Cu of 2.229(3) Å and defines angles of 93.8(1), 98.3(1), 95.2(1) and 91.9(1)^o with atoms O_2, O_{45}, N_6, and N_{81}.

The crystal packing of Cu($^{t\text{-Oct}}$sao)$_2$ and Ni($^{t\text{-Oct}}$sao)$_2$ are compared in Figure 3. Due to the bulky *t*-octyl chains, π-overlap of the planar portions of the molecules is not favoured and the interplanar distance between overlapping aromatic rings is 6.97 Å in Cu($^{t\text{-Oct}}$sao)$_2$.DMSO, 7.58 Å in Cu($^{t\text{-Oct}}$sao)$_2$, and 7.12 Å in Ni($^{t\text{-Oct}}$sao)$_2$.

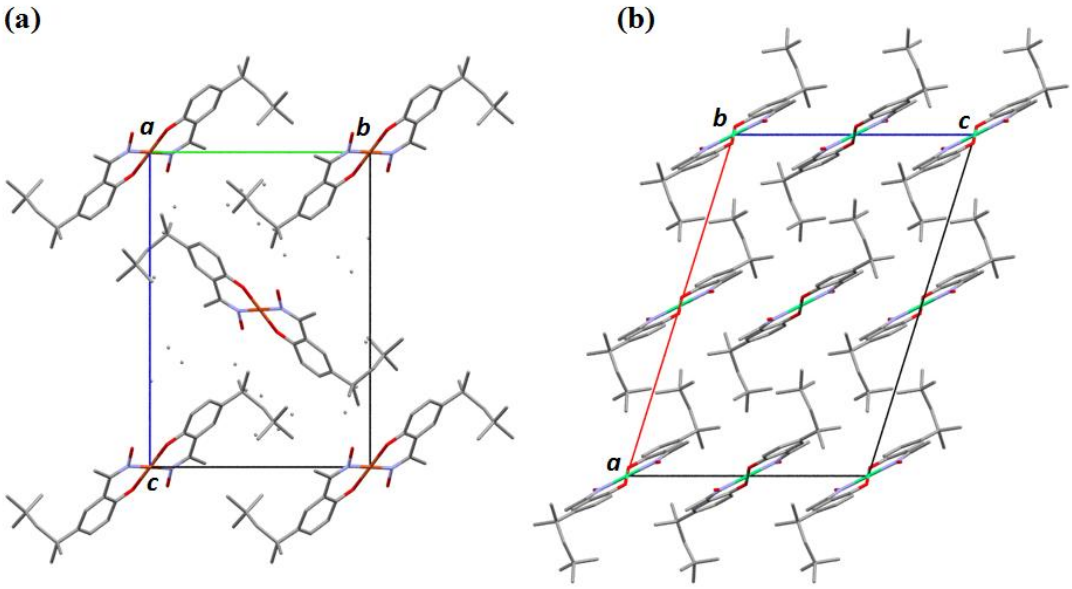

Figure 3 The unit cells of (a) Cu($^{t\text{-Oct}}$sao)$_2$ viewed along the a-axis and (b) Ni($^{t\text{-Oct}}$sao)$_2$ viewed along the b-axis. Hydrogen atoms have been omitted for clarity and only the higher occupancy site of one of the octyl groups, which is disordered in Cu($^{t\text{-Oct}}$sao)$_2$, is shown.

Ni($^{n\text{-Pr}}$sao)$_2$ and Cu($^{n\text{-Pr}}$sao)$_2$ are isomorphous and, in contrast to M($^{t\text{-Oct}}$sao)$_2$, display a herringbone packing motif with the π-stacking of the molecules extending along the *b*-axis in a regular stack (Figure 4). The interplanar packing distance is slightly longer, 3.22 Å, in Ni($^{n\text{-Pr}}$sao)$_2$ than in Cu($^{n\text{-Pr}}$sao)$_2$, 3.17 Å.

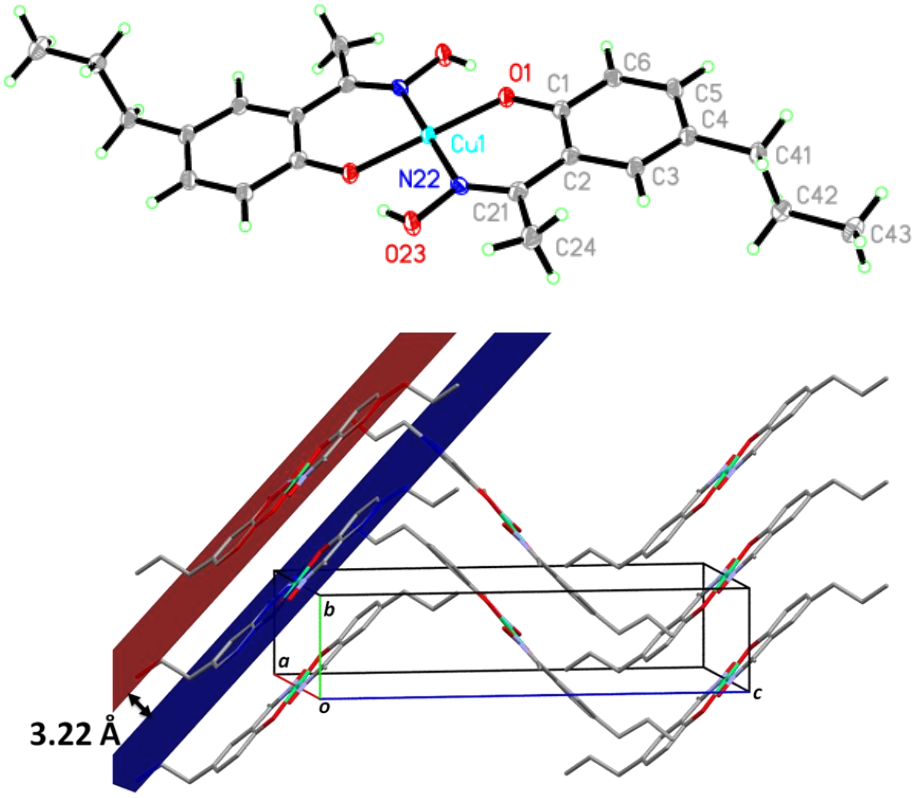

Figure 4 Top, crystal structure of Cu($^{n\text{-Pr}}$sao)$_2$ displaying the general numbering scheme that has been employed for each of the unsolvated crystal structures. Bottom**,** the crystal packing of Ni($^{n\text{-Pr}}$sao)$_2$. The mean planes (red and blue) have been calculated using both aromatic rings on each molecule using the program Mercury 2.3.[22-25] Hydrogen atoms have been omitted for clarity.

The steric effects of the ^{t}octyl, ^{n}propyl and H substituents clearly have an impact on the solid state packing of the complexes. The complexes synthesised from $^{n\text{-Pr}}$saoH form a one-dimensional stack with short intermolecular distances suggesting strong π-π interactions, whereas those formed from $^{t\text{-Oct}}$saoH have larger interplanar distances, too great for effective π-overlap. This presents an opportunity to investigate the effect of inter-molecular π-stacking interactions on magnetic and conduction properties, as the M(^{R}sao)$_2$ complexes share a common core electronic structure. It provides a comparison between materials comprised of essentially, electronically identical molecules that interact in the solid state with those that are effectively isolated.

3.3.2. Electrochemistry

The more soluble $^{t\text{-}Oct}$saoH and $^{n\text{-}Pr}$saoH ligands were studied in the range of -2 to 2 volts at various scan rates and both display similar behaviour. The cyclic voltammetry (CV) measurements indicate that $^{t\text{-}Oct}$saoH and $^{n\text{-}Pr}$saoH are oxidised irreversibly at 1.41 and 1.42 V. $^{n\text{-}Pr}$saoH displays another irreversible oxidation at 1.78 V which is not as well defined in the CV of $^{t\text{-}Oct}$saoH. Due to the similarities in electronic structure, it is assumed that the electrochemistry of the poorly soluble ^{H}saoH ligand and M(^{H}sao)$_2$ complexes is similar to that of the more soluble analogues.

The voltammograms of the complexes are very similar to those of the uncomplexed ligands, which implies that the redox processes involved are predominantly ligand based. Each complex exhibits an irreversible oxidation occurring at approximately the same potential, indicating that the HOMO of each complex is substantially localised on the ligand. Replacement of the phenolic protons by Ni^{2+} has little effect on the redox processes compared with the free ligands and no other redox processes have been generated through the redox activity of the metal. None of the samples displayed a reduction process between 0 and -2 V.

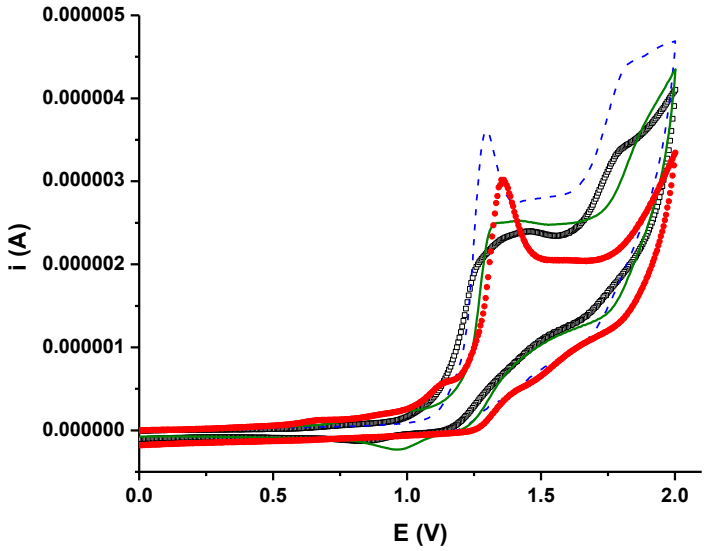

Figure 5 Cyclic voltammetry of complexes Cu($^{t\text{-Oct}}$sao)$_2$ [□], Ni($^{t\text{-Oct}}$sao)$_2$ [---], Cu($^{n\text{-Pr}}$sao)$_2$ [—] and Ni($^{n\text{-Pr}}$sao)$_2$ [●], at a scan rate of 0.1 V/s between 0 and 2 volts in DCM.

Table 3 Electrochemical data measured by CV and DPV. The second oxidation process was not well defined in complexes Cu($^{n\text{-Pr}}$sao)$_2$ and Ni($^{n\text{-Pr}}$sao)$_2$ by CV.

Sample	**Cyclic voltammetry**		**Differential pulse voltammetry**	
	E_{pc} (V)		**E_{pc} (V)**	
^{tOct}saoH	1.40	1.80	1.32	1.75
^{nPr}saoH	1.42	1.78	1.34	1.71
Cu(^{tOct}sao)$_2$	1.43	1.80	1.22	1.72
Ni(^{tOct}sao)$_2$	1.29	1.82	1.24	1.74
Cu(^{nPr}sao)$_2$	1.40	-	1.27	1.82
Ni(^{nPr}sao)$_2$	1.35	-	1.20	1.73

3.3.3. Absorption spectroscopy

The UV-Vis spectra of the ^{R}saoH ligands in the range 250 - 800 nm (Figure 6) are very similar. The spectra are dominated by a strong absorption band occurring at 315 nm in the case of $^{n\text{-}Pr}$saoH and $^{t\text{-}Oct}$saoH, and at 306 nm in ^{H}saoH, which is assigned as a π-π^* transition. The bis-ligand Ni(II) and Cu(II) complexes formed from $^{n\text{-}Pr}$saoH and $^{t\text{-}Oct}$saoH have also been studied by UV-Vis absorption spectroscopy (Figure 7). The absorption spectra for the Ni and Cu complexes are similar in overall structure; however, there is a marked red shift in the Ni spectra relative to that of Cu. The spectra for both Ni complexes are almost identical, and are dominated by a strong absorption band at 305 nm, with a weaker band observed at 383 nm whereas the Cu spectra for both complexes show a prominent UV band around 260 nm, with a weaker band appearing around 346 nm. At high concentrations all of the complexes display Laporte forbidden d-d transitions in the region 606-654 nm. The more intense bands centred between 346 and 383 nm (Figure 7) are assumed to be predominantly intraligand in character but their energies are dependent on the nature of the complexed metal. A similar trend is also observed when comparing the solution absorption spectra of ^{H}saoH with the Cu and Ni complexes, M(^{H}sao)$_2$, formed using this ligand (Figure 8). The bis-ligand copper complex, Cu(^{H}sao)$_2$, has a peak absorbance at 336 nm, whereas the analogous Ni complex has a peak absorbance at 374 nm. The difference in energy of the UV absorptions when comparing the Cu and Ni complexes indicates a metal orbital contribution to the transition, whilst the differing groups at the 5 position on the ligand exert only a minimal influence. These transitions are in the same general range as that witnessed in the free ligand, indicating metal and ligand orbital mixing is limited, although noticeably greater for Ni than for Cu.

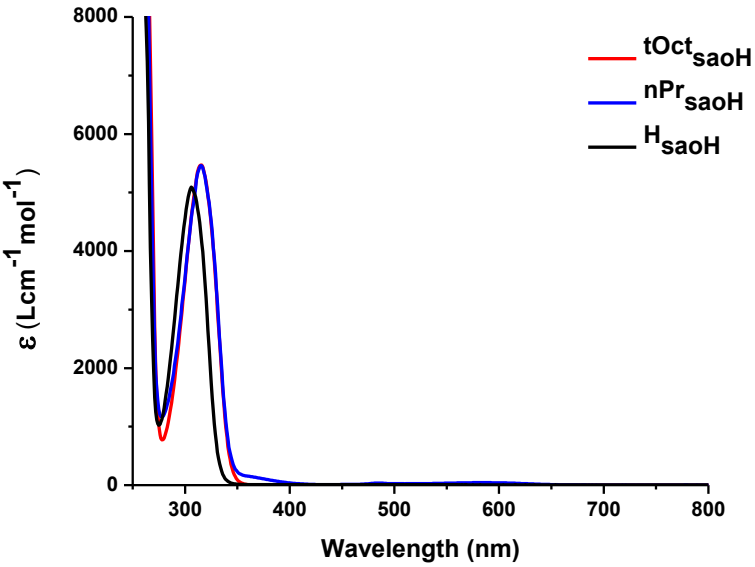

Figure 6 Solution UV/vis spectra of the free ligands in DCM between 250-800 nm.

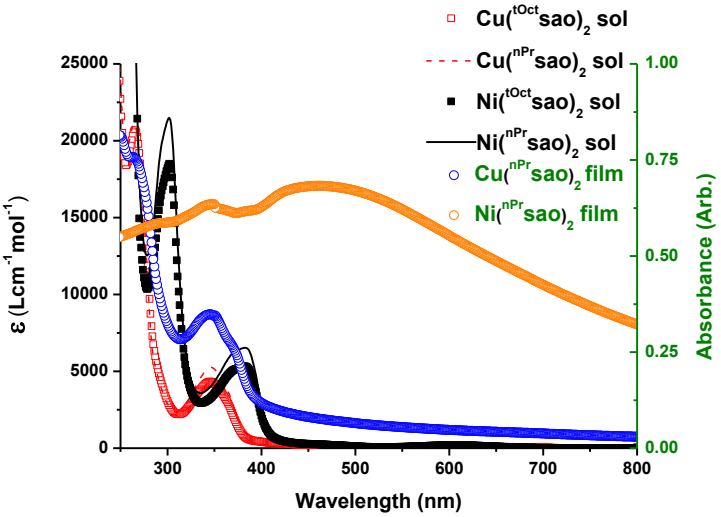

Figure 7 UV/vis spectra of DCM solutions of the complexes overlaid with thin film absorption spectra of $M(^{nPr}sao)_2$ complexes on SiO_2 substrates (arbitrary absorbance units).

The electronic absorption spectra of 100 nm thin films of the $M(^{nPr}sao)_2$ and $M(^{H}sao)_2$ complexes on quartz are shown in Figure 7 and Figure 8, respectively. The thin film spectrum of the Cu(II) complexes closely resembles their solution spectra but for the Ni(II) complexes there is a noticeable degree of red shifting, particularly

in the case of Ni(^{nPr}sao)$_2$. The lack of red shifting in the Cu(II) complexes could infer that the intermolecular interactions in the solid state are weaker, attributed to the different metal ions affecting intermolecular interactions. For example, with the Ni(II) complexes, the larger involvement of the metal in the frontier orbitals of the individual molecules may facilitate stronger orbital interaction between molecules.

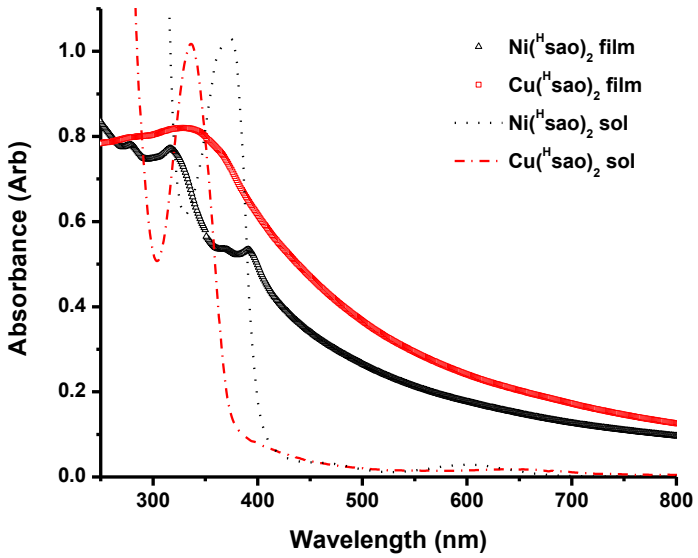

Figure 8 Solution UV/vis spectra of M(^{H}sao)$_2$ complexes in DCM overlaid with the thin film UV/vis spectra on SiO_2 substrates (arbitrary absorbance units).

3.3.4. Computational

3.3.4.1 Nickel(II) complexes

In order to estimate the energies of the HOMO and LUMO in our complexes, single molecule gas phase calculations were carried out at the B3LYP/6-31G(d,p) level of theory for complexes Cu(^{nPr}sao)$_2$ and Ni(^{nPr}sao)$_2$. The extended alkyl chain on the ^{tOct}saoH complexes or the lack of a solubilising alkyl group on the ^{H}saoH complexes is not expected to alter the electronic properties significantly from that of the ^{nPr}saoH based complexes. The results (inset Figure 9) indicate that the HOMO of Ni(^{nPr}sao)$_2$ is of mixed metal/ligand character and is delocalised over both the aromatic part of the molecule and the Ni(II) centre. They also show that the LUMO is localised solely on the ligand. The energy of the HOMO has been calculated as -5.18 eV and the LUMO is -1.33 eV. The energies of the frontier orbitals and the large HOMO-LUMO gap of 3.85 eV is consistent with the observation of accessible oxidation but no accessible reduction in the electrochemistry.

The electronic transitions witnessed in solution have been assigned using time-dependent DFT, with the simulated spectrum in good agreement with that obtained experimentally (Figure 9). The transition at 383 nm has been assigned as being from the HOMO to LUMO (92%) whereas the transition at 305 nm is from HOMO-2 to LUMO (62%) and HOMO-3 to LUMO (24%). The HOMO is composed of Ni(d_{yz}) and Lπ character with the LUMO assigned as a Lπ* orbital. The HOMO-2 is of mixed metal (d_{xz}) and ligand character, but the HOMO-3 is solely based on the d_z^2 orbital.

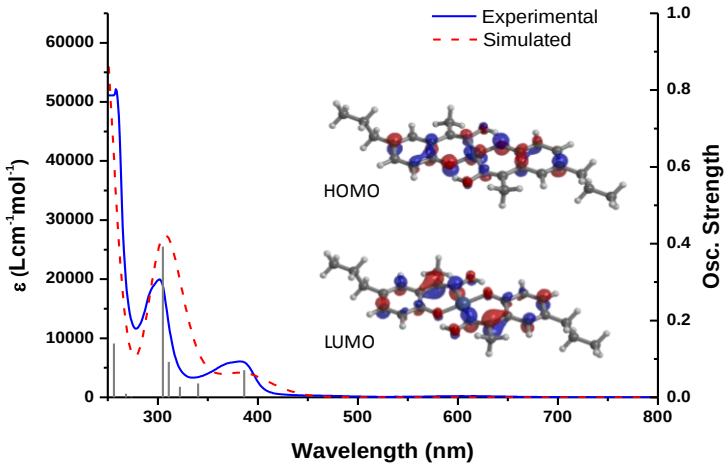

Figure 9 Time dependent DFT generated UV-Vis spectrum (red dashed) overlaid with the experimental spectrum (blue solid) of Ni(^{nPr}sao)$_2$.

3.3.4.2 Cu(II) complexes

The calculation of the electronic structure of Cu(II) containing complexes continues to be a challenge for electronic structure methods. Recent work on Cu(II) phthalocyanines has shown that the predicted electronic structure, particularly the ordering of the occupied valence orbitals, is sensitive to the level of theory applied, and in the case of DFT, sensitive to the nature of the functional employed.[26-29] Whilst in most cases the unpaired electron is calculated to reside in the Cu-based dx^2-y^2 orbital, in agreement with experimental evidence from EPR measurements,[30, 31] contradictory results place it variously above and below the doubly occupied HOMO orbital.

During the course of this work, similar effects were also observed for the copper(II) complexes, where not just the electronic structure, but also the geometry was seen to be sensitive to the nature of the functional chosen. Relatively large basis sets, 6-

31+g(d,p) and cc-pVTZ, were used in combination with a number of functionals to investigate the sensitivity of the electronic structure to the level of theory (Table 1 – Appendix 1). The density functionals (OLYP, OPBE, PBE, SVWN and BLYP)[32-34] tend to place the SOMO within the HOMO-LUMO gap, predicting that the lower energy HOMO is a doubly occupied ligand-based π-orbital. HF and the hybrid and long-range corrected functionals (B3LYP, M06-HF, PBE1PBE, BH&HLYP, CAM-B3LYP),[35, 36] in contrast, tend to place the SOMO at an energy below the doubly-occupied ligand-based π-HOMO. In the case of OLYP, OPBE, PBE and B3LYP(VWN5) the geometry of the copper complexes was predicted to be significantly non-planar around the Cu(II) centre.

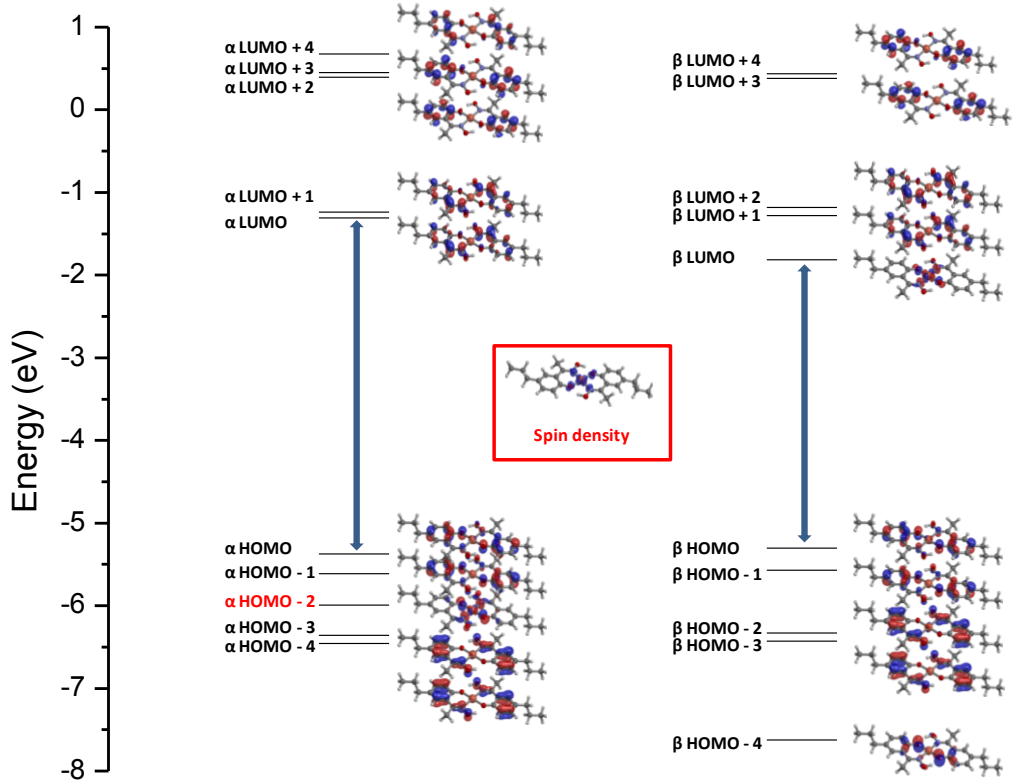

Figure 10 Alpha and beta orbital energies of Cu($^{n\text{-}Pr}$sao)$_2$ at the B3LYP/6-31G(d,p) level of theory. The electron spin density is based on the alpha HOMO-2, which is lower in energy than the predominantly ligand based π-HOMO.

Recent work by Kronick *et al.*[37] has suggested the self-interaction error, inherent in the majority of DFT functionals, is responsible for the difference in the electronic structures predicted by local and hybrid functionals. The self-interaction error, which is more pronounced in the non-hybrid functionals, tends to destabilise more localised orbitals, in this case the singly occupied Cu-based dx^2-y^2 orbital, raising it in energy above the doubly occupied ligand-based HOMO. By including a fraction of HF exchange in the hybrid functionals the self-interaction error is reduced, and the Cu-based dx^2-y^2 orbital is calculated to lie lower in energy than the HOMO (Figure 10 and Table 1 – Appendix 1).

Irrespective of the functional employed, all computational methods consistently predict that the unpaired electron does indeed reside in the mainly Cu-based dx^2-y^2 orbital, consistent with the experimental EPR results (Section 3.9). The insensitivity of the electrochemical redox peaks to the choice of central metal atom and the lack of an observable oxidation from the Cu(II) SOMO also supports a doubly occupied ligand based orbital as the HOMO. Figure 10 (centre) depicts the calculated spin density of the unpaired electron on the Cu(II) complex using the B3LYP/6-31G(d,p) level of theory. As expected the unpaired electron appears to be based in the dx^2-y^2 orbital of the metal, with some delocalisation onto the donor atoms of the ligand.

3.3.5. Thin film X-ray diffraction

Complexes of the type $M(^{n\text{-}Pr}sao)_2$ and $M(^{H}sao)_2$ were found to be volatile and thin films on various substrates have been prepared by sublimation under reduced pressure. XRD measurements were carried out at room temperature between angles of 5° and 40° (2θ). Infra red (IR) spectroscopy carried out on these films indicates that the thin films are structurally the same as the powder sample prior to

deposition (Figure 10 – Appendix 1). This also reassures us that sample decomposition has not taken place during volatilisation.

XRD measurements carried out on powder samples of Cu($^{n\text{-}Pr}$sao)$_2$ matches the calculated powder pattern generated from the single crystal data indicating the bulk powder is in the same crystallographic phase as that which was isolated from solution as a single crystal. However, XRD measurements on powdered Ni($^{n\text{-}Pr}$sao)$_2$ appears to show additional peaks that do not correspond to the structure obtained from the single crystal data. This indicates that the sample contains a mixture of crystallographic phases or a trace amount of a crystalline impurity.

Shown in Figure 11 is the out-of-plane thin film XRD of Cu($^{n\text{-}Pr}$sao)$_2$ on a Si wafer. Contrasting it with the predicted powder pattern appears to suggest a different crystallographic phase in the thin film from that present in the single crystal. Note that the intense peak at 33° (2θ) is due to the substrate. The large peaks at 6.18° and 8.38° (2θ) in the thin film XRD correspond to a d-spacing of 14.28 and 10.54 Å, respectively, but have not been indexed due to the lack of distinct peaks available. From the single crystal data, the intense peaks at 8.13, 9.00 and 12.45° correspond to a d-spacing of 10.86, 9.81 and 7.10 Å, respectively. These peaks are due to reflections from the (100), (002) and (102) planes.

As witnessed with the Cu(II) complex, the analogous Ni(II) sample also appears to exhibit a different structure when thermally grown on a Si thin film, as can be observed in Figure 12. The prominent peaks at 8.04 and 10.47° (2θ) correspond to an intermolecular d-spacing of 10.98 and 8.23 Å, respectively. Contrasting this with the single crystal data, the dominant peaks are at 8.13, 8.92 and 12.30°, similar to the thin film obtained from the volatile Cu(II) complex, with the same assignment of planes.

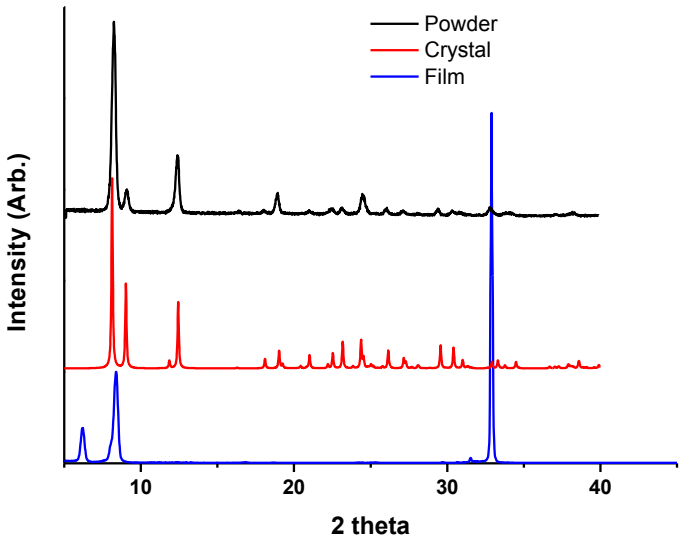

Figure 11 Out of plane thin film XRD of Cu($^{n\text{-Pr}}$sao)$_2$ on a Si substrate (blue) overlaid with the calculated powder pattern from the single crystal data (red) and the experimental powder pattern (black).

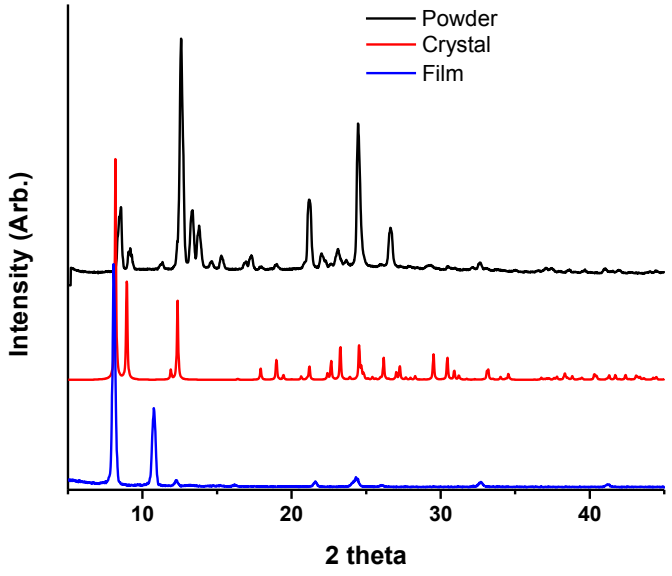

Figure 12 Out of plane thin film XRD of Ni($^{n\text{-Pr}}$sao)$_2$ on a Si substrate (blue) overlaid with the calculated powder pattern from the single crystal data (red) and the experimental powder pattern (black).

From the single crystal XRD data the Cu($^{n\text{-}Pr}$sao)$_2$ and Ni($^{n\text{-}Pr}$sao)$_2$ complexes appear isomorphous but on a thin film these materials are clearly exhibiting a different phase to each other. The single crystal data have all come from solution grown samples but in order to explore the possibility of polymorphism from vapour grown samples, single crystals by sublimation methods have also been prepared. However, sublimed crystals thus far have not exhibited a different crystallographic phase to the crystals isolated from solution.

From Figure 13, the Cu(^{H}sao)$_2$ thin film displays three broad peaks at low angles of 9.98, 11.22 and 12.84° (2θ). The diffraction peaks at 9.98 and 11.22°, although broad, may correspond to reflections expected from the single crystal structure. However, the broad peak at 12.84° does not appear in the predicted powder pattern based on the single crystal data. This may be due to the compound exhibiting a different phase as a result of the compound's interaction with the substrate or it could be due to a crystalline impurity or decomposition product from the sublimation process. The peak at 32.88° is from the Si substrate. Also of importance - although more so for the modelling of magnetic data - is that the single crystal and powder pattern appear to correspond to the same structure.

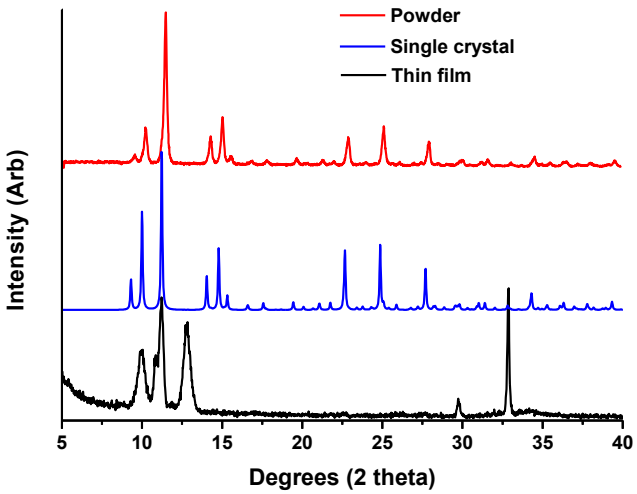

Figure 13 Out of plane thin film XRD of Cu(^{H}sao)$_2$ on a Si substrate (blue) overlaid with the calculated powder pattern from the single crystal data (red) and the experimental powder pattern (black).

Similar to what was observed in the case of Cu(^{H}sao)$_2$, the out of plane thin film diffraction pattern from the Ni(II) analogue produces a diffraction pattern distinct from that of the predicted pattern based upon the single crystal data (Figure 14). The thin film diffraction pattern has one intense peak at 8.60°, with a less prominent peak at 11.30° (2θ). Although the reported single crystal structures of Cu(^{H}sao)$_2$ and Ni(^{H}sao)$_2$ are isomorphous, the thin film packing of these materials is not the same in both materials. This may reflect the intricate role that the central metal defines in dictating molecular packing when considering the interaction of the substrate with the compound. Additionally, thin film IR data on Si substrates is available for these M(^{H}sao)$_2$ compounds in Figure 11, Appendix I.

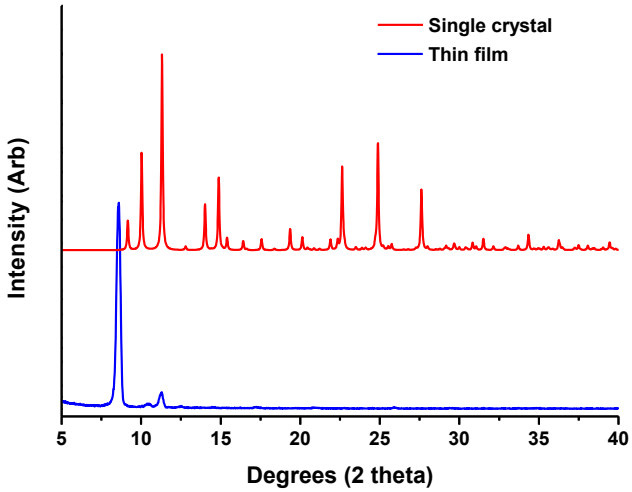

Figure 14 Out of plane thin film XRD of Ni(^{H}sao)$_2$ on a Si substrate (blue) overlaid with the calculated powder pattern from the single crystal data (red).

3.3.6. Magnetic susceptibility

Magnetic measurements have been carried out on powder samples of each of the three paramagnetic Cu(II) complexes from 1.8 – 300 K under an applied magnetic field of 0.1 T . The data from each sample have been modelled using the Curie-Weiss law and, if appropriate, an additional model has been utilized to estimate the magnitude of the exchange interaction (J), the g-value and any temperature independent paramagnetic contribution. Measurements carried out on a powder sample of Cu($^{t\text{-Oct}}$sao)$_2$ are shown in Figure 15, which clearly indicate paramagnetic behaviour exhibited by the sample with no indication of any significant magnetic ordering or interactions at low temperature. This result is expected due to the steric bulk of the tertiary octyl group present on the ligand, $^{t\text{-Oct}}$saoH. The steric effect of the ligand on the crystal packing results in a large intermolecular distance between Cu(II) centres, approximately 7 Å, such that the molecule behaves as an isolated paramagnet.

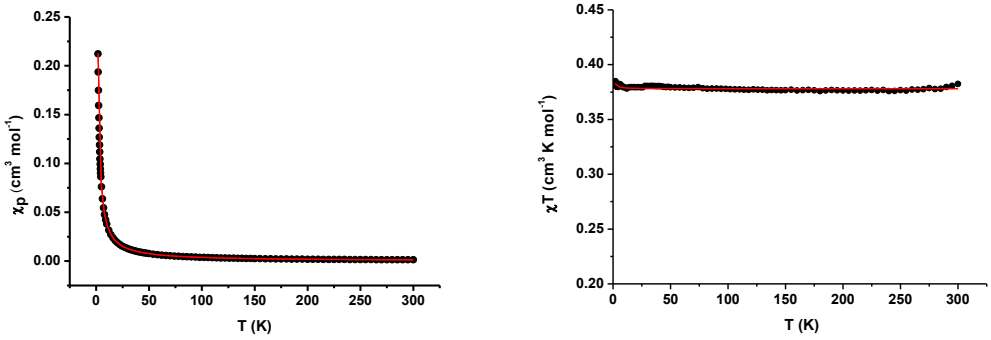

Figure 15 χ vs. T plot (left) and χT vs. T plot (right) of Cu($^{t\text{-Oct}}$sao)$_2$ fit to the Curie-Weiss law.

Fitting the χ vs. T plot to the Curie-Weiss law over the range 1.8 – 300 K (Figure 15, left) the Curie constant has been determined as 0.3794(5) cm^3 K mol^{-1}, leading to a g factor of 2.012, and a Weiss constant of 0.011(3) K. From the fit to the χT vs. T curve, a similar Curie constant of 0.3779(2) cm^3 K mol^{-1} has been calculated, leading to a g factor of 2.007, and a Weiss constant of 0.023(3) K. Due to the spin orbit

coupling present in Cu(II) the g-value is often anisotropic and typically lies between 2.0 and 2.30.[38] As the g factor is close to the free electron value of 2.002, this would suggest the unpaired electron has significant ligand character.

At low temperature the χT vs. T plot for Cu($^{n\text{-Pr}}$sao)$_2$ shows a downward trend indicating the metal centres are interacting antiferromagnetically (Figure 16). Treating the sample as a 1-D chain of interacting S = 1/2 molecules, the experimental data were fit to the Bonner-Fisher expression[39] modified by Estes et al.[40] This calculates the isotropic g-value as 2.024 and J as -0.49 cm^{-1}. The small J value indicates a weak antiferromagnetic coupling, giving a susceptibility peak ca. 6 K. The g-value is rather low; however, this is also consistent with the Curie-Weiss fit of Cu($^{n\text{-Pr}}$sao)$_2$, which calculates g as 2.026 based upon a Curie constant of 0.385(1) cm^3 K mol^{-1} and a Weiss constant of -0.51(1) K (Figure 17).

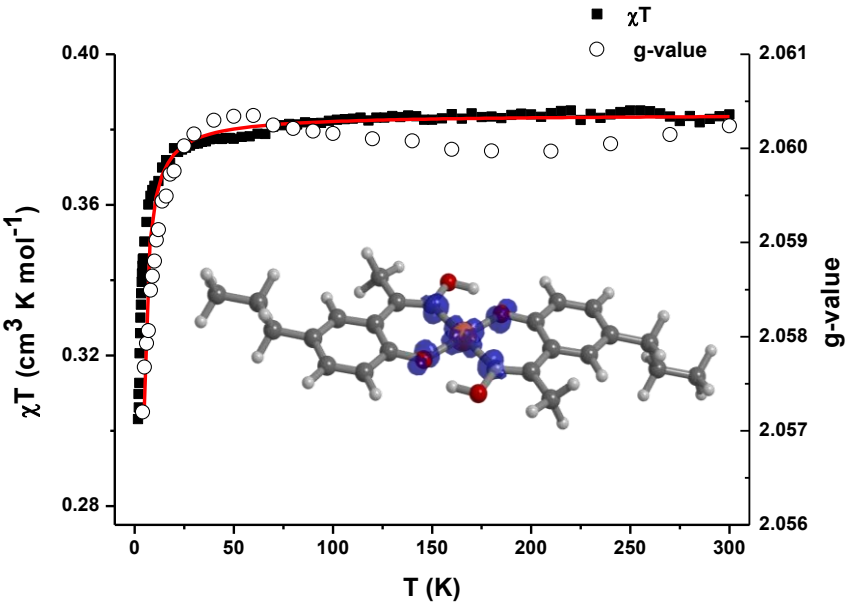

Figure 16 χT vs. T plot of Cu($^{n\text{-Pr}}$sao)$_2$ from 1.8 – 300 K. The Bonner-Fisher model curve (red line) displays a good fit to the experimental data (black squares). The curve has been corrected for a temperature independent paramagnetic parameter of 3.15 x10^{-4} cm^3 mol^{-1}. Powder EPR of Cu($^{n\text{-Pr}}$sao)$_2$ showing the change in g-factor with temperature (hollow circles) has been overlaid. Inset is shown the calculated spin-density at the B3LYP/6-31G(d,p) level of theory.

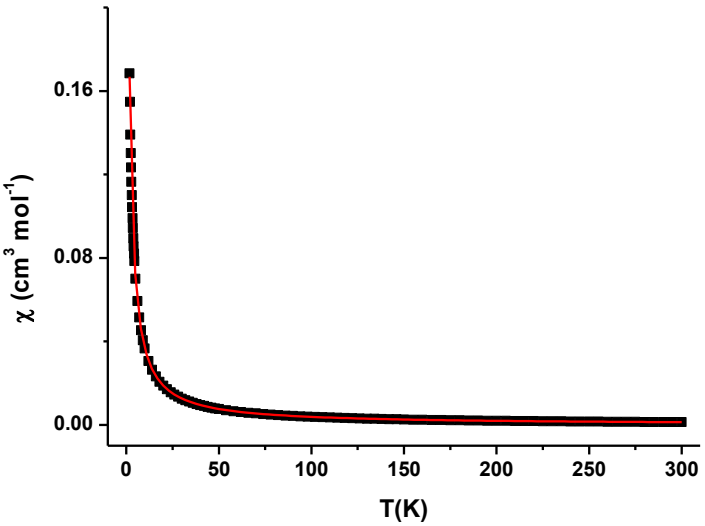

Figure 17 χ vs. T plot of Cu($^{n\text{-}Pr}$sao)$_2$ from 1.8 – 300 K fit to the Curie-Weiss law.

In the case of complex Cu(^{H}sao)$_2$, the results of the magnetic susceptibility measurements have been fit to the Bleaney-Bowers equation[41] owing to the strong dimerisation that the material exhibits in the solid state. Powder XRD measurements have been used to confirm that the single crystal phase is the same as the powder phase, and therefore, this equation is a suitable choice. From the Bleaney-Bowers fit to the experimental data (Figure 18, left), J has been calculated as -0.163(2) cm^{-1} and the g-value as 2.1328(5). Modelling the data using the Curie-Weiss law produces a Curie constant of 0.428(1) cm^3 K mol^{-1} and a Weiss constant of -0.20(1) K. From this Curie constant the associated g-value is 2.136, which is consistent with the g-value obtained from the Bleaney-Bowers model.

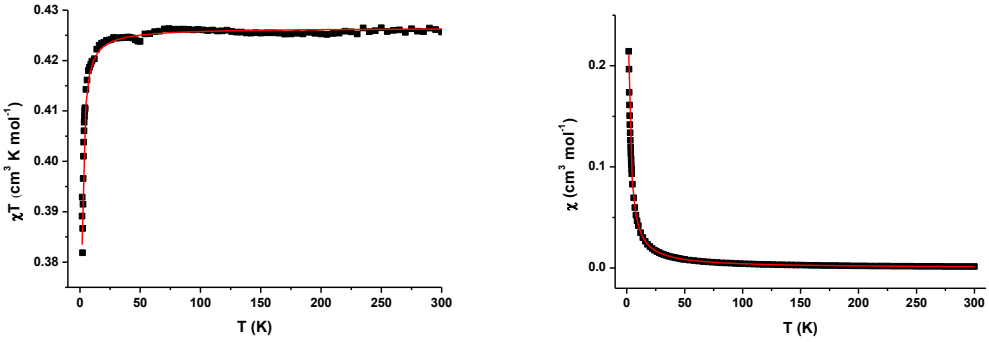

Figure 18 χT vs. T plot of Cu(^{H}sao)$_2$ fit to the Bleaney-Bowers model curve (left) and the χ vs. T plot fit to the Curie-Weiss law (right).

The outcome of modifying the 5-position on the chelating ligand can be directly seen by comparing the magnetic data. The observation of paramagnetic behaviour in Cu($^{t\text{-}Oct}$sao)$_2$ from weak antiferromagnetic coupling in Cu($^{n\text{-}Pr}$sao)$_2$ can be attributed to the interplanar distance decreasing from ~7 Å to ~3 Å. The ^{n}propyl chain has caused equidistant, interplanar π-π stacking distances between molecules and as a result the Cu(II) centres can now interact magnetically through the 1-dimensional chain. The use of the less sterically restricting ^{H}sao ligand has resulted in a strongly dimerised structure in complex Cu(^{H}sao)$_2$ with short intermolecular Cu…O distances of 2.67 Å,[19] where the interactions are essentially intra-dimer without any extended interactions. As such, the magnetic data can be modelled successfully by only considering an intra-dimer interaction, without incorporating an inter-dimer term.

3.3.7. Electron paramagnetic resonance

Due to experimental limitations in magnetic susceptibility measurements, a more accurate estimation of the g-value is obtained from EPR. Measurements have been carried out on solution samples of both soluble Cu(II) complexes at room temperature. In the case of Cu($^{t\text{-}Oct}$sao)$_2$ (Figure 19) the EPR signal is split into a

quartet of pentets owing to the Cu nuclear spin of 3/2 (quartet) and two ^{14}N nuclei each of spin 1 (pentet). Note that both isotopes of Cu have the same nuclear spin. From the EPR simulation, the following values have been determined: coupling to the ^{63}Cu nuclei of 90.5 G, coupling to the ^{65}Cu nuclei of 94.5 G, coupling to both the ^{14}N nuclei of 14.3 G, a linewidth of 10.0 G and g_{iso} of 2.11. At lower magnetic field the resolution of the hyperfine coupling is not well resolved and thus simulation is only possible for the resolved part of the spectrum at higher magnetic field; a higher frequency EPR experiment may improve the resolution. The coupling of the unpaired electron to the ^{14}N nucleus indicates that in the complex it is not completely localised on the Cu(II) centre but some of the electron density is on the N donor atoms of the ligand, which implies that the SOMO of the complex is delocalised onto part of the ligand. This is consistent with the computational results above. The simulated g factor is slightly larger than that determined by fit to the susceptibility data although broadly consistent.

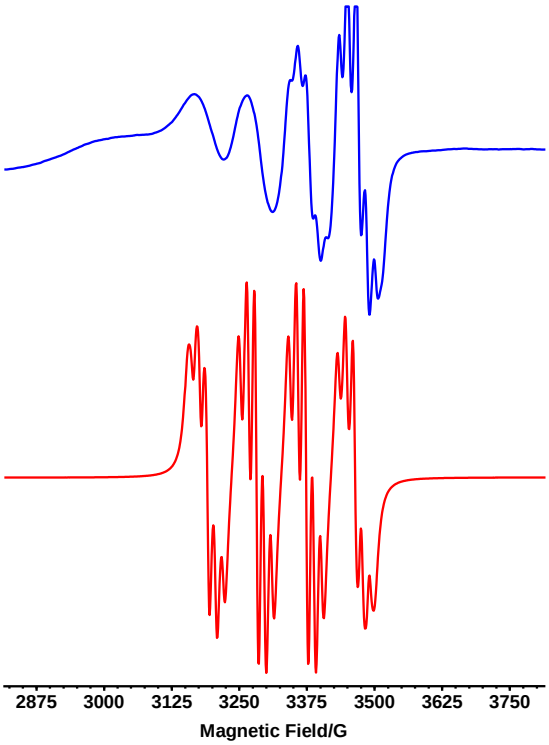

Figure 19 Solution EPR results for Cu($^{t\text{-}Oct}$sao)$_2$ (upper) and simulated spectrum (lower). Measurement carried out in DCM at 25 °C.

A similar spectrum was obtained for Cu($^{n\text{-}Pr}$sao)$_2$ (Figure 20) indicating as expected that the paramagnetic systems are closely related. From the EPR simulation, the following values have been determined: coupling to the ^{63}Cu nuclei of 90.5 G, coupling to the ^{65}Cu nuclei of 96.5 G, coupling to both the ^{14}N nuclei of 15.8 G, a linewidth of 10.0 G and g_{iso} of 2.10. Again we see a delocalisation of the SOMO onto the N donor on the ligand, the extent of which is almost identical to Cu($^{t\text{-}Oct}$sao)$_2$ by estimation from the simulation parameters. Complexes such as Cu(II) tetraphenyl porphyrin (TTP) have been previously studied by EPR[30] and reported to have an average metal coupling of 95 G, ^{14}N coupling of 14 G and a g-factor of 2.117. In this Cu(TTP) example where the spin is based in the dx^2-y^2 orbital, the simulation parameters closely match that of our system implying the unpaired electrons are in similar environments with similar delocalisation onto ligand orbitals.

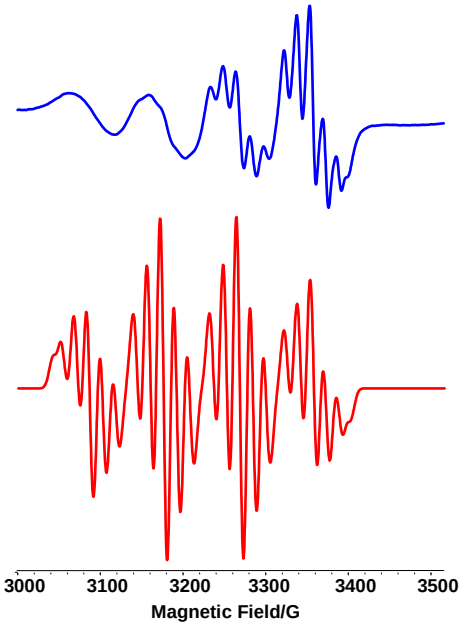

Figure 20 Solution EPR results for Cu($^{n\text{-}Pr}$sao)$_2$ (upper) and simulated spectrum (lower). Measurement carried out in DCM at 25 °C.

The powder EPR results of Cu(^{nPr}sao)$_2$, (Figure 16), display how the g-factor changes as the material magnetically orders at low temperature. In this case the g-

factor indicates a greater degree of electron delocalisation than was estimated by simulation from the solution measurement. The value falls from approximately 2.060 to almost 2.057 as the antiferromagnetic interactions become more significant at lower temperature. Reassuringly, the change in g-factor broadly resembles the χT vs. T data from magnetic susceptibility measurements. This reaffirms that using a sterically smaller ligand is having the desired effect on the intermolecular interactions in the solid state.

Thin film EPR of Cu(^{H}sao)$_2$ is shown below (Figure 21) displaying the change in g-factor as a function of temperature; of note is that the film showed no angle dependence with respect to the magnetic field. This would indicate that the film is composed of an array of isotropically ordered crystallites with no preferential alignment on the PET substrate. At room temperature a g-factor of 2.078 was measured from the thin film sample; as the temperature is lowered this value decreases to 2.065 at 200K before steadily increasing to 2.075 at 70 K. Below 70 K the g-factor remains relatively consistent around 2.075 but begins to drop below 5 K, possibly as a consequence of magnetic ordering interactions, which are observed around this point in the SQUID data. The initial sudden change in the g-factor between 300 K and 200 K may indicate the occurrence of a phase change or magnetic interaction associated with the thin film packing of the material, since no such behaviour is observed at this temperature from SQUID measurements on powder samples. However, it should be noted that there are not a lot of data points available in the high temperature regime on which to base solid conclusions.

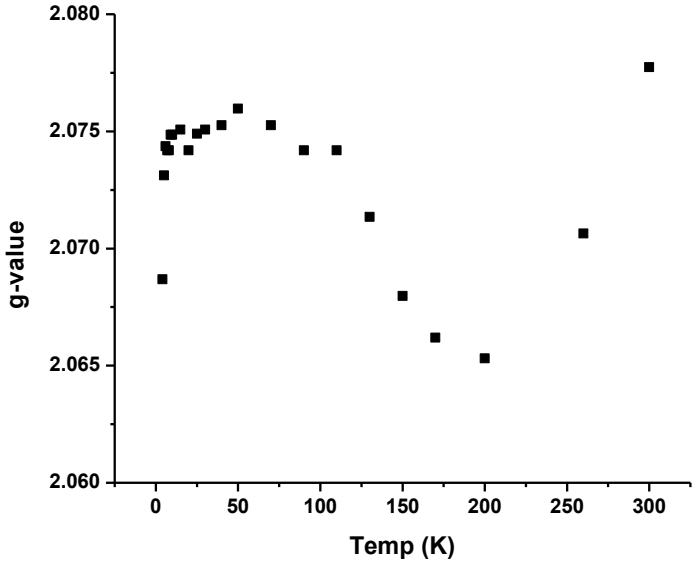

Figure 21 Thin film EPR results for Cu(^{H}sao)$_2$ displaying a change in g-value with temperature.

3.3.8. Scanning electron microscopy

The performance of a thin film device, such as a transistor, can be influenced by crystallinity and grain boundaries[42, 43] so SEM has been carried out to investigate the thin film morphology. The Ni(II) and Cu(II) $^{n\text{-}Pr}$sao based complexes appear to exhibit different morphologies to each other on both ITO and Si substrates. The Cu(II) crystals appear needle-like in shape while the Ni(II) film consists of crystallites of various shapes with less uniform coverage of the substrate. SEM images of the thin films on Si, ITO and FET substrates at different magnifications (Figure 22, Figure 23), highlight that the Ni(II) complex has not formed homogeneous films. The source-drain gap of our FET substrates is only 2 μm so the films, although not ideal, should still be suitable for FET studies. Both films were formed under similar conditions but a higher temperature was reached in the deposition of Cu($^{n\text{-}Pr}$sao)$_2$ and this may be responsible for the pronounced change in morphology. Both films were deposited at a rate of 0.1 - 0.3 Å per second but in the

deposition of Cu($^{n\text{-}Pr}$sao)$_2$ a maximum temperature of 213°C was reached as opposed to 157°C in the deposition of Ni($^{n\text{-}Pr}$sao)$_2$. The solution deposited materials, in contrast to the vacuum grown films, form large needle-like crystallites much bigger than those which are formed by sublimation. The solution grown crystallites effectively bridge the source-drain gap of 2 μm whereas not all the vacuum deposited particles are this large.

Strikingly, the thin film morphology of M(^{H}sao)$_2$ complexes display a strong dependence on the substrate type as well as the central metal (Figure 24 and Figure 25). On ITO, Cu(^{H}sao)$_2$ appears as thin, curved needle like crystallites but on Si substrates the crystallites are more angular, with straighter edges and contain a wider distribution of crystallite sizes and shapes. When deposited by PVD onto FET devices containing Pt electrodes and a SiO_2 dielectric layer, the crystallites appear as small curved needles, similar to those observed on ITO substrates (Figure 24). In contrast, Ni(^{H}sao)$_2$ exhibits a similar morphology of elongated, rectangular platelets across all of the substrates that films were grown on. However, the average crystallite sizes do appear to be much larger on Si rather than on FETs or ITO.

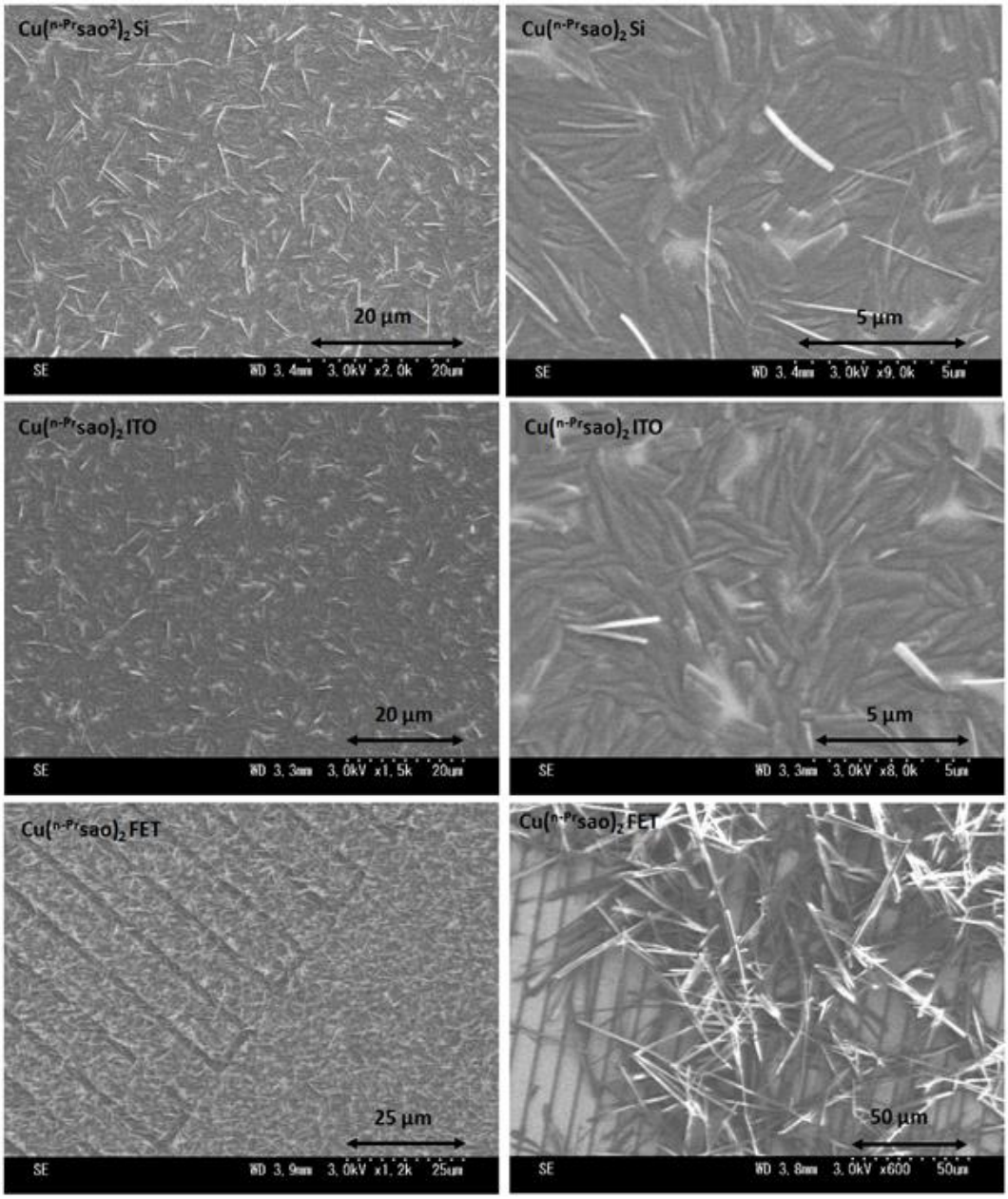

Figure 22 SEM images of the Cu($^{n\text{-}Pr}$sao)$_2$ complexes on Si and ITO substrates (upper four images). Shown at the bottom are vacuum deposited (left) and drop coated (right) films covering FET interdigitated electrodes with a 2µm gap. Drop cast sample deposited from a saturated solution of DCM. Scale shown inset.

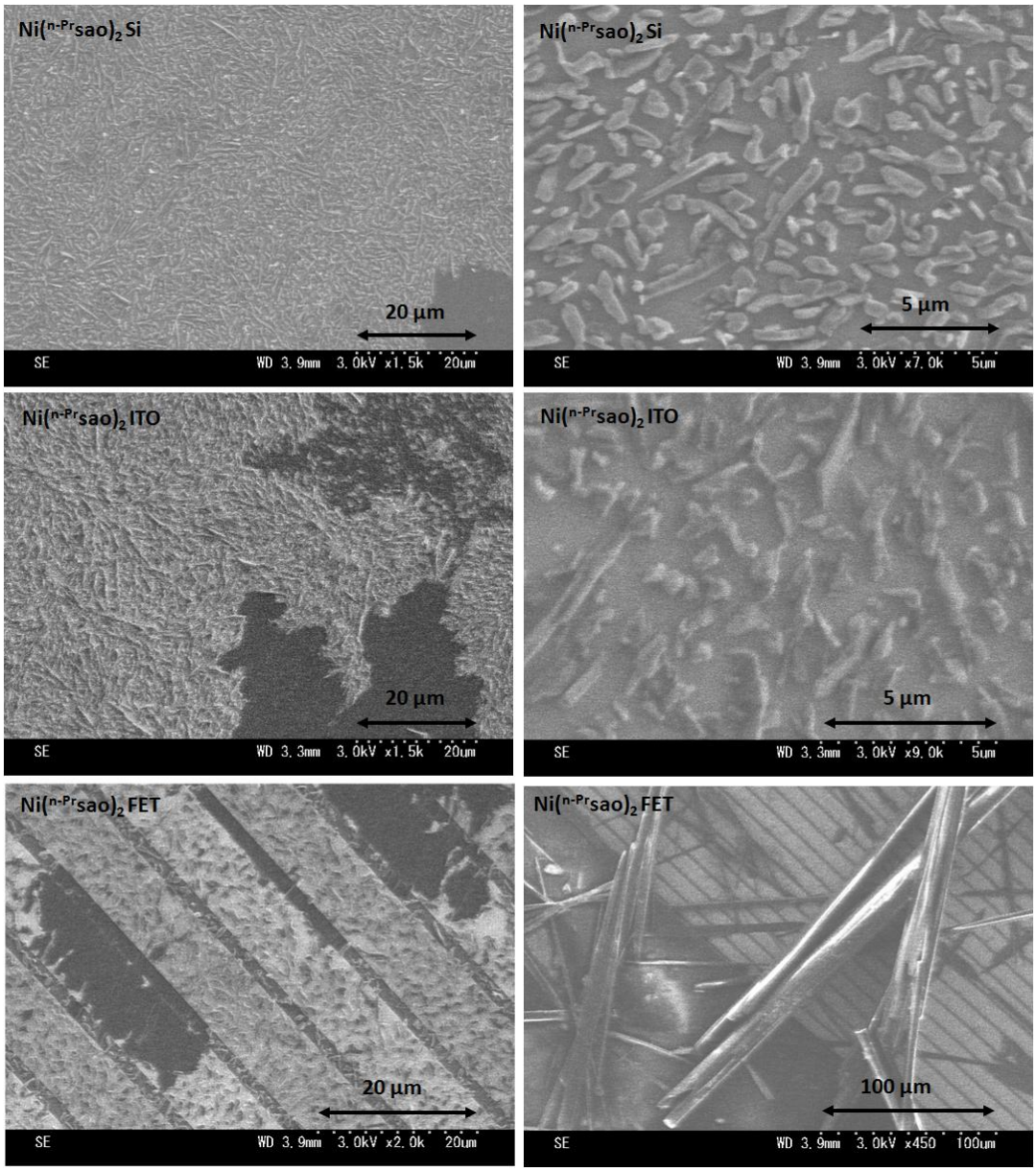

Figure 23 SEM images of the Ni($^{n\text{-}Pr}$sao)$_2$ complexes on Si and ITO substrates (upper four images). Also shown at the bottom are vacuum deposited (left) and drop coated (right) films covering FET interdigitated electrodes with a 2µm gap. Drop cast sample deposited from a saturated solution of DCM. Scale shown inset.

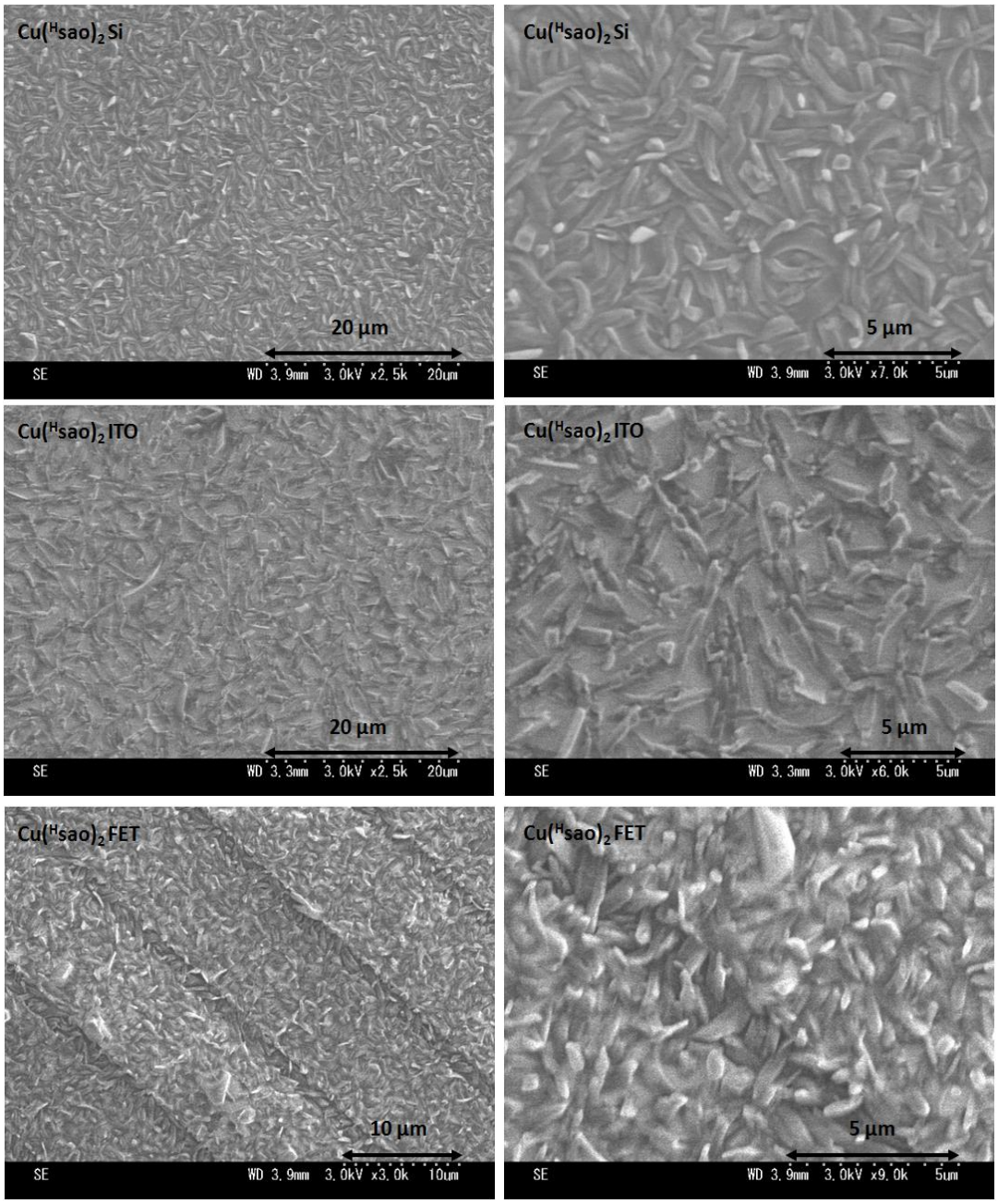

Figure 24 SEM images of the Cu(^{H}sao)$_2$ complexes on Si and ITO substrates (upper four images). Shown at the bottom are FET devices that have interdigitated electrodes with a 2µm gap. Samples were deposited onto substrates via vacuum sublimation. Scale shown inset.

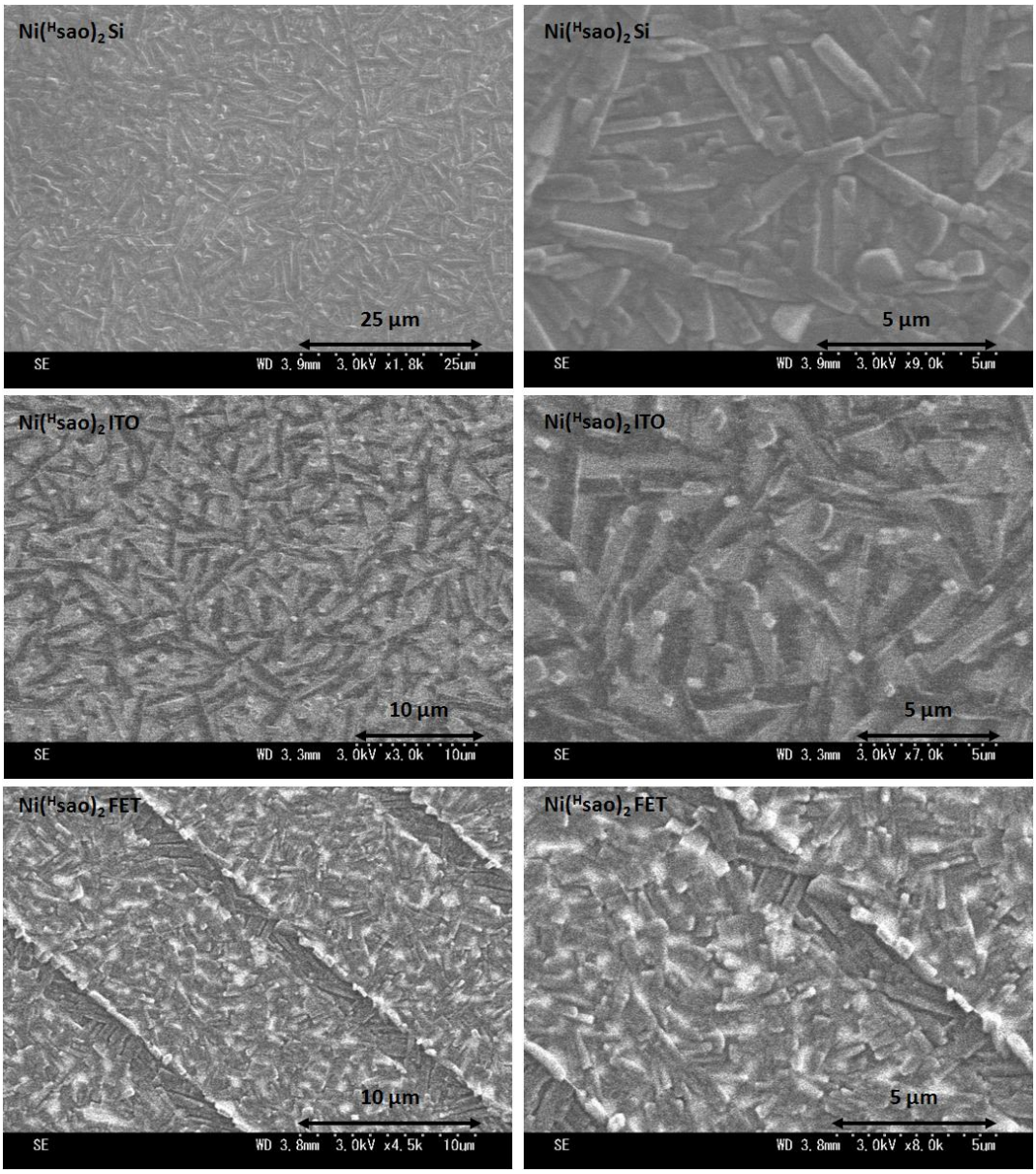

Figure 25 SEM images of the Ni(^{H}sao)$_2$ complexes on Si and ITO substrates (upper four images). Shown at the bottom are FET devices that have interdigitated electrodes with a 2µm gap. Samples were deposited onto substrates via vacuum sublimation. Scale shown inset.

3.3.9. FET measurements

A series of FET measurements was carried out using the less sterically hindered, M($^{n\text{-Pr}}$sao)$_2$, complexes to form thin films by both vapour processing and solution coating. From the cyclic voltammetry it appears that these materials are weak electron donors therefore p-type conduction may be expected. However, none of these complexes produced gate voltage effects when measurements were carried out using the FET configuration described earlier. Instead each material exhibited insulating behaviour under a gate potential in an FET device, despite the films being highly crystalline and the π-stacking capability designed into the complexes. The poor performance may be due to an unfavourable arrangement of the molecules in the solid state, however a likely contributing factor is the lack of significant mixing of metal d-orbitals with the ligand frontier orbitals, particularly for the Cu(II) complexes. The lack of mixing will limit the delocalisation of any introduced holes over the molecule shown by the little difference between the oxidation potential of the metal complexes and the uncomplexed ligand. In addition, the localised ligand-based frontier orbitals that result will limit the extent of intermolecular interactions, reducing the likelihood of effective charge transport.

3.4. Conclusions

Variation of the substituent *para* to the hydroxyl group in 2-hydroxy-acetophenone oxime has allowed control over the intermolecular interactions in all of the Ni(II) and Cu(II) complexes. A bulky alkyl substituent electronically isolates the molecules in the solid state, whilst a smaller alkyl chain allows short 1D, intermolecular distances, as witnessed by comparisons of single crystal X-ray structures, whilst still retaining sufficient solubility to enable solution processing. Where the solubilising group *para* to the hydroxyl group has been replaced by a proton then strongly dimerised structures are observed with limited solubility, as reported elsewhere.[19, 20] These materials have been shown to be volatile and processable via vacuum sublimation methods, consistent with the stability imposed through the pseudo-macrocyclic structure. In addition, single crystals of these materials can be prepared by sublimation under reduced pressure.

From the electrochemical studies, absorption spectroscopy and the computational work, the materials appear to have a large energy gap between the HOMO and LUMO, and the electrochemical processes, within the solvent window, are irreversible. FET results indicate that these materials are insulators and likely not suitable for this application. In keeping with this, computational, EPR and magnetic measurements on the Cu(II) complexes have indicated that intermolecular magnetic interactions are weak, which is affirmed by thin film absorption spectroscopy. The poor FET performance appears, in part, attributable to the minimal mixing of metal d-orbitals with the ligands frontier orbitals, and consequently the lack of facile redox processes. This lack of strong orbital overlap within the molecule, evidenced by the ligand-based electrochemistry, may also play a role in the weak intermolecular interactions. Successful molecular semiconductors based upon transition metal complexes rely on a strongly delocalised electron structure to maximise intermolecular interactions suitable for electron transport. Notable examples of such materials include metal phthalocyanines and metal-*bis*-1,2-dithiolene complexes; in

the latter the choice of central metal plays an electronic role in mediating delocalisation across the complex, whereas in the former electronic delocalisation is inherent from the conjugated, macrocyclic ring.

EPR spectroscopy indicated a largely Cu(II) centred radical, with a similar degree of metal-ligand spin density distribution to that of a Cu-porphyrin complex with some spin density delocalised onto the donor nitrogen atoms. In such Cu(II) complexes, we noted the computational complexity that has previously been observed regarding the relative energy of the SOMO compared with the other orbitals. Experimentally, the electrochemical observation of ligand-based oxidation rather than Cu-centred oxidation suggests a doubly-occupied ligand-based orbital as the HOMO. Extensive survey of different levels of theory provides guidance on the ability of different methods to generate theoretical results consistent with this interpretation. This assessment of a range of functionals will aid future computational study of similar Cu(II) coordination complexes.

Still of interest is the characterisation and further study of the thin film crystal packing, in particular how the magnetic properties alter with crystal packing. The SEM results, coupled with thin-film XRD, have shown visually how deposition technique and substrate can have a major impact on the film morphology and crystal size but further exploration of how the deposition conditions affects thin film morphology is required to attempt to understand the thin film polymorphism.

Design of new families of metal complexes suitable for functional materials should therefore focus on a good energetic match between orbitals of the metal and the delocalised ligand, or should select polydentate or macrocyclic ligands that already possess extensive delocalisation analogous to the properties of phthalocyanines, leading to more redox activity and more delocalised frontier orbitals.

3.5. References

1. Shimazaki, Y.; Yajima, T.; Takani, M.; Yamauchi, O., *Coordination Chemistry Reviews* **2009,** *253*, 479-492.
2. Jia, J.; Hubberstey, P.; Champness, N.; Schröder, M.; Hosseini, M. W., Supramolecular Chemistry of 4,4′-Bipyridine-N,N′-dioxide in Transition Metal Complexes: A Rich Diversity of Co-ordinate, Hydrogen-Bond and Aromatic Stacking Interactions. In Springer Berlin / Heidelberg: 2009; Vol. 132, pp 135-161.
3. Ye, B.-H.; Tong, M.-L.; Chen, X.-M., *Coordination Chemistry Reviews* **2005,** *249*, 545-565.
4. Mercuri, M. L.; Deplano, P.; Pilia, L.; Serpe, A.; Artizzu, F., *Coordination Chemistry Reviews* **2010,** *254*, 1419-1433.
5. Cho, J.-Y.; Domercq, B.; Jones, S. C.; Yu, J.; Zhang, X.; An, Z.; Bishop, M.; Barlow, S.; Marder, S. R.; Kippelen, B., *Journal of Materials Chemistry* **2007,** *17*, 2642-2647.
6. Deplano, P.; Pilia, L.; Espa, D.; Mercuri, M. L.; Serpe, A., *Coordination Chemistry Reviews* **2010,** *254*, 1434-1447.
7. Bao, Z.; Lovinger, A. J.; Dodabalapur, A., *Applied Physics Letters* **1996,** *69*, 3066-3068.
8. Noro, S.-i.; Chang, H.-C.; Takenobu, T.; Murayama, Y.; Kanbara, T.; Aoyama, T.; Sassa, T.; Wada, T.; Tanaka, D.; Kitagawa, S.; Iwasa, Y.; Akutagawa, T.; Nakamura, T., *Journal of the American Chemical Society* **2005,** *127*, 10012-10013.
9. Shin-ichiro, N.; Taishi, T.; Yoshihiro, I.; Ho-Chol, C.; Susumu, K.; Tomoyuki, A.; Takayoshi, N., *Advanced Materials* **2008,** *20*, 3399-3403.
10. Smith, A. G.; Tasker, P. A.; White, D. J., *Coordination Chemistry Reviews* **2003,** *241*, 61-85.
11. Tasker, P.; Gasperov, V., Ligand Design for Base Metal Recovery. In *Macrocyclic Chemistry*, 2005; pp 365-382.
12. Szymanowski, J., *Hydroxyoximes and Copper Hydrometallurgy*. CRC Press: Boca Raton, USA, 1993.
13. *WIN-EPR Simfonia*, 1.25; Bruker Analystische Messtechnik GmbH: Rheinstetten, 1996.
14. Becke, A. D., *J. Chem. Phys.* **1993,** *98*, 5648-5652.
15. Lee, C.; Yang, W.; Parr, R. G., *Phys. Rev. B* **1988,** *37*, 785-789.
16. Ditchfield, R.; Hehre, W. J.; Pople, J. A., *The Journal of Chemical Physics* **1971,** *54*, 724-728.
17. Frisch, M. J.; Trucks, G. W.; Schlegel, H. B.; Scuseria, G. E.; Robb, M. A.; Cheeseman, J. R.; Montgomery, J. A.; Vreven, T.; Kudin, K. N.; Burant, J. C.; Millam, J. M.; Iyengar, S. S.; Tomasi, J.; Barone, V.; Mennucci, B.; Cossi, M.; Scalmani, G.; Rega, N.; Petersson, G. A.; Nakatsuji, H.; Hada, M.; Ehara, M.; Toyota, K.; Fukuda, R.; Hasegawa, J.; Ishida, M.; Nakajima, T.; Honda, Y.; Kitao, O.; Nakai, H.; Klene, M.; Li, X.; Knox, J. E.; Hratchian, H. P.; Cross, J. B.; Bakken, V.; Adamo, C.; Jaramillo, J.; Gomperts, R.; Stratmann, R. E.; Yazyev, O.; Austin, A. J.; Cammi, R.; Pomelli, C.; Ochterski, J. W.; Ayala, P. Y.; Morokuma, K.; Voth, G.

A.; Salvador, P.; Dannenberg, J. J.; Zakrzewski, V. G.; Dapprich, S.; Daniels, A. D.; Strain, M. C.; Farkas, O.; Malick, D. K.; Rabuck, A. D.; Raghavachari, K.; Foresman, J. B.; Ortiz, J. V.; Cui, Q.; Baboul, A. G.; Clifford, S.; Cioslowski, J.; Stefanov, B. B.; Liu, G.; Liashenko, A.; Piskorz, P.; Komaromi, I.; Martin, R. L.; Fox, D. J.; Keith, T.; Laham, A.; Peng, C. Y.; Nanayakkara, A.; Challacombe, M.; Gill, P. M. W.; Johnson, B.; Chen, W.; Wong, M. W.; Gonzalez, C.; Pople, J. A., Gaussian 03, Revision E.01. In *Gaussian, Inc., Wallingford CT*, Wallingford CT, 2004.

18. Thompson, M. A. *ArgusLab 4.0.1*, Planaria Software LLC: Seattle, WA.

19. Z. Kangjing; Z. Chengming; C. Xing; Chenge, Y., *Kexue Tongbao (Chin.)* **1985,** *30*, 266.

20. Antonis, G. H.; Monir, U.; Lalia-Kantouri, M., *Zeitschrift für anorganische und allgemeine Chemie* **1997,** *623*, 627-632.

21. Ramakrishnan, C.; Geetha, Y., *Journal of Chemical Sciences* **1990,** *102*, 481-496.

22. Taylor, R.; Macrae, C. F., *Acta Crystallographica Section B* **2001,** *57*, 815-827.

23. Bruno, I. J.; Cole, J. C.; Edgington, P. R.; Kessler, M.; Macrae, C. F.; McCabe, P.; Pearson, J.; Taylor, R., *Acta Crystallographica Section B* **2002,** *58*, 389-397.

24. Macrae, C. F.; Edgington, P. R.; McCabe, P.; Pidcock, E.; Shields, G. P.; Taylor, R.; Towler, M.; van de Streek, J., *Journal of Applied Crystallography* **2006,** *39*, 453-457.

25. Macrae, C. F.; Bruno, I. J.; Chisholm, J. A.; Edgington, P. R.; McCabe, P.; Pidcock, E.; Rodriguez-Monge, L.; Taylor, R.; van de Streek, J.; Wood, P. A., *Journal of Applied Crystallography* **2008,** *41*, 466-470.

26. Marom, N.; Hod, O.; Scuseria, G. E.; Kronik, L., *The Journal of Chemical Physics* **2008,** *128*, 164107-6.

27. Aristov, V. Y.; Molodtsova, O. V.; Maslyuk, V. V.; Vyalikh, D. V.; Zhilin, V. M.; Ossipyan, Y. A.; Bredow, T.; Mertig, I.; Knupfer, M., *The Journal of Chemical Physics* **2008,** *128*, 034703-6.

28. King, E. R.; Betley, T. A., *Journal of the American Chemical Society* **2009,** *131*, 14374-14380.

29. Westcott, B. L.; Gruhn, N. E.; Michelsen, L. J.; Lichtenberger, D. L., *Journal of the American Chemical Society* **2000,** *122*, 8083-8084.

30. Basu, P., *Journal of Chemical Education* **2001,** *78*, 666-null.

31. Calle, C.; Schweiger, A.; Mitrikas, G., *Inorganic Chemistry* **2007,** *46*, 1847-1855.

32. Chunying, R.; Shixun, L.; Dulin, Y.; Bin, S.; Aiguo, Z.; Bartolotti, L.; Shubin, L., *Journal of Chemical Physics* **2006,** *125*, 174102.

33. Takagi, N.; Krapp, A.; Frenking, G., *Canadian Journal of Chemistry* **2010,** *88*, 1079-1093.

34. Yang, K.; Peverati, R.; Truhlar, D. G.; Valero, R., *Journal of Chemical Physics* **2011,** *135*, 044118.

35. Tekarli, S. M.; Drummond, M. L.; Williams, T. G.; Cundari, T. R.; Wilson, A. K., *The Journal of Physical Chemistry A* **2009,** *113*, 8607-8614.

36. Laury, M. L.; Carlson, M. J.; Wilson, A. K., *Journal of Computational Chemistry* **2012,** *33*, 2380-2387.

37. Marom, N.; Kronik, L., *Applied Physics A: Materials Science & Processing* **2009,** *95*, 159-163.
38. Carlin, R. L., *Magnetochemistry*. Springer-Verlag Berlin and Heidelberg GmbH & Co. K: 1986.
39. Bonner, J. C.; Fisher, M. E., *Physical Review* **1964,** *135*, A640.
40. Estes, W. E.; Gavel, D. P.; Hatfield, W. E.; Hodgson, D. J., *Inorganic Chemistry* **1978,** *17*, 1415-1421.
41. Bleaney, B.; Bowers, K. D., *Proceedings of the Royal Society of London. Series A. Mathematical and Physical Sciences* **1952,** *214*, 451-465.
42. Sung Hoon, K.; Sun Hee, L.; Jin, J., *Electron Device Letters, IEEE* **2010,** *31*, 1044-1046.
43. Tello, M.; Chiesa, M.; Duffy, C. M.; Sirringhaus, H., *Advanced Functional Materials* **2008,** *18*, 3907-3913.

Chapter 4: Tetraaza[14]annulenes

4.1. Introduction

Porphyrins and phthalocyanines represent some of the most promising candidates for a range of applications due to their fascinating optical and electronic properties.[1] These planar, π-conjugated macrocycles commonly find widespread use as the semiconducting layer in field effect transistors,[2-4] organic light emitting diodes[5] and as the light harvesting component in solar cells.[6, 7] An attractive feature is the ability to functionalise the periphery and/or incorporate a wide range of metal ions into the central cavity of these macrocycles, in order to tune their physical, optical and electronic properties. In addition to its electronic effect, it has previously been demonstrated that the size of the central metal ion can play a key role in the charge carrier mobility, by dictating the intermolecular distance in the crystal lattice,[8] with the smaller metal facilitating better overlap of the ligand based frontier orbitals.

Although porphyrins have been utilised less in FETs compared with other organic electronic devices,[9] these molecules typically demonstrate p-type conductivity with respectable mobilities in the range of 10^{-6} to 10^{-1} $cm^2V^{-1}s^{-1}$.[4] Phthalocyanines on the other hand, have slightly higher reported mobilities in the range10^{-3} to 1.0 $cm^2V^{-1}s^{-1}$ depending on the central metal and the device specifications.[10, 11] An interesting feature of phthalocyanine chemistry is that their semiconducting behaviour can be switched from p-type to n-type, going from the unsubstituted compound to the hexadecafluorinated analogue.[12, 13] Substitution of the hydrogen atoms for electron

withdrawing fluorine atoms has the effect of sufficiently lowering the LUMO energy such that electron transport can be realised. Along with their attractive qualities such as planarity, high number of π-electrons and suitable crystal packing, the high thermal and chemical stability of these macrocycles is of importance in FET applications as this allows high purity films to be easily grown by vacuum sublimation techniques.[14]

A well known, but less studied, porphyrin analogue is the class of dibenzotetraaza[14]annulenes.[15] These tetradentate ligands commonly bind metal ions in the dianionic form but complexes have also been reported from the neutral ligand.[16] The geometry of the macrocycle can vary depending on the substituents on the 1,3-propanediiminato linkage and the size of the metal ion in the central cavity.[17] In the absence of any substituents on the 1- or 3-positions of the propanediiminato moiety, the free ligand is usually planar but the introduction of methyl groups into these positions will disrupt this planarity, through steric interactions with the benzene ring, and the ligand will adopt a buckled or saddle shaped conformation. Thus substituents on the 1- or 3-positions of the propanediiminato linkage will result in marked changes in the solid state crystal packing, which has important implications for conducting applications.

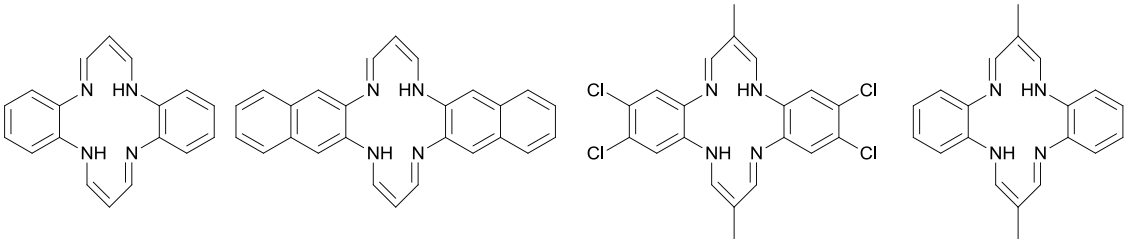

H_2dbtaa H_2dntaa H_2dbtaaCl_4Me_2 H_2dbtaaMe_2

Figure 1 Structures of dibenzo[14]tetraazaannulene (H_2dbtaa), dinaphtho[14]teraazaannulene (H_2dntaa), tetrachlorodimethyldibenzo[14]tetraazaannulene (H_2dbtaaCl_4Me_2) and dimethyldibenzo[14]tetraazaannulene (H_2dbtaaMe_2).

In this work we have examined the electronic, magnetic, optical and charge transport properties of a series of metal complexes using dibenzo- and dinaphtho-tetraazaannulene macrocyclic ligands (Figure 1). This class of macrocycle has been previously shown to exhibit conductive behaviour when doped with iodine,[18] but despite this, the thin film charge transport properties have until now been unexplored.

4.2. Experimental

4.2.1 Synthesis

The starting materials 4,5-dichloro-*o*-phenylenediamine (97 %), 1,1,3,3-tetramethoxypropane (99 %), propargyl alcohol (99 %), and 3-ethoxymethacrolein (96 %) were purchased from Sigma Aldrich and used without further purification. However, o-phenylenediamine (99.5 %) and 2,3-diaminonaphthalene (≥95 %), were recrystallised from DCM prior to use as they have a tendency to decompose in air over time. The dbtaa complexes were synthesised from o-phenylenediamine, 1,1,3,3-tetramethoxypropane and the corresponding metal(II) acetate salt, using an approach adapted from the literature.[19] The resulting complexes were purified by vacuum sublimation at 300 °C under a reduced pressure of 10^{-4} mbar. The metal-free macrocycles were synthesised following the method of Hiller *et al*.[20] by condensation of propargyl aldehyde[21] with the corresponding diamine. Single crystals of Co(dbtaa), Cu(dbtaa), and Ni(dntaa) were grown by vacuum sublimation. The crystal of Co(dbtaa).Cl was grown from a solution of DCM/toluene by slow evaporation.

Propargyl aldehyde. A three-necked 1 L RBF was fitted with a dropping funnel, a nitrogen inlet and a vacuum outlet attached to three traps. The first trap is cooled to -15 °C, with the remaining two traps cooled to -78 °C. To 180 ml of a 33% solution of propargyl alcohol (60 ml, 1 mol) is added a cooled solution of 40% sulphuric acid

(110 ml). The resulting mixture is cooled in an ice bath, and the pressure of the system is reduced to 55 mbar as N_2 is bubbled through the solution. A solution of CrO_3 (0.7 mol, 70 g) in H_2O (133 ml) and sulphuric acid (45 ml) is added dropwise to the reaction mixture over 3 hours, whilst maintaining the ice bath temperature between 2 and 10 °C. After addition of CrO_3, the ice bath is removed and the solution is warmed to RT as the pressure is reduced to 20 mbar to remove the last of the aldehyde. The distillate of the first trap contains mostly water and is discarded; the remaining two traps contain the desired product and are combined (21 g, 38 % yield). The product is reported to polymerise explosively at RT so was transferred to the freezer immediately.

H_2dbtaa. To a solution of o-phenylenediamine (15.12 g, 0.14 mol) in DMF/MeOH (1:1, 18 ml) was added propargyl aldehyde (5.38 ml, 0.14 mol) dropwise. The resulting reddish brown reaction mixture was refluxed for 1 hour, cooled to RT and filtered. The precipitate was washed with MeOH (50 ml) to leave a purple solid (7.01 g, 35 % yield) MS (EI): m/z (%) = 288.1 (100.0%) [M^+], 289.1 (21.55%). Calculated for $C_{18}H_{16}N_4$, C 74.98, H 5.59, N 19.43; found C 74.88, H 5.48, N 19.54. ^{1}H NMR ($CDCl_3$): δ (ppm) = 5.06 (t, 1H, 6 Hz), 6.94 (m, 2H, 4 Hz), 7.08 (m, 2H, 4 Hz), 7.69 (t, 2H, 6.5 Hz), 13.78 (s, 1H). ^{13}C NMR ($CDCl_3$): δ (ppm) = 96.34, 113.61, 124.45, 137.66, 146.36. ^{1}H NMR (DMSO-d6): δ (ppm) = 5.08 (t, 1H), 6.94 (m, 2H), 7.28 (m, 2H), 7.90 (t, 2H), 13.67 (t, 1H).

H_2dntaa. To a solution of 2,3-diaminonaphthalene (1.27 g, 8 mmol) in DMF/MeOH (1:1, 4 ml) was added propargyl aldehyde (0.31 ml, 8 mmol) dropwise. The resulting reddish brown reaction mixture was refluxed for 2 hours, cooled to RT and filtered. The precipitate was washed with MeOH (20 ml) to leave an orange brown solid (704 mg, 45 % yield). MS (EI): m/z (%) = 388.2 (21.71%) [M^+], 389.2 (6.35%). Calculated for $C_{26}H_{20}N_4$, C 80.39, H 5.19, N 14.42; found C 71.38, H 10.68, N 5.63.

H_2dbtaaMe$_2$. To a solution of o-phenylenediamine (1.08 g, 10 mmol) in DMF (80 ml) was added 3-ethoxymethacrolein (1.19 ml, 10 mmol) dropwise. The reaction mixture was refluxed for 48 hours, cooled to RT and stored in a freezer overnight. Black single crystals were isolated by filtration (30 mg, 2 % yield). MS (EI): m/z (%)

= 316.1 (100.00%) [M^+]. Unit cell of single crystal matches that of a previously reported structure.[17]

Ni(dbtaa). Under an atmosphere of N_2, nickel acetate tetrahydrate (8.05 g, 32 mmol) and 2,3- o-phenylenediamine (7 g, 65 mmol) were combined in aqueous DMF (50: 150 ml) with stirring. The reagents were heated at reflux for 1 hour before 1,1,3,3-tetramethoxypropane (10.7 ml, 65 mmol) was added dropwise, and refluxing continued for a further 16 hours. The reaction mixture was cooled to RT, filtered and washed with MeOH (80 ml) to leave a purple precipitate (6.85 g, 62% yield). Product purified by vacuum sublimation at 300 °C under a reduced pressure of 10^{-4} mbar. ^{1}H NMR ($CDCl_3$): 5.44 (m, 2H, 5.5 Hz), 6.90 (m, 4H, 3 Hz), 7.35 (m, 4H, 3.5 Hz), 7.71 (d, 4H, 6 Hz). MS (EI): m/z (%) = 344.1 (100.00%) [M^+]. Calculated for $C_{18}H_{14}NiN_4$, C 62.66, H 4.09, N 16.24; found C 62.55, H 3.98, N 16.13.

Cu(dbtaa). Under an atmosphere of N_2, copper acetate monohydrate (2.00 g, 10 mmol) and 2,3- o-phenylenediamine (2.16 g, 20 mmol) were combined in aqueous DMF (35: 50 ml) with stirring. The reagents were heated at reflux for 1 hour before 1,1,3,3-tetramethoxypropane (3.28 ml, 20 mmol) was added dropwise, and refluxing continued for a further 16 hours. The reaction mixture was cooled to RT, filtered and washed with H_2O (100 ml) MeOH (50 ml) to leave a purple precipitate (1.05 g, 30% yield). Product purified by vacuum sublimation at 300 °C under a reduced pressure of 10^{-4} mbar. MS (EI): m/z (%) = 349.0 (100.00%) [M^+]. Calculated for $C_{18}H_{14}CuN_4$, C 61.79, H 4.03, N 16.01; found C 61.63, H 3.91, N 15.92.

Co(dbtaa). Under an atmosphere of N_2, cobalt acetate tetrahydrate (1.24 g, 5 mmol) and 2,3- o-phenylenediamine (1.08 g, 10 mmol) were combined in aqueous DMF (20: 35 ml) with stirring. The reagents were heated at reflux for 1 hour before 1,1,3,3-tetramethoxypropane (1.64 ml, 10 mmol) was added dropwise, and refluxing continued for a further 48 hours. The reaction mixture was cooled to RT, filtered and washed with H_2O (100 ml) MeOH (100 ml) to leave a purple precipitate (480 mg, 28% yield). Product purified by vacuum sublimation at 300 °C under a reduced pressure of 10^{-4} mbar. MS (EI): m/z (%) = 345.0 (100.00%) [M^+]. Calculated for $C_{18}H_{14}CoN_4$, C 62.62, H 4.09, N 16.23; found C 62.69, H 3.97, N 16.18.

Zn(dbtaa). Under an atmosphere of N_2, a stirring solution of zinc acetate tetrahydrate (110 mg, 0.5 mmol) in DMF (5 ml) was refluxed with dbtaaH_2 (144 mg, 0.5 mmol) for 10 mins. The reaction mixture was then cooled to RT, filtered and washed with MeOH (10 ml) to leave black crystalline product. (80 mg, 46 % yield). ^{1}H NMR (DMSO-d6): δ (ppm) = 4.64 (t, 1H, 8 Hz), 6.71 (m, 2H, 4.5 Hz), 7.07 (m, 2H, 3.5 Hz), 7.64 (d, 2H, 7.5 Hz). MS (EI): m/z (%) = 350.1 (42.71%) [M^+].

Ni(dntaa). Under an atmosphere of N_2, nickel acetate tetrahydrate (620 mg, 2.5 mmol) and 2,3-diaminonapthalene (790 mg, 5 mmol) were combined in aqueous DMF (20: 30 ml) with stirring. The reagents were heated at reflux for 1 hour before 1,1,3,3-tetramethoxypropane (0.82 ml, 5 mmol) was added dropwise, and refluxing continued for a further 16 hours. The reaction mixture was cooled to RT, filtered and washed with MeOH (30 ml) to leave a purple precipitate (355 mg, 32% yield). Product purified by vacuum sublimation at 320 °C under a reduced pressure of 10^{-4} mbar. MS (EI): m/z (%) = 444.1 (100.00%) [M^+]. Calculated for $C_{26}H_{18}NiN_4$, C 70.15, H 4.08, N 12.59; found C 69.99, H 3.99, N 12.56.

Ni(dbtaaCl_4Me_2). Under an atmosphere of N_2, 4,5-dichloro-*o*-phenylenediamine (177 mg, 1 mmol) and nickel(II) acetate tetrahydrate (124 mg, 0.5 mmol) were refluxed for one hour in DMF (4 ml). To the dark brown solution, 3-ethoxymethacrolein (0.124 ml, 1 mmol) was added dropwise with stirring. The resulting reaction mixture was refluxed for 16 hours, cooled to RT and then filtered. The precipitate was washed with EtOH (20 ml) to yield a purple product, which was then purified by vacuum sublimation at 280 °C under a reduced pressure of 10^{-2} mbar. (217 mg, 85 % yield). MS (EI): m/z (%) = 509.9 (5.01%) [M^+], 512.0 (4.28%), 507.9 (3.00%). Calculated for $C_{20}H_{14}NiN_4Cl_4$, C 47.02, H 2.76, N 10.97; found C 47.10, H 2.73, N 10.89. Melting point: >360°C

4.2.2 Experimental methods

Images of the crystal structures have been produced using the software Mercury 2.3.[22-25] All cyclic voltammetry measurements were carried out in dry DCM using 0.3 M $TBAPF_6$ electrolyte in a three electrode system, with each solution being purged with N_2 prior to measurement. The working electrode was a sealed Pt wire with an exposed surface area 2 mm in diameter. The reference electrode was Ag/AgCl calibrated against ferrocene/ferrocenium in the background electrolyte, and the counter electrode was a Pt rod. All measurements were made at room temperature using an μAUTOLAB Type III potentiostat, driven by the electrochemical software GPES. Solution UV/Vis spectra were recorded in DCM using a quartz cell of path length 1 cm on a Perkin-Elmer Lambda 9 spectrophotometer, controlled by a datalink PC, running UV/Winlab software and thin films on quartz were measured on a Jasco V-570 UV/Vis/NIR spectrophotometer. Magnetic susceptibility measurements were performed on powder samples from 1.8 to 300 K using a Quantum Design MPMS-XL SQUID magnetometer with MPMS MultiVu Application software to process the data. The magnetic field used was 0.1 T. Diamagnetic corrections were applied to the observed paramagnetic susceptibilities by using Pascal's constants.[26] Single point and geometry optimisation calculations of the isolated complexes were carried out at the B3LYP/6-31G(d,p) level of theory,[27-29] using Gaussian 03.[30] Time dependant DFT calculations were carried out using the polarisable continuum model (PCM) for DCM which takes into account the effect of solvation. The X-ray crystallographic coordinates were used as the starting structures for all computational calculations. The molecular orbital isosurfaces were visualised using ArgusLab 4.0.[31] Out-of-plane thin film XRD measurements were carried out on a Rigaku ultraX-18HB at room temperature. Data were collected from 2θ angle of 5-40° at a rate of 2° per minute. Powder XRD was carried out using a Bruker AXS D8 diffractometer. All the substrates for deposition, except the FETs, were cleaned in individual solutions of IPA, acetone and then chloroform prior to use. Deposition of Ni(dbtaa) was carried out via vacuum sublimation in a temperature range between 335°C and 345°C at a

pressure of 5.0 x 10^{-4} Pa. This resulted in a growth rate of 0.2-0.4 Å/s which was monitored using a quartz crystal microbalance (QCM). Cu(dbtaa) was deposited between 220°C and 240°C at a pressure of 7.5 x 10^{-4} Pa, which resulted in a growth rate of 0.2-0.4 Å/s. The less volatile Co(dbtaa) was deposited between 375°C and 385°C at a pressure of 5.2 x 10^{-4} Pa, which resulted in a growth rate of 0.1 Å/s. Ni(dntaa) was deposited between 425°C and 470°C at a pressure of 6.0 x 10^{-4} Pa, which resulted in a growth rate of 0.1 Å/s. The materials to be sublimed were heated inside an inert crucible by applying a current. Films of 50 nm thickness were produced according to the QCM. The actual thin film thickness was measured using a profilometer (Appendix II, Figures 1-4). The FET substrates used have gold source and drain electrodes with a width of 2 μm and a gap of 2 or 8 μm. The measurements were carried out in darkness and under vacuum using a Keithley 2636A sourcemeter equipped with Labtracer 2.0 software. Imaging of thin films was carried out using a Hitachi S-4300 Scanning Electron Microscope.

4.3. Results and discussion

The Ni, Cu and Co dbtaa and dntaa macrocycles have been extensively studied and their thin film properties explored. The analogous Zn(dbtaa) was synthesised, as confirmed by NMR and MS, but problems were obtained separating the metallated complex from the free macrocycle. It was observed that Zn(dbtaa) was less stable to heating than the Co, Cu and Ni analogues. dbtaa complexes of Co, Cu and Ni form readily in refluxing DMF and appear to be stable at elevated temperatures for extended periods of several hours. On refluxing dbtaaH and Zn^{2+} for greater than 10 minutes, neither the starting material or the desired product remained, but without refluxing DMF no insertion of Zn was observed even after 24 hours, with and without a base present. Zn(II) in a square planar coordination environment is not commonly observed due to its d^{10} electron configuration, but it can be found in this conformation if the metal ion is placed inside a structurally rigid, conjugated macrocycle. Many examples of Zn(II) porphyrin and phthalocyanine complexes are known in the literature.[32-34] In contrast with porphyrins and phthalocyanines which can be described as fully delocalised, aromatic systems since they satisfy Huckel's rule (4n+2), tetraaza[14]annulenes are described as anti-aromatic (4n) judging from Huckel's criteria.[15] It is thought that the propanediimine bridge and the benzo or naphtho rings are separate conjugated units with very little delocalisation between the two moieties.[15, 17] This lack of conjugation between the donor nitrogen and the aromatic ring may give the macrocycle a degree of structural flexibility not afforded in fully aromatic macrocycles. Structural flexibility in the macrocyclic ligand may account for the inability to isolate the Zn(II) species as an insoluble, planar complex in the same manner as the Co(II), Cu(II) and Ni(II) species were prepared.

The compounds prepared with substituents on the benzo ring and/or the propanediimine bridge, H_2LMe_2 and $H_2LCl_4Me_2$, have been synthesised but their thin film properties not studied due to restrictions with equipment available at the time of synthesis. However, by successfully synthesising H_2LMe_2 and $H_2LCl_4Me_2$

macrocycles, we have highlighted that a potentially wide range of modified tetraaza[14]annulenes can be readily prepared through combinations of various diaminobenzenes and/or aldehydes. Such a study would allow subtle structural modifications to be made to the dbtaaH or dntaaH backbone facilitating a systematic study relating thin film properties to molecular design. The study can then be further extended by incorporating a wide range of 1st row transition metal ions into the macrocyclic cavity to investigate their effect on the electronic structure of the resulting complex.

4.3.1 Crystallography

The single crystal structure of Ni(dbtaa) and the unit cell dimensions of Co(dbtaa) have previously been reported[35] and were shown to be isomorphous. Single crystals of Ni(dbtaa) grown in our lab match the unit cell dimensions previously reported. However, we have also grown crystals of Co(dbtaa) and found the structure to be orthorhombic rather than monoclinic, as was previously reported based upon measurement of the unit cell dimensions and comparison with Ni(dbtaa).[35] Herein we also report the single crystal structure of the analogous Cu(dbtaa) complex and of Ni(dntaa). In addition, a Co(III) complex, Co(dbtaa)Cl, has been isolated by recrystallising Co(dbtaa) from DCM and toluene (Table 1).

Table 1 Crystallographic information for Co(dbtaa), Cu(dbtaa), Ni(dntaa) and Co(dbtaa)Cl.toluene.

Complex	**Co(dbtaa)**	**Cu(dbtaa)**	**Ni(dntaa)**	**Co(dbtaa)Cl.toluene**
Morphology	Black needle (0.18 × 0.03 × 0.01 mm)	Red prism (0.12 x 0.09 x 0.04 mm)	Red prism (0.06 x 0.05 x 0.04 mm)	Black block (0.25 x 0.11 x 0.06)
Empirical formula	$C_{18}H_{14}CoN_4$	$C_{18}H_{14}CuN_4$	$C_{26}H_{18}N_4Ni$	$C_{43}H_{36}Cl_2Co_2N_8$
T (K)	100	150.1	150.1	100
Space group	$Pna2_1$	$P2_1/c$	$Cmc2_1$	P -1
M_r	345.26	349.88	445.15	853.58

a	14.707(2)	19.416(5)	20.428(4)	9.3850(9)
b	5.1858(8)	5.1511(12)	12.905(2)	13.3040(12)
c	17.973(3)	14.878(4)	6.9730(12)	15.3654(11)
α	90	90.00	90.00	74.895(7)
β	90	112.394(3)	90.00	81.155(7)
γ	90	90.00	90.00	75.541(8)
V	1370.8(4)	1375.8(6)	1838.3(6)	1785.5(3)
D_c	1.673	1.689	1.608	1.59
μ	1.256	1.592	1.079	9.023
No. of reflections measured	7681	10218	7216	34656
No. of reflections used	1461	3454	2063	6975
θ_{max}	20.66	27.5	27.48	72.96
Z	4	2	4	2
R_{int}	0.0964	0.048	0.035	0.101
T_{min}/T_{max}	0.8055/0.9875	0.866/ 0.938	0.892/0.958	0.32/0.58
R_1 (I > 2σ(I))	0.0535	0.0364	0.0377	0.0833
wR (F^2) (I > 2σ(I))	0.1272	0.1050	0.0962	0.0728

Table 2 Selected bond lengths and angles of Co(dbtaa), Co(dbtaa).Cl, Cu(dbtaa) and Ni(dntaa).

Bond length / Angle	**Co(dbtaa)**	**Cu(dbtaa)**	**Ni(dntaa)**	**Co(dbtaa)Cl.toluene**
M1-N (Å)	1.896(11), 1.886(10) 1.836(11), 1.870(10)	1.926(2), 1.927(2)	1.866(2), 1.865(2)	1.887(3), 1.887(2) 1.893(4), 1.881(2)
M2-N (Å)	-	1.927(2), 1.928(1)	-	1.885(3), 1.895(3) 1.899(3), 1.889(2)
M1-N-C (Å) **[M1-N-C-C-N]**	1.438(15), 1.51(2), 1.37(2), 1.428(15)	1.413(3), 1.409(3)	1.415(3), 1.416(3)	1.394(5), 1.408(5), 1.403(5), 1.403(5)
M1-N-C (Å)	1.318(18), 1.337(17),	1.325(2), 1.322(2)	1.328(3),	1.350(5), 1.330(5),

[M1-N-C-C-C-N]	1.323(17), 1.316(19)		1.334(3)	1.332(5). 1.331(4)
M2-N-C (Å) **[M2-N-C-C-N]**	-	1.406(2), 1.406(2)	-	1.414(4), 1.400(4), 1.400(5), 1.397(5)
M2-N-C (Å) **[M2-N-C-C-C-N]**	-	1.320(3), 1.328(3)	-	1.328(4), 1.329(5), 1.331(5), 1.330(5)
N-M1-N (°)	84.7(7), 87.0(6)	84.50(7)	84.98(9)	84.4(1), 84.0(1)
N-M1-N' (°)	92.8(6), 95.4(7)	95.50(7)	95.07(9)	94.5(1), 93.9(1)
N-M2-N (°)	-	84.53 (7)	-	83.7(1), 84.1(1)
N-M2-N' (°)	-	95.47(7)	-	94.4(1), 94.6(1)
N···N bite distance (Å) [N-C-C-N]	2.55(2), 2.55(2)	2.591(2), 2.593(1)	2.520(3)	2.535(4), 2.526(4) 2.539(4), 2.523(4)
N···N' distance (Å) **[N-C-C-C-N]**	2.70(2), 2.79(2)	2.852(3), 2.853 (2)	2.752(3)	2.766(4), 2.762(4) 2.770(4), 2.789(4)

Unlike Ni(dbtaa), the crystal structure of Co(dbtaa) contains one molecule in its asymmetric unit. The molecules are packed in a herringbone motif with short, equidistant 1-D interplanar distances of 3.240 Å. The π-stacking is slipped with the propanediimine linkages overlapping effectively with a short contact of 3.29(2) Å, similar to what is observed in Ni(dbtaa) and Cu(dbtaa) (Figure 3). The geometry around the Co(II) centre is square planar, as expected, with varying Co-N bond lengths of 1.896(11), 1.886(10), 1.836(11) and 1.870(10) Å. The N-Co-N bite angles are 84.7(7) and 87.0(6)°. The short contact between the Co(II) centre and the closest C atom on the adjacent molecules is 3.45(1) Å indicating that a possible axial Co-C interaction could be present.

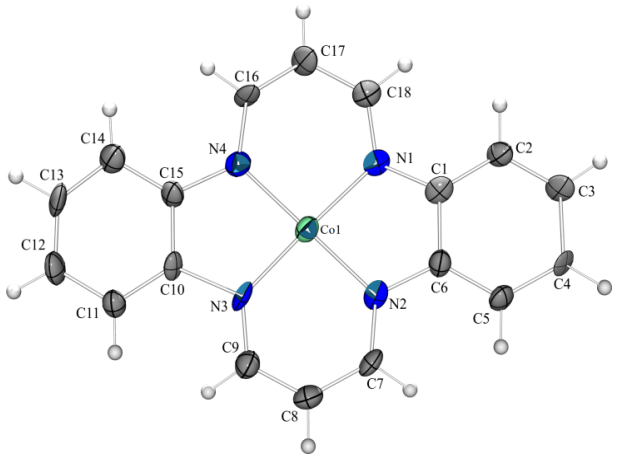

Figure 2 Structure of Co(dbtaa). Displacement ellipsoids are at the 50% probability level.

Unsurprisingly, the crystal structure of Cu(dbtaa) is isomorphous to Ni(dbtaa). The asymmetric unit contains two crystallographically-independent Cu(dbtaa) molecules, with each ligand coordinating Cu(II) in a square planar manner. With regard to the environment around the metal centre, the first Cu(dbtaa) molecule shows Cu-N bonds of 1.926(2) and 1.927(2) Å, with the second molecule displaying Cu-N lengths of 1.927(2) and 1.928(1). These bonds are slightly longer than the Ni-N lengths of 1.869(2) and 1.872(2) Å, and 1.868(2) and 1.871(2) Å reported for Ni(dbtaa).[35] The N-Cu-N bite angles within the diaminobenzene fragment of 84.50(7)° and 84.53(7)° are similar to the 85.25(8)° and 85.16(9)° reported in the case of Ni(dbtaa). Similar to Co(dbtaa), the material crystallises in a herringbone fashion with short 1-D interplanar distances (3.238 Å) (Figure 3, left). The planar, aromatic nature of the complexes combined with the short interplanar distances makes these molecules suitable candidates for study as conducting materials. The molecules are π-stacked in a slipped fashion with the propanediimine linkages overlapping, but with very little overlap of the aromatic rings (Figure 3, right). The short contact between the Cu(II) centre and the closest C atom on the adjacent molecules at 3.468(2) Å is similar to that observed in Co(dbtaa).

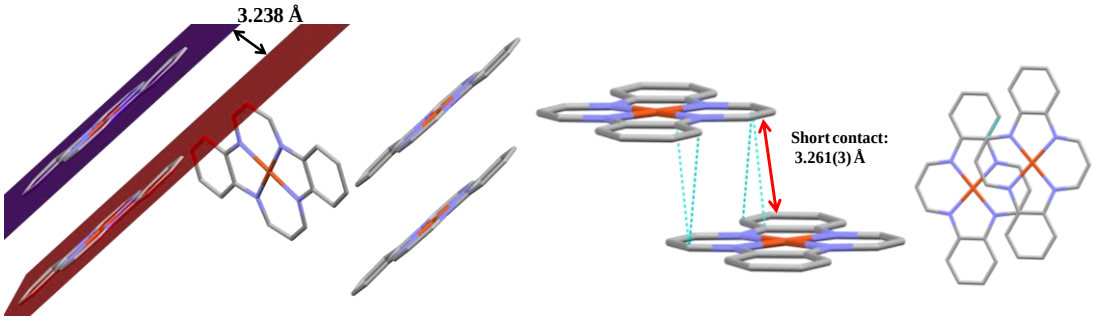

Figure 3 Crystal packing of Cu(dbtaa) showing short interplanar distances (left) and molecular overlap of Cu(dbtaa) as it stacks along the b-axis (right).

From the single crystal structure of Ni(dntaa) (Figure 4) it can be seen that, surprisingly, the increased π-conjugation of the naphthalene ring has resulted in a non-planar structure. This non-planarity has resulted in a larger face-to-face π-stacking distance (~6 Å) but the edge to face π-stacking distance is much shorter (~2.5 Å) (Figure 4, right). The non-planar structure may be a result of crystal packing forces, which have forced the molecule to adopt a twisted geometry to minimise repulsive interactions between naphthalene rings. In contrast to Cu(dbtaa) and Ni(dbtaa), the asymmetric unit of Ni(dntaa) contains only one molecule. The Ni-N distances of 1.866(2) and 1.865(2), as well the N-Ni-N bite angle of 84.98(9)° indicate that the coordination environment around the metal centre is almost identical to what was observed with Ni(dbtaa).

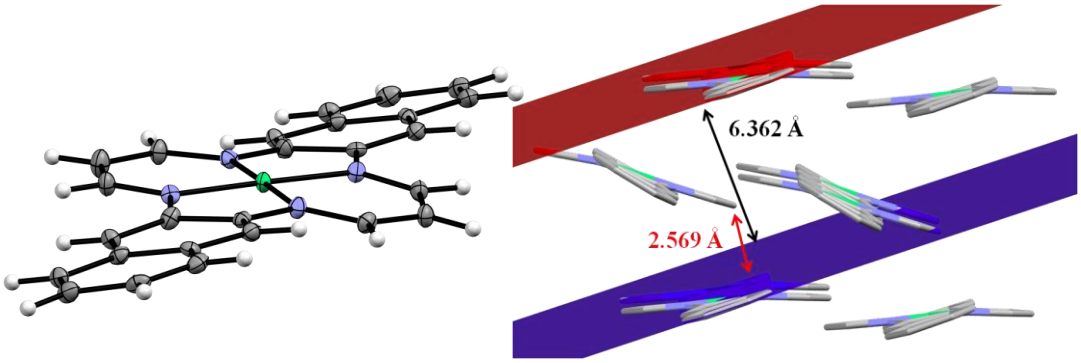

Figure 4 The crystal structure of Ni(dntaa) showing the naphthalene backbone twisted away from the propanediimine bridge (left) and crystal packing of Ni(dntaa) displaying interplanar distances (right).

The structure of Co(dbtaa)Cl is shown below (Figure 5) without the disordered toluene present in the structure. The coordination geometry around the Co(III) centre is square based pyramidal with the chloride ion bound in the axial position. In contrast to Cu(dbtaa) and Ni(dbtaa), it appears that the metal centre in Co(dbtaa) is susceptible to oxidation when left to crystallise in dichloromethane under an air environment over a period of a week. However, when in the solid, powder form Co(dbtaa) is air stable indefinitely. Solvent of crystallisation is also present in the unit cell; in this case toluene is present in a 1:1 ratio with the complex, although the solvent has a high degree of disorder. Since the complexes will be thermally evaporated onto substrates in the absence of solvent, the solid state packing of Co(dbtaa)Cl is not relevant in rationalising the FET performance.

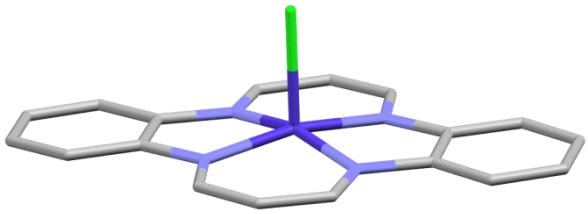

Figure 5 Structure of Co(dbtaa)Cl with solvent of crystallisation omitted. Hydrogens have also been omitted for clarity.

It is evident from each of the crystal structures that, in general, the N-C bonds on the propanediimine bridge are relatively short at ~1.33 Å and contain significant double bond character, but in contrast, the N-C bonds between the donor nitrogen and the aromatic ring (benzo and naphtho) are significantly longer at ~1.41 Å, in most cases (Table 2). Carbon to nitrogen bond lengths of 1.407(3) Å are reported for the free ligand, 1,2-diaminobenzene, and 1.279(8) Å for 1,2-benzoquinone diimine.[36] Related to this, the structure of a bis-ligand 1,2-benzosemiquinone diimine Ni(II) complex is reported to have average N-C bond lengths of 1.38(2) Å and Ni-N bond lengths of 1.832(11),[37] with an analogous bis-naphthosemiquinone diimine Co(II) complex containing N-C bond lengths of 1.360(5) Å and Co-N bond lengths of 1.816 Å.[38] The bond lengths in these complexes are significantly shorter than those observed in the

tetraaza[14]annulene series and indicate that such metal complexes combined with non-innocent ligands give rise to significantly delocalised electronic structures. However, in the tetraaza[14]annulene complexes this nitrogen to carbon (on the aromatic ring) bond appears to be of single bond character. This suggests, that as we expected, we have two separate conjugated units with negligible delocalisation between the aromatic ring and the propanediimine bridge.

4.3.2 Electrochemistry

Despite the poor solubility of these planar molecules, cyclic voltammetry (CV) measurements on dbtaa have previously been reported,[39] with the macrocycle displaying several electrochemically accessible redox processes at -1.77, 0.75 and 1.06 V (vs. saturated calomel reference electrode). However, owing to the poor solubility of the metallated macrocycles we found differential pulse voltammetry (DPV) to be a more useful technique in the study of these materials due to its enhanced sensitivity. The effect of a metal centre on these potentials is shown in Table 3. The differential pulse and cyclic voltammograms are given below (Figures 6 and Figures 7) and in Appendix II (Figure 5-10).

Table 3 Redox potentials as measured by differential pulse from -2 to 1.8 V.

Sample	E_{pc} **(V)**	E_{pa} **(V)**
Co(dbtaa)	-1.07, -1.41, -1.62, -1.89	0.24, 0.79, 1.30, 1.51, 1.73
Cu(dbtaa)	-1.49	0.52, 1.08, 1.41
Ni(dbtaa)	-1.68	0.66, 1.38
Ni(dntaa)	-1.67	0.46, 0.99, 1.72

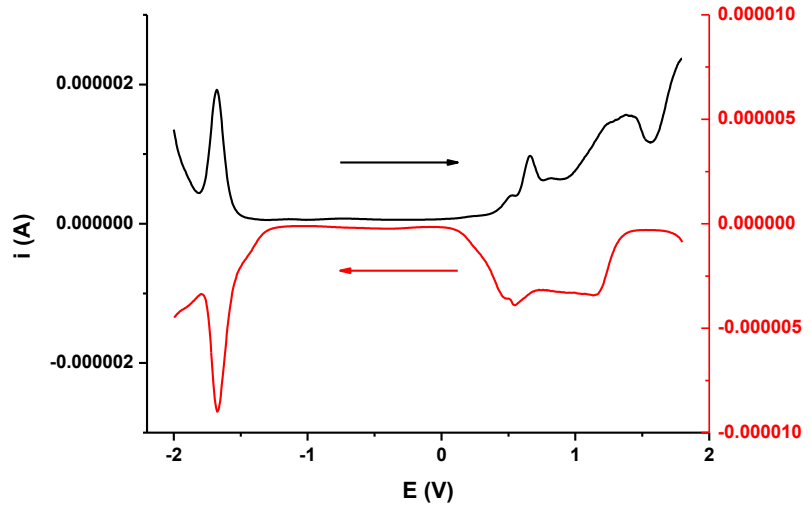

Figure 6 Differential pulse voltammogram of Ni(dbtaa) in 0.3M $TBAPF_6$/DCM.

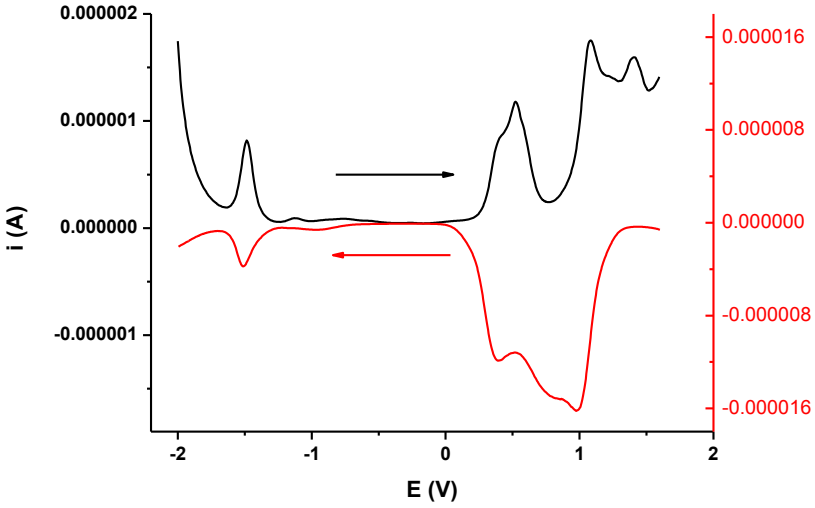

Figure 7 Differential pulse voltammogram of Cu(dbtaa) in 0.3M $TBAPF_6$/DCM.

The cyclic voltammetry analysis of these complexes is hampered by the poor solubility of the macrocyclic complexes, but in the case of Ni(dbtaa), which appears to be the most soluble, some interesting behaviour was observed. When the potential was scanned from 0 to 2 V, 2 to –2 V and then back to 0 V, two oxidations were observed at positive potential, 0.66 and 1.38 V, and one reduction at negative

potential, -1.77 V (Figure 8). On repeating this scan a further four times, the reduction process disappears completely and the first oxidation at 0.66 V grows in intensity. The second oxidation peak changes in shape after the second scan and appears at a less positive potential; at 1.20 V by the fifth scan. This behaviour is indicative of a deposited film forming on the working electrode and this was seen to be the case when the electrode was removed from solution (Figure 8, left). In fact, the electrochemical polymerisation of similar compounds has already been reported.[40, 41] Macrocycles of this type have previously been shown to first dimerise through the meso- position of the propanediimine linkage,[42] before then undergoing further polymerisation under an applied potential. On further studying Ni(dbtaa) in the range –2 to 1 V we found that the oxidation and reduction potentials are largely unchanged, except that the current associated with the reductive process is decreasing (Figure 8, right). The peak potentials still occur in the same position, indicating that when scanning to this less positive potential the sample is not polymerising, and that, although not electrochemically reversible, there is potentially some chemical reversibility associated with the oxidation. The solubility of the other three complexes is lower than that of Ni(dbtaa), making meaningful analysis by CV challenging; peaks appear broad with little definition and small peak current. Therefore, assessment of the reversibility of their redox processes becomes difficult.

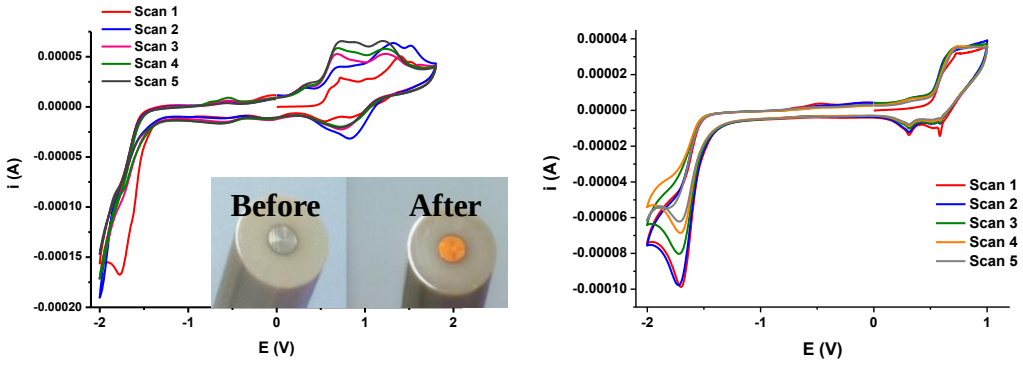

Figure 8 Left: cyclic voltammetry of Ni(dbtaa); five scans were carried out starting from 0 V, sweeping to 2 V then to –2 V, before returning to the initial starting point. Left, inset: Pt working electrode before and after scan. Right: five scans carried out starting from 0 V, sweeping to 1 V then to –2 V, before returning to the initial starting point.

In comparison to the other the complexes, Co(dbtaa) displays many more redox processes when studied using differential pulse voltammetry. This could be partly due to the facile nature of the Co(II) to Co(III) oxidation but the number of additional processes could indicate the complex is decomposing or structurally changing. As shown earlier (Figure 5) it is possible for Co(dbtaa) to be oxidised to Co(dbtaa)Cl in the presence of DCM, thus it is plausible that additional redox processes could be the result of this species also existing in solution.

In summary, each of the materials displays at least two oxidations and one reduction, and these processes appear to be electrochemically and mostly chemically irreversible. The electrochemistry however indicates two important things, Firstly, in each of the complexes, with the exception of Co(dbtaa), the frontier orbitals are predominantly ligand based, shown by the similarity in redox processes between the Cu and Ni examples. Secondly, due to the energies of the frontier orbitals the complexes are more suitable as electron donating materials than electron acceptors in FET devices.

4.3.3 Magnetic susceptibility

Susceptibility measurements were carried out on Cu(dbtaa) and Co(dbtaa) over the temperature range 1.8 – 300 K. The data were fit to the Curie-Weiss law. For Cu(dbtaa), the Curie constant obtained (Appendix, Figure 11) of 0.392 $cm^3\,K\,mol^{-1}$ is in good agreement with that expected for an S=1/2 paramagnet. A small negative Weiss constant of -0.496(6) K was also obtained, suggesting weak antiferromagnetic exchange interactions. Analysis of the crystal packing indicates that the Cu(dbtaa) molecules stack as 1D, linear chains, therefore data were fit to the modified Bonner-Fischer model, appropriate for linear chains of Heisenberg spins ($H = -J\Sigma S_i S_{i+1}$),[43] over the range 1.8-300 K. From the experimental fitting, the following parameters were obtained; g of 2.04(1) and J of -0.4(1) cm^{-1}. The g value deviates from the free

electron value indicating that, as we expect, the unpaired electron is significantly metal based, with the small J value indicating that the intermolecular magnetic interaction is weak, consistent with the Curie-Weiss fit.

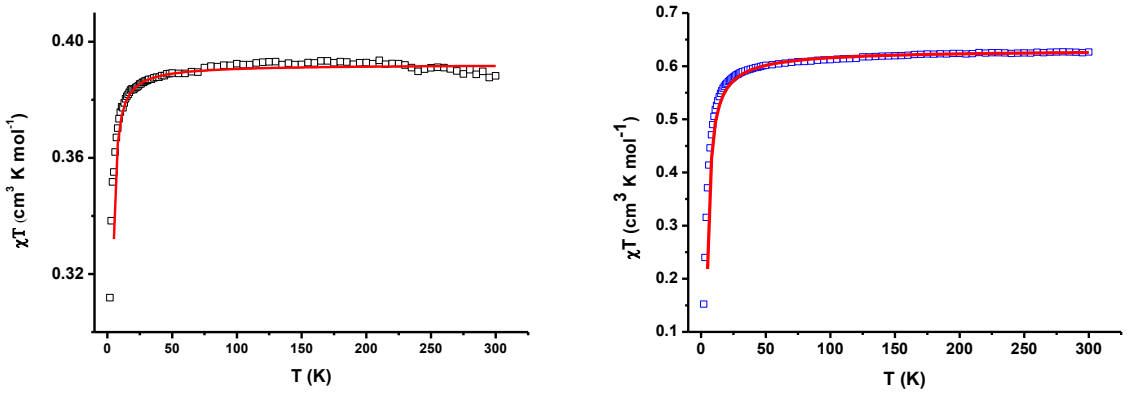

Figure 9 χT vs. T of Cu(dbtaa) in black (left), and Co(dbtaa) in blue (right). The curves of Cu(dbtaa) and Co(dbtaa) have been corrected for temperature independent paramagnetic (TIP) contributions of 3.56 $x10^{-4}$ cm^3 mol^{-1} and 2.61 $x10^{-4}$ cm^3 mol^{-1}, respectively. The solid red lines are the fits to the Bonner-Fisher model for a linear chain of Heisenberg S = ½ centres.

In contrast to the Cu(II) analogue, the Curie-Weiss plot of Co(dbtaa) (Appendix II, Figure 12) gives the Curie constant as 0.639(2) cm^3 K mol^{-1} and the Weiss constant as -3.2(1) K, suggesting the antiferromagnetic exchange interaction is greater than in Cu(dbtaa). Consistent with this, fit to the Bonner-Fisher model also indicates much stronger magnetic coupling with a J value of -2.4(1) cm^{-1} and a g-value of 2.59 within the range expected for Co(II). For an S = ½ ion with g = 2.59, a Curie constant of 0.63 cm^3 K mol^{-1} is predicted, consistent with the Curie-Weiss fit. From computational calculations, in the gas phase (see Section 4.3.4 below), it has been predicted that the unpaired electron of Co(dbtaa) resides predominantly in the dxy orbital, whereas with Cu(dbtaa) the unpaired electron is based in the dx^2-y^2 orbital. It is perhaps surprising that the magnetic exchange interactions differ so greatly, given that in both cases, the SOMO lies in the molecular plane and therefore it could reasonably be expected that similar superexchange interactions should be prevalent.

A stronger interaction between molecules in the Co(II) derivative, which may have some bearing on the magnetic exchange, was noted experimentally during sublimation; much higher temperatures were required to volatilise Co(dbtaa) compared to Cu(dbtaa). Interestingly, in related compounds such as Co(II) phthalocyanine, the unpaired electron has been found to be based predominantly in the dz^2 orbital.[44] If the unpaired electron in our system were based in the dz^2 orbital then axial Co-π interactions would help to rationalise the behaviour we observe.

4.3.4 Computational

Calculations have been used to understand the nature of the frontier orbitals as well as assign the electronic transitions witnessed by absorption spectroscopy. In the case of the dibenzotetraazaannulene (dbtaa) complexes, molecular structures obtained from geometry optimisations at the B3LYP/6-31G(d,p) level of theory were in good agreement with the structures obtained by crystallisation in terms of bond lengths, bond angles and overall planarity of the molecule. With regard to Ni(dbtaa), the electronic structure of the frontier orbitals is depicted in Table 4, indicating the HOMO and LUMO are ligand based π-orbitals. A similar theme is witnessed with Co(dbtaa) and Cu(dbtaa); in both cases the HOMO and LUMO are ligand based π-orbitals, with the unpaired electron residing in a SOMO lower in energy than the ligand based HOMO (Appendix II Tables 1 and 2). In the case of Cu(dbtaa) it is quite clear from the orbital energies and the spin density image that the unpaired electron is based in the dx^2-y^2 orbital (Figure 10), which is the α-HOMO-1 orbital (labelled as α-SOMO) with the corresponding β-SOMO being the β-LUMO+2. An additional study of the electronic structure of Cu(dbtaa) at the UB3LYP/TZVP level (Appendix II, Figure 15) indicates a similar ordering of the filled molecular orbitals, with the energies of the frontier orbitals in reasonable agreement. For Co(dbtaa), the unpaired electron is based in the α-HOMO-1 and the spin density (Appendix II, Figure 14) is metal centred, lying out of the plane of the molecule and in keeping

with the greater magnetic exchange observed for Co(dbtaa) compared with Cu(dbtaa).

Table 4 Ni(dbtaa) and Ni(dntaa) molecular orbitals generated from DFT calculations at the B3LYP/6-31G level of theory with the orbital energy in eV (vs. vacuum) underneath.

Orbital	Ni(dbtaa)	Ni(dntaa)
LUMO+2	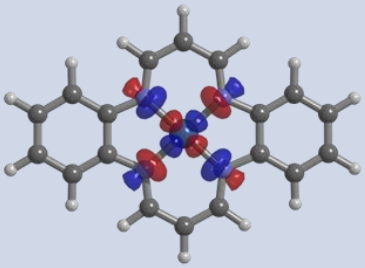 **-0.57**	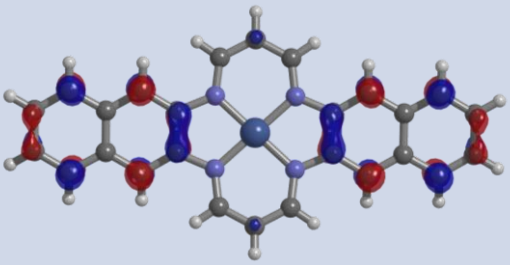 **-0.73**
LUMO+1	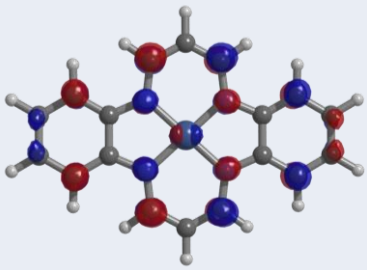 **-1.27**	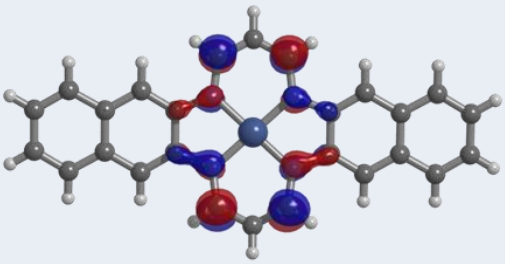 **-1.67**
LUMO	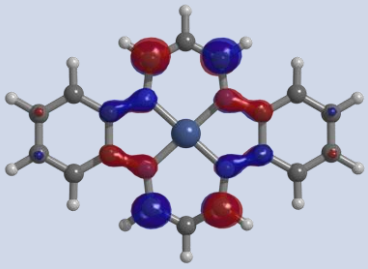 **-1.70**	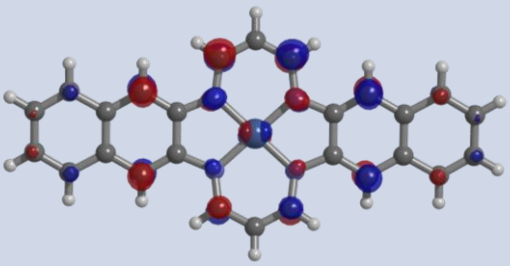 **-1.72**

HOMO	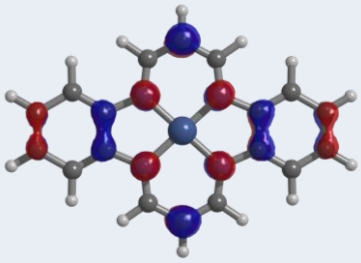 **-4.85**	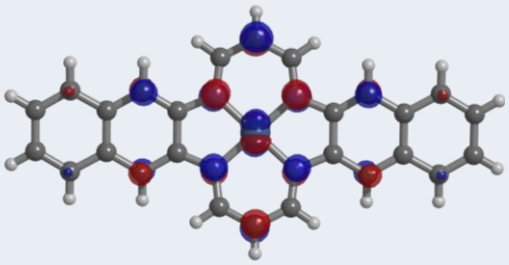 **-4.79**
HOMO-1	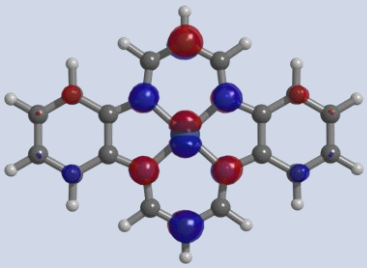 **-5.12**	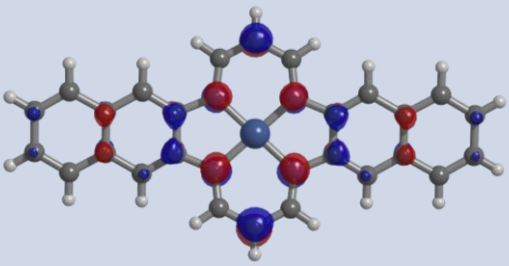 **-4.98**
HOMO-2	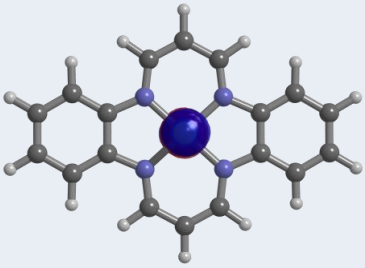 **-5.89**	 **-5.68**
HOMO-3	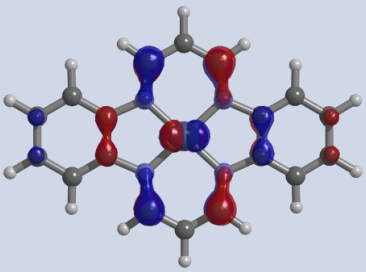 **-5.95**	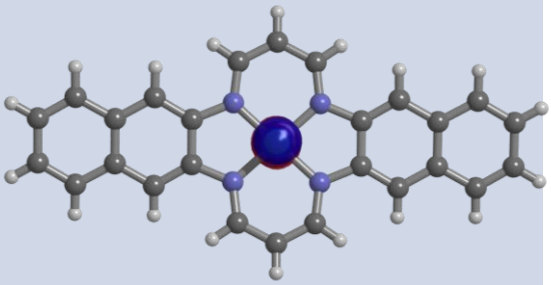 **-5.83**

HOMO-4	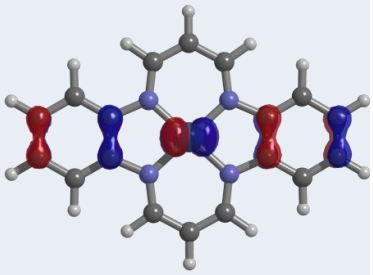 **-6.54**	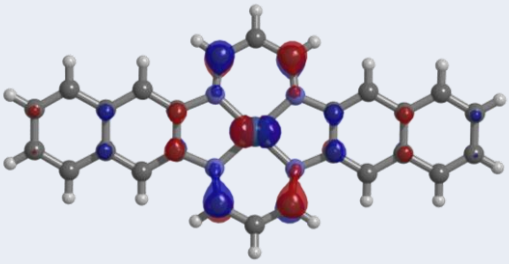 **-5.91**
HOMO-5	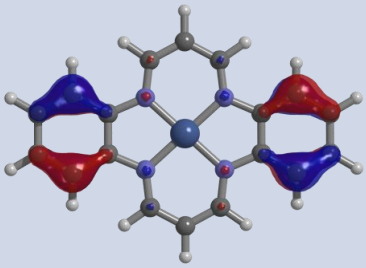 **-6.59**	 **-6.11**
HOMO-6	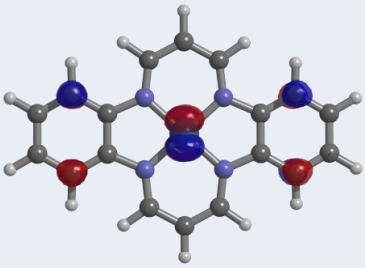 **-6.76**	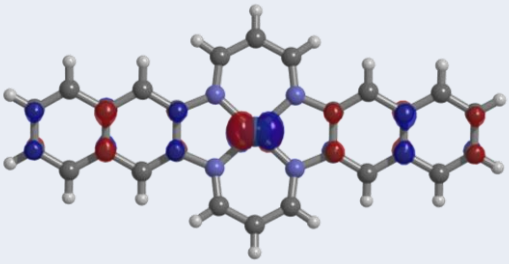 **-6.35**

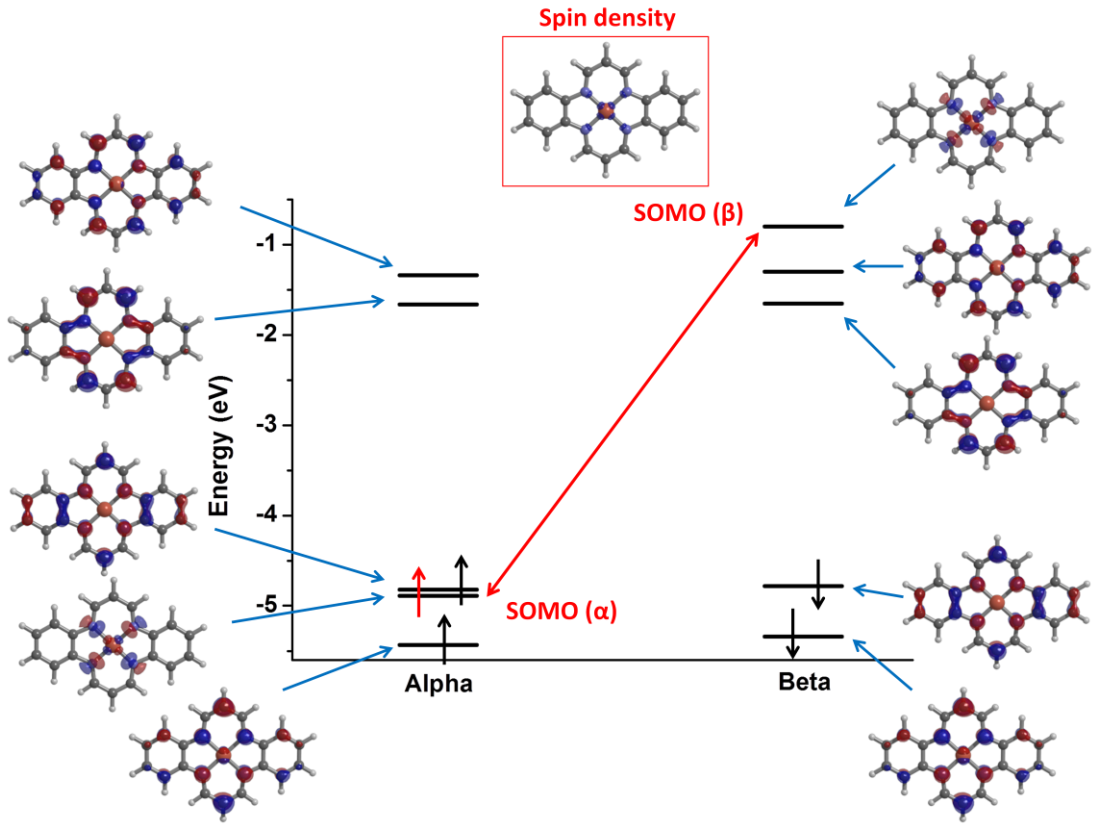

Figure 10 Cu(dbtaa) calculation at the B3LYP/6-31G(d,p) level of theory showing the energies of the frontier orbitals and the spin density.

In the case of the dinaphthotetraazaannulene (dntaa) complex, the optimised geometry varies significantly from that obtained by crystallisation (Appendix II, Figure 13) in terms of planarity, but both conformations, crystallised and geometry optimised, still show excellent agreement when comparing bond lengths and angles. There also appears to be more metal character to the frontier orbitals compared with the dbtaa complexes (Table 4), with both the HOMO and LUMO delocalised across the metal and ligand.

From TD-DFT calculations using the same basis set, the calculated absorption spectrum of Ni(dbtaa) shows good agreement with the experimental data, with regard to peak absorption position and molar absorptivity (Figure 11). From calculations,

the peak absorbance measured at 425 nm (calculated 387 nm) has been assigned to an excitation from the HOMO to LUMO+1 energy level. The peak at 290 nm in the TD-DFT generated spectrum has been assigned as HOMO-6 to LUMO. An assignment of the low energy, high intensity peaks is shown below (Table 5) with a complete assignment of transitions for each of the complexes given in Appendix II, Table 3.

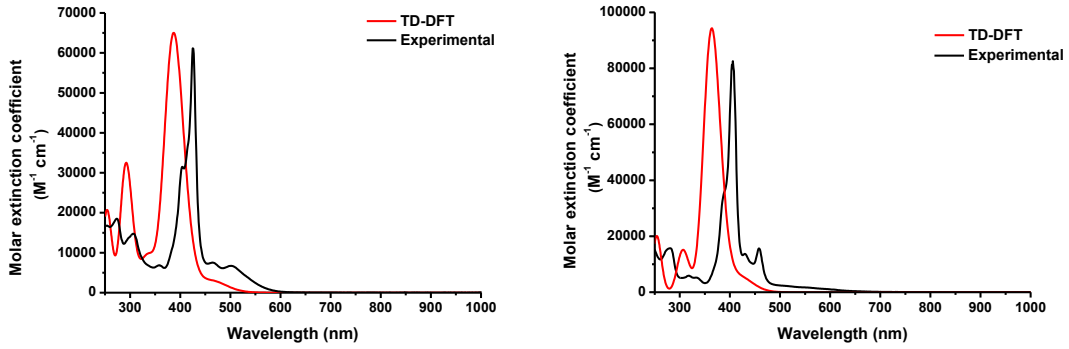

Figure 11 TD-DFT generated spectra (red) overlaid with the experimental plot (black) of Ni(dbtaa) [left] and Cu(dbtaa) [right].

The TD-DFT generated spectrum of Cu(dbtaa) is also in general agreement with the experimental data. The TD-DFT generated spectrum of Co(dbtaa) displays the absorption maxima in the same region as that observed experimentally but the magnitude of the molar extinction coefficient is not well estimated (Appendix II, Figure 16). The experimental value is approximately half the predicted value. It is possible this indicates difficulty in dissolving the complex, leading to an underestimation of the experimental value of the absorption coefficient. This may also apply to Ni(dntaa).

As expected, the absorption spectrum of Ni(dntaa) displays a bathochromic shift when compared to Ni(dbtaa), as a result of the increased conjugation from the naphthalene moiety. Despite the experimental and calculated spectra closely resembling each other in terms of peak position (Appendix II, Figure 17), the molar

extinction coefficient has also been calculated to be larger than the experimental value in the case of Ni(dntaa). The materials all display a similar HOMO-LUMO gap of around 3 eV but since none of these complexes show a direct HOMO-LUMO transition from TD-DFT, it is not possible to estimate the magnitude of this splitting, both in solution and solid state, by absorption spectroscopy. Therefore we should exercise caution when trying to directly compare HOMO-LUMO gaps measured by electrochemical methods with those estimated from absorption spectroscopy.

Table 5 TD-DFT assignment of electronic absorption spectra. Only λ max values are shown. H and L correspond to HOMO and LUMO; A and B correspond to alpha and beta orbitals.

Sample	Measured absorption (nm)	Calculated absorption (nm)	Oscillator strength	Major contribution
Co(dbtaa)	392	345	1.0341	H-1(A)-> L(A) (11%), H(A)-> L+1(A) 13%), H-3(B)->L(B) (51%)
Cu(dbtaa)	406	363	1.3016	H-2(A)-> L(A) (29%), H(A)-> L+1(A) (12%), H-1(B)-> L(B) (22%), H(B)->L+1(B) (15%)
Ni(dbtaa)	425	387	0.8806	HOMO->L+1 (72%)
Ni(dntaa)	452	419	1.5829	H-1->LUMO (67%), HOMO->L+1 (10%)

4.3.5 Thin film X-ray diffraction

The out-of-plane thin film diffraction patterns from each of the dibenzotetraazaannulene metal (II) complexes display a single reflection indicating the thin films are highly ordered. The XRD pattern of Ni(dbtaa) is shown below (Figure 12, left) with the Co(II) and Cu(II) analogues shown in Appendix II (Figure 18 and Figure 19). In the case of Ni(dbtaa) and Cu(dbtaa) the reflection at approximately 9° (2θ) is attributed to the (200) plane (Appendix II, Figure 20), by comparison with the single crystal data. With the Co(dbtaa) complex the peak

observed by thin film XRD is assigned as a reflection coming from the (002) plane. The thin film diffraction pattern for all of these complexes on Si (100) indicates the molecules are stacking edge-on onto the substrate. Assuming that the surface of the Si substrate has oxidised in air over time, we should expect a similar molecular orientation in our FETs, where the gate dielectric is SiO_2. This molecular alignment on the substrate is highly desirable in FET devices, as it means that the 1-D stacking axis is parallel to the substrate facilitating charge transport between the source and drain electrodes (Figure 13).

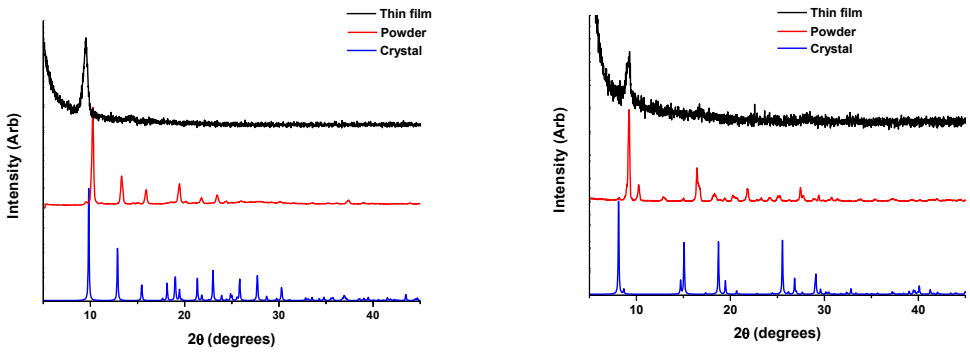

Figure 12 Left: thin film diffraction pattern of Ni(dbtaa) in black, overlaid with the powder pattern (red) and the predicted powder pattern from the single crystal data (blue). Right: Thin film diffraction pattern of Ni(dntaa) in black, overlaid with the powder pattern (red) and the predicted powder pattern from the single crystal data (blue).

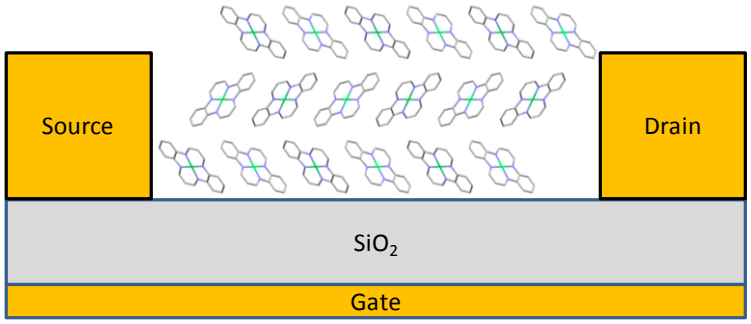

Figure 13 Proposed alignment of molecules stacking "edge on" to the SiO_2 dielectric in a FET device.

Although the diffraction pattern of Ni(dntaa) appears to be ordered with the molecules stacked in a particular orientation, the film is not as crystalline as the films produced by the dibenzo- analogues, judging from the peak width and intensity. Indexing the thin film pattern is not straightforward as both the powder and single crystal patterns exhibit two reflections, corresponding to different planes, very close to one another – the reflection from the thin film sample could correspond to either of these planes. From the single crystal structure, the peak at 8.23° (2θ) corresponds to a reflection from the (110) plane and the peak at 8.73° (2θ) is from the (200) plane (Appendix II, Figure 21). Therefore, elucidating the orientation of the molecules on the substrate is not possible. Note also, comparison between the powder diffraction and the predicted powder pattern from the single-crystal structure of this complex suggests differences in the phase (or phases) present in the powder compared with the single crystal.

4.3.6 Thin film absorption spectroscopy

Films deposited onto quartz substrates were studied by absorption spectroscopy and contrasted with solution measurements to see if any change is witnessed between the spectra obtained from an isolated molecule in solution and the spectra obtained from a solid sample. The solution and film spectra are similar and as expected, each of the thin film spectra displays a significant broadening compared to solution measurements (Figure 14, below and Appendix II, Figures 22 and 23). The lack of any large change indicates intermolecular interactions are relatively weak consistent with a material where weak non covalent interactions are prevalent. Interestingly, in the case of Ni(dntaa) the peak absorbance has red shifted slightly (Figure 14, left), which could indicate the formation of a band like structure resulting from the intermolecular interactions in the thin film. The dibenzotetraaazaannulenes display no such red shifting of the maximum, as illustrated for Cu(dbtaa) in Figure 14 (right), which may indicate the naphthalene ring is increasing the strength of intermolecular interaction in the solid state. Since these films appear to be poorly crystalline from

the thin film XRD results, the bathochromic shift could also be due to the material forming amorphous aggregates in the solid state.

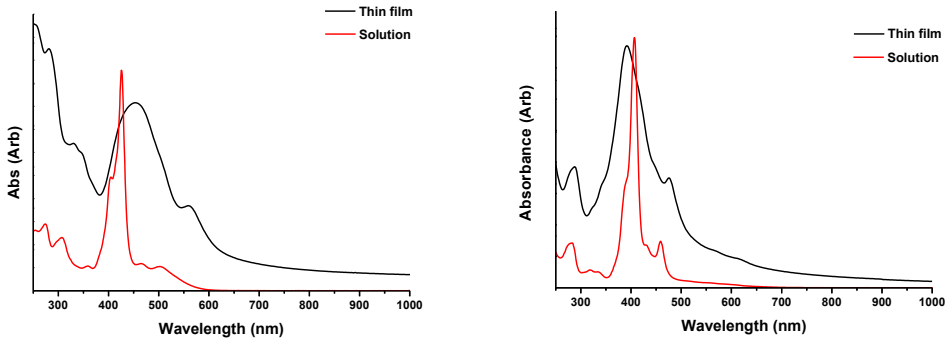

Figure 14 Thin film absorption of Ni(dntaa) [left] and Cu(dbtaa) [right] with solution spectrum overlaid.

4.3.7 Scanning electron microscopy

The micrographs were taken on FET substrates with an electrode width of 2 μm and gap of 8 μm. The image of Ni(dbtaa) (Figure 15, bottom left) indicates a polycrystalline thin film with many grain boundaries between the electrodes; individual crystallites themselves are very small, less than 1 μm. FET measurements were also carried out on substrates with an electrode gap and width of 2 μm so the crystallites themselves are not large enough to bridge the gap between the source and drain.

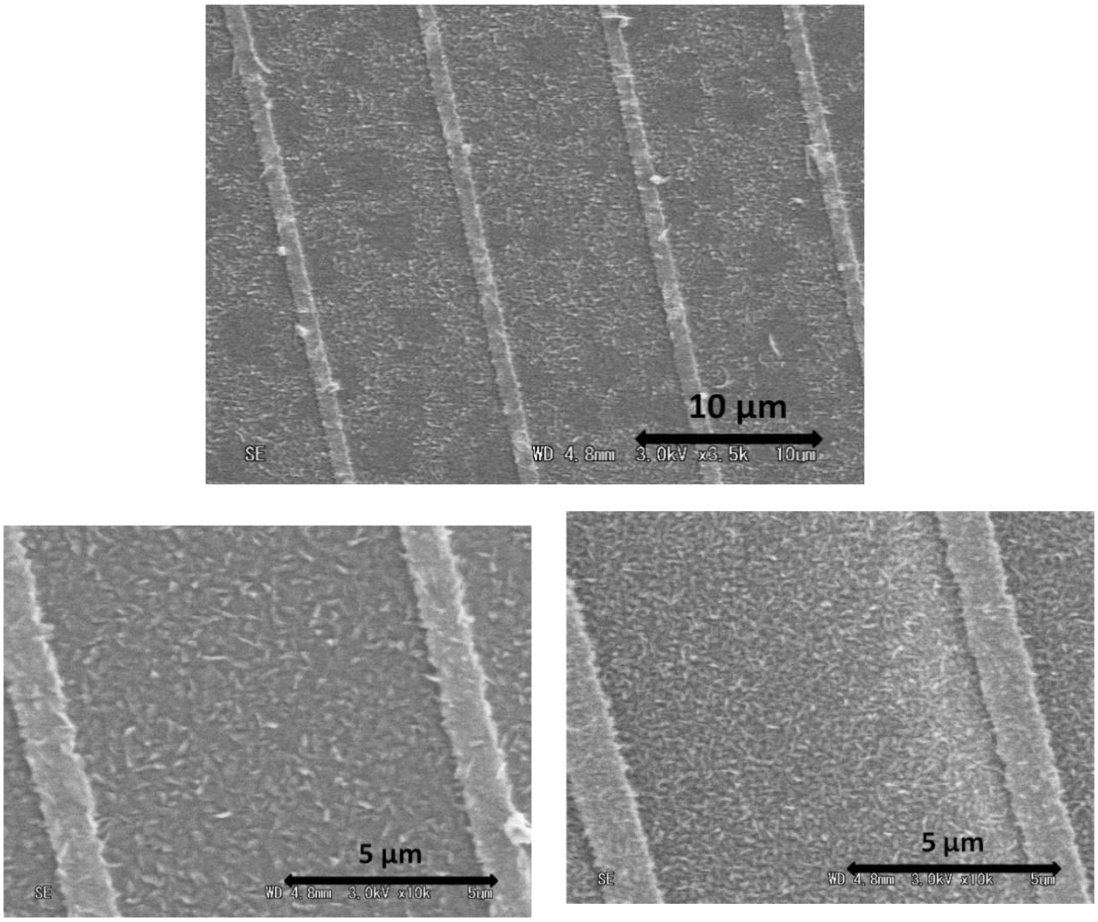

Figure 15 SEM image of Co(dbtaa) (top, centre), Ni(dbtaa) (bottom, left) and Ni(dntaa) (bottom, right) on a SiO_2 substrate with Au electrodes.

Similar to Ni(dbtaa), the thin films of the Co(II) analogue appear to display a polycrystalline morphology consisting of very small crystallites (Figure 15, top). However, this image shows dark islands in amongst the film, possibly indicating the substrate coverage is not homogeneous. Such a discontinuous film is not observed in the micrographs of the other films that were imaged.

Despite several attempts, it was not possible to acquire a satisfactory SEM image of Cu(dbtaa) where the surface morphology could be resolved. The micrograph of Ni(dntaa) (Figure 15, bottom right) shows a crystalline film but, again, the

crystallites are very small, presenting many grain boundaries to the movement of charge carriers.

4.3.8 FET measurements

As expected from the electrochemistry results, each of the four samples is an electron donor and, in keeping with this, we observed hole transport behaviour in a device with gold source and drain electrodes. The hole mobilities have been calculated from the transfer characteristics using Equation 1.

Equation 1 $$\mu = \frac{\partial I_{DS}}{\partial V_{GS}} \left(\frac{L}{Ci\, W\, V_{DS}} \right)$$

The on/off ratios extracted from the transfer characteristics have been taken where the "on" current is the I_D value at V_G= -60 V and the "off" current is I_D at V_G= 0 V. The threshold voltage, at which the FET is effectively switched on, has been estimated by fitting a straight line to the linear regime in the transfer curve and extrapolating the point at which the x-axis is intercepted.

Each of the four complexes studied displays a well-defined gate voltage effect. Ni(dbtaa) and Cu(dbtaa) display similar FET performance with regard to charge carrier mobility. Both values are of the same order of magnitude, but there is a marked difference in the on/off ratio (Table 6). The large difference in on/off ratio is unexplained at present, but could be related to oxygen doping of films; the "on" current of Cu(dbtaa) is an order of magnitude higher than the "on" current observed in Ni(dbtaa). Despite the QCM predicting that the film thickness of each material was approximately 50 nm, profilometry indicates that the thin films of Ni(dbtaa) were ~100 nm and the films of Cu(dbtaa) were ~60 nm (Appendix II, Figure 1 and 3). Since these materials are not intrinsically conducting, it could be possible that if

the Cu(dbtaa) film was less robust to oxygen penetration than that of Ni(dbtaa) then the generation of holes may occur in air more readily.

Unsurprisingly, the transfer curves of Ni(dbtaa) display different values of I_D between the forward and reverse sweeps of V_G (Figure 16, right). Such hysteresis effects are commonly observed in organic field effect transistors and limit their use in integrated organic circuits.[45] The lower back sweep current (BSC) hysteresis observed here is usually attributed to charge carrier trapping at the surface of the dielectric, which can be caused by water and/or oxygen at the surface of the insulating dielectric layer.[46] OH functional groups at the semiconductor/dielectric interface are thought to act as charge traps to the movement of electrons[47, 48] but through the use of SAMs, or dielectrics not containing OH groups, the effects of such traps can be reduced.[46] In addition to reducing hysteresis effects, modified dielectric layers through the use of SAMs have previously been shown to enhance charge carrier mobilities in FETs.[49, 50] Since only wet cleaning of FET substrates was available at the time of study, wide hysteresis loops are expected to be prevalent across all samples but, interestingly, Cu(dbtaa) did not display such obvious hysteresis effects.

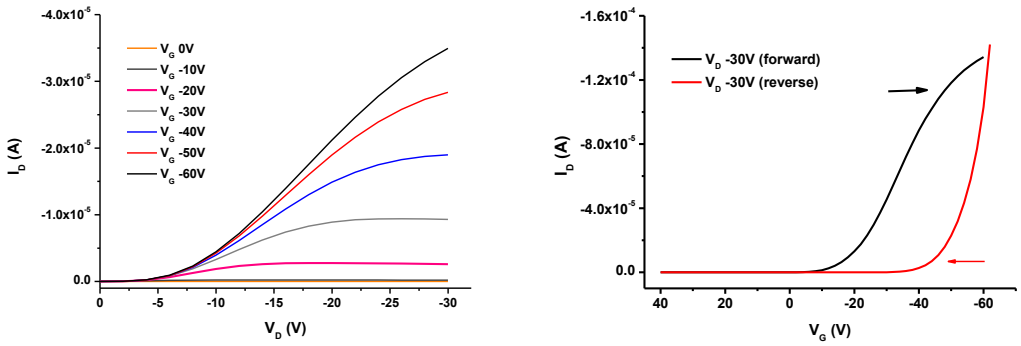

Figure 16 Output characteristics (left) and transfer characteristics (right) of Ni(dbtaa) on 2x2 μm substrates.

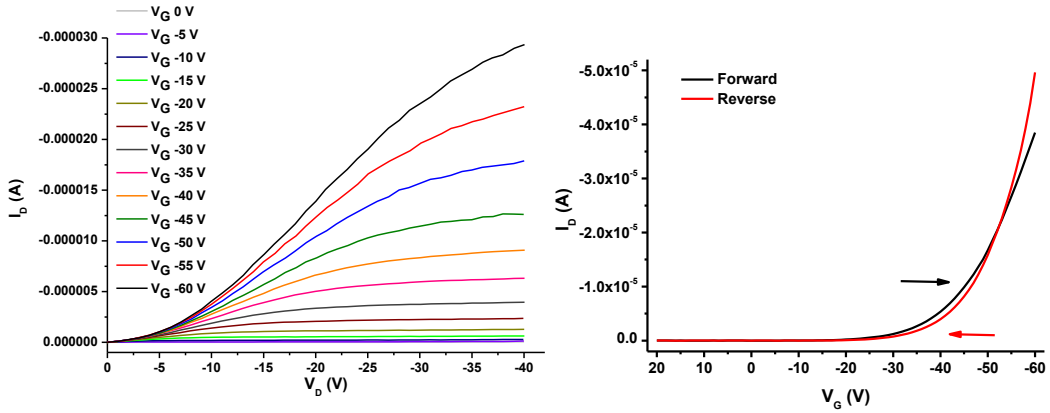

Figure 17 Output characteristics (left) and transfer characteristics (right) of Cu(dbtaa) on 2x2 μm substrates.

Table 6 FET results from measurements carried out on devices with an electrode gap and width of 2 μm. No significant effect on the device performance was observed by increasing the electrode gap to 8 μm.

Sample	***On/off ratio***	***Threshold voltage (V)***	***Mobility (cm^2 V^{-1} s^{-1})***
Co(dbtaa)	96	-12	1.72 x10^{-8}
Cu(dbtaa)	3500	-26	1.55 x10^{-5}
Ni(dbtaa)	21,000	-19	2.57 x10^{-5}
Ni(dntaa)	560	-14	4.79 x10^{-9}

In comparison, the mobilities of Co(dbtaa) and Ni(dntaa) are much lower, with the key parameters illustrated in Table 6. The poor performance of Ni(dntaa) can be explained by the weak face-to-face π-stacking in the solid state, with the resulting large interplanar distance affecting the charge carrier mobility. The thin films produced from this material appear to be poorly crystalline compared with the dibenzo (dbtaa) analogues, which could also explain the low mobility as crystal boundaries or structural inhomogeneity can result in traps to the movement of charge carriers.[51, 52] The large difference in the mobility and on/off ratio of Co(dbtaa) compared with its isostructural Cu(II) and Ni(II) analogues may simply be due to incomplete surface coverage between the source and drain electrodes of the FET (Figure 15, top centre), which may have resulted from the different deposition temperatures required to volatilise Co(dbtaa). The Co(II) complex displays a well-defined gate effect judging from the output characteristics (Figure 18, right), but

unlike the Cu and Ni analogues, the source-drain current never reaches saturation. It is well known for FETs with a small source-drain gap to suffer from short channel effects, most notably, an inability of the source-drain current to saturate.[53, 54] However, short channel effects cannot be the reason here as the saturation regime is observed in the study of Cu(dbtaa), Ni(dbtaa) and Ni(dntaa) using the same device configuration.

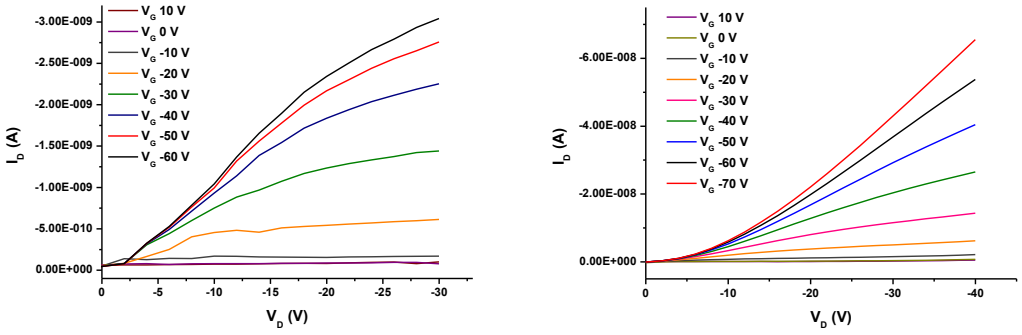

Figure 18 Output characteristics of Ni(dntaa) [left] and Co(dbtaa) [right] on 2x2 μm substrates.

Magnetoresistance measurements were carried out on the Cu(dbtaa) sample at cryogenic temperatures but the conductivity of Co(dbtaa) was too poor to study at low temperatures, since conductivity in organic semiconductor systems is usually thermally activated. A constant gate voltage, along with a source-drain voltage, was applied to the Cu(dbtaa) sample as the source-drain current was measured. In the absence of an applied gate potential the material fails to conduct a measurable source-drain current. The IV characteristics of Cu(dbtaa) were studied at various temperatures down to 4.35 K under a magnetic field swept between 5 T and -5T. However, no significant magnetoresistance was witnessed. At 4.35 K a small positive magnetoresistance (Figure 19) was observed but this was attributed to Lorentz forces from the magnetic field scattering the charge carriers flowing perpendicular to the field, as opposed to an intrinsic material property.

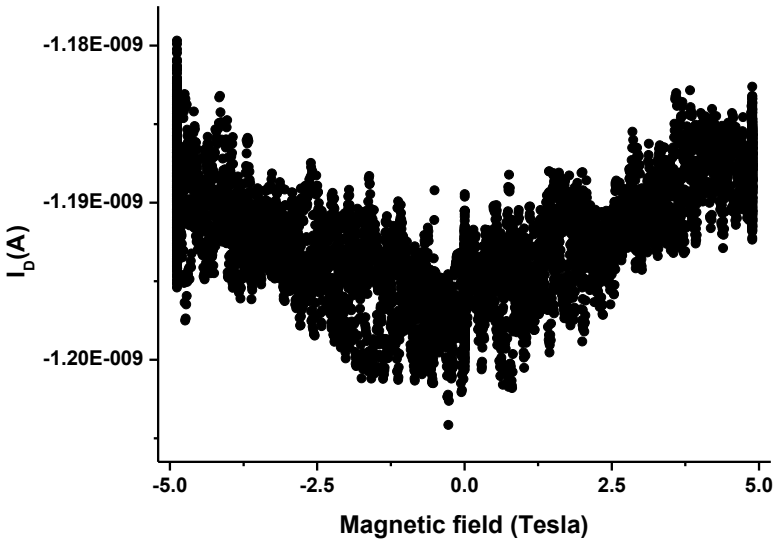

Figure 19 Magnetoresistance measurement on Cu(dbtaa) at 4.35 K when applying a gate voltage of -60 V and a drain voltage of -40 V while sweeping the magnetic field from -5 to 5 T.

4.4 Conclusions

We have prepared a series of planar Ni, Cu and Co tetraaza[14]annulene macrocyles and have carried out the first assessment of these porphyrin analogues in thin-film devices. As discussed earlier (Section 4.3.1), it is evident from analysis of the single crystal structures that there appears to be insufficient delocalisation between the benzo or naphtho rings and the propanediimine bridges. The "break" in conjugation at this position, between the donor nitrogen atom and the aromatic ring, may also help to explain why we observed a twisted structure in the case of Ni(dntaa). However, despite tetraaza[14]annulene macrocyles lacking a completely delocalised electron structure, each of the complexes exhibit p-type semiconductivity with a gate effect in an FET configuration. From inspection of the crystal packing, it is apparent that each of the dbtaa complexes π-stacks in a slipped manner but with effective overlap of the propanediimine bridges with the benzo rings, extending along the *b*-axis. If we assume that this packing exists between the source and drain electrodes in an FET - which it is suggested to from thin film XRD analysis - then a 1D pathway exists through which the charge carrier can propagate along as far as the crystallite or single crystal exists.

The thin films formed are highly ordered as demonstrated by thin film XRD, however, the hole mobilities are low. The failure of these materials to achieve FET mobilities similar to fully delocalised macrocycles, such as porphyrins and phthalocyanines, may be expected as a consequence of the lack of delocalisation inherent in the tetraaza[14]annulene structure. Additionally, the poor performance can also be rationalised by examination of the SEM images, which indicate polycrystalline films with many grain boundaries. Accordingly, improvement of the film crystallinity is likely to lead to much enhanced FET performance and this provides an area for future study using modified tetraaza[14]annulene ligands, or existing tetraaza[14]annulene ligands coupled with device modification. Following these initial promising results, device performance may be optimised by further

studies involving surface modifying treatments to enhance the crystallite size and reduce the negative effects of oxygen and water on the dielectric layer of the FET. It is highly likely that ozone cleaning of the SiO_2 dielectric coupled with a non-polar surface treatment, such as HMDS or OTS, will produce much improved FET performance, with respect to the charge carrier mobility and a reduction in hysteresis effects. Other strategies to realising enhanced performance may involve ligand modification to tune the electronic properties and/or the associated film-forming abilities of the compound. Additionally, the preparation of soluble analogues would allow for the preparation of films by solution deposition methods, and would offer an interesting comparison with films of analogous complexes grown by vacuum deposition in terms of morphology and device performance. Another potential avenue to explore may include electropolymerisation directly onto an FET; the cyclic voltammetry analysis showed that it was possible to grow orange polymeric films of Ni(dbtaa) by applying a potential greater than 1.4 V (vs Ag/AgCl). Scanning beyond the second oxidation potential may give rise to the fully aromatic 14π electron Huckel (4n+2) complex.[42, 55] The conducting properties of these materials as conjugated polymers may provide an alternative to the study of the conducting properties of the 16π electron anti-aromatic (4n) molecular material deposited by PVD or spin coating.

Variation of the central metal has a marked impact on the resulting FET properties. The key influence of the metal is in influencing the sublimation temperature and the resulting film morphology. The different compounds necessitate slightly different deposition conditions due to their different solid-state interactions, leading to different degrees of crystallinity in the films, even for isomorphous materials. Due to the dominant effect of the film morphology, it is difficult to directly compare the role of the central metal between analogous complexes in terms of its electronic influence. Such a study would require comparison of single crystal FET results or films of consistent morphology. Given however, the consistent observation of gate-modulated transport across this series despite the non-ideal film characteristics, these

complexes provide an interesting alternative to porphyrins in the study of metal complexes in FETs, with potential also in other electronic and optical devices.

4.5 References

1. Zhang, Y.; Cai, X.; Bian, Y.; Jiang, J., Organic Semiconductors of Phthalocyanine Compounds for Field Effect Transistors (FETs) Functional Phthalocyanine Molecular Materials. In Springer Berlin / Heidelberg: 2010; Vol. 135, pp 275-321.
2. Garnier, F.; Peng, X.; Horowitz, G.; Fichou, D., *Molecular Engineering* **1991,** *1*, 131-139.
3. Bao, Z.; Lovinger, A. J.; Dodabalapur, A., *Applied Physics Letters* **1996,** *69*, 3066-3068.
4. Ma, P.; Chen, Y.; Cai, X.; Wang, H.; Zhang, Y.; Gao, Y.; Jiang, J., *Synthetic Metals* **2010,** *160*, 510-515.
5. Hohnholz, D.; Steinbrecher, S.; Hanack, M., *Journal of Molecular Structure* **2000,** *521*, 231-237.
6. Kim, H.-S.; Wamser, C. C., *Photochemical & Photobiological Sciences* **2006,** *5*, 955-960.
7. Martinez-Diaz, M. V.; de la Torre, G.; Torres, T., *Chemical Communications* **2010,** *46*, 7090-7108.
8. Minari, T., *Appl. Phys. Lett.* **2007,** *91*, 123501.
9. Hoang, M. H.; Kim, Y.; Kim, S.-J.; Choi, D. H.; Lee, S. J., *Chemistry – A European Journal* **2011,** *17*, 7772-7776.
10. Chaure, N. B.; et al., *Science and Technology of Advanced Materials* **2011,** *12*, 025001.
11. Liqiang Li; Qingxin Tang; Hongxiang Li; Wenping Hu; Xiaodi Yang; Zhigang Shuai; Yunqi Liu; Zhu, D., *Pure Appl. Chem.* **2008,** *80*, 2231–2240.
12. Plyashkevich, V.; Basova, T.; Yushina, I.; Igumenov, I., *Journal of Surface Investigation: X-ray, Synchrotron and Neutron Techniques* **2008,** *2*, 423-428.
13. Basova, T.; Kol'tsov, E.; Hassan, A.; Tsargorodskaya, A.; Ray, A.; Igumenov, I., *physica status solidi (b)* **2005,** *242*, 822-827.
14. Puigdollers, J.; Voz, C.; Fonrodona, M.; Cheylan, S.; Stella, M.; Andreu, J.; Vetter, M.; Alcubilla, R., *Journal of Non-Crystalline Solids* **2006,** *352*, 1778-1782.
15. Mountford, P., *Chemical Society Reviews* **1998,** *27*, 105-116.
16. Bell, L. G.; Dabrowiak, J. C., *Journal of the Chemical Society, Chemical Communications* **1975**, 512-513.
17. Lukes, P. J.; Crayston, J. A.; Ando, D. J.; Harman, M. E.; Hursthouse, M. B., *Journal of the Chemical Society, Perkin Transactions 2* **1991**, 1845-1849.
18. Lin, L.-S.; Marks, T. J.; Kannewurf, C. R.; Lyding, J. W.; McClure, M. S.; Ratajack, M. T.; Whang, T.-C., *Journal of the Chemical Society, Chemical Communications* **1980**, 954-955.
19. Cutler, A. R.; Alleyne, C. S.; Dolphin, D., *Inorganic Chemistry* **1985,** *24*, 2276-2281.
20. Hiller, H.; Dimroth, P.; Pfitzner, H., *Justus Liebigs Annalen der Chemie* **1968,** *717*, 137-147.

21. Wille, F.; Saffer, L.; Weißkopf, W., *Justus Liebigs Annalen der Chemie* **1950,** *568*, 34-46.
22. Taylor, R.; Macrae, C. F., *Acta Crystallographica Section B* **2001,** *57*, 815-827.
23. Bruno, I. J.; Cole, J. C.; Edgington, P. R.; Kessler, M.; Macrae, C. F.; McCabe, P.; Pearson, J.; Taylor, R., *Acta Crystallographica Section B* **2002,** *58*, 389-397.
24. Macrae, C. F.; Bruno, I. J.; Chisholm, J. A.; Edgington, P. R.; McCabe, P.; Pidcock, E.; Rodriguez-Monge, L.; Taylor, R.; van de Streek, J.; Wood, P. A., *Journal of Applied Crystallography* **2008,** *41*, 466-470.
25. Macrae, C. F.; Edgington, P. R.; McCabe, P.; Pidcock, E.; Shields, G. P.; Taylor, R.; Towler, M.; van de Streek, J., *Journal of Applied Crystallography* **2006,** *39*, 453-457.
26. Bain, G. A.; Berry, J. F., *Journal of Chemical Education* **2008,** *85*, 532.
27. Becke, A. D., *J. Chem. Phys.* **1993,** *98*, 5648-5652.
28. Lee, C.; Yang, W.; Parr, R. G., *Phys. Rev. B* **1988,** *37*, 785-789.
29. Ditchfield, R.; Hehre, W. J.; Pople, J. A., *The Journal of Chemical Physics* **1971,** *54*, 724-728.
30. Frisch, M. J.; Trucks, G. W.; Schlegel, H. B.; Scuseria, G. E.; Robb, M. A.; Cheeseman, J. R.; Montgomery, J. A.; Vreven, T.; Kudin, K. N.; Burant, J. C.; Millam, J. M.; Iyengar, S. S.; Tomasi, J.; Barone, V.; Mennucci, B.; Cossi, M.; Scalmani, G.; Rega, N.; Petersson, G. A.; Nakatsuji, H.; Hada, M.; Ehara, M.; Toyota, K.; Fukuda, R.; Hasegawa, J.; Ishida, M.; Nakajima, T.; Honda, Y.; Kitao, O.; Nakai, H.; Klene, M.; Li, X.; Knox, J. E.; Hratchian, H. P.; Cross, J. B.; Bakken, V.; Adamo, C.; Jaramillo, J.; Gomperts, R.; Stratmann, R. E.; Yazyev, O.; Austin, A. J.; Cammi, R.; Pomelli, C.; Ochterski, J. W.; Ayala, P. Y.; Morokuma, K.; Voth, G. A.; Salvador, P.; Dannenberg, J. J.; Zakrzewski, V. G.; Dapprich, S.; Daniels, A. D.; Strain, M. C.; Farkas, O.; Malick, D. K.; Rabuck, A. D.; Raghavachari, K.; Foresman, J. B.; Ortiz, J. V.; Cui, Q.; Baboul, A. G.; Clifford, S.; Cioslowski, J.; Stefanov, B. B.; Liu, G.; Liashenko, A.; Piskorz, P.; Komaromi, I.; Martin, R. L.; Fox, D. J.; Keith, T.; Laham, A.; Peng, C. Y.; Nanayakkara, A.; Challacombe, M.; Gill, P. M. W.; Johnson, B.; Chen, W.; Wong, M. W.; Gonzalez, C.; Pople, J. A., Gaussian 03, Revision E.01. In *Gaussian, Inc., Wallingford CT*, Wallingford CT, 2004.
31. Thompson, M. A. *ArgusLab 4.0.1*, Planaria Software LLC: Seattle, WA.
32. Du, B.; Harvey, P. D., *Chemical Communications* **2012,** *48*, 2671-2673.
33. Kang, M. S.; Kang, S. H.; Kim, S. G.; Choi, I. T.; Ryu, J. H.; Ju, M. J.; Cho, D.; Lee, J. Y.; Kim, H. K., *Chemical Communications* **2012,** *48*, 9349-9351.
34. Walter, M. G.; Rudine, A. B.; Wamser, C. C., *Journal of Porphyrins and Phthalocyanines* **2010,** *14*, 759-792.
35. Weiss, M. C.; Gordon, G.; Goedken, V. L., *Inorganic Chemistry* **1977,** *16*, 305-310.
36. Carugo, O.; Djinovic, K.; Rizzi, M.; Castellani, C. B., *Journal of the Chemical Society, Dalton Transactions* **1991**, 1551-1555.
37. Hall, G. S.; Soderberg, R. H., *Inorganic Chemistry* **1968,** *7*, 2300-2303.
38. Liaw, D.-S.; Peng, S.-M.; Chern, S.-S.; Sheu, S.-C., *Acta Crystallographica Section C* **1986,** *42*, 402-404.

39. Lukes, P. J.; McGregor, A. C.; Clifford, T.; Crayston, J. A., *Inorganic Chemistry* **1992,** *31*, 4697-4699.
40. Hochgesang, P. J.; Bereman, R. D., *Inorganica Chimica Acta* **1988,** *149*, 69-76.
41. Miry, C.; Le Brun, D.; Kerbaol, J.-M.; L'Her, M., *Journal of Electroanalytical Chemistry* **2000,** *494*, 53-59.
42. McElroy, F. C.; Dabrowiak, J. C., *Journal of the American Chemical Society* **1976,** *98*, 7112-7113.
43. Estes, W. E.; Gavel, D. P.; Hatfield, W. E.; Hodgson, D. J., *Inorganic Chemistry* **1978,** *17*, 1415-1421.
44. Assour, J. M.; Kahn, W. K., *Journal of the American Chemical Society* **1965,** *87*, 207-212.
45. Kim, S. H.; Jang, J.; Jeon, H.; Yun, W. M.; Nam, S.; Park, C. E., *Applied Physics Letters* **2008,** *92*, 183306-183306-3.
46. Egginger, M.; Bauer, S.; Schwödiauer, R.; Neugebauer, H.; Sariciftci, N., *Monatshefte für Chemie / Chemical Monthly* **2009,** *140*, 735-750.
47. Lee, S.; Koo, B.; Shin, J.; Lee, E.; Park, H.; Kim, H., *Applied Physics Letters* **2006,** *88*, 162109-3.
48. Chua, L.-L.; Zaumseil, J.; Chang, J.-F.; Ou, E. C. W.; Ho, P. K. H.; Sirringhaus, H.; Friend, R. H., *Nature* **2005,** *434*, 194-199.
49. Salleo, A.; Chabinyc, M. L.; Yang, M. S.; Street, R. A., *Applied Physics Letters* **2002,** *81*, 4383-4385.
50. Lim, S. C.; Kim, S. H.; Lee, J. H.; Kim, M. K.; Kim, D. J.; Zyung, T., *Synthetic Metals* **2005,** *148*, 75-79.
51. Kaake, L. G.; Barbara, P. F.; Zhu, X. Y., *The Journal of Physical Chemistry Letters* **2010,** *1*, 628-635.
52. Tello, M.; Chiesa, M.; Duffy, C. M.; Sirringhaus, H., *Advanced Functional Materials* **2008,** *18*, 3907-3913.
53. Haddock, J. N.; Zhang, X.; Zheng, S.; Zhang, Q.; Marder, S. R.; Kippelen, B., *Organic Electronics* **2006,** *7*, 45-54.
54. Hirose, T.; Nagase, T.; Kobayashi, T.; Ueda, R.; Otomo, A.; Naito, H., *Applied Physics Letters* **2010,** *97*, 083301.
55. Davies, D. L.; Grist, A. J., *Inorganica Chimica Acta* **1994,** *216*, 217-221.

Chapter 5: Thiadiazole Macrocycles

5.1 Introduction

Phthalocyanine (Pc) molecules exhibit strong, 1D π-stacking interactions but intercolumnar interactions are thought to be impeded by the terminal hydrogens on the benzo rings.[1] Thiadiazole functionalised phthalocyanine macrocycles, such as tetrakis(1,2,5-thiadiazole)porphyrazine (Figure 1), have been previously synthesised and shown to form highly ordered 2D structures in the solid state.[2, 3] The 2D order is a result of strong π-π overlap and short S...N interactions projected in different crystallographic axes. Such multidimensional interactions are highly desirable for conducting applications as they give rise to multiple pathways in the film or crystal through which the hole or electron can propagate.

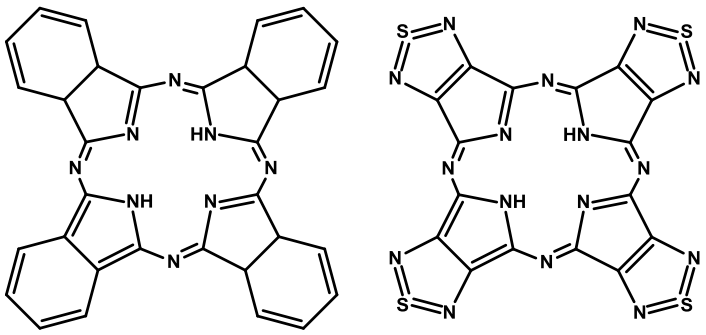

H_2Pc **H_2TTDPz**

Figure 1 Structures of metal free phthalocyanine (H_2Pc) and metal free tetrakis(1,2,5-thiadiazole)porphyrazine (H_2TTDPz).

Another interesting aspect of thiadiazole functionalised phthalocyanines is the effect they have on the energy of the LUMO. Compounds such as H_2Pc and CuPc

typically give p-type semiconductors.[4] However, previous studies on fluorinated phthalocyanines demonstrated that by addition of an electron withdrawing group to the periphary of the macrocycle, the energy of the LUMO can be lowered such that n-type conductivity is realised.[5] The energy barrier between this orbital and the work function of the electrode becomes small enough to allow electrons to be injected into the active semiconducting layer. In the case of H_2TTDPz it has been observed that the electron withdrawing nature of the thiadiazole ring also gives rise to n-type conductivity in an FET,[6] with mobilities as high as 0.001 $cm^2V^{-1}s^{-1}$ in some cases.[7]

In the course of this work, we have synthesised a dibenzotetraazaaanulene analogue, replacing the benzo groups with thiadiazole moieties to try to enhance the intermolecular interactions prevalent in the solid state. The synthesis of similar molecules, with alkyl, hydroxypropyl and ethoxycarbonyl substituents in the 6- and 13- positions, has previously been reported in one publication but no structural data were reported due to their low solubility.[8] However, no comment is made on the volatility of these complexes. It is hoped that by incorporating this heterocyclic ring multidimensional order can be achieved in these dithiadiazoletetraazaannulene macrocycles through supramolecular interactions such as S...S, S...N, π-π etc. The compounds prepared for this study are illustrated in Figure 2; various unsubstituted macrocycles were prepared, M(dttaa), but the poor solubility of these compounds limited the processing methods available to us. Thus, attempts to improve their solubility were made through functionalisation of the propanediiminato bridge, Ni(dttaaMe_4), and at the meso (6- and 13-) positions of the macrocycle, Ni(dttaaBzOR).

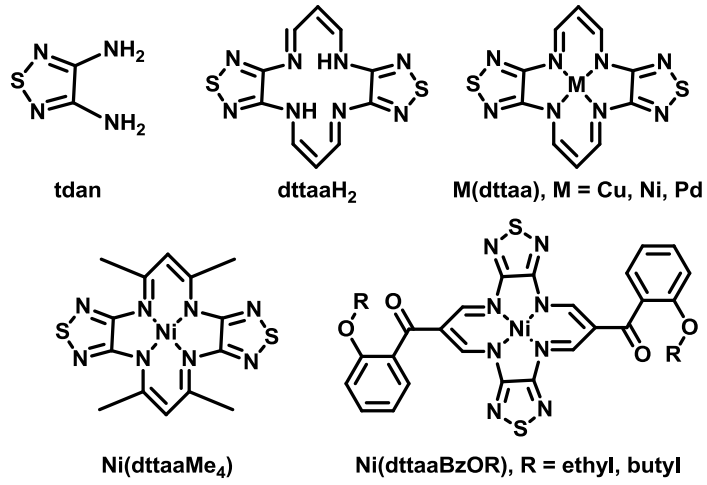

Figure 2 The molecules discussed in this chapter with their abbreviations inset.

5.2 Experimental

5.2.1 Synthesis

The starting materials 3,4-dichloro-1,2,5-thiadiazole (97%), propargyl alcohol (99%), 3-formylchromone (97%) and acetylacetone (≥99%) were purchased from Sigma-Aldrich and used without further purification.

3,4-Diamino-1,2,5-thiadiazole (tdan)

The synthesis was modified from a literature procedure with hydrazine monohydrate being used to hydrolyse the 3,4-diphthalimidothiadiazole product in the second step, as opposed to ammonia gas.[9] Potassium phthalimide (52.97 g, 0.29 mols) was heated at 100 °C with 3,4-dichlorothiadiazole (20.15 g, 0.13 mol) in dry DMF (500 ml) under an atmosphere of nitrogen for 1 hour. During that time the reaction mixture changed colour from a cloudy white suspension to a dark red solution. The reaction mixture was then cooled to RT and poured into water (1 l), causing a yellow/white solid to precipitate. The solid was collected by

filtration and washed by stirring in acetone (200ml) before refiltering. The cream white solid was then dried under vacuo (25.04 g, 51.19 % yield). The 3,4-diphthalimidothiadiazole product (25.04 g, 0.067 mol) was then refluxed in ethanol (600 ml) with hydrazine monohydrate (20 g, 0.4 mol) for 1.5 hours. After this period the solution was filtered hot and the white filter cake washed with ethanol (2x100 ml). The filtrates were concentrated under vacuo to yield a yellow precipitate (6.71 g). The precipitate was then purified by sublimation at 140 °C under a vacuum of ~2 $x10^{-2}$ mbar, to yield the desired product as a white crystalline solid with a faint yellow tinge (5.29 g, 67.98 % yield). Single crystals were grown by slow evaporation of a 1:1 ethanol/water solution. MS (EI): m/z (%) = 116.0 (64.32%) [M^+]. ^{1}H NMR ($(CD_3)_2SO$): δ (ppm) = 6.30 (s). ^{13}C NMR ($(CD_3)_2SO$): δ (ppm) = 149.51 (s). Calculated for $C_2H_4N_4S$, C 20.68, H 3.47, N 48.24; found C 20.77, H 3.38, N 48.18.

Dihydrodithiadiazoletetraaza[14]annulene (H_2dttaa)

To a stirring solution of 3,4-diamino-1,2,5-thiadiazole (940 mg, 8.1 mmol) in MeOH/DMF (1:1, 4 ml) was added propargylaldehyde (0.31 ml, 8.1 mmol) dropwise. The reaction mixture was refluxed for 1 hour before being cooled to RT. The brown product was precipitated by addition of MeOH (5 ml) and collected by filtration (171 mg, 13.8 % yield). MS (EI): m/z (%) = 364.9 (100.00%) [M^+], 366.9 (54.39%), 365.9 (15.38%). Calculated for $C_{10}H_8N_8S_2$, C 39.46, H 2.65, N 36.82; found C 37.73, H 1.91, N 30.47. Melting point: >360°C.

Synthesis of Cu and Ni dithiadiazoletetraazaannulene [M(dttaa)] complexes

To a stirring solution of 3,4-diamino-1,2,5-thiadiazole (200 mg, 1.72 mmol) in methanol/ethanol (1:1, 3 ml) was added propargylaldehyde (66 μl,1.72 mmol) dropwise. The solution was gently heated to reflux as a hot methanolic solution (10 ml) containing hydrated metal(II) acetate (0.86 mol) was added dropwise. Upon addition of the metal salt, the colourless reaction mixture turned cloudy brown almost immediately. The reaction mixture was then refluxed for one hour before

being cooled to RT and filtered. The precipitated product was washed with methanol (2x10 ml) and dried under vacuum.

Cu(dttaa)

Synthesised using metal templating reaction described above. 26.78 % yield. The compound was purified by vacuum sublimation at 270℃ under an applied vacuum of $1x10^{-4}$ mbar. MS (EI): m/z (%) = 364.9 (100.00%) [M^+], 366.9 (54.39%), 365.9 (15.38%). Calculated for $C_{10}H_6CuN_8S_2$, C 32.83, H 1.65, N 30.63; found C 32.70, H 1.64, N 30.55. Melting point: >360°C.

Ni(dttaa)

Synthesised using metal templating reaction described above. 30.69 % yield. The compound was purified by vacuum sublimation at 270℃ under an applied vacuum of $1x10^{-4}$ mbar. MS (EI): m/z (%) = 359.9 (100.00%) [M^+], 361.9 (46.20%), 360.9 (13.41%). Calculated for $C_{10}H_6NiN_8S_2$, C 33.27, H 1.68, N 31.04; found C 33.34, H 1.76, N 30.88. Melting point: >360°C

Pd(dttaa)

To a stirring solution of dttaaH_2 (0.05 g, 0.163 mmol) in DMF (5 ml) was added palladium acetate (0.037 g, 0.163 mmol). The resulting reaction mixture was refluxed for 4 hours before being cooled to RT and filtered. The brown/red precipitate was washed with MeOH until the filtrates were colourless (~30 ml), before being dried under vacuum. 56 % yield. MS (EI): m/z (%) = 407.9 (18.72%) [M^+], 409.9 (17.34%), 406.9 (15.44%). Calculated for $C_{10}H_6PdN_8S_2$, C 29.38, H 1.48, N 27.41; found C 26.36, H 2.17, N 19.70. Melting point: >360°C

Ni(dttaaMe$_4$)

Under an atmosphere of nitrogen 3,4-diamino-1,2,5-thiadiazole (232 mg, 2 mmol) and $NiCl_2$ (129.6 mg, 1 mmol) in DMF (15 ml) were heated to 50 °C with stirring. Acetylacetone (200.3 mg, 2 mmol) was added dropwise to the cloudy yellow solution. Within a few minutes the reaction mixture had turned a deep red/brown colour. The reaction mixture was heated to reflux for 16 hours before being cooled to RT and filtered. An insoluble, black crystalline product (34 mg, 8.2 % yield) was collected after washing with MeOH (10 ml). Mass spec indicated formation of the desired product, but microanalysis indicated that it was impure. Purification of the material is limited to vacuum sublimation, due to its insolubility, but attempts, thus far, have been unsuccessful. MS (EI): m/z (%) = 415.9 (95.25%) [M^+], 416.9 (20.05%), 417.9 (46.11%). Calculated for $C_{14}H_{14}NiN_8S_2$, C 40.31, H 3.38, N 26.86; found C 35.22, H 3.35, N 12.69. Decomposition point: 300 °C

Ni(dttaaBzOEt)

Under an atmosphere of nitrogen 3,4-diamino-1,2,5-thiadiazole (581 mg, 5 mmol) and $Ni(OAc)_2.4H_2O$ (622 mg, 2.5 mmol) in DMF (20 ml) were heated at reflux for one hour. 3-formylchromone (871mg, 5 mmol) was added portionwise and the reaction mixture refluxed for 5 hours to produce a bright red suspension. The reaction mixture was then stirred overnight at room temperature, before being cooled on ice, and filtered. The insoluble red solid was collected, washed with MeOH (50 ml) and dried under vacuum (1.13 g, 75% yield). 195 mg of this red solid (0.32 mmol) was heated to 80 °C with K_2CO_3 in DMF (75 ml). Once at 80 °C, bromoethane (52 μl, 0.7 mmol) was added dropwise with stirring and the reaction mixture heated for 16 hours at this temperature. After this, the reaction mixture was cooled to RT and poured into $CHCl_3$:H_2O (1:1, 200 ml). The organic layer was extracted and washed with brine (50 ml) and H_2O (3x50 ml). The organic layer was then concentrated under vacuo (21 mgs, 10% yield). MS (ESI): m/z (%) = 657.12 (68.55%) [M-H]$^-$, 659.12 (30.33%), 658.15 (22.89%). Calculated for $C_{28}H_{22}NiN_8O_4S_2$, C 51.16, H 3.37, N 17.05; found C 51.18, H

3.41, N 16.84. Decomposition point: 259 °C

Ni(dttaaBzOBu)

Synthesised using the same procedure as Ni(dttaaBzOEt) except that in the second step of the reaction 1-bromobutane (75 μl, 0.7 mmol) was used instead of 1-bromoethane. The sample was purified by size exclusion chromatography using Bio-Beads SX-3 and DCM as eluent. (19 mgs, 8 % yield). MS (ESI): m/z (%) = 713.26 (49.52%) $[M-H]^-$, 714.21 (24.36%), 712.33 (12.12%). Calculated for $C_{32}H_{30}NiN_8O_4S_2$, C 53.87, H 4.24, N 15.71; found C 53.87, H 4.16, N 15.62. Melting point: 231-232°C.

5.2.2 Experimental methods

Single crystals of Ni(dttaa) and Cu(dttaa) were grown and the structures solved by Dr Yoshiaki Shuku of Nagoya University. The crystals were grown by vacuum sublimation at 270 °C under an applied vacuum of $x10^{-4}$ mbar. The 3,4-diamino-1,2,5-thiadiazole ligand was crystallised by slow evaporation from ethanol. Single crystal structure measurements were made on a Rigaku Saturn CCD area detector with graphite monochromated Mo-Kα radiation. Structure solution and refinement was carried out using SHELX software.[10] Powder XRD was carried out using a Bruker AXS D8 diffractometer. Images of the crystal structures have been produced using the software Mercury 2.3.[11-14] Magnetic susceptibility measurements were performed on powder samples from 1.8 to 300 K using a Quantum Design MPMS-XL SQUID magnetometer with MPMS MultiVu Application software to process the data. The magnetic field used was 0.1 T. Diamagnetic corrections were applied to the observed paramagnetic susceptibilities by using Pascal's constants.[15] Single point and geometry optimisation calculations of the isolated complexes were carried out at the B3LYP/6-31G(d,p) level of theory[16-18], using Gaussian 03.[19] Initial thin film studies were carried out by Dr Simon Dalgleish of Nagoya University. The substrates used for deposition were quartz and ITO, which was cleaned by sequential ultrasonication in IPA, acetone and chloroform (15 mins each). Initial thin film

electrochemistry measurements were recorded on ITO substrates vs. Ag/Ag^+ reference electrode in 0.3M $TBAPF_6$/MeCN. Further spectroelectrochemical studies carried out in Edinburgh were recorded on ITO substrates vs. Ag/AgCl reference electrode in 0.3M $TBAPF_6$/MeCN. Absorption spectroscopy was measured on films deposited on a quartz substrate, with a bare quartz slide being used for the background correction. For FET characterisation, both a bottom contact (Pt), bottom gate configuration and top contact (Au), bottom gate configuration were used. For both configurations, a heavily doped silicon wafer served as both the substrate and global gate electrode, with a 300 nm thermally grown SiO_2 layer as the gate dielectric. For bottom contact devices, platinum source and drain electrodes were defined using standard photolithographic techniques at S/D distances of 5μm. The FET substrates were cleaned by mild ultrasonication (50 Hz) for 5 mins in chloroform, and were blown dry under a stream of N_2. Three different surface treatment conditions were tested. One third of the substrates were subjected to UV/ozone etching (2 mins) and one third of the substrates were treated, post etching, with HMDS vapour by placing chips in a flask containing a few drops of HMDS which was heated to 150°C for one hour. The final third were treated with OTS by immersing the substrates in a 1 mmol solution of OTS in dry toluene under a nitrogen atmosphere for 2 hrs, rinsed carefully with toluene and annealed for 1 hr at 120°C for one hour under nitrogen. The substrates were loaded into the PVD chamber immediately after processing. For the bottom gate, top contact FETs, the substrates (in triplicate) were treated in 3 different ways. To one third of the substrates, a thin layer of PMMA (30nm) was spin coated from toluene. Another third were treated with HMDS, and the final third were treated with OTS, as described above. Thin films were fabricated by vacuum vapour deposition at an initial pressure of 2×10^{-6} mbar. Films were grown at a rate of 0.2 ± 0.1 $Å s^{-1}$ to a thickness of 30nm (measured by QCM, calibrated from profilometry). For the top contact devices, a 50nm layer of gold, with a source-drain gap of 30 μm was deposited through a shadow mask, and contact was made using silver paste to connect copper wires. The devices were tested immediately after opening the PVD chamber. The measurements were carried out in darkness and under vacuum using a

Keithley 2636A sourcemeter equipped with Labtracer 2.0 software. Imaging of thin films was carried out using a Hitachi S-4300 Scanning Electron Microscope.

5.3 Results and discussion

The unsubstituted copper [Cu(dttaa)] and nickel [Ni(dttaa)] macrocycles were synthesised in modest yields by employing a metal-templated condensation reaction. Both complexes are extremely insoluble making recrystallisation and solution studies impossible. The purified products were obtained as crystalline solids by vacuum sublimation; in the case of Cu(dttaa), black block-like crystals were grown but in the case of Ni(dttaa), red needles were obtained. The palladium complex, Pd(dttaa), was prepared by reaction of the metal salt with the metal free ligand ($dttaaH_2$), but the reaction produced an insoluble product of low purity. Prior to carrying out complexation reactions, unsuccessful attempts were also made at purifying the free macrocycle ($dttaaH_2$) by sublimation, which resulted in minimal purified product and large amounts of decomposed material. Presumably the addition of a central metal ion, such as Ni or Cu, can help to improve the thermal stability of the free macrocycle. Compound Ni($dttaaMe_4$) was synthesised in an attempt to make a soluble analogue of Ni(dttaa) but it was found that the addition of methyl groups on the propanediiminato linkage had little improvement on the solubility of the resulting complex. Problems were encountered trying to purify Pd(dttaa) and Ni($dttaaMe_4$) in sufficient yields for materials study due to subtantial sample decomposition during sublimation, resulting in minimal pure, sublimed material being retrieved. Scaling up the synthesis of Pd(dttaa) and Ni($dttaaMe_4$) is required in order to obtain sufficient pure material for device fabrication. The more soluble Ni(dttaaBzOR) compounds contain bulky alkoxybenzoyl substituents, which can result in large intermolecular distances in the solid state, possibly too large to witness effective charge transport. However, the isolated molecular properties of these materials Ni(dttaaBzOR) can be studied with greater ease than their insoluble analogues, Cu(dttaa) and Ni(dttaa). It is also reasonable to assume that the isolated electronic properties of Ni(dttaaBzOR) will be similar to Ni(dttaa) considering that the electronic core of each of these molecules is the same, with the addition of non-conjugated solubilising groups to the macrocyclic core unlikely to have a substantial effect on the electronic properties. In the interest of time, only the unsubstituted macrocycles Cu(dttaa) and Ni(dttaa) have

been thoroughly studied in the context of their thin film properties at the present moment. Since they lack solubilising groups, which can impede intermolecular interactions, they represent the most promising candidates to show semiconducting behaviour.

5.3.1 Crystallography

Crystal structures of the Cu and Ni dithiadiazoletetraazaannulene macrocycles, Cu(dttaa) and Ni(dttaa), have been solved from crystals grown by vacuum sublimation. An example of red Ni(dttaa) crystals prepared by sublimation is shown in Figure 3. In addition, the single crystal structure of 1,2,5-thiadiazole-3,4-diamine (tdan) is also reported (Figure 4). Unlike the Ni and Cu dibenzotetraazaannulenes complexes, Ni(dbtaa) and Cu(dbtaa), discussed in Chapter 4, which are isomorphous, the central metal ion in these thiadiazole based macrocycles has an effect defining the solid-state packing. The first obvious clue to the change in crystal packing associated with the central metal ion was in the physical morphology of the crystals grown; the Ni complex formed red needles whereas the Cu complex formed black, block-like crystals. The crystallographic data are given below (Table 1) with the structures shown in Figure 5 and Figure 6.

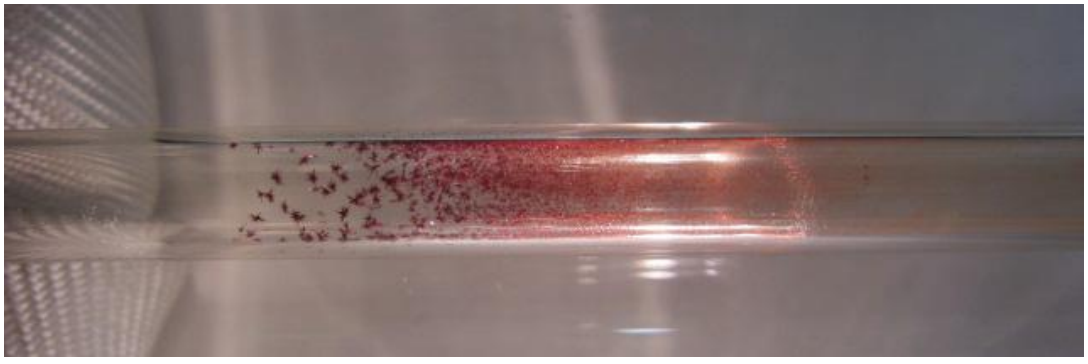

Figure 3 Clusters of needle-like crystals of Ni(dttaa) grown by vacuum sublimation.

Table 1 Crystallographic data for tdan, Cu(dttaa) and Ni(dttaa).

Complex	tdan	Cu(dttaa)	Ni(dttaa)
Morphology	Colourless rod (0.42 x 0.09 × 0.09 mm)	Red block (0.1 x 0.01 x 0.01 mm)	Red prism (0.09 x 0.03 x 0.01 mm)
Empirical formula	$C_2H_4N_4S$	$C_{10}H_6CuN_8S_2$	$C_{10}H_6NiN_8S_2$
T (K)	100	123	123
Space group	$P2_1/c$	C 2/m	P -1
M_r	116.15	365.88	361.03
a	11.1545(3)	11.643(6)	3.659(3)
b	11.3456(3)	13.600(7)	8.939(8)
c	7.4193(2)	3.7043(18)	17.565(17)
α	90	90	94.532(13)
β	108.8800(10)	90.246(6)	91.852(18)
γ	90	90	91.09(2)
V	888.43	586.55	572.283
D_c	1.737	2.072	2.095
μ	0.573	2.223	2.066
No. of reflections measured	17587	2226	4538
No. of reflections used	9604	685	2484
θmax	27.12	27.28	27.4
Z	8	2	2
Rint	0.039	0.030	0.060
Tmin/Tmax	0.9498/0.9498	0.855/0.978	0.747/0.980
R1 (I > 2σ(I))	0.0268	0.0332	0.0683
wR (F2) (I > 2σ(I))	0.0731	0.0872	0.1763

Colourless, rod-like single crystals of 1,2,5-thiadiazole-3,4-diamine (tdan) have been obtained by slow evaporation from a saturated solution of ethanol. The structure of the free ligand, tdan, has been solved and its bond lengths compared with that of the macrocyclic metal complexes, Cu(dttaa) and Ni(dttaa). The two molecules of tdan in the asymmetric unit, along with their respective bond lengths, are shown in Figure 4.

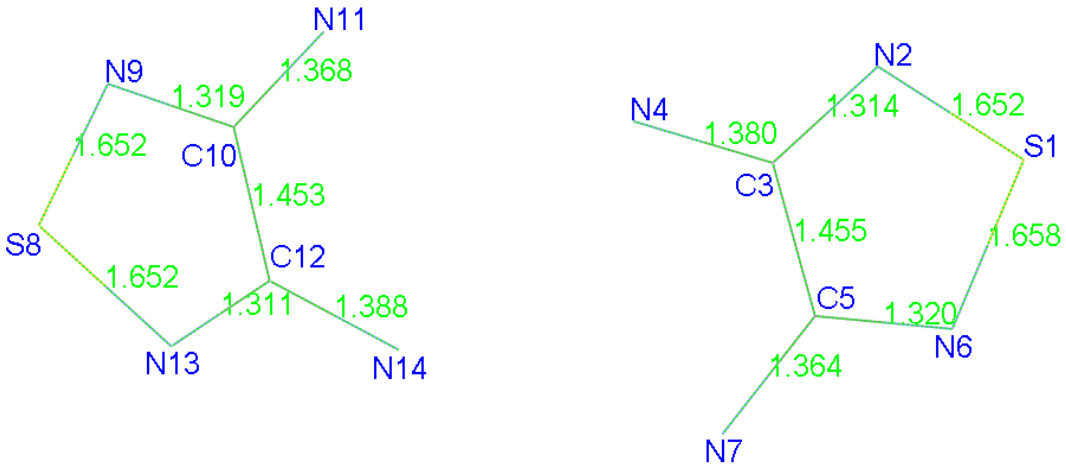

Figure 4 Asymmetric unit of diaminothiadiazole (tdan) with atomic labels (blue) and bond lengths inset (green).

The Cu complex, Cu(dttaa), contains two crystallographically equivalent molecules in its unit cell with two perpendicular mirror planes across the centre of the molecule giving it equivalent Cu-N bond lengths and N-Cu-N bite angles. However, the Ni analogue contains two crystallographically independent molecules in its unit cell with inversion centres on the Ni(II) complex ions. Comparing and contrasting the coordination chemistry of Cu(dttaa) and Ni(dttaa) (Table 2) it is immediately clear that in Cu(dttaa) the Cu-N distances are significantly longer than the Ni-N distances in Ni(dttaa). This may be rationalised by considering the electronic structure of the two metal ions and their square planar coordination environment; Ni(II) has a d^8 electron configuration with an empty dx^2-y^2 orbital but Cu(II) has a d^9 structure with a singly occupied dx^2-y^2 orbital, thus elongated Cu-N bonds will help to minimise electron-electron repulsion between electrons in the sigma orbitals of the N-donor and the electron in the dx^2-y^2 orbital. These elongated Cu-N bonds result in a larger N…N bite distance within the N-C-C-N chelate, compared to Ni(dttaa), as the two

donor atoms are forced further apart to accommodate the longer M-N bonds. Also of interest when comparing structures is the C-C bond length in the thiadiazole ring; in the free ligand, tdan, this length is 1.453(2), in the case of C10-C12, and 1.455(2) Å in the case of C3-C5 (Figure 3), whereas in Cu(dttaa) this equivalent bond length is 1.452(3) and in Ni(dttaa) the bond length is 1.417(9). These C-C bond lengths would suggest that in the Cu(II) complex, Cu(dttaa), the level of electronic delocalisation across the thiadiazole ring is similar to the free ligand, tdan, but in the Ni(II) complex, Ni(dttaa), this bond length is significantly shorter suggesting more π-orbital character to this bond. From this reduced bond length one might expect Ni(dttaa) to possess a more delocalised electronic structure than the analogous Cu(dttaa). The bond lengths between the donor N atom and the C atom on the thiadiazole ring, for example C1-N2 in the case of Cu(dttaa), are fairly similar between the three molecules crystallised and fall in the range 1.36-1.39 Å, with no substantial difference between the free ligand and the macrocycles, indicating that the macrocyclic structure results in no added electronic delocalisation across this bond. The carbon to nitrogen bonds on the propanediiminato linkage of the macrocycles, C2-N2 in the case of Cu(dttaa), fall in the range 1.33-1.34 Å, indicating that these bonds possess significantly more π-orbital contributions than the C (ring) – N (donor atom) bonds previously mentioned. The C-C bonds of the propanediiminato linkage of Cu(dttaa), C2-C3, and Ni(dttaa), C3-C4, C4-C5, C8-C9 and C9-C10, are in the range 1.37-1.39 Å, indicating these bonds are conjugated in nature. Thus, from analysis of the crystal structures, it is difficult to consider the macrocycles as fully delocalised structures. Instead they consist of a conjugated thiadiazole ring and a conjugated propanediiminato moiety electronically separated from each other by a C (ring) – N (donor atom) bond, which possesses substantial single bond character. This is also known to be the case with dibenzotetraazaannulenes (discussed in Chapter 4) where there is insufficient electronic delocalisation between the two conjugated fragments.[20, 21] However, this does not necessarily impede their use as the active material in FETs.[22]

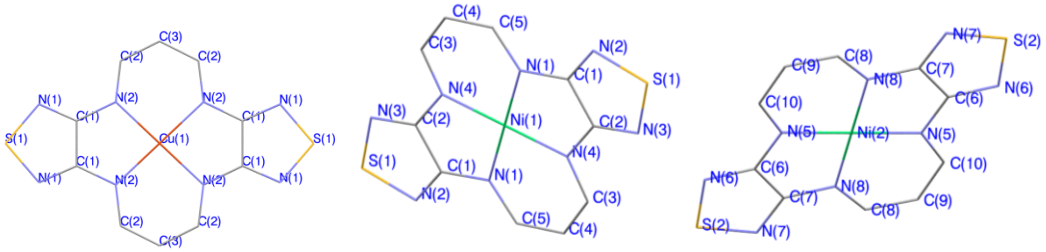

Figure 5 Independent molecules in the unit cell; Cu(dttaa) with atomic labels (shown left), and Ni(dttaa) with atom labels (shown right).

Table 2 Selected bond lengths, angles and distances of Cu(dttaa) and Ni(dttaa). The compound Ni(dttaa) contains two molecules in its asymmetric unit.

Cu(dttaa)		**Ni(dttaa)**		
		Molecule 1 [Molecule 2]	**Molecule 1**	**Molecule 2**
Bond	**Length (Å)**	**Bond**	**Length (Å)**	**Length (Å)**
Cu(1)-N(2)	**1.931(2)**	**Ni(1)-N(4) [Ni(2)-N(5)]**	**1.852(6)**	**1.869(6)**
		Ni(1)-N(1) [Ni(2)-N(8)]	**1.865(6)**	**1.882(6)**
N(2)-C(1)	**1.385(4)**	**N(4)-C(2) [N(5)-C(6)]**	**1.391(9)**	**1.360(9)**
		N(1)-C(1) [N(8)-C(7)]	**1.391(9)**	**1.366(9)**
N(2)-C(2)	**1.338(3)**	**N(4)-C(3) [N(5)-C(10)]**	**1.329(8)**	**1.328(8)**
		N(1)-C(5) [N(8)-C(8)]	**1.331(8)**	**1.294(9)**
C(1)-C(1)	**1.452(3)**	**C(1)-C(2)[C(6)-C(7)]**	**1.417(9)**	**1.417(9)**
C(1)-N(1)	**1.313(4)**	**C(2)-N(3) [C(6)-N(6)]**	**1.302(9)**	**1.322(9)**
		C(1)-N(2) [C(7)-N(7)]	**1.319(9)**	**1.310(9)**
C(2)-C(3)	**1.390(3)**	**C(3)-C(4) [C(10)-C(9)]**	**1.38(1)**	**1.39(1)**
		C(4)-C(5) [C(9)-C(8)]	**1.37(1)**	**1.38(1)**
Angle	**Degree (°)**	**Angle**	**Degree (°)**	**Degree (°)**
N(2)-Cu(1)-N(2) bite angle	**87.3(1)**	**N(4)-Ni(1)-N(1) [N(5)-Ni(2)-N(8)] bite angle**	**88.5(2)**	**87.8(2)**
N(2)-Cu(1)-N(2)	**92.7(1)**	**N(2)-Ni(1)-N(2) [N(5)-Ni(2)-N(8)]**	**91.5(2)**	**92.2(2)**
Distances	**Length (Å)**	**Distances**	**Length (Å)**	**Length (Å)**
N…N bite (N-C-C-N)	**2.665(3)**	**N…N bite (N-C-C-N)**	**2.594(7)**	**2.600(7)**
N…N' (N-C-C-C-N)	**2.794(4)**	**N…N' (N-C-C-C-N)**	**2.661(8)**	**2.704(8)**

In the case of Cu(dttaa), the material stacks in a "brickstone" (Figure 6) fashion but in the case of Ni(dttaa) the material stacks in a "herringbone" motif (Figure 7). Similar packing morphologies are witnessed in the case of metal-free phthalocyanines, where the α-phase is known to form "brickstone" arrangements with the β-phase packing in a "herringbone" manner.[23, 24] In the case of the H_2Pc species, the β-phase can be readily prepared by vacuum sublimation and crystallisation at high temperature; resubliming these crystals, sublimation onto substrates kept at room temperature or recrystallisation of the β-phase compound from sulphuric acid can produce crystals in the α-phase. An irreversible phase change from the α-form to the β-form is reported to occur if the crystals are heated above 475 K for extended time periods.[24, 25] Incidentally, the electrical conductivity of the α-phase is reported to be as high as 100,000 times greater than that of the β-form.[25] In the M(dttaa) packing morphologies the compounds appear to exhibit 2-D supramolecular interactions, which are highly desirable for conducting materials. Both compounds have short face-to-face π-stacking distances between 3.30 and 3.34 Å in one direction and then S…S distances of 3.7 to 3.8 Å in another direction. These distances are slightly too large to be considered as a true S…S contact given that the van der Waals radius of sulfur is usually given as 1.8 Å,[26] but in some cases it has been given as 1.84 Å.[27] Therefore, the S to S orbital interaction, if it actually exists, is likely to be weak.

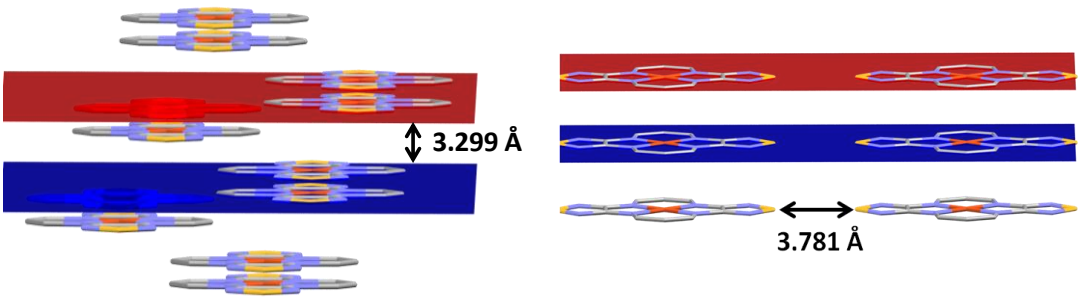

Figure 6 Cu(dttaa) stacking along the c-axis with short, equidistant, interplanar distances (left) and along the b-axis intermolecular S…S distances of 3.781 Å (right).

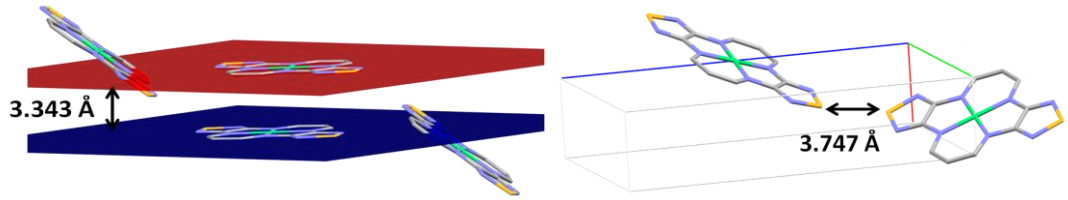

Figure 7 Stacking of Ni(dttaa) along the a-axis with equidistant, interplanar distances of 3.343 Å (left) and intermolecular S…S distances of 3.747 Å (right)**.**

5.3.2 Magnetic susceptibility

Magnetic measurements have been carried out on powder samples of the paramagnetic Cu(II) complex, Cu(dttaa), in order to learn whether it exhibits any magnetic ordering at low temperature or behaves as an isolated S=1/2 paramagnet. Powder XRD measurements have been carried out to ensure that the bulk material is in the same crystallographic phase as the single crystal (Figure 8) and that the choice of this magnetic model is justified. The data clearly indicate that, in both single crystal and powder samples, the interplanar distances are the same and thus we can be confident that the two samples are isomorphous.

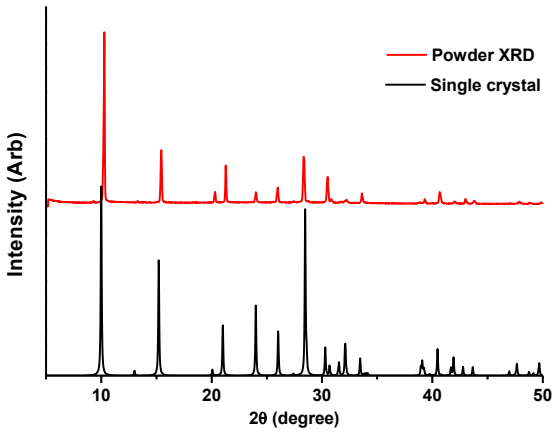

Figure 8 XRD patterns of Cu(dttaa) comparing the measured room temperature powder phase (red) with the simulated powder pattern generated from the single crystal structure (black).

Inspection of Figure 9 clearly indicates that the material displays predominantly antiferromagnetic interactions. The intermolecular Cu to Cu distance is 3.704(2) Å and the intermolecular N to Cu distance is 3.595(3) Å. The N…Cu distance is the shortest intermolecular metal to atom distance and as such the magnetic interactions occurring between the paramagnetic Cu(II) centres can be thought of as a superexchange interaction mediated through the non-magnetic nitrogen atom. The magnetic susceptibility data have been corrected for a temperature independent paramagnetism (TIP) contribution of 1.94 $x10^{-3}$ cm^3 mol^{-1}. The TIP value calculated is slightly larger than the value of 6 $x10^{-5}$ cm^3 mol^{-1} commonly employed for Cu(II) complexes,[28, 29] but the value calulated here may include additional factors such as an overestimated diamagnetic contribution or a trace amount of ferromagnetic impurity. Fitting the plot of χT vs. T to the Curie-Weiss law from 1.8 to 300 K (R^2 = 0.995), gives a Curie constant (C) of 0.4133(7) cm^3 K mol^{-1} and a Weiss constant (θ) of -2.81(3) K. From the fitting results, a g-value of 2.10 has been calculated based on a S=1/2 ion with a Curie constant of 0.4133 cm^3 K mol^{-1}, which is reasonable for a square planar Cu(II) system. Fitting to the χ vs. T plot across the same temperature regime (R^2 = 0.998) calculates a larger Curie constant (C) of 0.458(6) cm^3 K mol^{-1} and a Weiss constant (θ) of -3.69(9) K. Using this greater value of C produces a g-value of 2.21 for a S=1/2 ion, much larger than the value predicted from the χT vs. T results. The fit to the χT vs. T plot is taken to give a more accurate reflection of the g-factor due to the higher weighting given to the higher T data in this plot.

From analysis of the single crystal structure it is appropriate to model the data using the Heisenberg chain model ($H = -J\Sigma S_i S_{i+1}$) given that the material displays equidistant, 1-D, face-to-face π-π interactions along the chain.[30] In this case, the interchain S...S interactions have not been taken into consideration when modelling the data. From the magnetic fit (R^2 = 0.954) the following parameters have been calculated: g-value = 2.090(5) and J = -2.14(6) K.

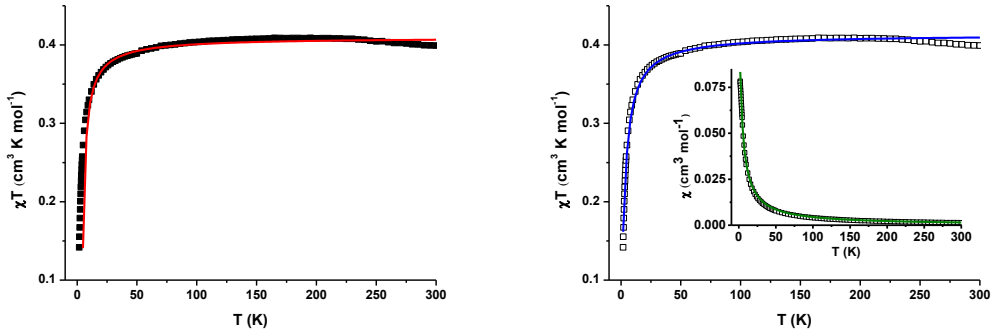

Figure 9 χT vs. T plot of Cu(dttaa) (black squares) fit to the Heisenberg Chain model (left - red line) and to the Curie-Weiss law (right - blue line), with the χ vs. T plot inset (green line).

The complex exhibits weak, antiferromagnetic interactions at low temperatures, as evidenced from the small negative θ from the Curie-Weiss plot, and from the magnitude (and sign) of J calculated from the Heisenberg chain model fitting. The good fit to the 1D-chain model implies that interchain interactions are weak. The χT vs. T magnetic fittings to both the Curie-Weiss and the Heisenberg chain model return similar g-values indicating that the results are consistent.

5.3.3 Computational

Hybrid-DFT calculations have been used to explore the nature of the frontier orbitals of both the diamagnetic Ni(II) complex, Ni(dttaa), and the paramagnetic Cu(II) complex, Cu(dttaa). Geometry optimisations were carried out in vacuum using the crystal structure as starting coordinates. The energy minimised stucture showed good agreement in terms of bond lengths and angles with the crystallised structure.

The Cu(II) complex, Cu(dttaa), shows the α and β-HOMO to be similar in energy at -5.56 and -5.52 eV, respectively, with the orbitals delocalised over the whole of the macrocycle but with no contribution from the metal centre (Table 3). Similarly, the α

and β LUMO orbitals, at -2.45 and -2.44 eV, are again localised over the plane of the molecule with no contribution from the metal centre. From inspection of the calculated spin density, the unpaired electron appears to be lower in energy than the HOMO, based on the α-HOMO-1 orbital with its matching β-orbital the LUMO+2. The energy of the α-HOMO-1 (-5.70 eV) and the β-HOMO-1 (-6.08 eV) do not match up, which supports this assignment of the α-HOMO-1 as the SOMO. The SOMO appears to be primarily based in the dx^2-y^2 orbital, which is expected for a square planar Cu(II) system.

Table 3 Frontier orbitals of Cu(dttaa) calculated at the B3LYP/6-31G(d,p) level of theory, with the orbital energies in eV (vs. vacuum) underneath. The spin density is also depicted at the bottom of the table. The SOMO appears to be lower in energy than the HOMO, based in the HOMO-1 orbital.

Orbital	Alpha	Beta
LUMO+2	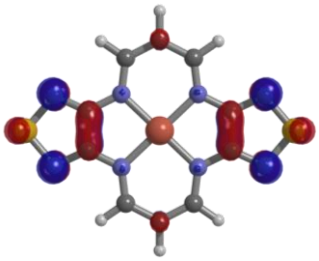	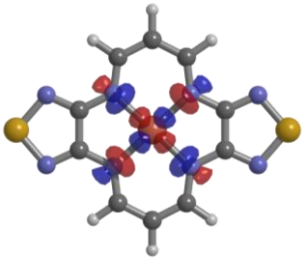
	-1.17eV	**-1.57 eV**
LUMO+1		
	-2.13 eV	**-2.12 eV**

LUMO	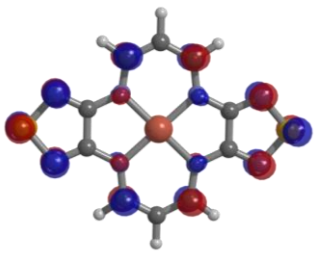	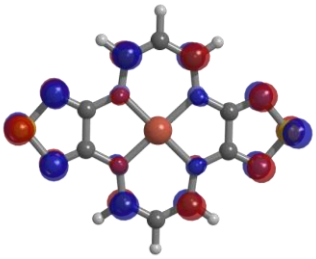
	-2.45 eV	**-2.44 eV**
HOMO	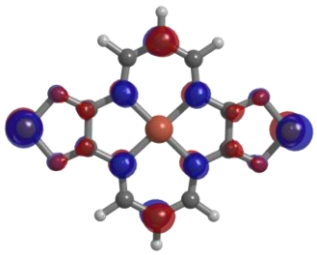	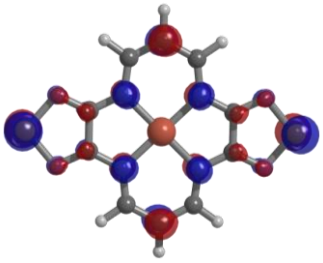
	-5.56 eV	**-5.52 eV**
HOMO-1	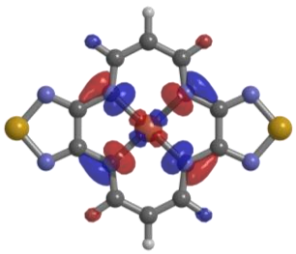	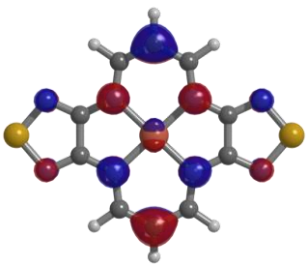
	-5.70 eV	**-6.08 eV**
HOMO-2	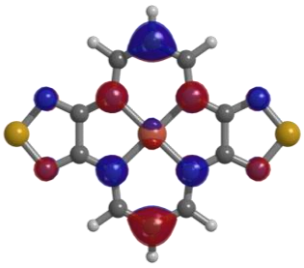	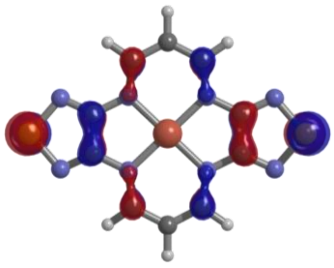
	-6.17 eV	**-6.74 eV**

Spin density

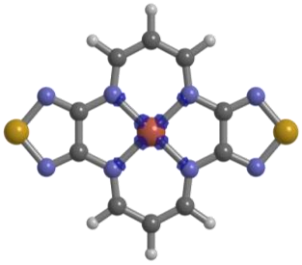

From the calculation on the analogous Ni(II) complex, Ni(dttaa), has its frontier orbitals delocalised over much of the complex (Table 4). However, in this case the LUMO contains a contribution from the metal d-orbitals. The energy of the frontier orbitals is almost identical to that of Cu(dttaa), with a HOMO-LUMO gap of approximately 3.1 eV, indicating that the metal contribution to the LUMO is having a minimal effect on the energy of this orbital.

Table 4 HOMO and LUMO orbitals of Ni(dttaa) calculated at the B3LYP/6-31G(d,p) level of theory, with the orbital energies in eV (vs. vacuum) underneath.

HOMO	LUMO
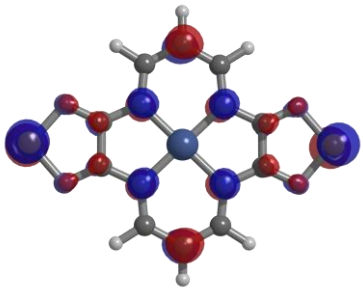	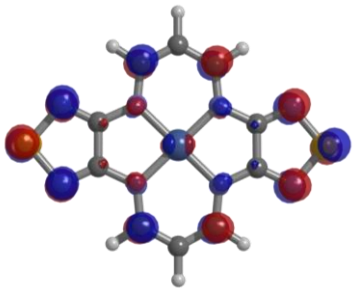
-5.57 eV	**-2.43 eV**

In both complexes, the calculations are consistent in that they predict the LUMO energy to be too high in energy for efficient electron injection from Au or Pt electrodes. Thus, unlike the tetrakis(1,2,5-thiadiazole)porphyrazine series discussed earlier, in these complexes hole transport is more likely than electron transport.

5.3.4 Absorption spectroscopy

Attempts have been made to measure solution spectra to compare with the thin film measurements, but owing to the exceedingly low solubility of these compounds these attempts have proved difficult. Despite using chlorinated solvents such as DCM, $CHCl_3$ and dichlorobenzene, as well as highly polar solvents such as DMF and DMSO, very little sample is solubilised and significant amounts of sample remain undissolved, making it impossible to accurately quantify the magnitude of the transitions. However, solution spectra have been obtained at low concentrations (~1 $x10^{-4}$ M) in DMF but the absorbance units are arbitrary owing to undissolved material within the solution (Figure 10). The Cu complex displays well-defined absorptions with lambda max values at 479 nm and 372 nm, with some shouldering of the latter at 391 nm. The Ni complex has a prominent absorption at 442 nm, with shouldering at shorter wavelengths of 415 and 373 nm.

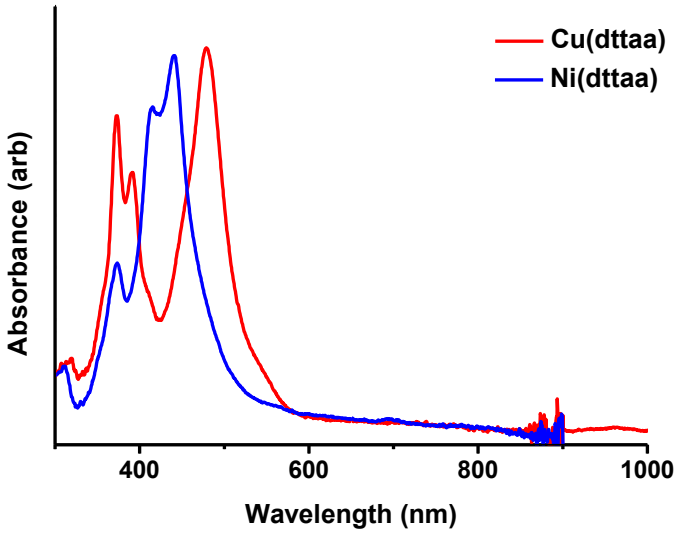

Figure 10 Solution UV/vis spectra of Cu(dttaa) and Ni(dttaa) in DMF between 300 and 1000 nm.

Solution absorption spectra of the analogous Ni(dttaaBzOEt) and Ni(dttaaBzOBu) complexes are shown in Figure 11. Despite their structural similarity, the solubility

of these two complexes is markedly different, with the shorter chain Ni(dttaaBzOEt) complex exhibiting a significantly lower solubility than the readily solubilised, longer chain Ni(dttaaBzOBu) complex. The alkyl chain length should have little to no effect on the electronic properties of these macrocycles, therefore the absorption spectra should appear close to identical between these two molecules. In both spectra absorption peaks are observed at 326 and 416 nm but there are differences in the peak widths between the two samples. The poor solubility of Ni(dttaaBzOEt) is intimated by comparing its absorption spectra with that of Ni(dttaaBzOBu); in the former the absorption peaks are less well defined, and slightly broader than those witnessed in the study of Ni(dttaaBzOBu), which may indicate some aggregation is occuring in the case of Ni(dttaaBzOEt). Assuming that the alkoxy benzoyl groups of Ni(dttaaBzOEt) and Ni(dttaaBzOBu) are contributing negligible electronic delocalisation to the planar macrocyclic core of the molecule then we may expect the absorption spectrum to resemble that of Ni(dttaa) shown in Figure 10. However, they are clearly different, which may indicate that the alkoxy benzoyl groups are having a marked effect on the electronic properties of the molecule, or that aggregation effects in the case of the low solubility Ni(dttaa) complex alter the spectra from that of an isolated molecule in solution.

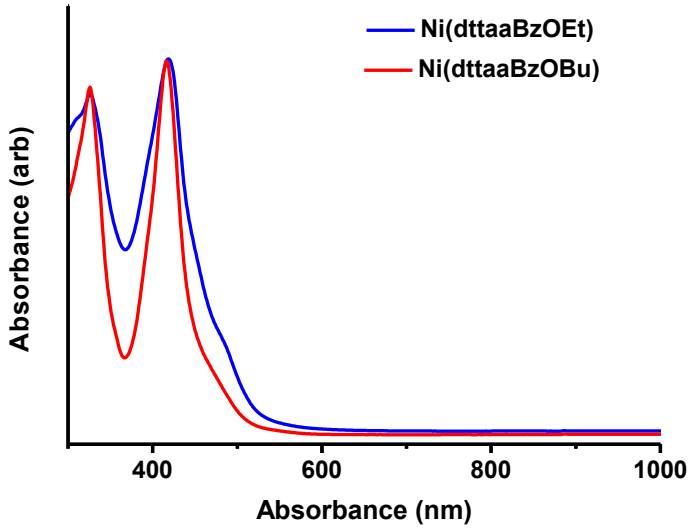

Figure 11 Solution UV/vis spectra of Ni(dttaBzOEt) and Ni(dttaBzOBu) in DCM between 300 and 1000 nm.

The thin films of Cu(dttaa) and Ni(dttaa) were studied between 200-2000 nm. The Cu macrocycle, Cu(dttaa), displays peak absorption at 360 nm with some shouldering and a smaller peak at 462 nm. The Ni macrocycle, Ni(dttaa), has peak absorption at 418 nm. Neither of the materials exhibits any bands out with the UV and visible regions. In both cases the absorptions appear broader with less defined peak maxima than the solution samples.

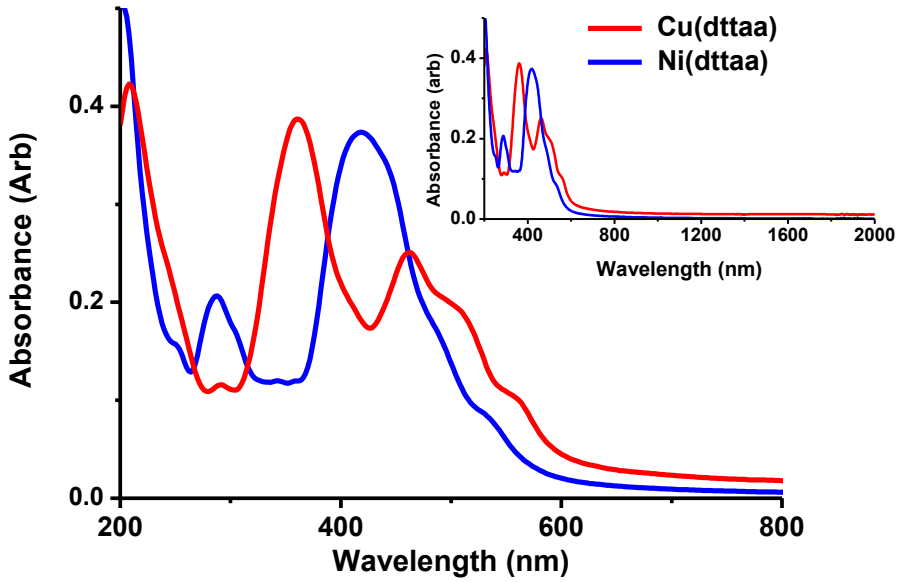

Figure 12 Thin-film UV/Vis spectra of Cu(dttaa) and Ni(dttaa) deposited on quartz substrates. Inset: expansion of the NIR region.

Diffuse reflectance measurements undertaken on powder samples of Cu(dttaa) and Ni(dttaa), in a matrix of $BaSO_4$, are similar to the thin film spectra on quartz in that no bands are observed in the NIR region of the spectrum; however, the onset to the visible transitions appears to be red-shifted in the spectra obtained by diffuse reflectance (Figure 13). In the thin film spectra of both complexes the onset of any optical transitions does not occur until approximately 600 nm. In contrast, with the powder sample of Cu(dttaa) this onset has red-shifted to approximately 800 nm and

in the case of Ni(dttaa) the onset is at almost 700 nm (Figure 13), which is significantly different to the thin film spectra. The large discrepancy between the powder sample and the thin film sample could imply that in the powder sample intermolecular interactions are strong causing a red shifting of the optical absorption, but in the thin film sample these interactions are significantly reduced, perhaps as a result of the deposition process or the material's interaction with the substrate. As such, the differing optical properties could be the result of different crystal packing arrangements in the thin film compared to the powder sample.

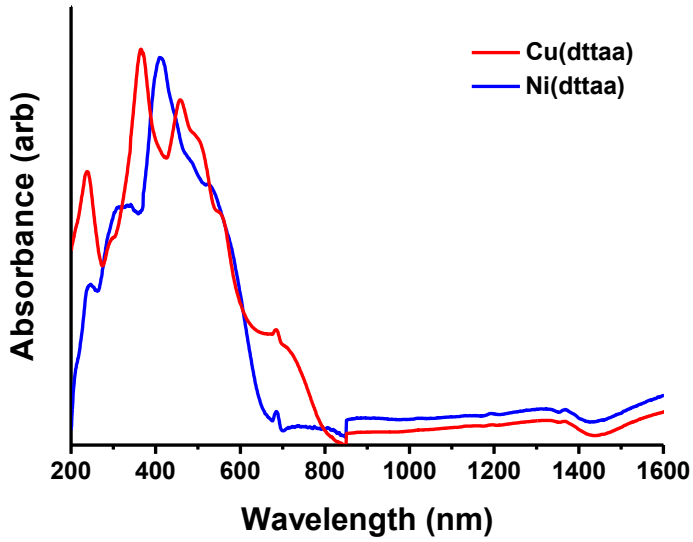

Figure 13 Diffuse reflectance measurement of Cu(dttaa) and Ni(dttaa) in $BaSO_4$ disks.

5.3.5 Electrochemistry

The redox properties of the soluble Ni(dttaaBzOBu) complex has been investigated as a prelude to carrying out thin film eletrochemistry studies on the insoluble Cu(dttaa) and Ni(dttaa) macrocycles. The shorter chain analogue, Ni(dttaaBzOEt), also possesses limited solubility in common organic solvents and thus solution electrochemistry studies have instead focused solely on Ni(dttaaBzOBu). The additional alkyl chain length of Ni(dttaaBzOBu) should not significantly alter the

electochemical properties from that of Ni(dttaaBzOEt), and indeed, the absorption spectra of both complexes appear to be very similar (Figure 11). In the absence of crystallographic data it is impossible to conclusively say why there is such a notable difference in solubility between the two complexes, Ni(dttaaBzOEt) and Ni(dttaaBzOBu), but it may be that with a shorter alkoxy chain such as ethoxy the benzoyl ring is lying in the plane of the macrocyclic core forming a completely planar structure that forms strong π-π interactions in the solid state. A longer, sterically more restrictive alkoxy chain such as butoxy may cause the benzoyl ring to twist away from the plane of the macrocyclic core preventing effective aggregation, thus enhancing the solubility.

Differential pulse voltammetry of Ni(dttaaBzOBu) reveals several chemically reversible redox processes occuring within the solvent window (Figure 14). At positive potentials a single oxidative peak is observed at 1.66 V on the forward scan. On scanning to negative potentials several processes are occuring; the first wave is observed at -0.90 V with a small shoulder peak at -1.00 V. Further reductive processes are then witnessed at -1.45 V and -1.66 V. The first oxidative and reductive processes have been investigated further using cyclic voltammetry as shown in Figure 11. The reductive sweep (Figure 15, left) to -1.2 V extends beyond the first reduction at -0.94 V and reaches a second reductive process occuring at -1.04 V. The return sweep to 0 V shows a reoxidation of the reduced species at -0.10 V. Scanning to -1 V and observing only the first reduction (Figure 11, left, inset) again shows a large, broad return wave with peak current at -0.10 V. Such a wide peak to peak separation may indicate a structural change associated with the reductive process or more likely decomposition of the reduced species. Likewise, the oxidative process at 1.66 V is also shown by cyclic voltammetry to be chemically irreversible.

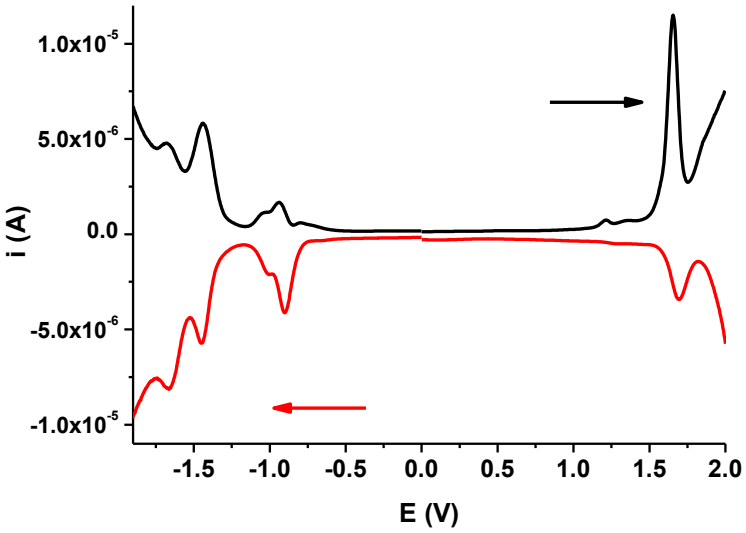

Figure 14 Differential pulse voltammetry of Ni(dttaaBzOBu) between -1.9 and 2 V. Electrochemistry carried out in 0.3 M $TBABF_4$ DCM electrolyte solution using a Ag/AgCl reference electrode.

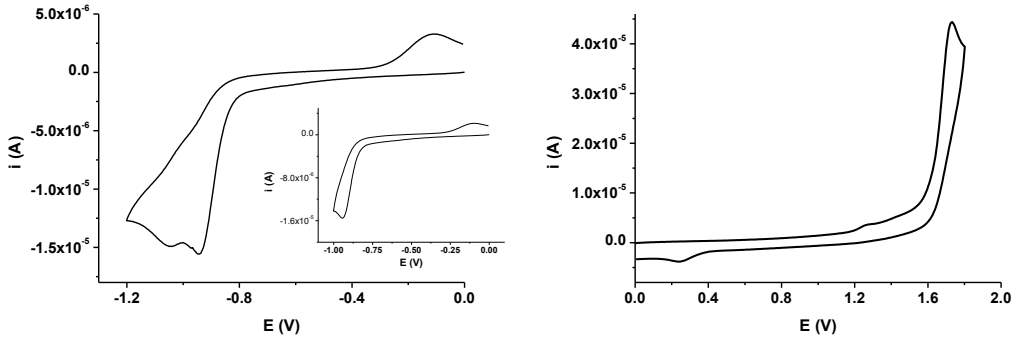

Figure 15 Cyclic voltammetry of Ni(dttaaBzOBu) between 0 and -1.2 V, with the voltammogram between 0 and 1 V shown inset (left), and 0 and 1.8 V (right). Electrochemistry carried out at scan rates of 0.1 V/s in 0.3 M $TBABF_4$ DCM electrolyte solution using a Ag/AgCl reference electrode.

Thin film electrochemistry was initally carried out by Dr Simon Dalgleish of Nagoya University on 30-40 nm films of Cu(dttaa) and Ni(dttaa) grown by vacuum sublimation onto ITO coated glass substrates. Scans were initially carried out at positive potentials based upon information attained by computational calculation, which estimated that the HOMO was electrochemically accessible but that the large

HOMO-LUMO gap would make it unlikely to observe a reductive process associated with the LUMO within the solvent window (Section 5.3.3.). Studies on the analogous soluble Ni(II) complex, Ni(dttaaBzOBu), indicates that macrocyclic complexes of this type may have electrochemically accessible reductive processes. However, exploration of the reductive regions may require use of an electrolyte that contains a cation significantly smaller than tetrabutylammonium.

The initial scan on Cu(dttaa) from 0 to 1.5 V (vs. Ag/Ag^{+}) is shown in Figure 16 (left); the initial scan shows that a large overpotential on the first cycle is required to oxidise the film. This large overpotential can be attributed to restructuring of the film as counter ions migrate into the lattice to balance out the charge as the material is oxidised. This first scan anomaly is a commonly observed effect in solid state electrochemistry.[31-33] Subsequent scans 2-5 appears to indicate significant chemical reversibility, although the current gradually decreases with increasing scan number. Further measurements (Figure 16 (right)) between 0 and 1.2 V reaffirm this assessment of the redox processes reversibility, with the peak current at 0.88 V (from Scan 2). Further exploration of the redox properties, scanning from 0 to 1.8 V (Figure 17 (left)), indicates an additional oxidation with the peak current at 1.62 V (from Scan 1). Repeatedly scanning to this potential results in a significant drop in the peak current of these oxidation processes in successive scans. Scanning beyond the second oxidation potential, with peak current at 1.62 V, appears to be detrimental to the film and the first process, with peak current at 0.88 V, quickly disappearing on scanning. This may be due to dissolution or decomposition of the film as the film colouration became lighter on scanning (even for the redox process occurring at 0.88 V). Overall, this electrochemistry was quite colourful, with the film going from orange, through pink (1^{st} oxidation) to green (start of 2^{nd} oxidation). The colours were reversible, though the colour depth was not, perhaps due to the film gradually deteriorating with scan number.

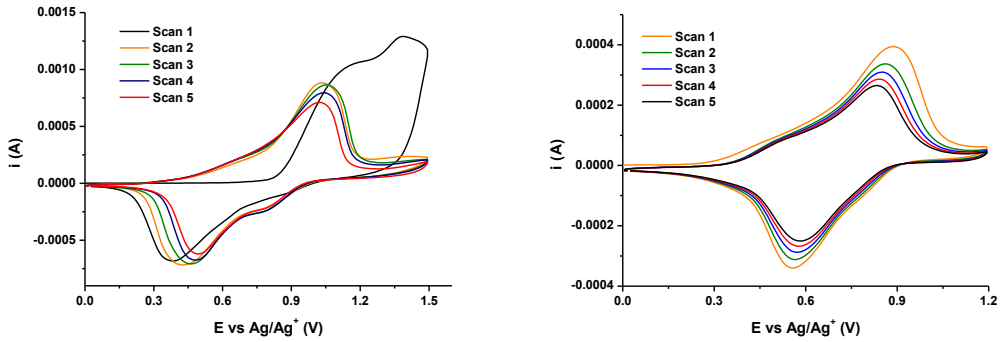

Figure 16 Thin film cyclic voltammogram of Cu(dttaa) between 0 and 1.5 V (left) and subsequent scans between 0 and 1.2 V (right) vs. Ag/Ag^+ at 0.1 V/s in 0.3M $TBAPF_6$/MeCN.

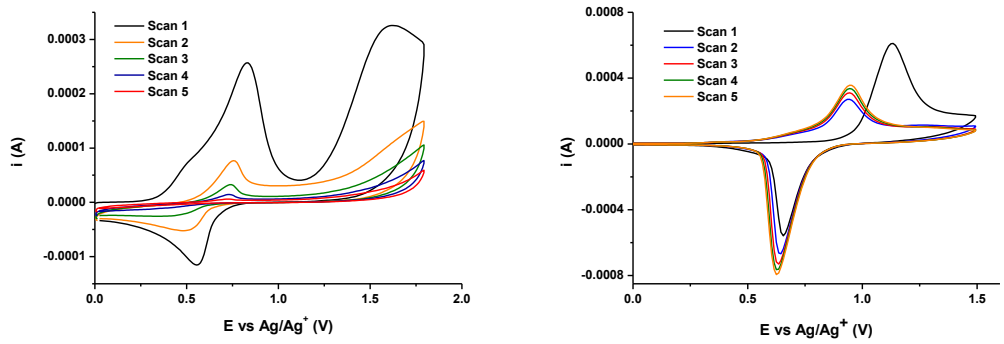

Figure 17 Thin film cyclic voltammogram of Cu(dttaa) between 0 and 1.8 V (left) and Ni(dttaa) between 0 and 1.5 V vs. Ag/Ag^+ at 0.1 V/s in 0.3M $TBAPF_6$/MeCN (right).

The thin film CV of Ni(dttaa) also displays an oxidation within the solvent window but no reduction processes were witnessed between 0 and -1 V. As was previously observed, the first scan results in a significant overpotential. The oxidative redox process - with peak current at 0.94 V (from Scan 2) - appears to be chemically reversible and the current grows with increasing scan number possibly due to the film becoming conditioned (Figure 17 (right)). Unlike the electrochromic Cu(II) complex, Cu(dttaa), this film is initially yellow and becomes darker upon oxidation, but no visible colour change is observed. The appearance of the film remained darker after cycling, possibly indicating a restructuring of the film or that residual counter ions could still be present in the film.

Spectroelectrochemistry measurements were carried out in Edinburgh on Ni(dttaa) thin films by applying a potential from 0 to 2 V (vs. Ag/AgCl) and from 2 to 0 V at 0.2 V intervals, while recording the absorption spectra between 200 and 1000 nm at each 0.2 V interval (Figure 18). The film appears to show no significant change in its optical properties with applied potential, however at 1.6 V on the forward scan the peak maxima absorption intensity increases slightly but then decreases on subsequent measurements at 1.8 and 2 V (Figure 18, top left), as well as the measurements from 2 to 0 V (Figure 18, top right). The coloumetry plots of charge vs. time show that towards the end of the first measurement, from 1.6 to 2 V, the charge flowing through the film is sharply increasing (Figure 18, bottom left). However, the second measurement from 2 to 0 V indicates an initial steep rise in charge but it then remains relatively consistent for the duration of the measurement to 0 V (Figure 18, bottom right). The results indicate that as the film is being oxidised counter ions are flowing in and out of the film but application of potential is having little to no effect on the optical properties of the thin film material, which may imply that the HOMO is not involved in the transitions observed. From Figure 18 (bottom) it is apparent that the amount charge measured from 2 to 0 V is much less than what was measured on the forward scan from 0 to 2 V, possibly indicating that residual charge carriers may have become trapped within the film.

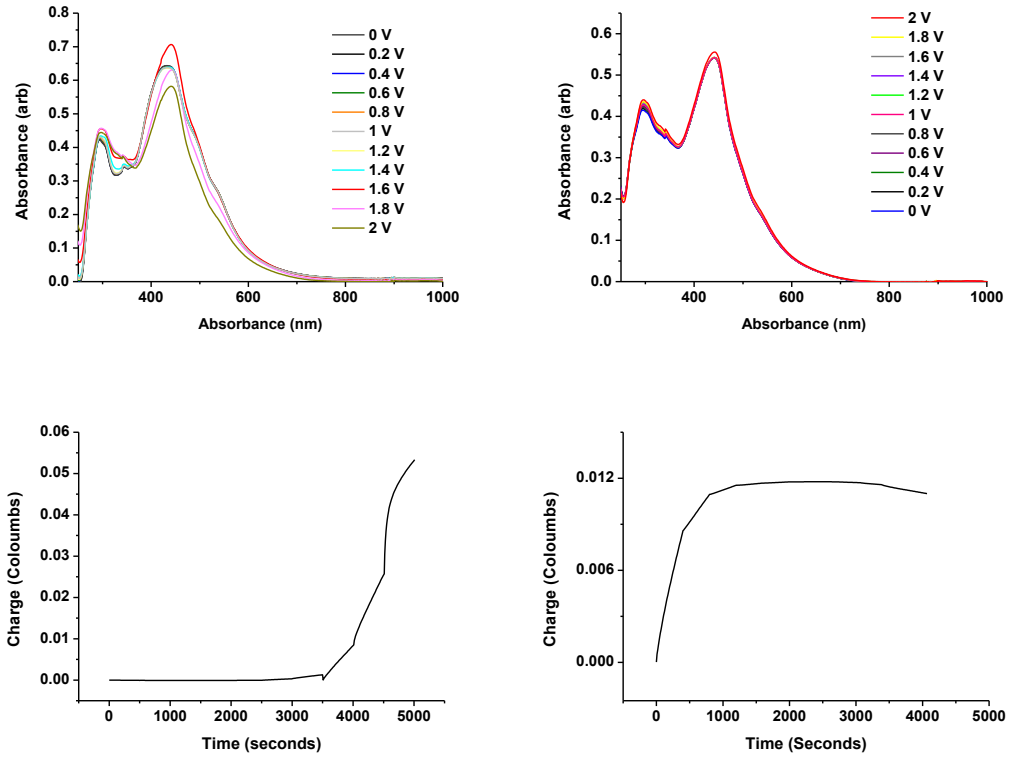

Figure 18 Absorption spectra of Ni(dttaa) thin film between 200 and 1000 nm on applying a voltage from 0 to 2 V (top, left) and from 2 to 0 V (top, right) in 0.2 V intervals vs. Ag/AgCl in 0.3M $TBABF_4$/MeCN. Coloumetry of the films during the 0 to 2 V (bottom, left) and 2 to 0 V (bottom, right) measurement.

Further cyclic voltammetry studies on Ni(dttaa) thin film between 0 and 2 V (vs. Ag/AgCl) have been carried out in a quartz cuvette using $TBABF_4$/MeCN electrolyte, as opposed to the $TBAPF_6$/MeCN previously used. The film was cycled 10 times between 0 and 2 V with the first 5 scans displaying a large peak to peak separation of approximately 600 mV with irregular peak shapes, possibly due to the film restructuring as anions move in and out of the lattice (Figure 19, left). The following scans 5 to 10 have a markedly shorter peak to peak separation of approximately 350 mV but the peak current appears to be decreasing with scan number. The shrinking oxidative peak and its associated return wave imply that the film is not stable to repeated scanning. Sweeping the Ni(dttaa) thin film to a negative potential of -2 V (Figure 19, right) appears to extend over three reductive processes

occurring at -1.39, -1.67 and -1.84 V. On scanning to these potentials it was observed that the film began to disintegrate with large "flakes" of material peeling off of the ITO substrate. Presumably, the film decomposing is a result of the penetration of several bulky TBA^+ cations into the lattice upon reduction, with the size of the counter ion likely to be too large to be accommodated in the film.

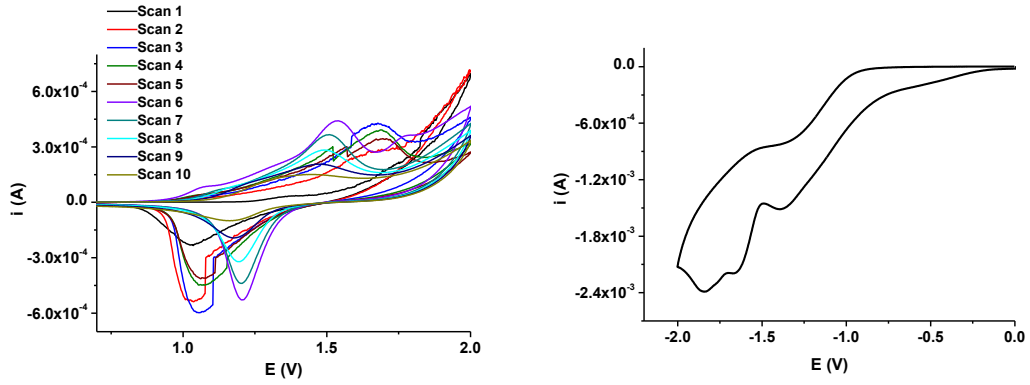

Figure 19 Thin film cyclic voltammogram of Ni(dttaa) repeatedly scanned between 0 and 2 V (left) and 0 and -2 V (right). vs. Ag/AgCl at 0.1 V/s in 0.3M $TBABF_4$/MeCN.

Spectroelectrochemistry measurements have been carried out on films of Ni(dttaa) that have first been subjected to 10 "conditioning" scans between 0 and 2 V by cyclic voltammetry (Figure 20, left); the film is initially held at 0 V while the absorption spectrum is measured, the potential is then switched to 2 V and the absorption spectrum measured, before switching the potential back to 0 V and re-measuring the absorption spectrum. Interestingly, this conditioned film does not show the peak at ~300 nm observed in previous films of this compound. The charge flowing through the film as a function of time has been measured during the potentiostatic coloumetry study (Figure 20, right); the marked steps in the curve indicate a switch in potential from 0 to 2 V at approximately 340 seconds, and then from 2 to 0 V at approximately 680 seconds. On applying a potential of 2 V and oxidising the Ni(dttaa) complex the measured charge at the working electrode is gradually increasing, resulting in charge carriers accumulating in the film, presumably BF_4^- counter ions. However, on switching the potential back to 0 V the measured charge decreases slightly and

plateaus but does not decrease close to its original value, possibly indicating that residual counter ions may be trapped in the film.

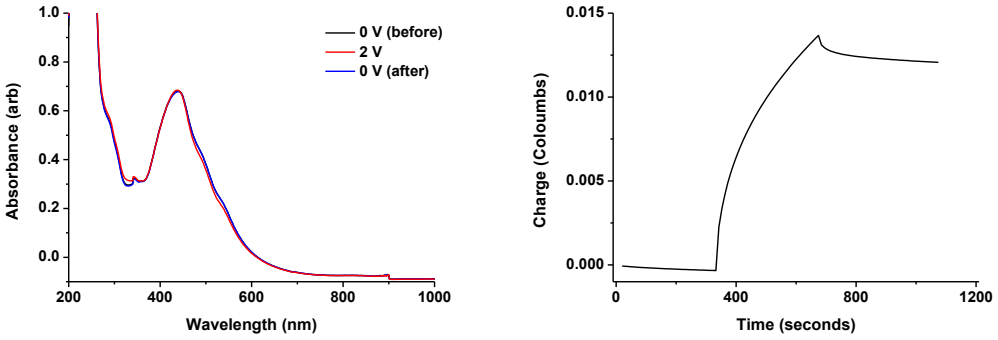

Figure 20 UV/vis/NIR thin film measurements on Ni(dttaa) under an applied potential of initial potential of 0 V, 2 V and then 0 V again (left) vs. Ag/AgCl in 0.3M $TBABF_4$/MeCN. The potentiostatic coloumetry associated with the measurement (right).

Despite observing distinct colour changes of the Cu(dttaa) thin films when carrying out cyclic voltammetry studies, we were not able to note any change in the absorption spectra when carrying out potentiostatic coloumetry (Figure 21). The absorption spectra measured at 0.2 V intervals between 0 and 2 V, and between 2 and 0 V appeared identical, indicating the applied potential was having no effect on the optical properties of the material. The plot of charge vs. time (Figure 21, bottom) would indicate that charge carriers are migrating through the film on the forward 0 to 2 V measurement, increasing steeply after 3200 seconds, which corresponds to applied voltages of 1.6 V and above, since the time taken to perform each UV/vis/NIR scan was approximately 400 seconds. The charge leaving the film on the reverse measurement, from 2 to 0 V, increases sharply for the first ~1000 seconds and then remains steady to 0 V, with the measured charge being approximately the same as observed during the forward 0 to 2 V measurement.

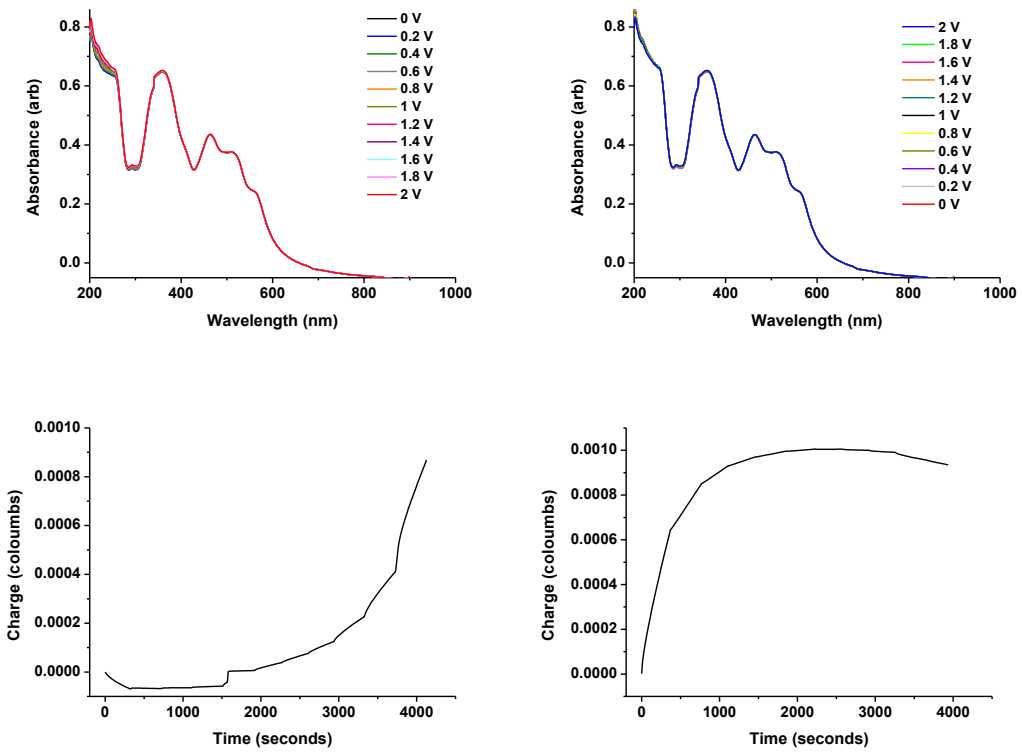

Figure 21 Absorption spectra of Cu(dttaa) thin film between 200 and 1000 nm on applying a voltage from 0 to 2 V (top, left) and from 2 to 0 V (top, right) in 0.2 V intervals vs. Ag/AgCl in 0.3M $TBABF_4$/MeCN. Coloumetry of the films during the 0 to 2 V (bottom, left) and 2 to 0 V (bottom, right) measurement.

Further thin film cyclic voltammetry studies on Cu(dttaa) have been carried out between 0 and 1.8 V (vs. Ag/AgCl) in a quartz cuvette using $TBABF_4$/MeCN electrolyte (Figure 22). Similar to previous studies carried out by Dr Dalgleish, we also observe a chemically reversible oxidative process, although at a different potential due to the change in reference electrode. The first scan displays a significant overpotential with the peak potential in the forward scan at 1.70 V due to the film restructuring but with subsequent scanning this oxidative peak is observed at ~1.50 V. A total of 13 scans were measured with Scans 2-11 displaying a progressive increase in peak current with scan number; however, after the eleventh cycle the peak current in subsequent Scans 12 and 13 began to drop and scanning was halted. A distinct colour change was observed, as noted previously, with the film turning from orange to pale pink. Unlike previous studies of this thin film material, where the film became less conductive with scan number, in this situation we observed the

film conductivity increasing with scan number up to a point. The fall in film current and possible deterioration of the film after Scan 11 may hint at a lack of robustness associated with the film and/or material.

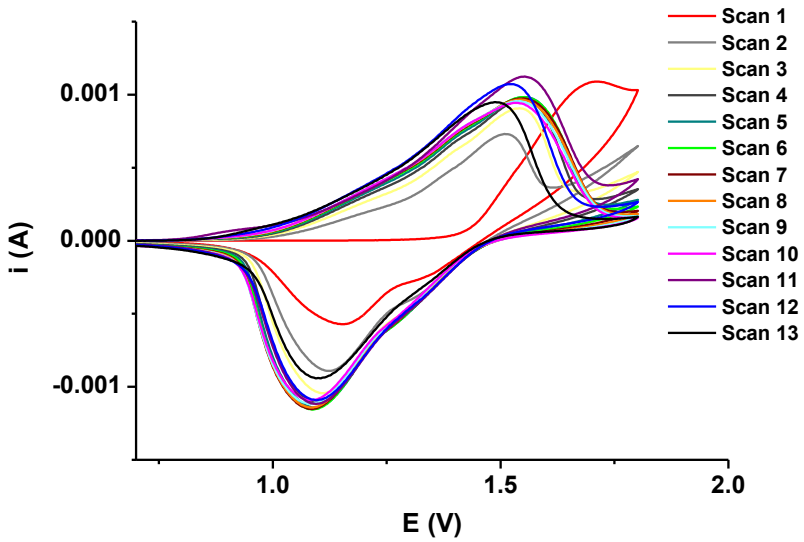

Figure 22 Thin film cyclic voltammetry of Cu(dttaa) between 0 and 1.8 V vs. Ag/AgCl at 0.1 V/s in 0.3M $TBABF_4$/MeCN.

Using this "conditioned" Cu(dttaa) film, which had been subjected to 13 scans, further spectroelectrochemistry studies were attempted. In this experiment the potential was stepped directly from 0 to 2 V and then back to 0 V, with substantial changes observed in the absorption spectra as shown in Figure 23. At 2 V the spectrum was markedly different to the initial spectrum obtained at 0 V and may account for the colour changes observed during previous cyclic voltammetry studies. Notably, the most significant feature of the spectrum at 2 V appears to be the rise of a sharp peak out with the visible region, at 278 nm. In general the peak absorptions of the film at 2 V appear to be much broader and more intense than the initial measurement at 0 V. Additionally, the final measurement at 0 V appears different to the initial measurement at 0 V with an increase in the intensity of the peak absorptions following the measurement at 2 V, perhaps indicating a restructuring of

the film. The reason the change in the thin film optical properties was not observed during the previous measurement is unclear at present and may require further thin film preparation and electrochemical analysis.

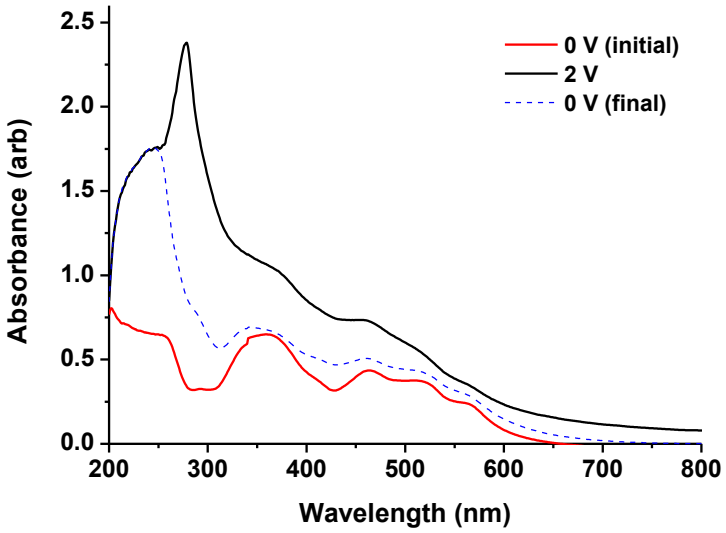

Figure 23 Absorption spectra of Cu(dttaa) thin film between 200 and 800 nm as the applied voltage was switched from 0 V to 2 V and back to 0 V again.

Further studies on Cu(dttaa) and Ni(dttaa) will comprise repeating these measurements with an electrolyte containing a smaller anion, as opposed to PF_6^- or BF_4^-, which may lead to enhanced stability of these films if less structural change is required to accommodate the counter ion into the lattice upon oxidation. Future work can also comprise investigating the use of an alternative cation smaller than TBA^+, which can penetrate into the thin film with less steric hindrance thus avoiding decomposition of the film upon reduction.

5.3.6 Thin-film X-ray diffraction

In order to understand how the compounds are orientated on a thin film, grazing incidence XRD has been carried out on films grown by vacuum sublimation on SiO_2. Out-of-plane and in-plane modes have been utilised to yield information on the crystallographic planes parallel and perpendicular to the substrate, respectively. Measurements on both Cu(dttaa) and Ni(dttaa) (Figure 24 and Figure 25) indicate that both films are crystalline as they give rise to several diffraction peaks. However, in both cases the out-of-plane and in-plane powder patterns appear almost identical indicating that the orientation parallel and perpendicular to the substrate is the same. Thus, the compounds show no preferred orientation on the SiO_2 substrate and instead appear randomly orientated. In the case of Cu(dttaa) the reflections witnessed at 10.0° and 28.5° correspond to the 110 and 20-1 planes, respectively, by comparison with the predicted powder pattern from the single crystal data. These reflections are interpretated as molecules aligning ‘edge on’ (110) and ‘face down’ (20-1) to the substrate. In the thin films of Ni(dttaa) the grazing incidence XRD reveals reflections at 10.0° and 28.1°, similar to Cu(dttaa), which again indicate alignment of the molecules in both an ‘edge on’ or ‘face down’ arrangement. However, with Ni(dttaa) clear indexing of the reflections from the thin film data is not straightforward as there are multiple planes in the single crystal structure which correspond to reflections at approximately 10.0° and 28.08°. From inspection of the single crystal generated powder pattern planes 010 and 002 appear at 9.91° and 10.15°, respectively, and planes 1-12 and 1-1-2 appear at 28.08° and 28.07° respectively. However, in both situations, both of the possible assignable planes witnessed correspond to reflections from planes indicating ‘edge on’ (010 and 002) and ‘face down’ (1-12 and 1-1-2) alignment. Additionally, both materials show a weak reflection at approximately 45° in the out-of-plane diffraction pattern but indexing this peak with any certainty is impossible since the single crystal generated powder patterns of both materials predict many low intensity reflections to occur around this angle. Since the out-of-plane reflections at 45° are relatively broad anyway, attributing it to one particular reflection would be controversial.

Such random molecular orientation is disadvantageous for conducting materials, where a highly ordered structure with the molecules aligned in one orientation, usually 'edge on' to the substrate, is required in order to realise high thin film conductivity.[34] Previous studies have shown that randomly orientated thin films of conducting materials give rise to high resistance and electrically insulating behaviour.[35]

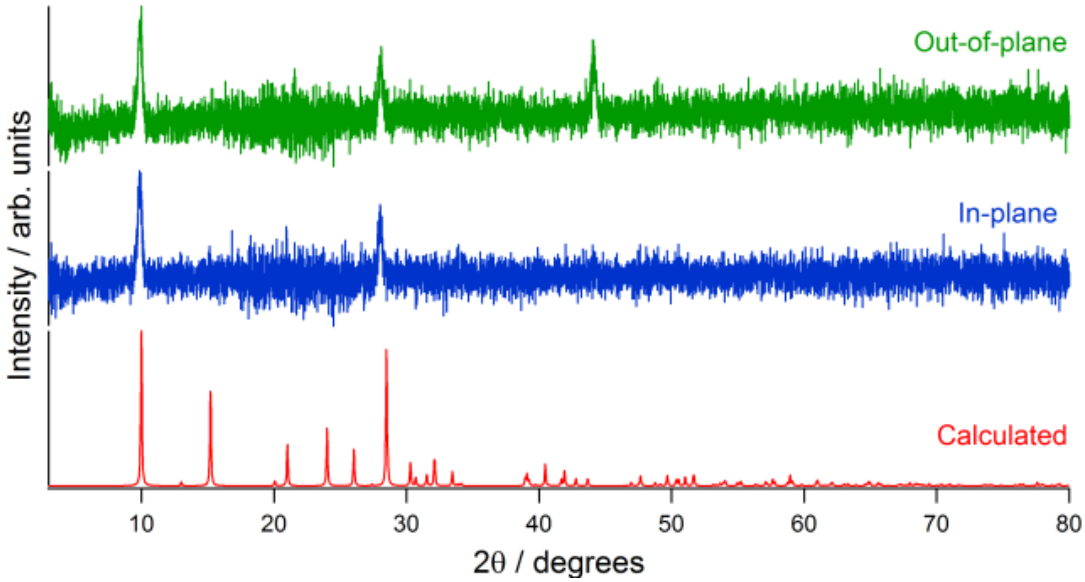

Figure 24 In-plane and out-of-plane thin film XRD measurements on Cu(dttaa) carried out on quartz compared with the predicted powder pattern from the single crystal structure. Thin film **s**pectra were baseline corrected for a bare quartz substrate.

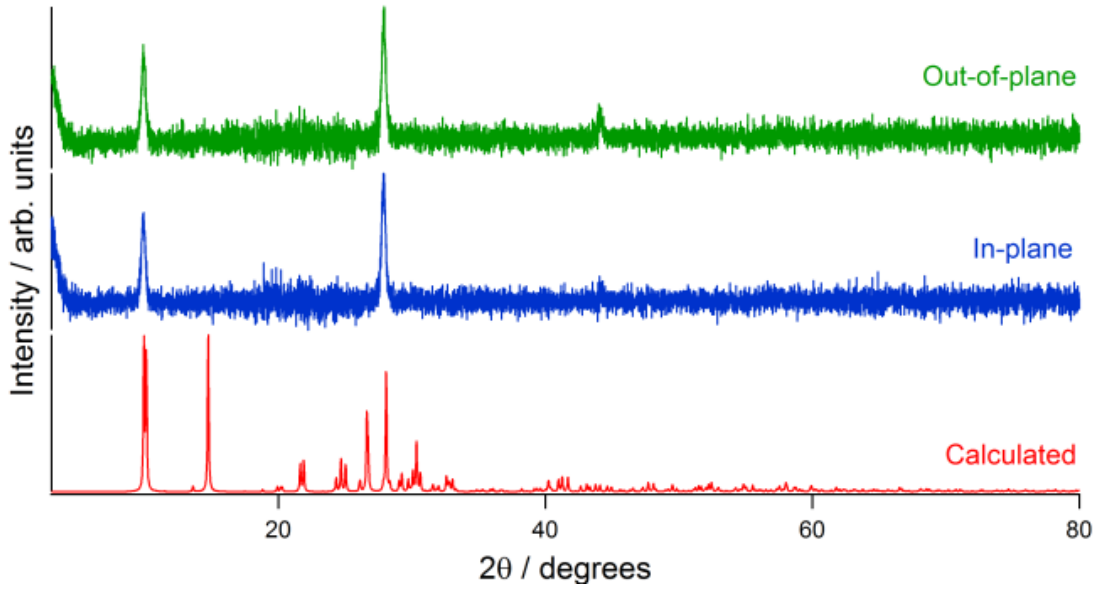

Figure 25 In-plane and out-of-plane thin film XRD measurements on Ni(dttaa) carried out on quartz compared with the predicted powder pattern from the single crystal structure. Thin film spectra were baseline corrected for a bare quartz substrate.

5.3.7 Scanning electron microscopy

SEM imaging of the compounds Cu(dttaa) and Ni(dttaa) on FET substrates was carried out on films grown on substrates which were both untreated and treated with HMDS. However, no detail of the film morphology was resolved (Figure 26). The films appear continuous over the part of the substrate imaged but the individual crystallites cannot be resolved and we must conclude that they are very small, much less than 2 μm, given that we can clearly observe the 2 μm source-drain gap (the dark channel in Figure 26). From the micrographs it also appears that the use of a surface treatment is having little effect on the size of the crystallites.

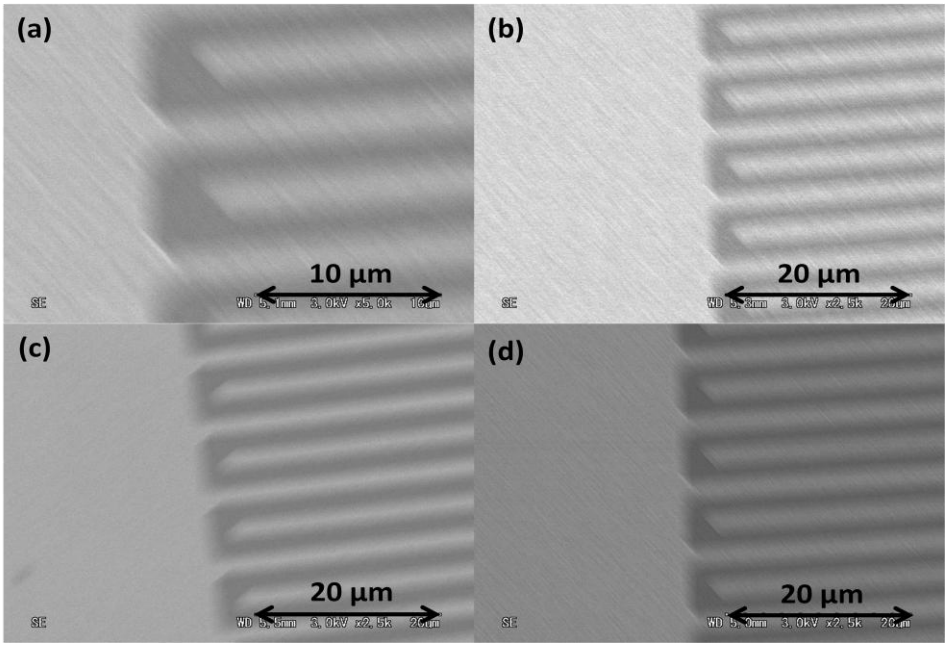

Figure 26 SEM imaging of Cu(dttaa) deposited across the interdigitated electrodes of an FET device without surface treatment (a) and after treating the surface with HMDS (b). Micrographs of Ni(dttaa) without surface treatment (c) and after HMDS surface treatment (d).

5.3.8 FET measurements

Despite several attempts, with multiple device configurations, no gate effect was observed with either Cu(dttaa) or Ni(dttaa) when carrying out FET studies. Gold and platinum electrodes were both used as source and drain contacts, which should be suitable metals judging from the estimated HOMO energy, but without realising FET behaviour. Both of the materials formed insulating films when formed by vacuum sublimation. Since charge injection is unlikely to be the problem, one must assume that either the materials lack a suitable electronic structure for conduction or that the film forming process is the problem. More specifically, the lack of a highly ordered phase on the substrate with many randomly orientated crystallites may be giving rise to a large number of crystal boundaries (charge traps) that are impeding the movement of charge carriers. FET studies of Ni(dttaaBzOEt) and Ni(dttaaBzOBu) that were drop cast from $CHCl_3$ (10 mg/ml) and DCE (10 mg/ml) onto substrates with gold source and drain electrodes also indicated insulating behaviour; however,

in this case less structural and crystallographic information is available to rationalise why this is the case. The lack of conductivity could be the result of various factors involving film preparation or it could likely be a consequence of the material being an intrinsically insulating compound.

5.4 Conclusions

In summary, we have synthesised a new thiadiazole based macrocyclic ligand and the resulting complexes it forms with Ni and Cu. The macrocycles have very low solubility, presumably due to their planarity and the strong intermolecular interactions inherent in the solid state. However, they are volatile under reduced pressure and elevated temperatures, which has allowed us to grow single crystals suitable for X-ray diffraction. The structural properties of these molecules have thus been characterised using single crystal XRD and comparisons drawn between the Cu and Ni complexes. Hybrid DFT has also been used to attempt to understand the electronic structures of these complexes and to quantify the energies of their frontier orbitals. In the case of the paramagnetic Cu complex (Cu(dttaa)) the magnetic properties have also been studied, with the complex found to exhibit weak antiferromagnetic interactions at low temperature. In addition, the thin film electrochemistry of Cu(dttaa) displays promise as an electrochromic material but further work is required to quantify the colour changes observed and to further explore the effect of the counter ion size on the redox properties. Soluble Ni(II) analogues, Ni(dttaaBzOEt) and Ni(dttaaBzOBu), have also been prepared and studied in the context of their absorption, electrochemical and FET properties.

Despite the promising crystal structures of Cu(dttaa) and Ni(dttaa), which indicated strong π-π stacking interactions and possible S...S interactions leading to the prospect of 2D conductivity, the films formed failed to conduct substantial current in FET devices. Attempts thus far at realising a gate effect with these macrocycles have been unsuccessful. The compounds that have been studied thus far, Cu(dttaa) and Ni(dttaa), are very insoluble and so the processing techniques available are limited solely to vacuum sublimation. At present it is unclear whether the poor charge transport results obtained are as a result of the film forming process or whether they are due to an intrinsic material property. The films were formed at a slow deposition rate (0.2 ± 0.1 $Å s^{-1}$), which tends to result in improved thin film formation as the

nucleation process is better controlled. However, even at this slow sublimation rate, the films formed lacked any preferential crystallographic order and the crystallites were so small that they could not be resolved by SEM, despite the film being crystalline by XRD. Even after surface treating the dielectric layer, with HMDS and OTS, the crystallites were still too small to be resolved by SEM.

Future work will look at optimising the thin film formation process, possibly looking into employing a surface treatment with a polar functional group at the end of the molecule, to contrast with the non-polar surface treatments already employed. An alternative strategy could also explore carrying out FET measurements on single crystals grown by sublimation, which would eliminate issues encountered in the growth of thin films e.g. randomly orientated, small crystallites. Single crystal measurements could reveal whether the lack of gate effect is an intrinsic material property or the result of poor film-forming ability of the compounds.

5.5 References

1. Miyoshi, Y.; Kubo, M.; Fujinawa, T.; Suzuki, Y.; Yoshikawa, H.; Awaga, K., *Angewandte Chemie* **2007,** *119*, 5628-5632.
2. Fujimori, M.; Suzuki, Y.; Yoshikawa, H.; Awaga, K., *Angewandte Chemie International Edition* **2003,** *42*, 5863-5865.
3. Suzuki, Y.; Fujimori, M.; Yoshikawa, H.; Awaga, K., *Chemistry – A European Journal* **2004,** *10*, 5158-5164.
4. Bao, Z.; Lovinger, A. J.; Dodabalapur, A., *Applied Physics Letters* **1996,** *69*, 3066-3068.
5. Bao, Z.; Lovinger, A. J.; Brown, J., *Journal of the American Chemical Society* **1998,** *120*, 207-208.
6. Miyoshi, Y.; Fujimoto, T.; Yoshikawa, H.; Matsushita, M. M.; Awaga, K.; Yamada, T.; Ito, H., *Organic Electronics* **2007,** *12*, 239-243.
7. Fujimoto, T.; Miyoshi, Y.; Matsushita, M. M.; Awaga, K., *Chemical Communications* **2011,** *47*, 5837-5839.
8. Bastian, H.; Breitmaier, E., *Chemische Berichte* **1985,** *118*, 1278-1281.
9. Komin, A. P.; Carmack, M., *Journal of Heterocyclic Chemistry* **1976,** *13*, 13-22.
10. Sheldrick, G., *Acta Crystallographica Section A* **2008,** *64*, 112-122.
11. Taylor, R.; Macrae, C. F., *Acta Crystallographica Section B* **2001,** *57*, 815-827.
12. Bruno, I. J.; Cole, J. C.; Edgington, P. R.; Kessler, M.; Macrae, C. F.; McCabe, P.; Pearson, J.; Taylor, R., *Acta Crystallographica Section B* **2002,** *58*, 389-397.
13. Macrae, C. F.; Bruno, I. J.; Chisholm, J. A.; Edgington, P. R.; McCabe, P.; Pidcock, E.; Rodriguez-Monge, L.; Taylor, R.; van de Streek, J.; Wood, P. A., *Journal of Applied Crystallography* **2008,** *41*, 466-470.
14. Macrae, C. F.; Edgington, P. R.; McCabe, P.; Pidcock, E.; Shields, G. P.; Taylor, R.; Towler, M.; van de Streek, J., *Journal of Applied Crystallography* **2006,** *39*, 453-457.
15. Bain, G. A.; Berry, J. F., *Journal of Chemical Education* **2008,** *85*, 532.
16. Becke, A. D., *J. Chem. Phys.* **1993,** *98*, 5648-5652.
17. Lee, C.; Yang, W.; Parr, R. G., *Phys. Rev. B* **1988,** *37*, 785-789.
18. Ditchfield, R.; Hehre, W. J.; Pople, J. A., *The Journal of Chemical Physics* **1971,** *54*, 724-728.
19. M. J. Frisch; G. W. Trucks; H. B. Schlegel; G. E. Scuseria; M. A. Robb; J. R. Cheeseman; J. A. Montgomery, J.; T. Vreven; K. N. Kudin; J. C. Burant; J. M. Millam; S. S. Iyengar; J. Tomasi; V. Barone; B. Mennucci; M. Cossi; G. Scalmani; N. Rega; G. A. Petersson; H. Nakatsuji; M. Hada; M. Ehara; K. Toyota; R. Fukuda; J. Hasegawa; M. Ishida; T. Nakajima; Y. Honda; O. Kitao; H. Nakai; M. Klene; X. Li; J. E. Knox; H. P. Hratchian; J. B. Cross; V. Bakken; C. Adamo; J. Jaramillo; R. Gomperts; R. E. Stratmann; O. Yazyev; A. J. Austin; R. Cammi; C. Pomelli; J. W. Ochterski; P. Y. Ayala; K. Morokuma; G. A. Voth; P. Salvador; J. J. Dannenberg; V. G. Zakrzewski; S. Dapprich; A. D. Daniels; M. C. Strain; O. Farkas; D. K. Malick; A. D. Rabuck; K. Raghavachari; J. B. Foresman; J. V. Ortiz; Q. Cui; A. G. Baboul; S. Clifford; J. Cioslowski; B. B. Stefanov; G. Liu; A. Liashenko; P. Piskorz; I. Komaromi; R. L. Martin; D. J. Fox; T. Keith; M. A. Al-Laham; C. Y. Peng; A. Nanayakkara; M. Challacombe; P. M. W. Gill; B. Johnson; W. Chen; M. W. Wong; C. Gonzalez; Pople, J. A. *Gaussian 03*, Revision E.01; Wallingford CT, 2004.

20. Mountford, P., *Chemical Society Reviews* **1998,** *27*, 105-116.
21. Miry, C.; Le Brun, D.; Kerbaol, J.-M.; L'Her, M., *Journal of Electroanalytical Chemistry* **2000,** *494*, 53-59.
22. Whyte, A. M.; Shuku, Y.; Nichol, G. S.; Matsushita, M. M.; Awaga, K.; Robertson, N., *Journal of Materials Chemistry* **2012,** *22*, 17967-17975.
23. Engel, M. K., *ChemInform* **2003,** *34*.
24. Amar, N. M.; Gould, R. D.; Saleh, A. M., *Current Applied Physics* **2002,** *2*, 455-460.
25. Wihksne, K.; Newkirk, A. E., *The Journal of Chemical Physics* **1961,** *34*, 2184-2185.
26. Bondi, A., *The Journal of Physical Chemistry* **1964,** *68*, 441-451.
27. Zefirov, Y. V.; Zorkii, P. M., *Journal of Structural Chemistry* **1977,** *17*, 644-645.
28. Ciurla, H.; Hanuza, J.; Talik, T.; Talik, Z.; Korabik, M.; MroziÅ„ski, J., *Journal of Alloys and Compounds* **2002,** *341*, 111-114.
29. Grove, H.; Julve, M.; Lloret, F.; Kruger, P. E.; Tornroos, K. W.; Sletten, J., *Inorganica Chimica Acta* **2001,** *325*, 115-124.
30. Estes, W. E.; Gavel, D. P.; Hatfield, W. E.; Hodgson, D. J., *Inorganic Chemistry* **1978,** *17*, 1415-1421.
31. Miyoshi, Y.; Takahashi, K.; Fujimoto, T.; Yoshikawa, H.; Matsushita, M. M.; Ouchi, Y.; Kepenekian, M.; Robert, V.; Donzello, M. P.; Ercolani, C.; Awaga, K., *Inorganic Chemistry* **2011**.
32. Kahl, J. L.; Faulkner, L. R.; Dwarakanath, K.; Tachikawa, H., *Journal of the American Chemical Society* **1986,** *108*, 5434-5440.
33. Green, J. M.; Faulkner, L. R., *Journal of the American Chemical Society* **1983,** *105*, 2950-2955.
34. Kline, R. J.; Hudson, S. D.; Zhang, X.; Gundlach, D. J.; Moad, A. J.; Jurchescu, O. D.; Jackson, T. N.; Subramanian, S.; Anthony, J. E.; Toney, M. F.; Richter, L. J., *Chemistry of Materials* **2012,** *23*, 1194-1203.
35. Ward, J. W.; Loth, M. A.; Kline, R. J.; Coll, M.; Ocal, C.; Anthony, J. E.; Jurchescu, O. D., *Journal of Materials Chemistry* **2012,** *22*, 19047-19053.

Chapter 6: Alkoxylated Complexes

6.1 Introduction

Functionalisation of planar, conjugated molecules with linear alkyl chains is attractive for several obvious reasons: the addition of alkyl chains helps to improve solubility, which is crucial to low cost processing; linear chains, unlike branched chains, do not tend to disrupt π-π stacking interactions; and structural flexibility attained by the addition of long, greasy chains - in conjunction with a rigid, planar core - can give rise to discotic phases. Discotic liquid crystalline materials tend to display either columnar or nematic phase behaviour, with the former being much more common.[1] Columnar phase liquid crystals have attracted interest for their use in conducting devices, with nematic phase materials being of particular interest for wide viewing angle LCDs.[2] In recent years, the preparation of liquid crystalline materials for conducting applications has garnered considerable attention,[3] with applications being found in field effect transistors,[4, 5] photovoltaics[6] and light emitting diodes.[7] Columnar liquid crystalline phases can arise if the molecule contains a rigid core with a flexible side chain pointing outwards.[8] In such systems high charge carrier mobilities are typically observed, with the anisotropic charge transport taking place via a hopping mechanism through the π-conjugated mesogens.[3] Since discotic molecules have a tendency to self assemble into columnar stacks, ease of processability is inherent, however, alignment of the stacks in the correct manner for conducting applications remains challenging.[9]

A large number of liquid crystalline materials are now known, many of which are based upon conjugated macrocycles such as phthalocyanines[4] and porphyrins.[10] Metal free dibenzotetraaza[14]annulenes have also been found to exhibit liquid

crystalline phases, when the peripherary of the macrocycle has been functionalised with alkyl chains.[11, 12] An example of such a molecule is shown below (Figure 1, left), where columnar discotic phase behaviour was reported by Grolik *et al.* In fact, as recently as late 2012 the same author reported another new example of a liquid crystalline dibenzotetraaza[14]annulene molecule, this time exhibiting a less commonly observed discotic nematic phase.[12] The molecule in question is shown in Figure 1 (right) and bears two dodecyloxy and two isobutoxy substituents around its planar core. The choice of substituents around the discotic core is said to play a crucial role in the resulting phase behaviour, with nematic mesophases only observed if intermolecular π-π stacking interactions can be reduced. If significant π-π stacking interactions are inherent then columnar phase behaviour prevails.[1, 2, 12]

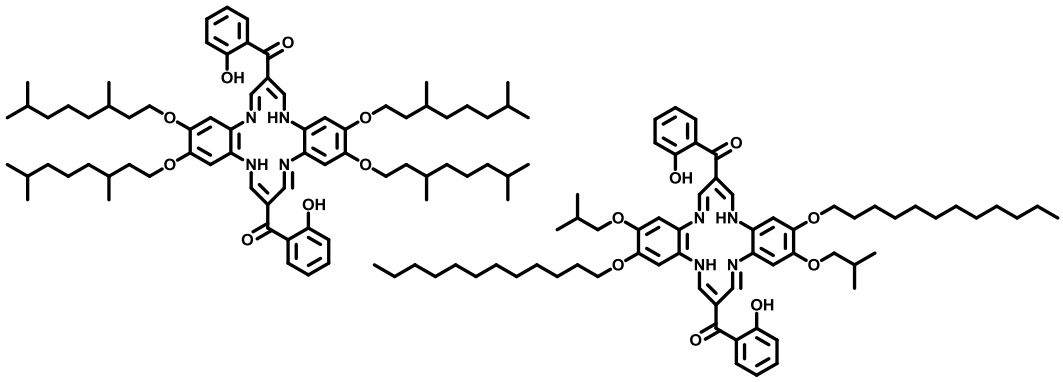

Figure 1 Examples of dibenzotetraaza[14]annulene molecules reported to exhibit liquid crystalline phase behaviour.[11, 12]

Earlier work by Forget *et al.* reported on the observation of LC behaviour in a series of related Ni(II) dibenzotetraaza[14]annulenes,[13-15] and in one preliminary study the potential application for such molecules in optical storage devices was illustrated.[16] However, other reported examples of LC dibenzotetraaza[14]annulenes remain scarce and, to the best of our knowledge, no study on the conducting properties of these systems has to date been carried out.

In addition to tetraaza macrocyclic complexes, bis-ligand diimine metal complexes may also provide an attractive proposition for conducting applications. Aromatic diimine complexes have been shown to give rise to planar, delocalised structures with small HOMO-LUMO gaps, through the use of non-innocent ligands such as *o*-semibenzoquinonediimine (shown in Figure 2 as L^{1-}).[17-19] Work by Noro *et al.*[20, 21] illustrated the potential application for use of bis-(o-diiminobenzosemiquinonate) nickel(II) in thin film transistors. This complex possessed a small HOMO-LUMO gap of *ca*. 0.8 V, giving rise to ambipolar charge transport with respectable hole and electron mobilities in the range of 10^{-3} to 10^{-2} $cm^2 V^{-1} s^{-1}$.[21]

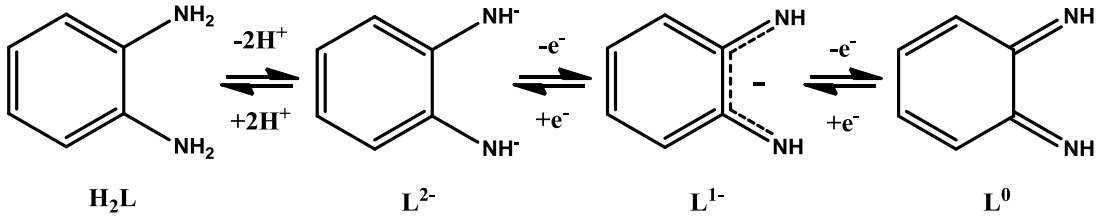

Figure 2 The various resonance forms of *o*-phenylene diamine upon deprotonation and subsequent oxidation.

A logical next step would be to study the effect of exchanging the central metal ion, varying the substituents on the semibenzoquinonediimine ligand or to expand the π-conjugation of the system by using a diamino naphthalene or phenanthrene ligand. In fact, a series of bis-ligand diimine Ni(II) complexes were reported in 1989 by Lelj *et al.* using 2,3-diiminonaphthalene (din) and 9,10-diiminophenanthrene (dip) as ligands. This study compared the conductivity of the three complexes in iodinated pressed pellets, with the authors reporting that the conductivity of $Ni(dip)_2I_x$ was 10^3-10^4 times greater than that of the analogous iodinated phenylenediimine Ni(II) compound.[22] However, to the best of our knowledge there exists no studies on similar bis-ligand diimine systems for use in thin film transistors, aside from the aforementioned work carried out by Noro and coworkers.

Herein we report the synthesis of a series of modified dibenzotetraazaannulenes complexes, as well as several analogous o-phenylenediimine metal complexes using the ligand 4,5-bis(dodecyloxy)benzene-1,2-diamine.

6.2 Experimental

6.2.1 Synthesis

All starting materials were purchased from Sigma Aldrich and used without further purification unless otherwise stated.

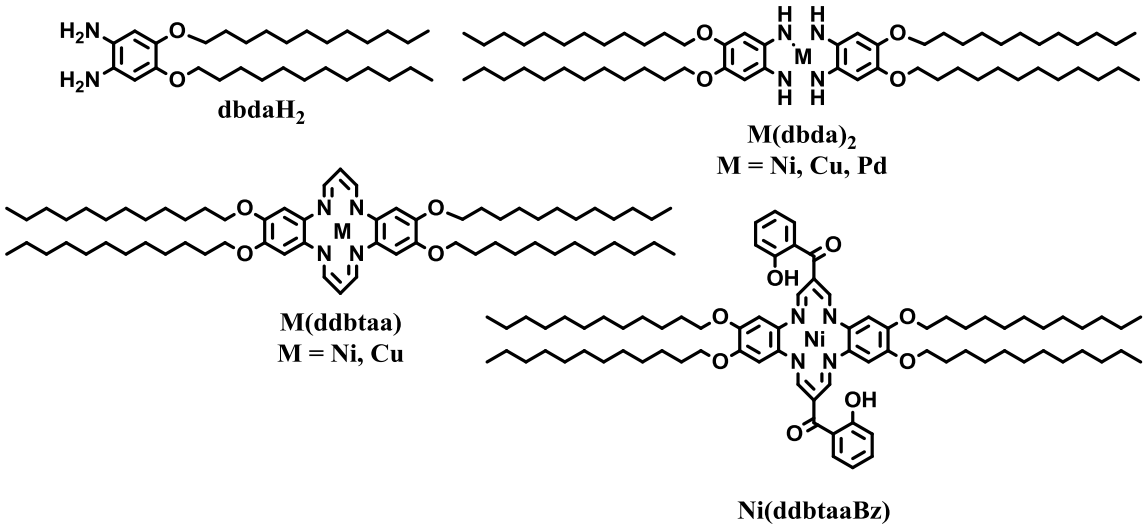

Figure 3 Structures of the molecules synthesised in this chapter with their references inset.

4,5-Bis(dodecyloxy)benzene-1,2-diamine ($dbdaH_2$)

4,5-bis(dodecyloxy)benzene-1,2-diamine was synthesised in three steps, starting from catechol (1,2-dihydroxybenzene), by a previously reported procedure.[23] Catechol (1.99 g, 18 mmol), potassium carbonate (10 g, 72.4 mmol) and 18-crown-6 (0.3 g, 1.1 mmol) were stirred in acetone (100 ml) as 1-bromodecane (9.56 ml, 39.8 mmol) was added dropwise. The resulting white reaction mixture was then heated to reflux for 24 hours under an atmosphere of nitrogen. The solution was filtered hot and the filtrates concentrated under vacuo to leave an off-white solid. The product was then washed with methanol and dried under vacuo. (7.38g, 97% yield). To a cooled, stirring solution of HNO_3 (16 ml, 70%) was added a DCM solution (40 ml)

containing the 1,2-bisdodecyloxybenzene product (3.32g, 7.4 mmol) dropwise over a period of 45 minutes. Concentrated H_2SO_4 (8 ml, 95%) was then added dropwise to the dark yellow reaction mixture. After which the reaction mixture was removed from the ice bath and stirred at RT for 2 hours. The orange/brown solution was then poured over ice (200 ml), causing a yellow solid to precipitate out of solution, which was then extracted in DCM (3x150 ml). The organic layer was then washed with saturated $NaHCO_3$ solution (40 ml) and H_2O (2x40 ml), before being concentrated under reduced pressure to yield a yellow solid (3.81g, 95 % yield). The final step of the reaction involves reducing the dinitroarene (1.25 g, 2.3 mmol) with Pd/C (10 %, 0.43 g) and hydrazine monohydrate (4.24 g, 4.8 mmol) in EtOH (175 ml). The reaction was carried out at 80 °C for 16 hours under an atmosphere of nitrogen. The hot solution was filtered through celite and the filtrate concentrated under reduced pressure to yield an off-white solid. The solid was washed with MeOH (20 ml) and collected by filtration (1.02 g, 93 % yield). ^{1}H NMR ($CDCl_3$): δ (ppm) = 0.88 (t, 3H, 7 Hz), 1.30 (m, 16H, 7.5 Hz), 1.43 (m, 2H, 7 Hz), 1.74 (m, 2H, 7 Hz), 3.88 (t, 2H, 6.5 Hz), 6.38 (s, 1H). MS (ESI): m/z (%) = 476.6 (100%) $[M+H]^+$.

Ni(dbda)$_2$

$Ni(NO_3)_2.6H_2O$ (0.128 g, 0.44 mmol) and 4,5-bis(dodecyloxy)benzene-1,2-diamine (0.418 g, 0.87 mmol) were stirred in MeOH (30 ml) under an air atmosphere. The yellow suspension was heated to reflux as triethylamine (0.5 ml, 3.6 mmols) was added dropwise. Within a few minutes the reaction mixture had turned a dark brown colour. The resulting reaction mixture was refluxed for one hour before being cooled to RT. The product was poured into hexane: water (1: 1, 200 ml) with the organic layer extracted, then washed with MeOH (2 x 100 ml) and H_2O (3 x 100 ml). The hexane was the removed under vacuo and the sample purified by size exclusion chromatography on Bio-Beads SX-3 using DCM as eluent. (65 mg, 15 % yield). MS (ESI): m/z (%) = 1005.66 (100.00%) $[M+H]^+$. ^{1}H NMR ($CDCl_3$): δ (ppm) = 0.91 (t), 1.29 (br s), 1.44 (br s), 1.60 (br s), 1.75 (br s), 3.67 (br s). Calculated for $C_{60}H_{108}NiN_4O_4$, C 71.48, H 10.80, N 5.56; found C 71.38, H 10.68, N 5.62. Melting point: 187-189 °C.

$Cu(dbda)_2$

$Cu(NO_3)_2.3H_2O$ (0.241 g, 1 mmol) and 4,5-bis(dodecyloxy)benzene-1,2-diamine (0.952 g, 2 mmol) were stirred in MeOH (60 ml) under an air atmosphere. The pale green suspension was heated to reflux as triethylamine (1.11 ml, 8 mmols) was added dropwise. The reaction mixture turned dark blue almost immediately following addition of base. Refluxing was continued for one hour before the reaction mixture was cooled to RT, and poured into hexane: water (1: 1, 300 ml). The organic fraction was extracted and washed with MeOH (100 ml), DMF (100 ml x 2) and water (2 x 100ml). The product was the concentrated under vacuo and purified by size exclusion chromatography on Bio-Beads SX-3 using DCM as eluent (111 mg, 11 % yield). MS (ESI): m/z (%) = 1011.70 (100.00%) $[M+H]^+$. Calculated for $C_{60}H_{108}CuN_4O_4$, C 71.13, H 10.75, N 5.53; found C 57.87, H 8.97, N 5.27. Melting point: 164-165 °C.

$Pd(dbda)_2$

Anhydrous $Pd(Cl)_2$ (0.089 g, 0.5 mmol) and 4,5-bis(dodecyloxy)benzene-1,2-diamine (0.476 g, 1 mmol) were stirred in MeOH (30 ml) under an air atmosphere. The reaction mixture was heated to reflux as triethylamine (0.57 ml, 4.1 mmol) was added dropwise. After several minutes the brown/red suspension turned dark green, almost black. The reaction mixture was refluxed in air for one hour before cooling to RT and pouring into DCM: water (1:1, 200 ml). The organic layer was extracted and washed with water (2 x 100 ml) before being dried under vacuo. The crude solid was redissolved in hexane (50 ml) and further washed with MeOH (2 x 100 ml). The hexane layer was evaporated to dryness and the product purified by size exclusion chromatography on Bio-Beads SX-3 using DCM as eluent. (21 mg, 4 % yield). MS (ESI): m/z (%) = 1053.55 (39.18%) $[M+H]^+$. ^1H NMR ($CDCl_3$): δ (ppm) = 0.90 (t, 3H), 1.29 (s, 20H), 1.59 (t, 2H), 3.67 (s, 1H). Calculated for $C_{60}H_{108}PdN_4O_4$, C 68.25, H 10.31, N 5.31; found C 63.08, H 9.71, N 4.94. Melting point: 169-170 °C.

Ni(ddbtaa)

$Ni(OAc)_2.4H_2O$ (0.080 g, 0.32 mmol) and 4,5-bis(dodecyloxy)benzene-1,2-diamine (0.300 g, 0.63 mmol) were stirred in DMF: MeOH (1:1, 4 ml) under an air atmosphere. The pale purple reaction mixture was heated to 70 °C and propargylaldehyde (0.024 ml, 0.63 mmol) was added dropwise, causing reaction mixture to turn dark red/purple. The reaction mixture was heated to reflux for one hour before being cooled to RT and filtered. The dark red precipitate was washed with MeOH (50 ml). The solid was then solubilised in $CHCl_3$ (50 ml) and washed with H_2O (2 x 50 ml) before being concentrated to dryness in vacuo. The dry solid was then redissolved in hexane (70 ml) before being washed with H_2O (2 x 50 ml) and MeOH (2 x 50 ml), before the hexane layer was then evaporated to dryness. The complex was further purified by size exclusion chromatography on Bio-Beads SX-3 using DCM as eluent (165 mg, 48 % yield). MS (MALDI): m/z (%) = 1079.74 $[M+H]^+$. Calculated for $C_{66}H_{110}NiN_4O_4$, C 73.24, H 10.24, N 5.18; found C 73.30, H 10.16, N 5.29. Melting point: 115-118 °C.

Cu(ddbtaa)

$Cu(OAc)_2.4H_2O$ (0.20 g, 1 mmol) and 4,5-bis(dodecyloxy)benzene-1,2-diamine (0.95 g, 2 mmol) were stirred in DMF: MeOH (1:1, 20 ml) under an air atmosphere. Propargylaldehyde (0.077 ml, 2 mmol) was added dropwise as the reaction mixture was heated to reflux. The reaction mixture was heated to reflux for one hour before being cooled to RT and poured into hexane: water (1:2, 300 ml). The organic layer was extracted then rewashed with H_2O (200 ml) and MeOH (100 ml), before the hexane fraction was concentrated under reduced pressure. The complex was further purified by size exclusion chromatography on Bio-Beads SX-3 using DCM as eluent (660 mg, 61 % yield). Calculated for $C_{66}H_{110}CuN_4O_4$, C 72.92, H 10.20, N 5.15; found C 71.77, H 10.09, N 4.99. Melting point: 120-122 °C.

Ni(ddbtaaBz)

$Ni(OAc)_2.4H_2O$ (0.190 g, 0.62 mmol) and 4,5-bis(dodecyloxy)benzene-1,2-diamine (0.264 g, 1.52 mmol) were heated to 40 °C in DMF: MeOH (2: 1, 15 ml) under an

atmosphere of nitrogen. 3-Formyl chromone (0.264 g, 1.52 mmol) was then added portionwise, with the reaction mixture turning red instantly. The reaction mixture was refluxed for 4 hours, by which point a large amount of red precipitate had formed around the sides of the round bottomed flask. The reaction mixture was cooled to RT and poured into DCM: H_2O (1:4, 250 ml). The organic layer was extracted and then further washed with H_2O (100 ml), brine (100 ml) and H_2O (2 x 100 ml), before being evaporated to dryness in vacuo. The crude product was then redissolved in petroleum ether (100 ml) and further washed with H_2O (100 ml) and MeOH (2 x 100 ml) before, again, being concentrated in vacuo. The sample was further purified by size exclusion chromatography on Bio-Beads SX-3 using DCM as eluent (408 mg, 50 % yield). MS (MALDI): m/z (%) = 1320.98 $[M+H]^+$ Calculated for $C_{80}H_{118}NiN_4O_8$, C 72.65, H 8.99, N 4.24; found C 72.55, H 8.86, N 4.35. Melting point: 233-235 °C.

6.2.2 Experimental methods

All cyclic voltammetry measurements were carried out in dry DCM using 0.3 M $TBABF_4$ electrolyte in a three electrode system, with each solution being purged with N_2 prior to measurement. The working electrode was a Pt wire surrounded by a plastic casing with an exposed surface area of 2 mm in diameter. The reference electrode was Ag/AgCl calibrated against ferrocene/ferrocenium in the background electrolyte, and the counter electrode was a Pt rod. All measurements were made at room temperature using an μAUTOLAB Type III potentiostat, driven by the electrochemical software GPES. Absorption spectroscopy was recorded using a Jasco V-670 UV/Vis/NIR spectrophotometer. Differential scanning calorimetry (DSC) was carried out between 25-300 °C by Dr John Liggat using a DSC Q1000. Measurements were carried out in aluminium pans using nitrogen as the carrier gas. Single point and geometry optimisation calculations of the isolated complexes were carried out at the B3LYP/6-31G(d,p) level of theory[24-26], using Gaussian 09.[27] Time-dependent DFT calculations were carried out using the polarisable continuum model

(PCM) for DCM which takes into account the effect of solvation. The molecular orbital isosurfaces were visualised using ArgusLab 4.0.[28] Thin films for FET measurements were prepared by spin coating using a WS-650S-6NPP/LITE spin coater made by Laurell Technologies. Films were prepared by rotating at 500 RPM for 30 seconds, followed by 2000 RPM for a final 30 seconds. Glass slides were cleaned by sonication for 15 minutes in solutions of decongestant, deionised water, IPA, acetone and $CHCl_3$. OTS treatment was accomplished by placing dry glass slides into a 5 mmol solution of OTS in anhydrous toluene for 16 hours under an atmosphere of N_2, before removing the slides and carefully rinsing with acetone and $CHCl_3$. For FET characterisation, a bottom contact (Au), bottom gate configuration was used. A heavily doped silicon wafer served as both the substrate and gate electrode, with a 300 nm thermally grown SiO_2 layer as the gate dielectric. FET substrates were cleaned by soaking in solutions of IPA, acetone and $CHCl_3$ for 5 minutes each before being dried under a stream of N_2. Two FET configurations were used, both used interdigitated source and drain electrodes; one possessed an electrode width and gap of 4 μm and the other with an electrode width and gap of 8 μm.

6.3 Results and discussion

Bis-ligand Ni, Cu and Pd complexes, $M(dbda)_2$, were prepared and were found to exhibit NIR absorptions, presumably as a result of the small energy gap between their HOMO and LUMO. The formation of the desired species was confirmed by mass spectrometry, with the expected molecular ion peak, and associated isotopic splitting pattern, being observed for each complex. However, difficulty was encountered in obtaining satisfactory microanalysis for the complexes $Cu(dbda)_2$ and $Pd(dbda)_2$. The proton NMR signals from the Ni(II) and Pd(II) complexes appear broad, with no resolution of peak multiplicity, quite unlike the NMR spectrum obtained for the free ligand, H_2dbda. This may be due to aggregation effects in the complexes. The complexes were purified by size exclusion chromatography using a long column (~ 1 m) and in the case of all three $M(dbda)_2$ complexes two fractions were observed. The first fraction, brown in colour, eluted first and was discarded whereas the second fraction was found to contain the desired compound and had a characteristic colour pertaining to that particular molecule. In all cases the fraction containing the desired complex was then recolumned. Each of the diimine complexes, as well as the free ligand used in the synthesis of these molecules, has a tendency to gradually decompose in the presence of air and light, even when stored under N_2. Prior to carrying out any studies the materials would first be columned as a precautionary measure to ensure that there was no decomposed material present prior to commencing any measurements.

Attempts were made to prepare a series of functionalised tetraaza[14]annulene macrocycles with a planar core and long alkoxy chains around the periphery. Despite obtaining satisfactory microanalysis, NMR and Mass Spectrometry results were less conclusive. Proton NMR signals from all the Ni(II) complexes, which were expected to be diamagnetic, appear broad with poor resolution of the peak multiplicity. The peak broadening may be a consequence of intermolecular aggregation affects resulting in the environment around the metal centre becoming octahedral, and thus

paramagnetic. The NMR of the paramagnetic Cu(II) species also appears broad but this was expected. A wide range of mass spectrometry techniques, including ESI, FAB and CI, were employed but failed to produce spectra assignable to any of the macrocyclic complexes synthesised. The presence of long aliphatic groups around the periphery of these macrocycles has made it difficult to grow single crystals suitable for single crystal XRD, which would definitively determine the reaction products.

As a consequence of the uncertainty surrounding the stability and purity of the majority of the complexes synthesised, the following sections have focused solely on the study of Ni(ddbtaa). The remaining complexes are available to be revisited at a later date.

6.3.1 Electrochemistry

The complex $Ni(dbda)_2$ was characterised using electrochemical techniques cyclic voltammetry (CV) and differential pulse voltammetry (DPV) as shown in Figure 4. The compound exhibits several facile redox processes occurring within the solvent window. Starting with the cyclic voltammetry measurements, on scanning to 0.5 V (vs. Ag/AgCl) an oxidative process was witnessed at 0.28 V with the associated return wave at 0.17 V. The process appears to be chemically reversible but the peak to peak separation of 110 mV is too large for the process to be considered electrochemically reversible by definition. On increasing the scan rate the peak current of the forward and reverse process grows with a slight shift in the peak position; on the forward scan at 0.1 V/s the peak position is at 0.28 V but applying a scan rate of 1 V/s causes the peak maximum to shift to 0.32 V. Likewise with the return wave, at 0.1 V/s the peak maximum is at 0.17 V but at 1 V/s the peak maximum is measured at 0.14 V. On applying negative potentials a reductive process is witnessed at -0.73 V with no return wave associated with this process. On

repeating this scan to -1 V at increased scan rates the reductive process disappears indicating the process is likely to be chemically irreversible. On inspection of the working electrode after scanning to -1 V an off-white, sticky film had been deposited onto the electrode indicating sample decomposition had occurred.

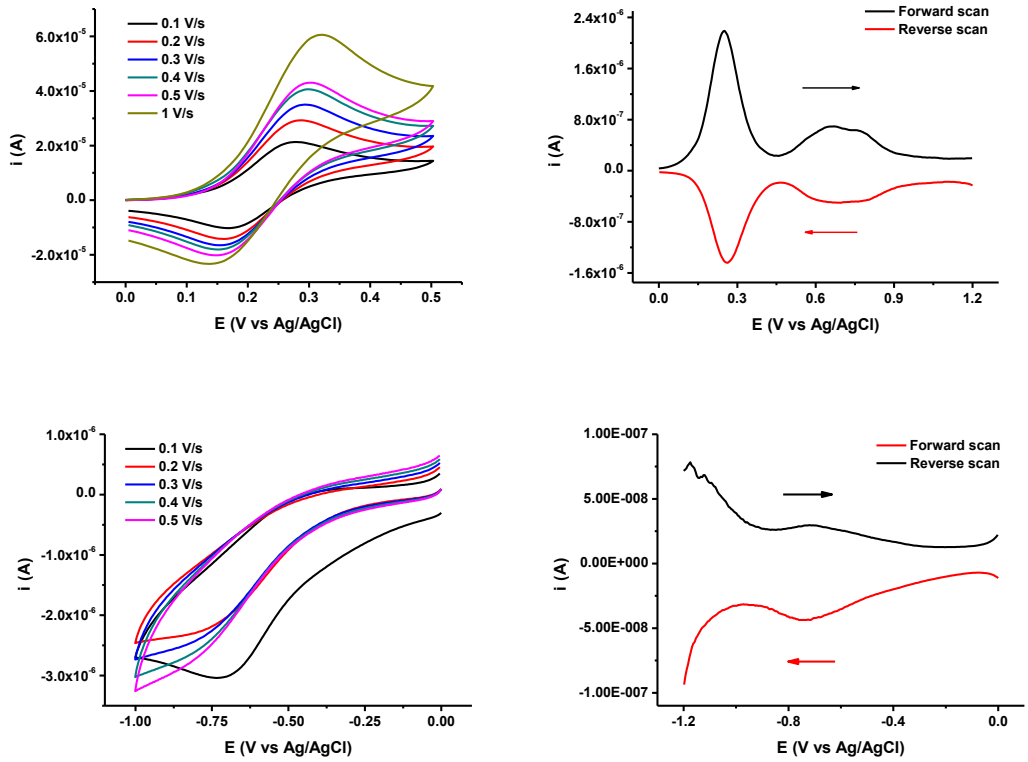

Figure 4 Cyclic voltammetry between 0 and 0.5V (top left), and 0 and -1V (bottom left) and differential pulse voltammogram of $Ni(dbda)_2$ between 0 and 1.2V (top right), and between 0 and -1.2V (bottom right). Measurements carried out in 0.3 M DCM with $TBABF_4$ supporting electrolyte.

Similar to the cyclic voltammetry analysis, differential pulse voltammetry from 0 to 1.2 V also highlights the occurrence of a facile oxidative process occurring at 0.25 V. On further scanning to positive potentials, a second oxidation is witnessed. This appears as a broad, poorly defined peak with a mid-point at approximately 0.7 V (shown in Figure 4, top right). On reversing the direction of the scan and sweeping from 1.2 to 0 V the associated return waves from the oxidative processes are

witnessed, indicating there is a degree of chemical reversibility attributed to both oxidative processes. Scanning from 0 to -1.2 V highlights the reductive process at -0.73 V, which reappears on the reverse scan from -1.2 to 0 V (Figure 4, bottom right).

6.3.2 Absorption spectroscopy

The Ni(II) bis-diaminobenzene complex, $Ni(dbda)_2$, displays a strong transition in the NIR region with lambda max at 1024 nm in DCM (Figure 5, left). Also, shown in the same Figure is the spectrum produced from the free ligand, $dbdaH_2$, in DCM, which shows no absorptions in the visible or NIR region. From the Beer-Lambert plot of $Ni(dbda)_2$ (Figure 5, right), the molar extinction coefficient has been calculated to be approximately 8500 L mol^{-1} cm^{-1}. The straight line fit of absorbance vs. concentration also indicates that this transition at 1024 nm is not the result of aggregation of molecules in solution, and is therefore not an intermolecular transition. Additional transitions were witnessed at 299 and 535 nm. The effect of solvent on the observed absorption spectra was studied in Figure 6; however, only slight differences were observed in the peak position of the low-energy transition. The peak position changed from 1024 nm in DCM, 1,2-dichloroethane and 1,2-dichlorobenzene to 971 nm in hexane and diethyl ether. In toluene this transition appeared at 1011 nm. The trend appears to indicate positive solvatochromism, where the peak position displays a bathochromic shift with increasing solvent polarity. The transitions within the UV and visible region appear largely unaffected by the solvents used and no change in the complex's appearance was noted by optical inspection. The compound has limited solubility in polar solvents such as DMF and alcohols but is more readily solubilised in chlorinated solvents compared to non-polar solvents such as hexane, diethyl ether and toluene.

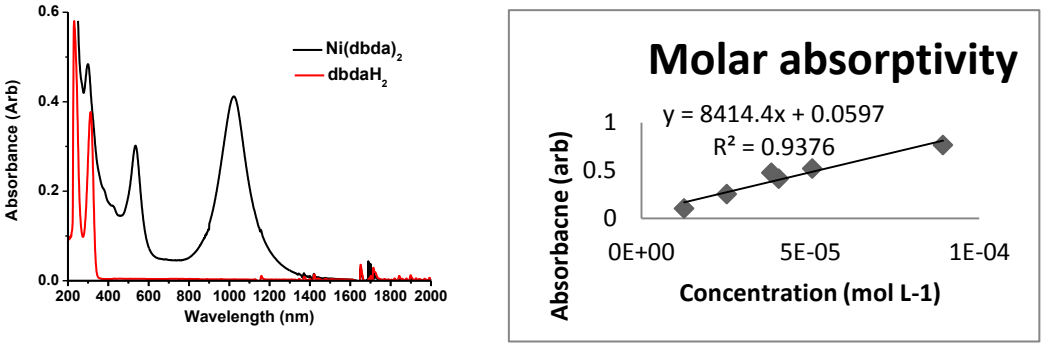

Figure 5 $Ni(dbda)_2$ and $dbdaH_2$ absorption spectra in DCM between 200 and 2000 nm (left) and Beer-Lambert law plot of Absorbance vs. Concentration for the charge transfer process observed at lambda max of 1024 nm in the spectra of $Ni(dbda)_2$ (right).

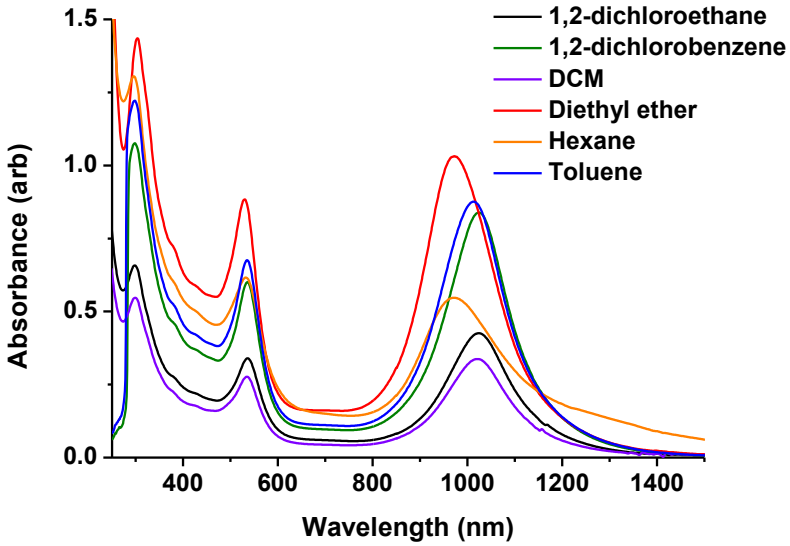

Figure 6 Absorption spectroscopy of $Ni(dbda)_2$ in various non-polar solvents.

Thin-film absorption spectra of $Ni(dbda)_2$ films deposited onto glass slides are shown in Figure 7. Solutions of 12 mg/L of $Ni(dbda)_2$ in 1,2-dichlorobenzene were deposited onto both untreated and OTS treated glass substrates using drop casting and spin coating methods. The effect of surface treatment on the absorption spectra was compared when drop casting material onto a glass substrate (Figure 7, top left);

the compound was deposited onto both a clean glass slide and another clean glass slide that had been subjected to OTS treatment. The resulting spectra appear identical regardless of whether or not surface treatment is employed, although the peak intensity is increased in the OTS coated film this is likely due to a difference in film thickness associated with the limitations of the drop casting method for thin film preparation. Films were also prepared by spin coating from the same solution and the effect of annealing on the resulting absorption spectra was studied (Figure 7, top right). Two films were prepared on cleaned glass, as described earlier, with one glass film annealed at 150 °C for 3 minutes under a blanket of N_2 following sample deposition. However, both spectra appear identical with transitions occurring at 533 and 983 nm regardless of annealing, indicating that thermal treatment at that temperature is having no affect on the structural order of the thin film. Films were also prepared by spin coating onto OTS treated glass slides (Figure 7, bottom) and the effect of thermal annealing compared. The red line shows the absorption spectra of the as prepared thin film; it appears broad and featureless but after annealing at 150 °C for 3 minutes under a blanket of N_2 transitions at 533 and 983 nm can be resolved (Figure 7, bottom). This may be the result of a restructuring of the film associated with the interaction between the OTS SAM and the compound of study. The solution studies indicate that the NIR transition undergoes a bathochromic shift in chlorinated solvents compared with the thin film spectra, with the thin film spectra more closely resembling measurements carried out in solvents such as hexane and diethyl ether.

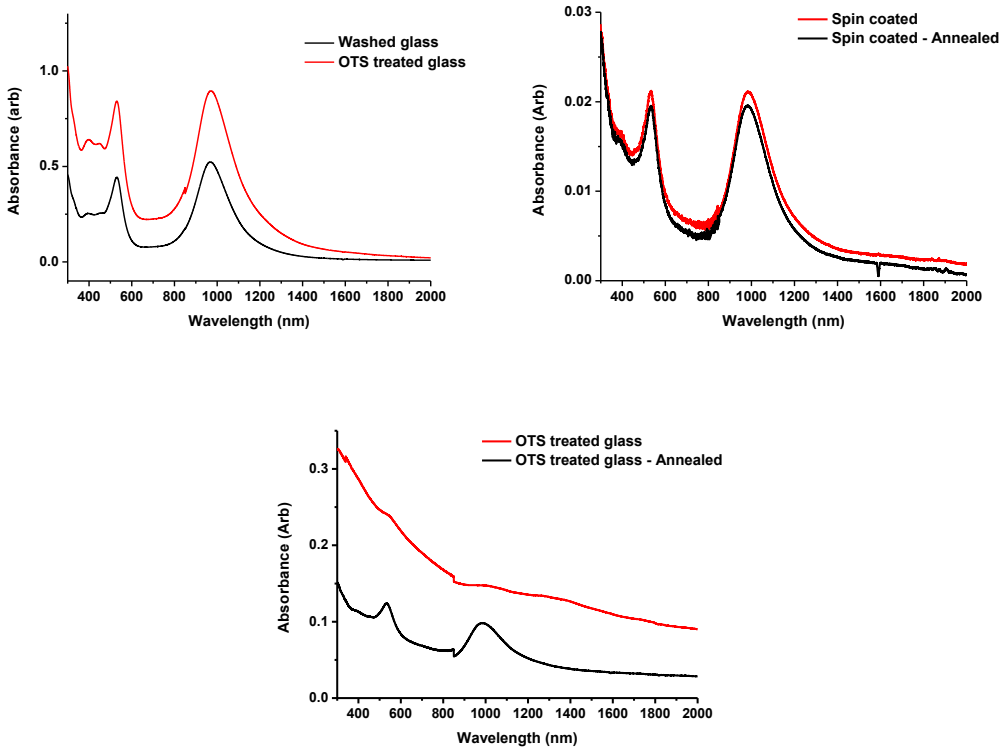

Figure 7 Thin film absorption spectra of $Ni(dbda)_2$ dropcast onto washed glass and OTS treated glass substrates (top, left), spin coated onto washed glass substrates (top, right) and spin coated onto OTS treated glass (bottom, centre). All measurements carried out between 2000 and 300 nm.

6.3.3 Differential scanning calorimetry

Differential scanning calorimetry (DSC) was carried out on $Ni(dbda)_2$ to investigate whether the complex exhibited any phase transitions between 25-350 °C. At 175 °C the onset of a small peak, corresponding to an exothermic process, is observed with a peak minimum at 182 °C. This process is likely due to the sample melting. Following this a large endothermic transition is observed with the peak maxima at 241 °C, which can likely be attributed to the sample decomposing. The lack of any additional peaks, aside from those corresponding to the sample melting and subsequently decomposing, indicates that $Ni(dbda)_2$ does not appear to exhibit liquid-crystalline behaviour.

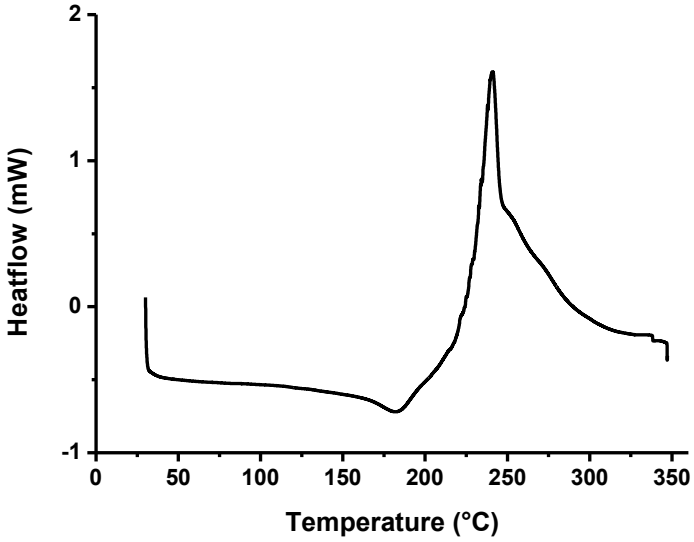

Figure 8 DSC of $Ni(dbda)_2$ between 25-350 °C.

6.3.4 Computational

Calculations have been carried out on $Ni(dbda)_2$ to estimate the energies of the HOMO and LUMO orbitals and to assign the transitions witnessed in the electronic absorption spectra. To save computational time, these calculations have been carried out on molecules carrying ethoxy substituents instead of dodecyloxy substituents; this slight modification should not impact significantly on the predicted electronic structure, from gas phase calculations. From Figure 9 it can be seen that the complex $Ni(dbda)_2$ has a fairly delocalised electronic structure. In the case of the LUMO (Figure 9 (top)) the wave functions are delocalised over the entire molecule with both metal and ligand contributions. In contrast, the HOMO is also delocalised but mainly ligand based. The energy of the HOMO has been calculated as -3.99 eV and the LUMO as –2.44 eV, with respect to the vacuum level. The small HOMO-LUMO gap of ca. 1.5 eV makes this complex, in terms of frontier orbital energies, potentially suitable for ambipolar charge transport in an FET device. The calculated HOMO-LUMO gap is considerably greater than the gap of approximately 1 eV measured electrochemically. The energy of the HOMO orbital indicates that the complex is

likely to be easily oxidisable, perhaps explaining its instability under atmospheric conditions.

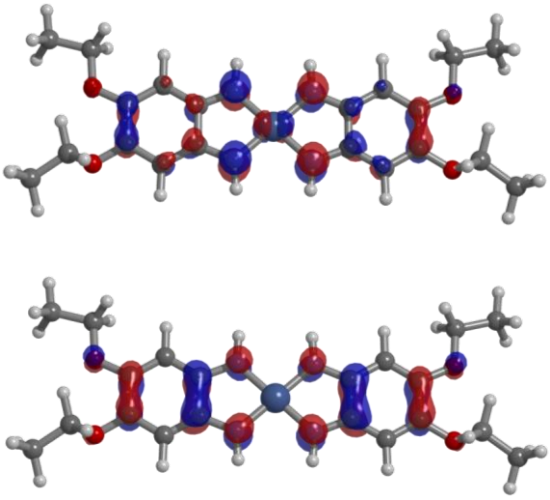

Figure 9 The LUMO (top) and HOMO (bottom) of $Ni(dbda)_2$.

TD-DFT calculations on $Ni(dbda)_2$ have been carried out using the functional B3LYP/6-31G(d,p) in vacuum. The calculation does not model the experimental data well, with the HOMO-LUMO transition observed at 671 nm and no transitions observed in the NIR region of the spectrum. Re-calculating the absorption spectrum using a polarisable continuum model (PCM) for DCM provides a closer match to the experimental data in terms of the lambda max peak position at 921 nm; however, the magnitude of the molar extinction coefficient at around 370,000 L mol^{-1} cm^{-1} is far greater than what was observed experimentally. Experimentally, this transition was recorded in DCM at 1024 nm with a molar extinction coefficient around 8500 L mol^{-1} cm^{-1}.

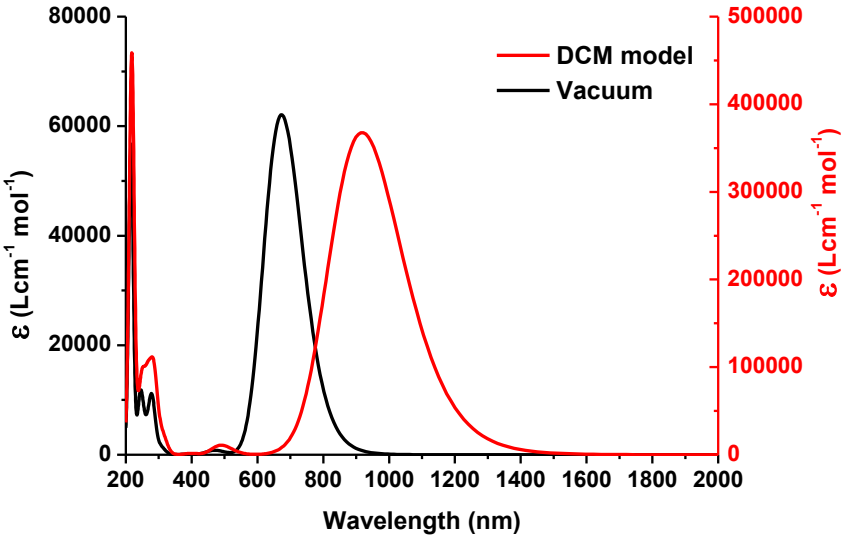

Figure 10 TD-DFT calculation carried out at the B3LYP/6-31G(d,p) level of theory.

6.3.5 FET measurements

The $Ni(dbda)_2$ complex was deposited onto FET substrates via, both, spin coating and drop casting from solutions of 12 mg/L of analyte in 1,2-dichlorobenzene and 12 mg/L of analyte in 1,2-dichloroethane. Two different FET configurations were used; one with Au source and drain electrodes with a width and gap of 4 μm and the other with a width and gap of 8 μm. However, regardless of FET type employed or solvent system use for film fabrication, insulating device behaviour was observed in every instance with no gate effect. The lack of conductivity in a device may be attributed to several factors: may be a consequence of the large mismatch in energy between the electrodes (~5.1 eV vs. vacuum)[29] and the frontier orbitals of the complex; the molecular orientation on the substrate may be unsuitable or the material may be intrinsically insulating. The large alkyl chains may also fold over the molecule and impede intermolecular interactions necessary for charge transport. In the absence of further investigation into the thin film structure and morphology it is impossible to attribute the reason for device failure.

6.4 Conclusions

The syntheses of several potentially interesting bis-ligand diimine metal complexes, M(dbda)2, have been reported. This class of novel complexes represent an interesting extension to the already known family of metal bis-ligand diimine complexes. However, owing to the orbital energy of the HOMO, the materials suffer from instability in air, which makes the necessary purification by column chromatography challenging.

Condensation reactions have been carried out to synthesise a series of soluble tetraaza[14]annulene macrocycles analogous to the compounds reported in Chapter 4. Microanalysis data were obtained indicating the products were of satisfactory purity but in the absence of additional structural information, the decision was taken to postpone further study of these materials until more data can be attained.

Electrochemical and optical analysis revealed that $Ni(dbda)_2$ possesses a small HOMO-LUMO gap, with a facile oxidative process measured electrochemically. FET studies indicated that the $Ni(dbda)_2$ complex was electrically insulating in an FET device with Au electrodes. Likewise, the thin film absorption spectroscopy studies showed no red shifting of the HOMO-LUMO transition indicating that intermolecular interactions were weak.

Future work will focus on the further exploration of modified compounds of this type for optical and electronic applications. In particular, replacement of the alkoxy group to a considerably shorter methoxy or ethoxy substituent may lead to compounds that are both volatile and more easily crystallisable. Single crystal data will provide important information on intermolecular interactions between molecules of this type, crucial to any potential device applications. Volatility may lead to compounds that

could be vapour processed, thus providing an alternative route to the preparation of thin films.

6.5 References

1. Kumar, S., *Pramana* **2003,** *61*, 199-203.
2. Kumar, S.; Varshney, S. K., *Organic Letters* **2001,** *4*, 157-159.
3. Mindyuk, O. Y.; Stetzer, M. R.; Heiney, P. A.; Nelson, J. C.; Moore, J. S., *Advanced Materials* **1998,** *10*, 1363-1366.
4. Dong, S.; Tian, H.; Song, D.; Yang, Z.; Yan, D.; Geng, Y.; Wang, F., *Chemical Communications* **2009**, 3086-3088.
5. Katz, H. E.; Lovinger, A. J.; Johnson, J.; Kloc, C.; Siegrist, T.; Li, W.; Lin, Y. Y.; Dodabalapur, A., *Nature* **2000,** *404*, 478-481.
6. Schmidt-Mende, L.; Fechtenkotter, A.; Mullen, K.; Moons, E.; Friend, R. H.; MacKenzie, J. D., *Science* **2001,** *293*, 1119-1122.
7. Lüssem, G.; Wendorff, J. H., *Polymers for Advanced Technologies* **1998,** *9*, 443-460.
8. Höger, S.; Enkelmann, V.; Bonrad, K.; Tschierske, C., *Angewandte Chemie International Edition* **2000,** *39*, 2267-2270.
9. Kaafarani, B. R., *Chemistry of Materials* **2011,** *23*, 378-396.
10. Patel, B. R.; Suslick, K. S., *Journal of the American Chemical Society* **1998,** *120*, 11802-11803.
11. Grolik, J.; Sieron, L.; Eilmes, J., *Tetrahedron Letters* **2006,** *47*, 8209-8213.
12. Grolik, J.; Dudek, L.; Eilmes, J., *Tetrahedron Letters* **2012,** *53*, 5127-5130.
13. Forget, S.; Veber, M.; Strzelecka, H., *Molecular Crystals and Liquid Crystals Science and Technology. Section A. Molecular Crystals and Liquid Crystals* **1995,** *258*, 263-275.
14. Forget, S.; Veber, M., *Molecular Crystals and Liquid Crystals Science and Technology. Section A. Molecular Crystals and Liquid Crystals* **1997,** *300*, 229-243.
15. Forget, S.; Veber, M., *Molecular Crystals and Liquid Crystals Science and Technology. Section A. Molecular Crystals and Liquid Crystals* **1997,** *308*, 27-42.
16. Forget, S.; Kitzerow, H. S., *Liquid Crystals* **1997,** *23*, 919-922.
17. Konno, Y.; Matsushita, N., *Bulletin of the Chemical Society of Japan* **2006,** *79*, 1046-1053.
18. Warren, L. F., *Inorganic Chemistry* **1977,** *16*, 2814-2819.
19. Carugo, O.; Djinovic, K.; Rizzi, M.; Castellani, C. B., *Journal of the Chemical Society, Dalton Transactions* **1991**, 1551-1555.
20. Noro, S.-i.; Chang, H.-C.; Takenobu, T.; Murayama, Y.; Kanbara, T.; Aoyama, T.; Sassa, T.; Wada, T.; Tanaka, D.; Kitagawa, S.; Iwasa, Y.; Akutagawa, T.; Nakamura, T., *Journal of the American Chemical Society* **2005,** *127*, 10012-10013.
21. Noro, S.-i.; Takenobu, T.; Iwasa, Y.; Chang, H.-C.; Kitagawa, S.; Akutagawa, T.; Nakamura, T., *Advanced Materials* **2008,** *20*, 3399-3403.
22. Lelj, F.; Morelli, G.; Ricciardi, G.; Brigatti, M. F.; Rosa, A., *Polyhedron* **1989,** *8*, 2603-2610.
23. Wicklein, A.; Muth, M.-A.; Thelakkat, M., *Journal of Materials Chemistry* **2010,** *20*, 8646-8652.

24. Becke, A. D., *J. Chem. Phys.* **1993,** *98*, 5648-5652.
25. Lee, C.; Yang, W.; Parr, R. G., *Phys. Rev. B* **1988,** *37*, 785-789.
26. Ditchfield, R.; Hehre, W. J.; Pople, J. A., *The Journal of Chemical Physics* **1971,** *54*, 724-728.
27. Frisch, M. J.; Trucks, G. W.; Schlegel, H. B.; Scuseria, G. E.; Robb, M. A.; Cheeseman, J. R.; Scalmani, G.; Barone, V.; Mennucci, B.; Petersson, G. A.; Nakatsuji, H.; Caricato, M.; Li, X.; Hratchian, H. P.; Izmaylov, A. F.; Bloino, J.; Zheng, G.; Sonnenberg, J. L.; Hada, M.; Ehara, M.; Toyota, K.; Fukuda, R.; Hasegawa, J.; Ishida, M.; Nakajima, T.; Honda, Y.; Kitao, O.; Nakai, H.; Vreven, T.; Montgomery, J. A.; Peralta, J. E.; Ogliaro, F.; Bearpark, M.; Heyd, J. J.; Brothers, E.; Kudin, K. N.; Staroverov, V. N.; Kobayashi, R.; Normand, J.; Raghavachari, K.; Rendell, A.; Burant, J. C.; Iyengar, S. S.; Tomasi, J.; Cossi, M.; Rega, N.; Millam, J. M.; Klene, M.; Knox, J. E.; Cross, J. B.; Bakken, V.; Adamo, C.; Jaramillo, J.; Gomperts, R.; Stratmann, R. E.; Yazyev, O.; Austin, A. J.; Cammi, R.; Pomelli, C.; Ochterski, J. W.; Martin, R. L.; Morokuma, K.; Zakrzewski, V. G.; Voth, G. A.; Salvador, P.; Dannenberg, J. J.; Dapprich, S.; Daniels, A. D.; Farkas; Foresman, J. B.; Ortiz, J. V.; Cioslowski, J.; Fox, D. J., Gaussian 09, Revision B.01. In *Gaussian 09, Revision B.01, Gaussian, Inc., Wallingford CT*, Wallingford CT, 2009.
28. Thompson, M. A. *ArgusLab 4.0.1*, Planaria Software LLC: Seattle, WA.
29. Lee, S.-H.; Lin, W.-C.; Chang, C.-J.; Huang, C.-C.; Liu, C.-P.; Kuo, C.-H.; Chang, H.-Y.; You, Y.-W.; Kao, W.-L.; Yen, G.-J.; Kuo, D.-Y.; Kuo, Y.-T.; Tsai, M.-H.; Shyue, J.-J., *Physical Chemistry Chemical Physics* **2011,** *13*, 4335-4339.